Dual-Phase, Compositionally Complex Alloys: An exploration of $L2_1$-Heusler Phase Reinforcement

---

A Doctoral Thesis Dissertation

Presented to

The faculty of the School of Engineering and Applied Science

At the University of Virginia

In Partial Fulfillment

Of the requirements for the Degree of

Doctor of Philosophy (Materials Science and Engineering)

By

Mark Andrew Wischhusen

December 2023

APPROVAL SHEET

This

Thesis

is submitted in partial fulfillment of the requirements for the degree of

Doctor of Philosophy

Author: Mark Wischhusen

This Thesis has been read and approved by the examining committee:

Advisor: Sean Agnew

Committee Member: Bi-Cheng Zhou

Committee Member: John Scully

Committee Member: James Fitz-Gerald

Committee Member: Joseph Poon

Accepted for the School of Engineering and Applied Science:

Jennifer L. West, School of Engineering and Applied Science

December 2023

Acknowledgements:

To properly acknowledge every person that helped me through graduate school would easily double the length of this document. As such, I will settle for the barest minimum of thanks. Please know that even if you are not mentioned directly here, if we interacted during my tenure at UVA, you likely gave me one of the many small, cumulative pushes I needed to survive.

I would like to thank my advisor, Prof. Sean Agnew, and our research scientist Dr. Jishnu Bhattacharyya for having my back when I needed it, and for keeping cool heads when I was inclined to panic. I would also like to thank my fellow students working under the ONR-CCA project: Samuel Inman, Jie Qi, Diego Ibarra and Peter Connors. Your insight and collaborative efforts were indispensable, as were your commiseration and encouragement. I thank my fellow office-mate Michael Ritzo, largely for tolerating me for such a prolonged period of time, but also for his determination to see our most arduous journeys through to the end. I would like to thank dogs, in general, for existing. I thank my friends and family outside of Virginia, however far they may be. And last, but not least, I would like to thank Tim Horton's Original Roast coffee. Michael, I swear, it's just as smooth today as it was all those years ago.

Table of Contents

List of Figures

List of Tables

Abstract

Many historical alloy development efforts have focused on the improvement of the mechanical properties of alloys, with fewer investigations focused on the improvement of corrosion performance, and fewer still that are focused on a concurrent design focused on both mechanical and corrosion properties. The present study is part of a larger effort which seeks to produce lightweight, low-cost alloys possessing room temperature strength, ductility, toughness and aqueous corrosion resistance. Modern alloy design efforts have produced a new class of metal alloys which are composed of many elements in significant proportion.

In the present case, it is advantageous in an alloy for marine applications to not experience a ductile-to-brittle transition (DBT) at or near its operation temperature, which could be as low as -30 °C. This consideration led to a focus on alloys with a face-centered cubic (FCC) crystal structure, which generally speaking do not suffer from a DBT. However, it was also recognized that many single-phase FCC alloys have only modest mechanical strength. Therefore, within an elemental palette informed by the aqueous corrosion performance of traditional alloys, it was sought to identify candidate 2-phase mixtures which could simultaneously realize strength, ductility and aqueous corrosion resistance. The alloy design process was guided by an innovative machine learning approach. As alloy compositions were varied, a ferritic phase began to emerge within one of the alloys predicted to be single phase FCC, and this second phase was stable even after homogenization annealing at 1070 °C for multiple hours. The alloy, $Al_6Cr_{10}Fe_{40}Mn_5Mo_3Ni_{30}Ti_6$, showed good corrosion performance, on par with stainless steel 316L.

The present dissertation research seizes upon this opportunity by exploring the adjacent chemical and phase space to determine if this corrosion-resistant phase can be leveraged for mechanical strengthening. Additionally, it was sought to determine how amenable these two-phase mixtures were to conventional thermomechanical processing strategies of cold rolling and static annealing, and to what extent their microstructures could be controlled. In-situ neutron diffraction experiments were performed to investigate stress and strain partitioning between phases in FCC matrix plus intermetallic compound reinforced composite alloys.

Scanning- and transmission electron microscopy, as well as x-ray diffraction experiments were able to identify the second phase as having the $L2_1$ "Heusler" phase (Cu_2MnAl archetype) structure. Although Heusler phase compounds are known to be quite brittle at room temperature, there has been little exploration of pairing the Heusler phase with a disordered FCC matrix. In the alloys synthesized, the room temperature brittleness of the Heusler phase was suppressed for two reasons: first it was determined that a level of hydrostatic pressure [1][2] is imposed upon the particles by the deforming ductile austenite matrix and this suppresses the tendency to fracture. The second reason will be detailed below.

The chemical phase space about the original composition was explored using Thermo-Calc software, and Al was identified as the most potent single element for promotion of the Ni_2TiAl Heusler phase. Alloys were synthesized across the predicted two-phase region to establish control over the volume fraction of reinforcing phase present. A strategy based in the "lever rule" was also

devised, whereby the volume fraction of phases may be controlled without altering phase chemistry.

In addition to the amount of reinforcement, it was also sought to establish control over the microstructure of the FCC + $L2_1$ alloys. The dual-phase alloys were found to be generally cold deformable up to 70% reduction in thickness without issue, though alloys with larger Heusler phase did prove to be less formable. The Heusler phase was found to promote finer microstructures after recrystallization annealing, and the alloys seem to adopt an unusual mechanism of continuous recrystallization. The texture of the deformed alloys, as well as the deformed and recrystallized alloys, was found to be generally weak. The FCC matrix showed textures similar to austenitic stainless steels, especially those which contain Mo. Plastic deformation in the $L2_1$ phase was confirmed, and the Heusler phase textures were reminiscent of a BCC metal which had undergone $\{hkl\}\langle 111\rangle$ "pencil glide". Despite the fact that the Heusler phase is an FCC lattice with an ordered basis, it can be visualized as a collection of BCC-like unit cells. Occurrence of BCC type slip behavior suggests that the antiphase domain boundary (APB) energy is low. In this way, the $L2_1$ Heusler phase in these alloys behaves similarly to B2-structured CuZn and FeAl. This ability to accommodate some plasticity via dislocation glide is the second reason why the present $L2_1$ material is not so brittle as previous observations may have suggested.

In-situ neutron diffraction experiments were performed both on a model, FCC + B2 steel (based upon the Fe-Mn-Al-Ni-C system) and the novel FCC + $L2_1$ alloys. Examination of the lattice strains of the FCC+B2 alloys revealed elastically anisotropic behavior in the FCC matrix phase, with considerably less anisotropy in the B2 reinforcement. Elastic constants were derived from the measured diffraction elastic moduli: For the FCC matrix, C_{11} = 174 GPa, C_{12} = 112 GPa, C_{44} = 99 GPa, μ = 56 GPa, E = 159 GPa and Zener anisotropy ratio Z = 3.17, and for the B2 phase, C_{11} = 260 GPa, C_{12} = 162 GPa, C_{44} = 77 GPa, μ = 61 GPa, E = 174 GPa and Z = 1.57. The tests also reveal that the high carbon added to the Fe-Mn-Al-Ni-C alloy is the major source of strength. Elastic constants were also derived for the FCC matrix of the FCC+$L2_1$ CCAs: C_{11} = 178 GPa, C_{12} = 93 GPa, C_{44} = 88 GPa, μ = 61 GPa, E = 167 GPa and Z = 2.08. Both types of alloy exhibit a strong Bauschinger effect, which is typical of such composite type alloys, due to elastoplastic mismatch between matrix and strengthening phases. The in-situ neutron diffraction data permits parsing of the contributions of composite (interphase) and intragranular (dislocation-based) sources of back-stress.

1. Introduction

1.1 Motivation and Background

The present study is part of a larger effort to design lightweight, low-cost compositionally complex alloys (CCAs) with optimized strength, ductility and aqueous corrosion resistance. Within a palette of elements chosen through more traditional corrosion and alloy design sensibilities, a machine learning algorithm has been trained using a combination of attributes from binary phase diagrams and the experimental results of synthesized alloys to efficiently predict which phases will form from a given chemistry. The focus of this design strategy was initially single-phase, FCC alloys, primarily due to their possessing a ductile-to-brittle transition temperature (DBTT) well below the temperature of frigid seawater and their intrinsic lack of galvanic coupling and solute depletion between phases. Despite the positive performance of the ML algorithm for phase prediction, it was found that alloys of a certain chemistry contained a second phase which remained after homogenization treatment. Serendipitously, not only did this unexpected phase not compromise the aqueous corrosion performance of the alloys, but it was also hard, and could potentially serve as a mechanical strengthener. Further study would identify this phase as the $L2_1$-structured "Heusler" phase of a Ni_2TiAl composition, for which Cu_2MnAl is archetypal. This work encompasses a preliminary study of the corrosion properties of $L2_1$-reinforced alloys, how the Heusler phase should solidify in a supposedly single-phase alloy, how the volume fraction of the Heusler phase can be controlled for the purposes of reinforcement and what strengthening effects this nominally brittle phase provides. Further details on the machine learning algorithm and the corrosion performance of these CCAs can be found elsewhere in the literature [3].

The $L2_1$ "Heusler" phase was discovered by German mining engineer and chemist Friedrich Heusler in 1903, who synthesized Cu_2MnAl. [4] At the time, this compound and those that followed it were known as ferromagnetic intermetallics. The "Full-Heusler" structure consists of 4 FCC sublattices, populated by three elements following an X_2YZ chemistry. Later studies would also reveal the "Half-Heusler" $C1_b$ structure, in which one of the X sublattices is unoccupied. Heusler compounds bear a striking similarity to a larger assembly of B2 unit cells, and both the B2 and $L2_1$ superlattices are frequently described as being based on the BCC structure [5][6]. The unit cells of the B2, $C1_b$ and $L2_1$ structures are shown in .1.

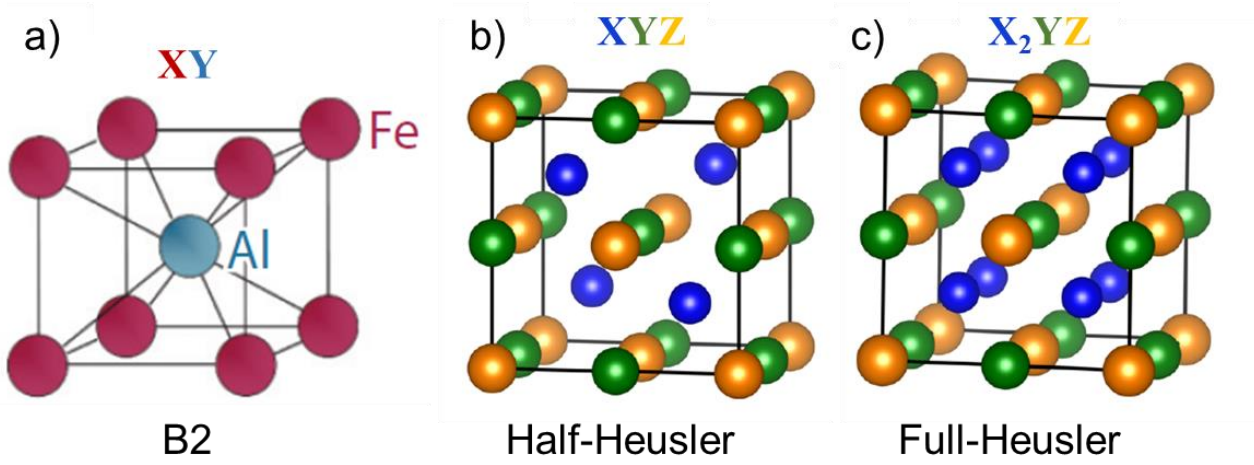

Figure 1.1 – The a) B2, b) "Half-Heusler" $C1_b$ and c) "Full-Heusler" $L2_1$ structures. Images adapted from a) [7] and b, c) [8].

Heusler phase compounds, both half- and full-, are popular topics of study in the fields of spintronics and magnetoelectronics [9], both of which relate to solid state electronics. In this context, Heusler compounds act as "half-metals," possessing the electronic qualities of both metals and semiconductors. Heusler compounds are also commonly observed in explorations of High Entropy Alloys (HEAs) [10]–[13]. The Heusler phase is usually observed alongside disordered FCC and/or BCC phases or various intermetallic compounds, including the $L1_2$ (ordered FCC, e.g. Ni_3Al), B2 (simple cubic, NiAl), Sigma (tetragonal) and Laves (cubic or hexagonal) phases. While the presence of multiple intermetallic phases does not automatically compromise the properties of a material, it does increase the likelihood of competition between phases for passivating elements.

Heusler phases are beginning to appear in studies of both HEAs in addition to their historical appearance in studies of standalone and multiphase intermetallic alloys that seek to develop materials with good high-temperature strength and creep resistance [6][13]–[16]. Such high-temperature intermetallic alloys utilize two- or three-phase microstructures, typically a combination of disordered FCC (γ), ordered $L1_2$ (γ), ordered B2 (β) and $L2_1$ Heusler (β') phases. Of the studies reviewed, combinations such as B2-$L2_1$, B2-$L2_1$-$L1_2$, and FCC-$L1_2$-B2 are the most common, with FCC-$L2_1$ alloys receiving very little attention. These studies unanimously note that the Heusler phase is "catastrophically brittle" [16] at room temperature, and the potential applications of Ni_2TiAl are "handicapped" [6] due to this lack of ductility at ambient temperatures. These same studies also note, however, that a multi-phase microstructure which utilizes a weaker, more ductile phase could compensate for this brittleness to some extent. Furthermore, studies of the room-temperature deformation of intermetallic compounds have noted that the application of hydrostatic pressure can greatly increase the fracture strain of polycrystalline intermetallics at ambient temperature [17][18]. These pressure effects have been observed to occur in two-phase alloys possessing a hard and a soft phase, often resulting in a hardening of the softer phase and a softening of the hard phase [19].

The present study seeks to combine a ductile FCC matrix with the under-utilized Heusler phase as reinforcement in a dual-phase microstructure that will suppress the room-temperature brittleness of the Heusler phase. This combination of phases is fairly novel, with literature dating back only in the past three years [20]–[22]. Inspiration has been taken from dual-phase steels, especially those that utilize ordered intermetallic phases for reinforcement. Two primary examples are a ferritic, B2+$L2_1$-strengthened alloy designed for high temperature creep resistance [14][23][24] and high specific-strength FCC+B2 steel [25]–[27]. The former alloy served as a preliminary study to cultivate characterization techniques for two-phase alloys and to assess the effect of the Heusler phase on the corrosion performance of two-phase alloys, while the latter served as a template for FCC-plus-deformable intermetallic microstructures which possess both high strength (above 1 GPa) and significant room temperature ductility (~30% elongation). It is also sought after to establish control over the volume fraction of the Heusler phase, such that the microstructure of the alloy can be optimized to maximize toughness.

This dissertation is organized as follows. After this introductory paragraph, a previously published preliminary study of the characterization and corrosion properties of dual-phase alloys (Chapter 2) is followed by three manuscripts in preparation (Chapters 3 through 5). The beginning of each chapter will give attribution to the contributions of collaborators. Chapter 3 discusses the origins of the observed $L2_1$ Heusler phase from the perspective of solidification behavior and thermodynamic stability, as supported by microscopy and related characterization methods (e.g. EDS, EBSD, etc.) Chapter 4 discusses the thermomechanical processing response of a series of novel alloys identified by this study, with varying volume fractions of the $L2_1$ Heusler phase, including the evolution of alloy microstructure and crystallographic texture. Chapter 5 discusses the strengthening mechanisms present in dual-phase alloys, and compares the lattice strain behaviors, obtained via neutron scattering experiments conducted at the Oak Ridge National Lab Spallation Neutron Source (BL-7, VULCAN), of a model FCC+B2 high specific strength steel to the novel FCC+$L2_1$ alloys. The references for each chapter are numbered independently, and a list of those references is included at the end of each chapter to facilitate the identification of relevant sources to each topic.

1.2 References

[1] J. J. Bhattacharyya and S. R. Agnew, “Microstructure Design of Multiphase Alloys I - Effects of Strength Contrast and Strain Hardening,” *J. Mech. Phys. Solids*, no. Manuscript submitted for publication.

[2] J. J. Bhattacharyya, M. A. Wischhusen, and S. R. Agnew, “Microstructure Design of Multiphase Alloys II - Use of a Genetic Algorithm and a Vanishing Cracked Particle Model,” *J. Mech. Phys. Solids*, no. Manuscript submitted for publication.

[3] J. J. Bhattacharyya *et al.*, “Lightweight, Low Cost Compositionally Complex Multiphase Alloys with Optimized Strength, Ductility and Corrosion Resistance: Discovery, Design and Mechanistic Understandings,” *Mater. Des.*, vol. 228, p. 111831, 2023, doi: 10.1016/j.matdes.2023.111831.

[4] F. Heusler, “Uber die Synthese ferromagnetischer Manganlegierungen von Fr. Heusler,” in *Verhandlungen der Deutschen physikalischen Gesellschaft*, K. Scheel and R. Assmann, Eds. 1903, pp. 217–220.

[5] M. Yamaguchi and Y. Umakoshit, “The Deformation Behaviour of Intermetallic Superlattice Compounds,” *Prog. Mater. Sci.*, vol. 34, pp. 1–148, 1991.

[6] R. Yang, J. A. Leake, R. W. Cahn, A. Couret, D. Caillard, and M. G., “An In-situ Observation of Dissociated <111> Glide of Ni2AlTi in a Three-Phase Alloy,” *Scr. Metall. Mater.*, vol. 25, no. c, pp. 2463–2468, 1991.

[7] M. Palm, F. Stein, and G. Dehm, “Iron Aluminides,” *Annu. Rev. Mater. Res.*, vol. 49, pp. 297–326, 2019, doi: 10.1146/annurev-matsci-070218-125911.

[8] T. Fang, X. Zhao, and T. Zhu, “Band structures and transport properties of high-performance half-heusler thermoelectric materials by first principles,” *Materials (Basel).*, vol. 11, no. 5, 2018, doi: 10.3390/ma11050847.

[9] I. Galanakis, “Theory of Heusler and Full-Heusler Compounds,” in *Heusler Alloys: Properties, Growth, Applications*, C. Felser and A. Hirohata, Eds. 2015, pp. 3–36.

[10] W. Łoński *et al.*, “Microstructure, magnetic properties, corrosion resistance and catalytic activity of dual-phase AlCoNiFeTi and AlCoNiFeTiSi high entropy alloys,” *J. Alloys Compd.*, vol. 934, 2023, doi: 10.1016/j.jallcom.2022.167827.

[11] C. W. Lin, M. H. Tsai, C. W. Tsai, J. W. Yeh, and S. K. Chen, “Microstructure and aging behaviour of Al5Cr32Fe35Ni22Ti6 high entropy alloy,” *Mater. Sci. Technol. (United Kingdom)*, vol. 31, no. 10, pp. 1165–1170, 2015, doi: 10.1179/1743284715Y.0000000025.

[12] J. Y. He *et al.*, “A precipitation-hardened high-entropy alloy with outstanding tensile properties,” *Acta Mater.*, vol. 102, pp. 187–196, 2016, doi: 10.1016/j.actamat.2015.08.076.

[13] A. W. Carruthers, H. Shahmir, L. Hardwick, R. Goodall, A. S. Gandy, and E. J. Pickering, “An assessment of the high-entropy alloy system VCrMnFeAlx,” *J. Alloys Compd.*, vol. 888, p. 161525, 2021, doi: 10.1016/j.jallcom.2021.161525.

[14] G. Song, “Microstructure and Creep Deformation Behavior of a Hierarchical-Precipitate-Strengthened Ferritic Alloy with Extreme Creep Resistance,” University of Tennessee, Knoxville, 2016.

[15] Y. Mishima, E. H. Lee, and C. T. Liu, “Microstructure, Phase Consitiution and Tensile Properties of Co-Ni-Ti-Al Base Multi-Phase Intermetallic Alloys,” *Mater. Trans.*, vol. 36, no. 8, pp. 1031–1040, 1995.

[16] R. W. Cahn, “Multiphase intermetallics,” *Philos. Trans. R. Soc. London A*, vol. 351, pp. 497–509, 1995.
[17] R. W. Margevicius and J. J. Lewandowski, “The Influence of Hydrostatic Pressure on Fracture of Single-Crystal and Polycrystalline NiAl,” *Metall. Mater. Trans. A*, vol. 25A, no. July, pp. 1457–1470, 1994.
[18] J. J. Lewandowski and P. Lowhaphandu, “Effects of hydrostatic pressure on mechanical behaviour and deformation processing of materials,” *Int. Mater. Rev.*, vol. 43, no. 4, pp. 145–187, 1998, doi: 10.1179/imr.1998.43.4.145.
[19] L. Zhonghua and G. Haicheng, “Hydrostatic Stresses and Their Effect on the Macroflow Behavior and Microfracture Mechanism of Two-Phase Alloys,” *Metall. Trans. A*, vol. 22A, pp. 2695–2702, 1991, doi: 10.1007/BF02851363.
[20] Z. Sun, “Microstructures and Mechanical Behavior of NiAl-Strengthened Ferritic Alloys at Room and Elevated Temperatures,” University of Tennessee, Knoxville, 2015.
[21] G. Song *et al.*, “Ferritic Alloys with Extreme Creep Resistance via Coherent Hierarchical Precipitates,” *Sci. Rep.*, vol. 5, pp. 1–14, 2015, doi: 10.1038/srep16327.
[22] S. Kim, H. Kim, and N. J. Kim, “Brittle intermetallic compound makes ultrastrong low-density steel with large ductility,” *Nature*, vol. 518, pp. 77–79, 2014, doi: 10.1038/nature14144.
[23] G. Park, C. H. Nam, A. Zargaran, and N. J. Kim, “Effect of B2 morphology on the mechanical properties of B2-strengthened lightweight steels,” *Scr. Mater.*, vol. 165, pp. 68–72, 2019, doi: 10.1016/j.scriptamat.2019.02.013.
[24] M. X. Yang, F. P. Yuan, Q. G. Xie, Y. D. Wang, E. Ma, and X. L. Wu, “Strain hardening in Fe-16Mn-10Al-0.86C-5Ni high specific strength steel,” *Acta Mater.*, vol. 109, pp. 213–222, 2016, doi: 10.1016/j.actamat.2016.02.044.

2. Pitting Corrosion Susceptibility of Microstructural Features in a Compositionally Complex, Ferritic Steel as a Function of Titanium Concentration

This chapter was submitted to CORROSION Journal and published online in March 2022 with co-authors Carol Glover, Peter K. Liaw, John R. Scully and Sean R. Agnew[1]:

Mark Wischhusen, Carol Glover, Peter K. Liaw, John R. Scully, Sean Agnew; Pitting Corrosion Susceptibility of Microstructural Features in a Compositionally Complex Ferritic Steel as a Function of Titanium Concentration. *CORROSION* 1 March 2022; 78 (3): 280–292. doi: https://doi.org/10.5006/3933

2.1 Abstract:

Compositionally and/or microstructurally complex alloys present multiple opportunities for achieving and optimizing desirable qualities that are not typically accessible through traditional single-principle-component alloying methodologies, without significant compromise. FBB8+Ti, a novel ferritic steel strengthened by Heusler- and B2-phase strengthening phases is one such alloy, and is investigated here across a range of Ti concentrations for its corrosion performance in a Cl^- environment. Pitting potentials, corrosion rates and passivation current densities were established for alloys of each composition when prepared to a 0.05 μm finish and, separately, with a subsequent ion-polish and fully immersed in 0.01 M NaCl. Scanning electron microscopy was used to identify microstructural phases that were vulnerable to metastable pitting on the scale of the microstructural features enabled by a series of potentiostatic holds in the passive region where nascent breakdown/repair occurs. No significant trend in corrosion behavior was observed with Ti content variance for specimens polished to a 0.05 μm finish within the range of compositions investigated, suggesting that alloy design may be optimized in terms of mechanical and thermal performance without penalty in corrosion behavior. Preferred sites of pit initiation were sensitive to the surface finish, highlighting the delicate balance between the possible pitting sites. Results were compared to SS 316L where the passive current density for the FBB8 alloys was found to be favorable, despite slightly lower pitting potentials.

[1] Author contributions: **Mark A. Wischhusen**: Investigation, Formal Analysis, Writing (Original Draft), **Carol Glover**: Investigation and Formal Analysis (Corrosion testing), Writing (Original Draft), **Peter K. Liaw:** Resources, **John R. Scully:** Conceptualization, Funding Acquisition and Writing (Review & Editing), **Sean R. Agnew:** Conceptualization, Funding Acquisition and Writing (Review & Editing)

2.2 Introduction

The ability to tune material properties is highly desirable when designing alloys for applications that involve harsh service conditions. Materials that can withstand the high steam temperature and pressure environment required for optimum thermal efficiency in fossil-fueled power plants is of particular interest. Currently, austenitic steels and Ni-based superalloys are capable of meeting the required creep resistance and high-temperature strengths [1][2], but neither possess adequate resistance to thermal fatigue [1][2]. In contrast, ferritic steels have superior resistance to thermal fatigue but are limited by their high-temperature creep and corrosion resistance and are therefore restricted to lower temperature applications [1][2]. Modification of ferritic steels to elevate the maximum operating temperatures, while retaining their lower cost [2] and fatigue resistance properties, is highly desirable for power generation applications.

A new class of compositionally and microstructurally complex, creep resistant ferritic steels, FBB8+Ti, was recently developed by researchers at the University of Tennessee [1][2]. This class of alloys is a strong candidate material for high temperature applications due to good creep resistance, which has been shown to be within the range from 0 – 6 wt% Ti [3]. The FBB8+Ti alloy system has been shown to transition from a coherent, hierarchical B2+Heusler ($L2_1$) precipitate structure at Ti concentrations less than 4 weight percent (wt%) to a semi-coherent Heusler phase precipitate structure at concentrations greater than or equal to 4 wt% Ti [1][3][4]. It has been theorized that this enhanced creep resistance is imparted by the hierarchical nature of the coherent B2+Heusler precipitates, with high misfit strains due to Ti additions [1]. Song et. al. suggest that the hierarchical structure impedes shearing of the strengthening precipitates by dislocations. [5] Compositionally and microstructurally complex alloys such as FBB8 provide a large number of degrees of freedom in alloy design (i.e., X% A, Y% B, Z% C), and such alloys suggest new paths to optimize multiple desirable properties in cases where traditional alloying methodologies cannot.

To date, there have been no quantitative investigations of the high temperature oxidation performance, nor room temperature aqueous corrosion behavior, of the FBB8+Ti alloy system to the authors' knowledge. The aim of the present study is to determine the effect of Ti content on the microstructure and the room temperature aqueous corrosion performance, to determine whether optimization based solely on mechanical properties induces severe consequences for corrosion resistance. The corrosion rate (icorr), pitting potential (Epit) and current density within the passive region (ipass) are assessed and compared to SS 316L. The location of metastable pitting is investigated to give further details on the pitting susceptibility of the alloys specific to phases within the microstructure. These experiments were conducted at two levels of surface finish i.e. at 0.05 µm and, separately, with a subsequent ion polish, to investigate an observed sensitivity to surface preparation. The link between the microstructure and aqueous corrosion performance of

this new class of compositionally and microstructurally complex, creep resistant ferritic steels is discussed.

2.3 Experimental Methods

The base alloy used is this study was a creep-resistant iron alloy known as FBB8 with a composition of Fe-6.5Al-10Cr-10Ni-3.4Mo-0.25Zr-0.005B (wt%). Systematic additions of Ti were made between 2 and 6 wt%. The alloys were prepared by Sophisticated Alloys, Inc. via arc-melting and drop-casting in a copper mold (Butler, PA). Full details about sample preparation can be found in the literature [3].

Specimens were sectioned using a diamond-abrasive wafering saw followed by homogenization at 1200 °C for 4 hours in a graphite furnace with a flowing-argon environment. Furnace cooling was carried out at a rate of 300 °C per hour (this was determined by the maximum available cooling rate of the furnace). All of the alloys investigated have been shown to have a BCC (ferrite) matrix, that is strengthened by thermally-stable, coherent and/or semi-coherent precipitates that have the full Heusler (Ni2TiAl) and B2 (NiAl) structures. Both precipitate structures exhibit solubility for Fe [1].

To assess the aqueous corrosion behavior of the FBB8+Ti alloys, samples containing each Ti concentration were prepared to a 0.05 μm finish and a second set was prepared where samples were flat-milled in a Hitachi 4000 Ion Polisher for 30 minutes, using an accelerating voltage of 6 kV, a rotation speed of 1 per second, and a tilt angle of 10°. This was performed in an effort to assess the intrinsic passivation behavior of each alloy chemistry and its associated microstructure, in the absence of extrinsic factors such as surface roughness and plastic damage [6]. A reference sample of 316L stainless steel was prepared using the same methods.

2.3.1 Scanning Electron Microscopy

Specimens of three different compositions, 2.0, 3.5, and 6.0 wt% Ti, were selected for SEM imaging and microstructure analysis. To prepare samples for imaging, standard metallographic grinding and polishing preparations down to a final 0.05 μm colloidal silica polish were used. To determine the average precipitate size and volume fraction, SEM micrographs were acquired on a FEI Quanta 650 FEG-SEM at 10,000 times magnification. Subsequent image analysis was performed using ImageJ software [7]. Most of the precipitates were equiaxed in appearance, so individual particles were approximated as circles to obtain average precipitate diameters. To detect the location of meta-stable pitting events using SEM, minimal ambiguity between phase contrast and polishing is required. As such, a more stringent polishing protocol was employed to minimize plastic damage introduced by polishing. The polishing steps described above were employed for

longer time periods to minimize the depth of strained material retained from the previous polishing step followed by flat-milling in a Hitachi 4000 Ion Polisher for 30 minutes.

The chemical composition of each alloy was determined using the Energy Dispersive Spectroscopy (EDS) capabilities of the Quanta 650 SEM and Oxford Instrument's AZtec® software. In order to get an accurate measurement of each phase, samples were mechanically polished, then further thinned to approximately 100 nm via twin-jet electropolishing in a 10 wt% perchloric acid (60% w/w) in methanol electrolyte at -30°C and an applied potential of 30 V. The polishing temperature was controlled with a chilled methanol bath. Due to the brittle nature of FBB8 at low temperatures, an ultrasonic disc cutter was used to prepare the 3 mm disks, rather than a punch. Foil samples, similar to those typically used for transmission electron microscopy (TEM), were prepared in order to reduce the amount of background signal generated by the electron interaction volume below the sample surface during EDS. In other words, a thin sample should allow a closer connection between what is visible in a micrograph and the data obtained from EDS.

2.3.2 X-ray Diffraction

Sample preparation for X-ray diffraction experiments used similar mechanical polishing procedures as detailed above, but were only performed to a 1200-grit SiC paper finish. Powder diffraction experiments were performed on bulk samples in a Malvern-Panalytical Empyrean X-ray Diffractometer utilizing Bragg-Brentano scanning geometry and a sample rotation speed of 1 revolution per second. A Cu X-ray source was used at an accelerating voltage of 45 kV and a beam current of 40 mA.

2.3.3 Optical Profilometry

Samples examined via optical profilometry were prepared using the mechanical and ion-polishing procedures described above. The sample surface at each preparation state was examined using a Zygo NewView 7300 white-light profilometer with a vertical resolution of 0.1 nm. Ten areas, measuring 110 μm by 140 μm were examined.

2.3.4 Electrochemical corrosion measurements

Anodic-upward potentiodynamic polarization scans were conducted on each alloy to determine the potential at which stable pitting occurs. This is denoted by a sharp increase in current density following a region of passivity, where the current density remains relatively constant with increasing applied potential [8]. An exposed area of 1 cm2 was fully immersed in aerated, 0.01 M

aqueous NaCl solution and held at the open circuit potential (OCP) for 30 min prior to anodic polarization using a standard calomel electrode (SCE) and a Pt mesh counter electrode. The ambient pH was approximately 5.6. Anodic polarization was conducted at a scan rate of 1 mV/sec until the pitting potential (Epit) was reached. A starting potential of -0.01mV vs. OCP was used in order to capture the open circuit corrosion potential (Ecorr). Experiments were conducted in triplicate in each condition in order to assess reproducibility.

To determine pit initiation sites, a procedure was used to ensure that early-stage pitting was captured in the meta-stable phase before pits grew beyond the size of the exposed microstructural features at which they originated. A series of potentiostatic holds was performed in the same solution conditions as described above, starting at + 0.25 V vs. SCE for each alloy, and the resultant current density was monitored. Potentiostatic holds were applied until the current decayed to zero, after which the specimen was held for 20 min at OCP. This process was continued in intervals, systematically increasing the potential by 0.05 V at each interval until Epit was reached. At that point, the specimen was immediately removed from solution and rinsed with DI water. Imaging was conducted with both secondary and backscattered electron signals at 20,000 times magnification using the Quanta 650 SEM. This analysis provides a somewhat controlled set of conditions to observe pit initiation at the sub-micrometer scale and enables metastable pitting events occurring in the passive region to be detected and related to the microstructure [9]-[11].

2.4 Results

2.4.1 Characterization of FBB8+Ti alloys using SEM imaging and X-ray Diffraction

Three compositions of the FBB8+Ti system were analyzed for precipitate size and volume fraction. As observed previously, no significant difference in microstructure was observed between the as-cast and homogenized state for any of the compositions investigated [12]. Therefore, only representative backscattered electron images of homogenized specimens with (a) 2 wt%, (b) 3.5 wt% and (c) 6 wt% Ti additions are presented in Figure 2.1.

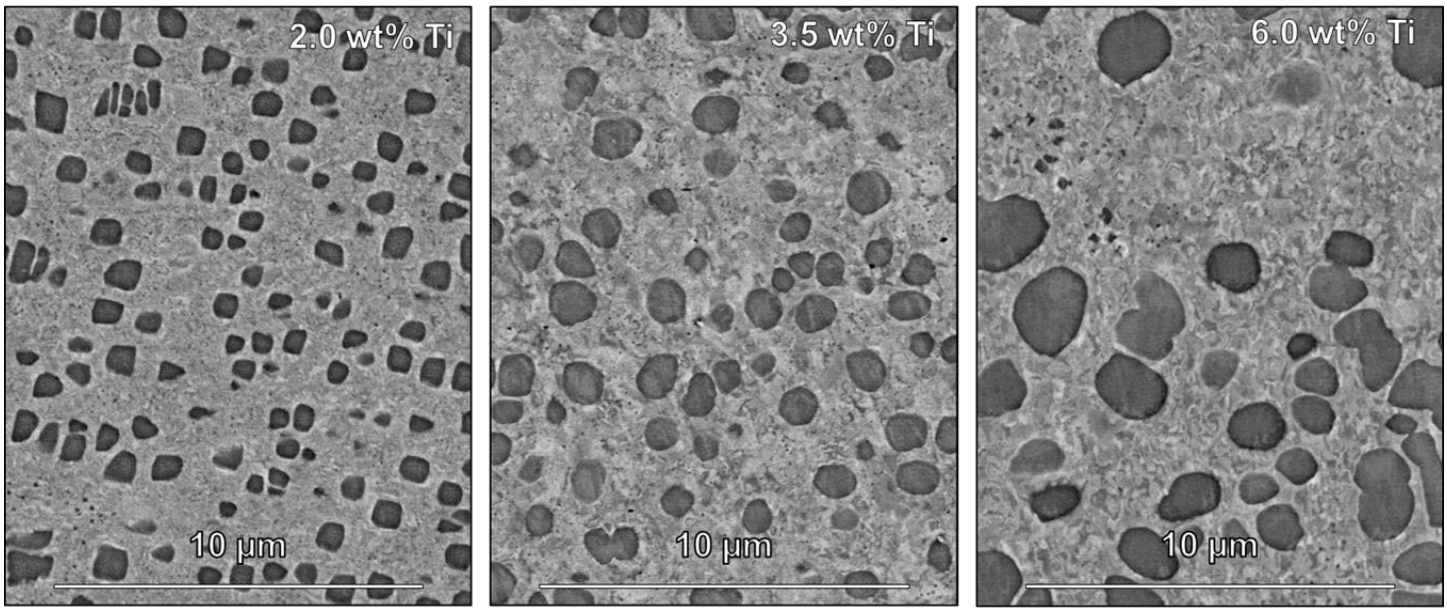

Figure 2.1: Representative backscattered electron images of homogenized (1200°C for 4 hrs) FBB8 specimens with (a) 2 wt%, (b) 3.5 wt% and (c) 6 wt% Ti additions.

The titanium additions are known to stabilize and preferentially partition to the Ni2TiAl Heusler phase, [1] which results in a monotonic relationship between the two, i.e., higher titanium content in the alloy leads to a higher volume fraction of larger Heusler phase precipitates. Volume fractions and average precipitate diameters as a function of Ti are listed in Table 2.1 and shown in Figure 2.2.

Table 2.1: Numerical data from Figure 2.2. The uncertainties listed are standard deviations.

Wt % Ti	Precipitate Diameter (µm)	Precipitate Volume Fraction (%)
2.0	0.608 ± 0.162	22.5 ± 1.6
3.5	0.846 ± 0.277	25.1 ± 2.4
6.0	1.152 ± 0.574	31.6 ± 3.8

The composition of each phase, obtained via SEM EDS, as well as the nominal compositions of the 2.5 and 6.0 wt% Ti alloys are listed in Tables 2.2 and 2.3. Representative EDS maps of 2.5 wt% Ti and 6.0 wt% Ti can be found in Figures 3 and 4, respectively.

Good agreement was observed between the observed compositions and those reported in the literature [1][4]. Ti preferentially partitions into the precipitate phase, which also contains Ni and Al, which can incorporate Fe in addition to small amounts of Cr and Mo leading to some off-stoichiometry (as compared to Ni2TiAl). In agreement with findings presented by Song, [1] an elevated ratio of Al to Ti was observed in the 2.5 wt% Ti specimens. However, this was not the

case for specimens with 6 wt% Ti. Across all samples, the ferrite matrix was enriched in Cr, Fe, and Mo, and the precipitate phase contained more Zr than the matrix. Some of the apparent differences in the composition of the precipitate in the 2.5 wt% Ti alloy are ascribed to the smaller size of the strengthening particles. EDS composition-color maps are shown in Figure 2.3 and Figure 2.4. While the precipitates in the 6 wt% Ti alloy are large enough to contain the electron interaction volume during EDS, the diameter of precipitates in the 2.5 wt% sample is typically smaller than the interaction volume. This leads to some sampling of the Fe matrix surrounding the particle when characterizing the 2.5 wt% samples.

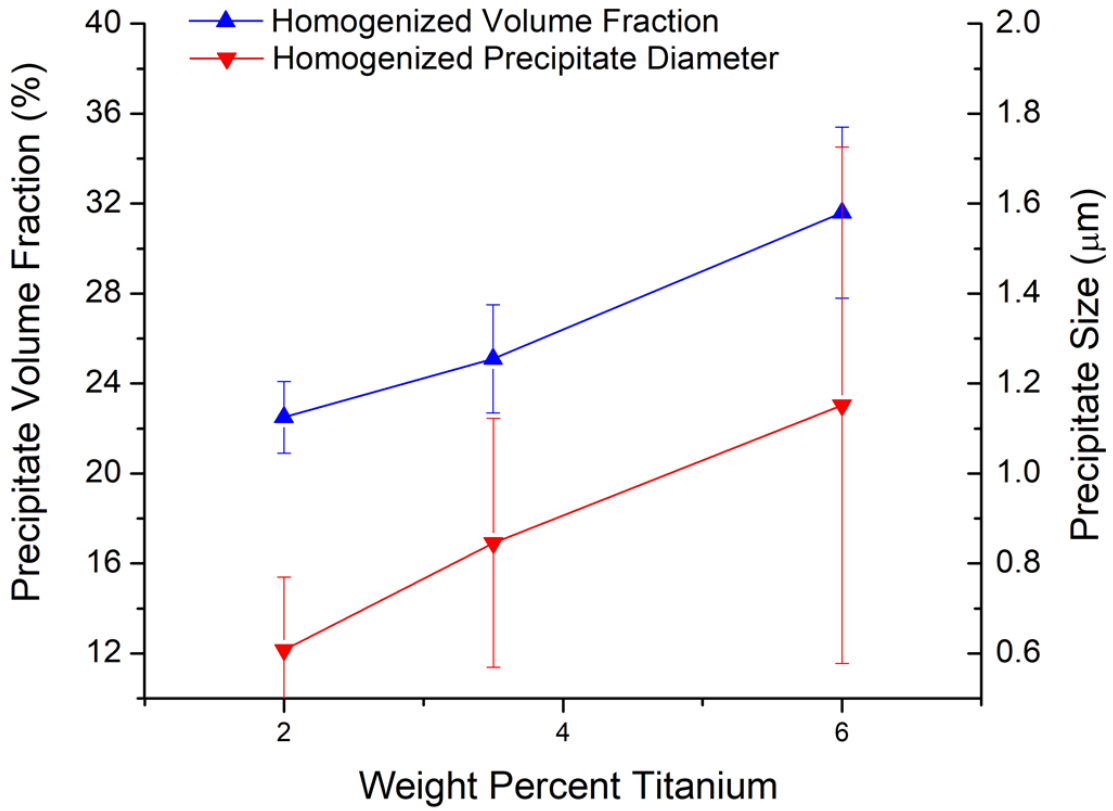

Figure 2.2: The volume fraction and size of the precipitate phase was found to vary monotonically with titanium concentration.

X-ray diffraction experiments confirm the presence of ferrite (110), (200), (211), and (220) peaks and the $L2_1$ (220), (422), and (440) peaks, but the B2 phase could not be clearly distinguished [14]. Diffraction data are shown in Figure 2.5, and it can be seen that the peaks corresponding to the $L2_1$ phase are displaced slightly in 2θ from those of the BCC matrix, indicative of the slight coherency mismatch present in this system. Differences in the relative intensities of equivalent peaks between samples can be attributed to texture in the material or a poor sampling of crystallites (i.e., large grain size.)

Table 2.2: SEM-EDS measured compositions, in atomic percent (at%), of each phase found in FBB8-2.5wt% Ti compared to those reported in the literature. Compositions for 2 wt% Ti are used as a closest available comparison. The uncertainties listed are standard deviations.

	(atomic %)	Al	Ti	Cr	Fe	Ni	Zr	Mo
Current Study FBB8-2.5 Ti	Precipitate	19.0 ± 0.1	8.3 ± 0.1	4.5 ± 0.1	38.1 ± 0.1	28.9 ± 0.1	0.2 ± 0.1	0.9 ± 0.1
	Matrix	7.4 ± 0.1	1.6 ± 0.1	12.4 ± 0.1	71.9 ± 0.1	4.6 ± 0.1	0.03 ± 0.04	1.9 ± 0.1
	Nominal	9.8 ± 0.02	3.3 ± 0.02	9.8 ± 0.04	64.4 ± 0.1	11.0 ± 0.1	0.04 ± 0.02	1.7 ± 0.04
Baik et. al. (2018) FBB8-2 Ti [4]	Precipitate	32.2 ± 0.5	13.1 ± 0.4	0.6 ± 0.1	17.4 ± 0.5	35.7 ± 0.5	0.3 ± 0.1	0.9 ± 0.1
	Matrix	6.6 ± 0.3	0.4 ± 0.1	12.5 ± 0.02	76.2 ± 0.4	1.8 ± 0.1	0.1 ± 0.02	2.2 ± 0.1
	Nominal	11.4	2.2	10.5	65.0	8.9	0.2	1.8
Song (2016) FBB8-2 Ti [1]	Precipitate	34.0 ± 0.2	9.8 ± 0.2	0.7 ± 0.1	18.3 ± 0.2	36.8 ± 0.2	---	0.4 ± 0.01
	Matrix	6.3 ± 0.1	0.3 ± 0.02	12.5 ± 0.1	77.2 ± 0.2	1.3 ± 0.04	---	2.3 ± 0.04
	Nominal	---	---	---	---	---	---	---

Table 2.3: SEM-EDS measured compositions, in atomic percent (at%), of each phase found in FBB8-6wt% Ti compared to those reported in the literature. Compositions for 4 wt% Ti are used as a closest available comparison. The uncertainties listed are standard deviations.

	(atomic %)	Al	Ti	Cr	Fe	Ni	Zr	Mo
Current Study FBB8-6 Ti	Precipitate	19.6 ± 0.1	19.6 ± 0.1	2.4 ± 0.1	29.1 ± 0.1	28.4 ± 0.1	0.2 ± 0.03	0.5 ± 0.04
	Matrix	6.2 ± 0.1	2.0 ± 0.1	13.3 ± 0.1	73.9 ± 0.1	2.4 ± 0.1	0.04 ± 0.04	2.3 ± 0.04
	Nominal	10.2 ± 0.04	7.7 ± 0.03	10.5 ± 0.03	59.8 ± 0.1	9.9 ± 0.1	0.05 ± 0.02	1.9 ± 0.02
Baik et. al. (2018) FBB8-4 Ti [4]	Precipitate	27.5 ± 0.3	18.2 ± 0.3	0.6 ± 0.2	19.3 ± 0.3	33.5 ± 0.3	0.1 ± 0.02	0.9 ± 0.1
	Matrix	6.8 ± 0.2	0.4 ± 0.04	13.1 ± 0.2	75.6 ± 0.3	2.0 ± 0.1	0.02 ± 0.01	2.1 ± 0.1
	Nominal	10.9	4.2	10.3	63.1	9.4	0.2	1.9
Song (2016) FBB8-4 Ti [1]	Precipitate	25.0 ± 2.0	16.5 ± 0.9	1.0 ± 0.7	22.9 ± 3.7	33.8 ± 1.9	0.5 ± 0.3	0.1 ± 0.1
	Matrix	7.0 ± 0.4	1.0 ± 0.1	12.8 ± 0.2	74.9 ± 0.5	2.1 ± 0.2	0.2 ± 0.1	2.0 ± 0.2
	Nominal	12.8	4.5	10.1	61.6	8.9	0.1	1.9

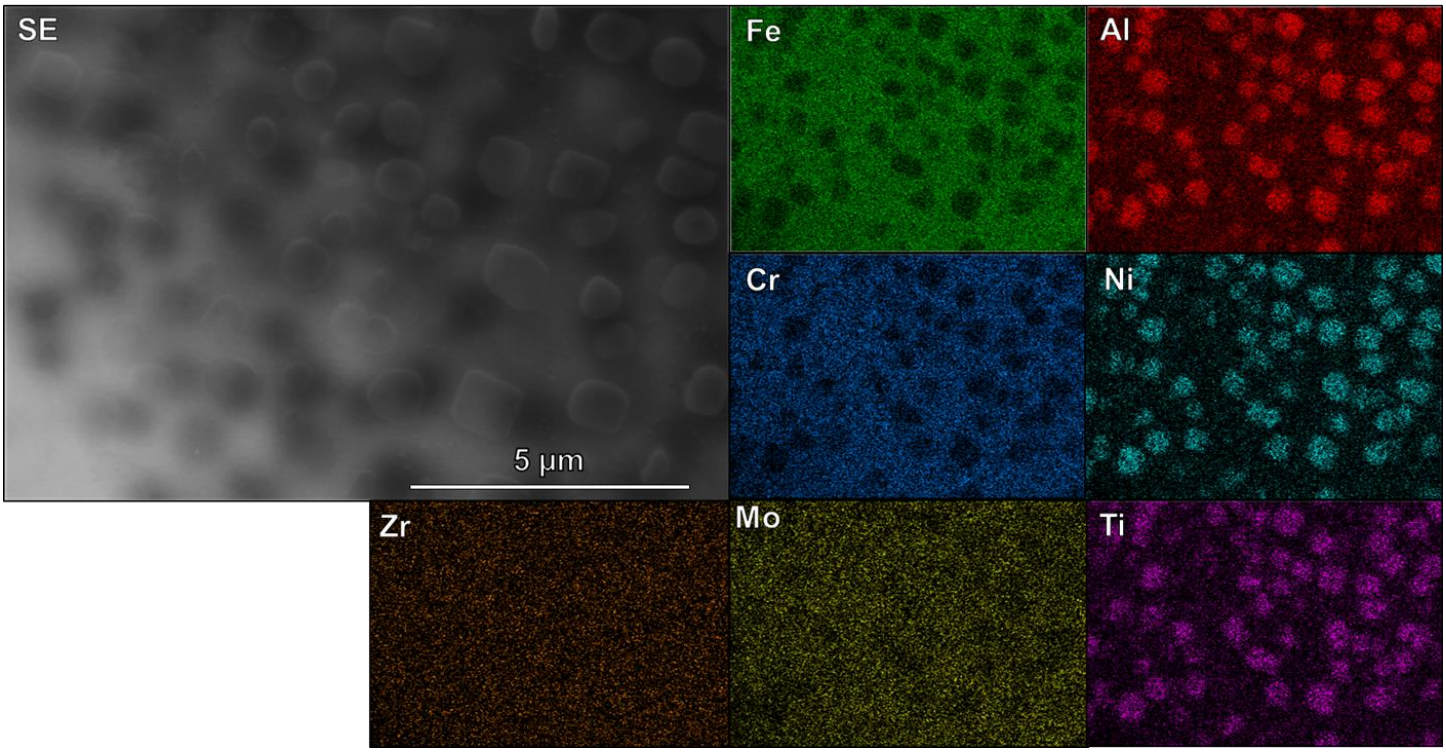

Figure 2.3: SEM-EDS map of the jet-thinned (TEM foil) 2.5 wt% Ti sample.

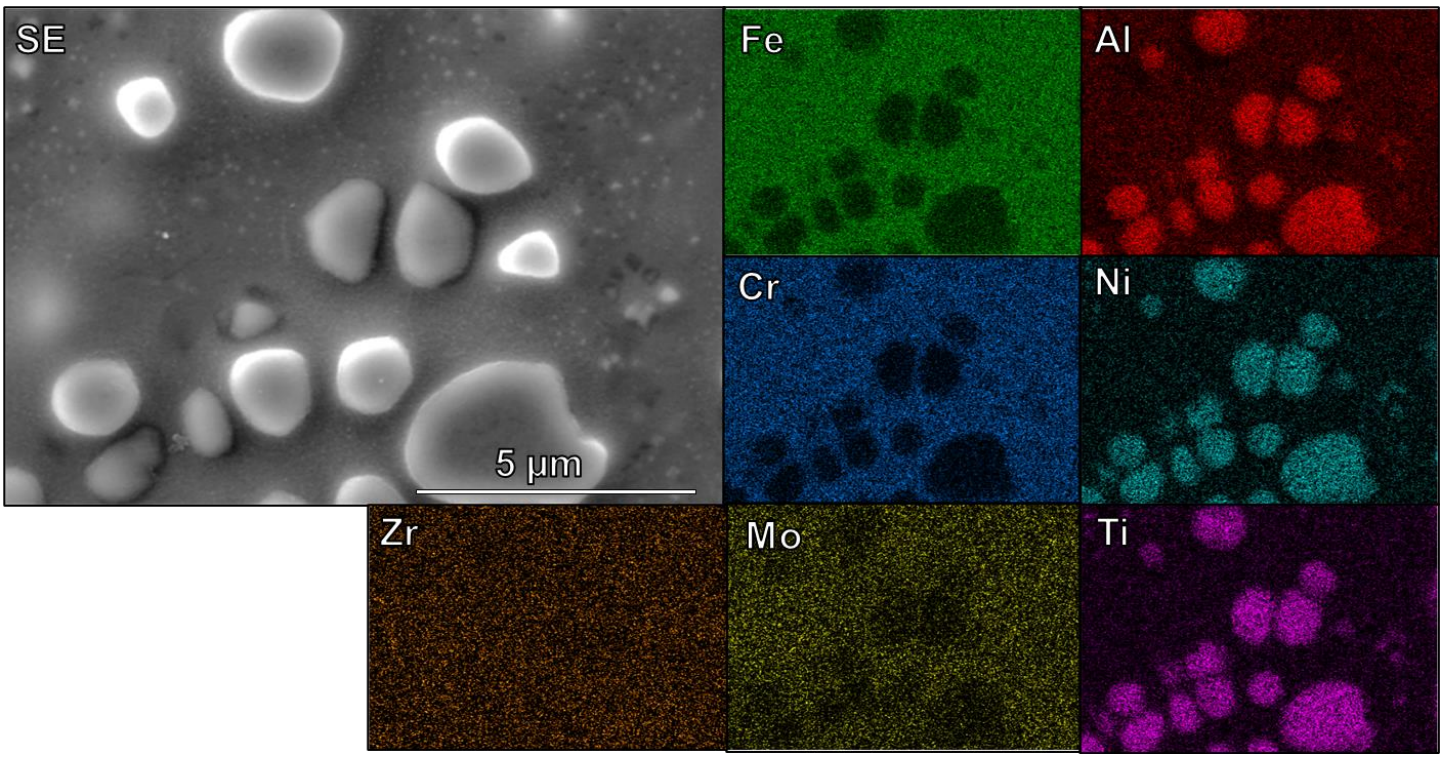

Figure 2.4: SEM-EDS map of the jet-thinned (TEM foil) 6.0 wt% Ti sample.

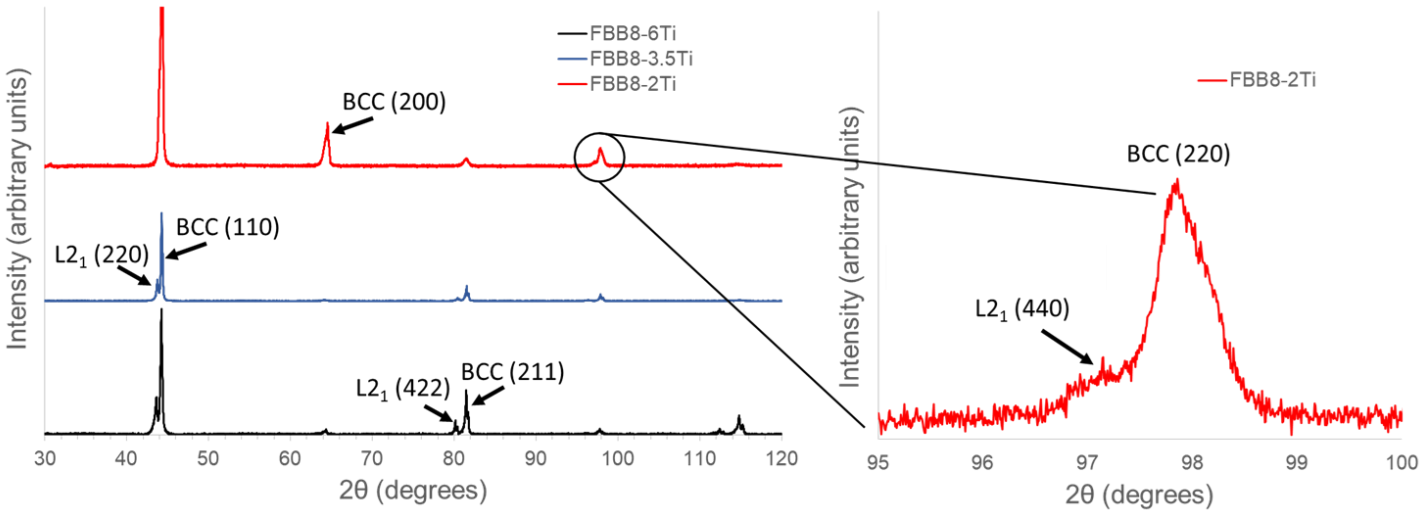

Figure 2.5: X-ray diffraction data of FBB8+Ti at various Ti contents.

2.4.2 The Effects of Ion Polishing

Note the "mottled" appearance of the lighter matrix phase in Figure 1 compared to the matrix in Figures 2.3 and 2.4. It appears that there is an additional source of contrast in the ferritic matrix of the mechanically polished samples that is not present in the electropolished state. It was hypothesized that his mottling was due to the presence of a high density of dislocations near the surface of the mechanically polished material [13]. Ion polishing of these mechanically polished samples was used in order to reduce the retained polishing damage on the surface of samples, in an effort to remove extrinsic effects from corrosion testing. It is acknowledged that ion polishing can alter a surface in other ways was well, including selective sputtering, faceting, and ion implantation [14]-[16].

To further test the hypothesis that plastic damage in the mechanically polished surface of the material is responsible for the mottled appearance of the back-scattered electron images, EBSD measurements were performed on FBB8+6wt% Ti in both the 0.05 µm- and ion-polished surface states. In the 0.05 µm-finished state, EBSD only yielded a diffraction pattern indexation rate of 15% (not shown), whereas the same sample, when ion-polished, yielded an identification rate of 95%, as seen in Figure 2.6.

Due to the aforementioned possibility of selective sputtering and faceting, it was the authors' expectation that ion polishing may lead to an increase in surface roughness, which is well known to play a role in pitting corrosion. [6] Profilometric measurements reveal a modest increase in the peak-to-valley ratio (PV), root-mean-squared roughness (rms) and average roughness (Ra) as presented in Table 2.4. Surface maps rendered using the Zygo software are even more revealing, showing a clear difference between the long wavelength undulations in the surface topology of the mechanically polished in comparison with much shorter wavelength

features in the ion polished surfaces presented in Figure 2.7. Faceting is one explanation for such an increase in surface roughness, as ion the ion polished surface seeks to adopt the lowest surface-energy state.

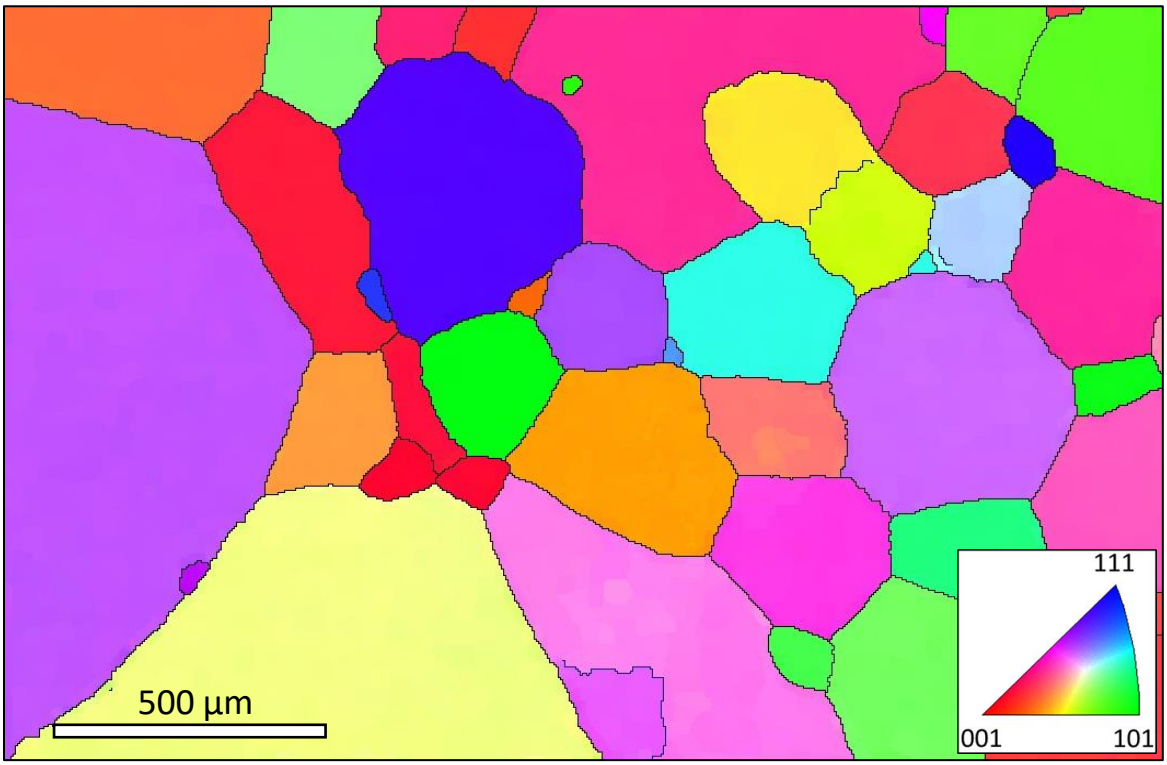

Figure 2.6: A grain map of FBB8+6wt% Ti obtained at the ion-polished finish, colored by IPF Z orientation. Zero solutions have been removed in this map, which primarily were found along grain boundaries.

Table 2.4: Average measured roughness values for the 0.05 µm finish and ion-polished finish for FBB8+2.5wt% Ti.

	FBB8 + 6wt% Ti – 0.05 µm colloidal silica finish			FBB8 + 6wt% Ti – ion polished finish		
	PV (µm)	rms (µm)	Ra (µm)	PV (µm)	rms (µm)	Ra (µm)
Average:	0.031	0.004	0.003	0.046	0.006	0.005
St Dev: ±	0.013	0.002	0.002	0.008	0.001	0.001

Selective sputtering can entail preferential attack of high surface energy sites, such as grain or phase boundaries, as well as different sputtering rates between elements and phases [14]. Previous studies have shown that lighter elements as well as those with lower binding energies are more easily sputtered and may escape a material from deeper beneath the surface. [14] Similarly, the odds of redeposition are higher for elements of greater mass. [14] This latter fact may be responsible for the observation of a new phase on the surface of ion-polished samples that was not detected in strictly mechanically polished samples. This phase is identified as Zr-rich by SEM-

EDS, as shown in Figure 2.8. With all of these chemical and microstructural features in mind, the corrosion performance of the FBB8+Ti samples was evaluated.

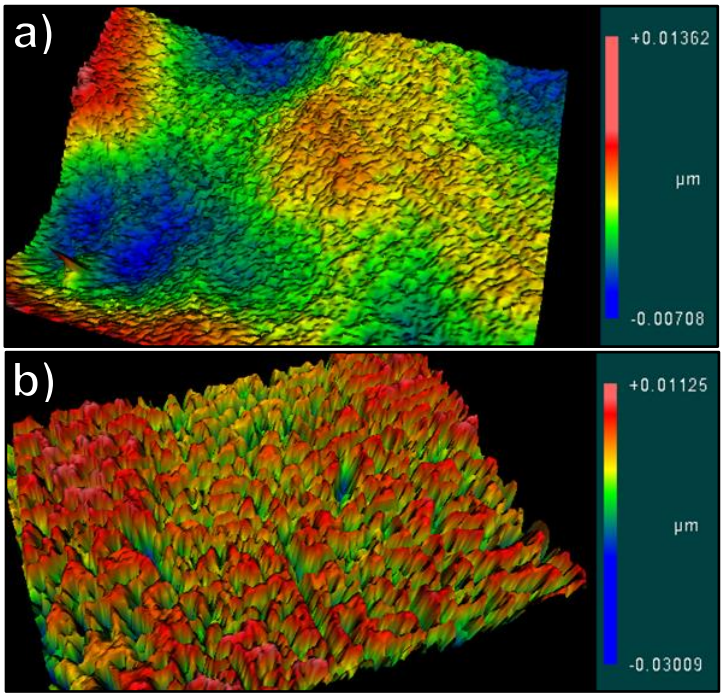

Figure 2.7: 3-D surface maps generated with the Zygo profilometer for the 0.05 µm colloidal silica finish (a) and the ion-polished finish (b).

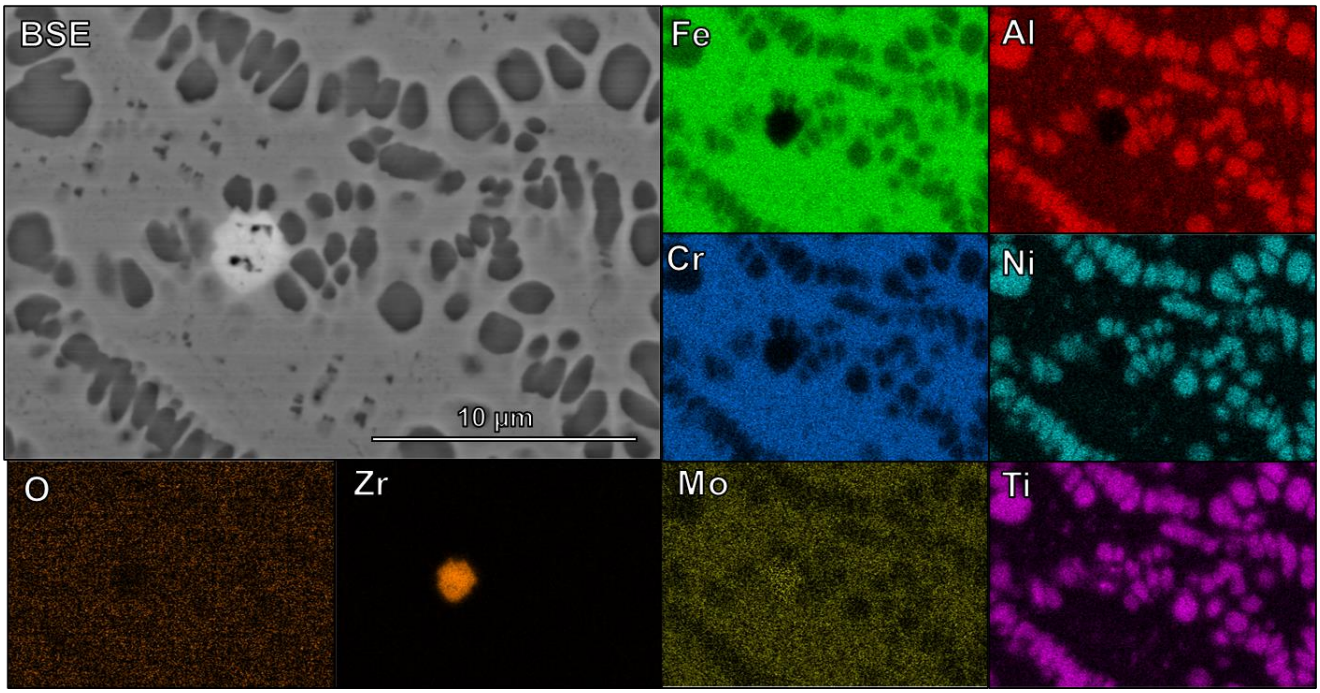

Figure 2.8: SEM-EDS map of ion-polished FBB8+6wt% Ti showing a phase that is rich in Zr. Such a phase had not been observed in samples that were only mechanically polished.

2.4.3 Corrosion performance of FBB8+Ti alloys using electrochemical techniques

Figure 2.9 presents anodic polarization curves for each FBB8+Ti alloy composition and 316L stainless steel, polished to a 0.05 □m finish. The corresponding E_{corr}, i_{corr} and i_{pass} values are listed in Table 2.5. For all specimens, the OCP values are shown to be within 0.1 V of each other with no correlation with Ti content. Very similar passive current density (i_{pass}) values of approximately 5×10-7 A·cm-2 were observed, again without any dependence on Ti content. Notably, the measured i_{pass} for all FBB8+Ti alloys was found to be one order of magnitude lower than that of SS 316L. The pitting potential (E_{pit}) was determined by measuring the potential at which a large increase in current density occurred after the passive region. For all of the 0.05 µm-finish specimens, no trend with regards to Ti composition was observed. E_{pit} was at least 0.1 V lower than that measured for SS 316L. However, prior to stable pitting at E_{pit}, SS 316L is shown to display substantial meta-stable pitting, denoted by the intense short-lived bursts of increased current density in this extended portion of the passive region. No sign of meta-stable pitting was observed on the FBB8+Ti specimens.

Table 2.5: Summary of electrochemical data for FBB8 alloys of varying wt% Ti

	E_{pit} (V vs. SCE)		**i_{corr} (i / Acm^{-2})**		**i_{pass} (i / Acm^{-2})**	
wt% Ti	0.05 µm finish	Ion polish	0.05 µm finish	Ion polish	0.05 µm finish	Ion polish
2.0	0.43	0.69	$4.5x10^{-8}$	$9.9 x10^{-9}$	$6.2 x10^{-7}$	$1.9 x10^{-7}$
2.5	0.32	0.91	$6.2 x10^{-8}$	$1.8 x10^{-8}$	$4.9 x10^{-7}$	$2.3 x10^{-7}$
3.0	0.51	1.05	$6.4 x10^{-8}$	$1.8 x10^{-8}$	$5.5 x10^{-7}$	$2.6 x10^{-7}$
3.5	0.48	0.91	$2.6 x10^{-8}$	$7.1x10^{-8}$	$2.8 x10^{-7}$	$1.5 x10^{-6}$
6.0	0.40	0.91	$5.2 x10^{-8}$	$1.2 x10^{-6}$	$4.7 x10^{-7}$	$2.4 x10^{-5}$

Anodic polarization experiments were repeated on specimens that received a subsequent ion polish after mechanical polishing (Figure 2.10). Interestingly, the pitting potential of the ion polished material is greater than that of samples with the 0.05 □m mechanical polish, despite the fact that the surface roughness is higher in the ion polished state than the mechanically polished. E_{pit} values are included in the summary plot in Figure 2.11, where it can be observed that the pitting potential of the ion-polished samples progressively increase with increasing Ti content up to 3 wt% Ti, and decrease slightly above this threshold. Notably, the uniform corrosion rate (i_{corr}) and passivation current density (i_{pass}) are found to be stable, for compositions well below the reported 4wt% Ti transition in precipitate structure (i.e. 2 wt%, 2.5 wt%, and 3 wt%) compared to those near or above the threshold (i.e. 3.5 wt% and 6 wt% Ti). The i_{corr} increases by approximately two orders of magnitude for alloys with 6 wt% Ti concentration. The corresponding i_{pass} increases by an order of magnitude for 3.5 wt% Ti and two orders of magnitude for 6 wt% Ti. These findings are summarized in Figure 2.12 and Table 2.5.

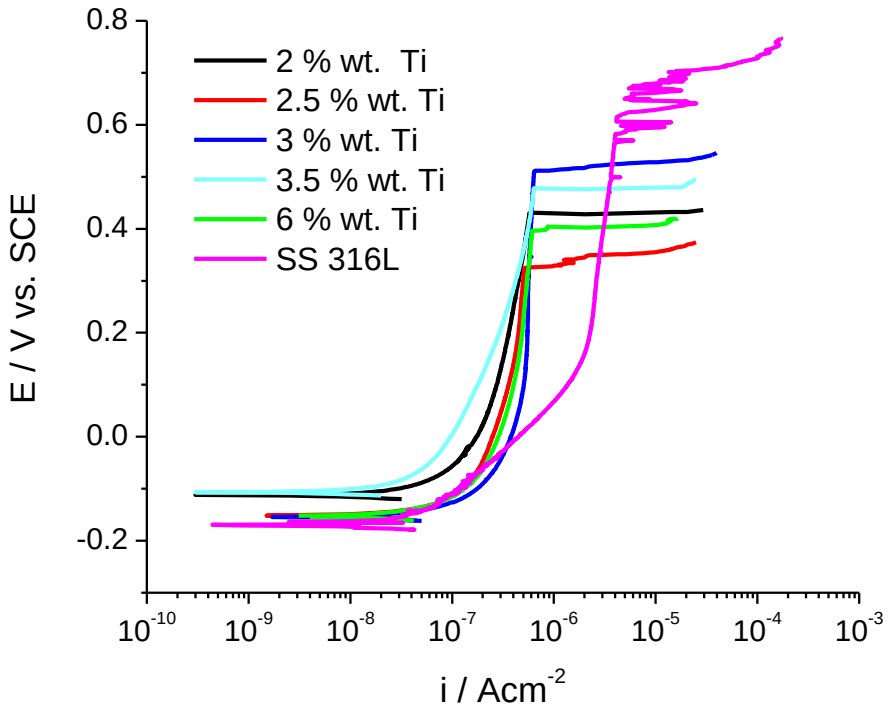

Figure 2.9: Anodic polarization curves of FBB8+Ti and SS 316L prepared to a 0.05 µm surface finish. 0.01 M NaCl.

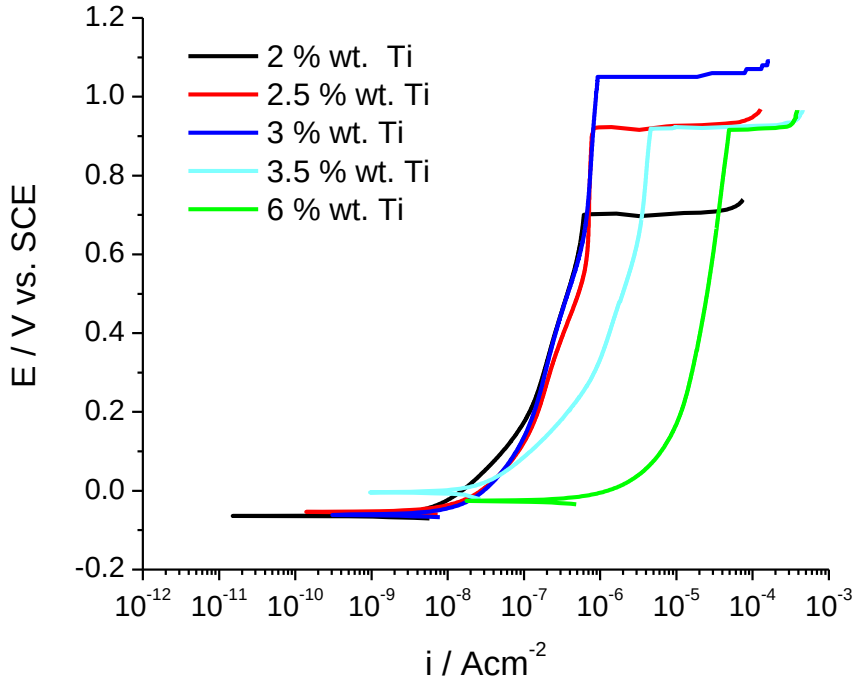

Figure 2.10: Anodic polarization curves for the ion-polished samples. Unlike the 0.05 µm surface finish, an increasing trend in passive current density is seen with titanium concentration. 0.01 M NaCl.

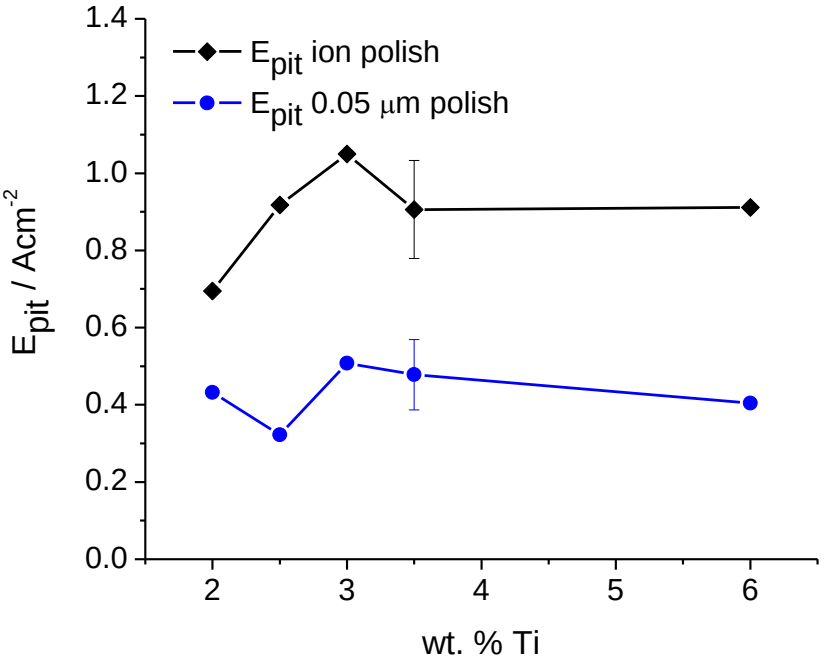

Figure 2.11: E_{pit} values for each surface preparation level and titanium concentration. A maximum is observed at 3 wt% Ti for both the ion-polished samples. It is unclear whether 3 wt% Ti is also a maximum for the 0.05 μm-finish samples.

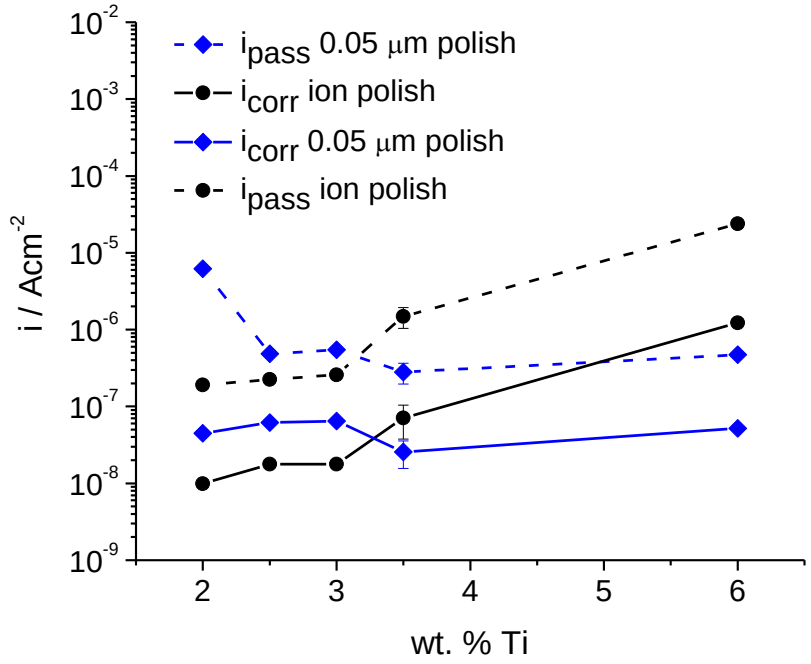

Figure 2.12: An increasing corrosion rate (i_{corr}) and passive current density are observed with increasing Ti concentration for ion-polished samples. Outside of the change observed beyond the

suspected 3 wt% Ti threshold for corrosion behavior (see Figure 7), differences between the 0.05 micron-finish samples do not appear to be statistically significant.

2.4.4 The location of pit initiation sites on FBB8+Ti alloys

Representative potentiostatic holds for FBB8 + 3 wt% Ti (a, b) and FBB8 + 6 wt% Ti (c), prepared with a 0.05 μm finish, are given in Figure 2.13 (a - c). The two compositions were selected to provide an assessment of an alloy above and below the 4 wt% Ti threshold for the transition from a coherent, hierarchical B2/$L2_1$ precipitate structure to a semi-coherent Heusler phase precipitate structure. A small amount of metastable pitting was observed in the experiment with the 3wt% Ti specimen, denoted by the intense short-lived bursts of increased current density (Figure 2.13 a - b). In contrast, no metastable pitting was detected in the experiment with the 6wt% Ti specimen (Figure 2.13 c).

Figure 2.14 shows micrographs of mechanically polished and ion polished samples of FBB8 + 6 wt% Ti before and after corrosion testing. Some of the pit initiation sites are denoted by the white arrows. For specimens prepared with the 0.05 μm finish, it is apparent that pit initiation occurs preferentially within the iron-rich ferrite matrix. This was found to be the case regardless of titanium concentration. Very different behavior was observed for the specimens prepared with an ion-polish finish; pitting sites were found almost exclusively on precipitates or at matrix/precipitate interfaces (Figure 2.14(b)). This observation may also hold a clue as to why there is an increasing passive corrosion rate in the ion polished material with higher Ti concentrations (Figure 2.10). For example, if corrosion is faster within the second phase of the ion polished material, the increased second phase content (Table 1 and Figure 2) of the alloys with higher Ti content seems consistent with an increased corrosion rate.

The ion-polished samples show a bright (high atomic number (Z)) corrosion product in the vicinity of the second phase particles which are associated with pit initiation. EDS reveals these sites to be elevated in Zr and O concentration as shown in Figures 2.15 and 2.16. The presence of oxygen marks this phase as distinct from the Zr-rich phase observed after ion polishing (see Figure 8.) These phases were not observed for strictly mechanically polished samples either before or after corrosion testing.

Note that Zr is rather uniformly distributed amongst the matrix and precipitate phases of the uncorroded alloy (see Figures 2.3 and 2.4), though it was shown that islands of Zr are redeposited on the sample surface (Figures 2.8, 2.15 and 2.16). This increase in surface Zr content of the ion-polished samples may provide a critical concentration of Zr cations in solution during uniform dissolution occurring in the passive phase, which motivates the deposition of a hydrated zirconium oxide ($ZrO2 \cdot 2(H2O)$) around but outside the acidic pitting initiation sites where an neutral or alkaline pH will exist. [17] Here, the minimum solubility of hydrated Zr(IV) oxides is between pH 6 and 7. Similar corrosion product formation is observed in the pitting corrosion of

stainless steels in chloride environments, where pitting initiates on inclusions and corrosion products are deposited on the cathodic surface near the pit. [18]

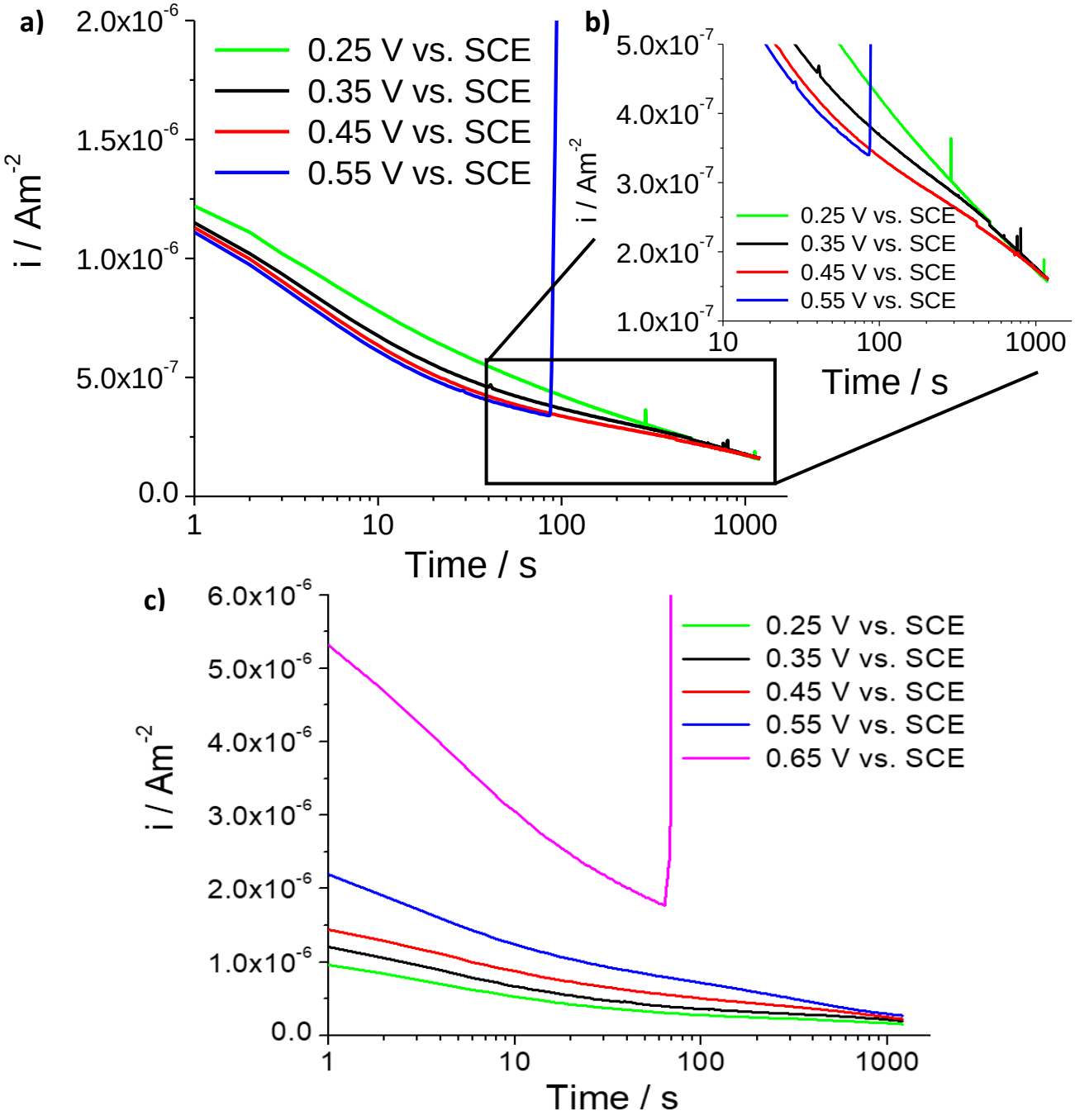

Figure 2.13: Potentiostatic holds following 20 minutes at OCP during full immersion in 0.01 M aqueous NaCl solution, where (a-b) is FBB8+3wt% Ti and (c) is FBB8+6wt% Ti. Both samples were polished to a 0.05 µm finish.

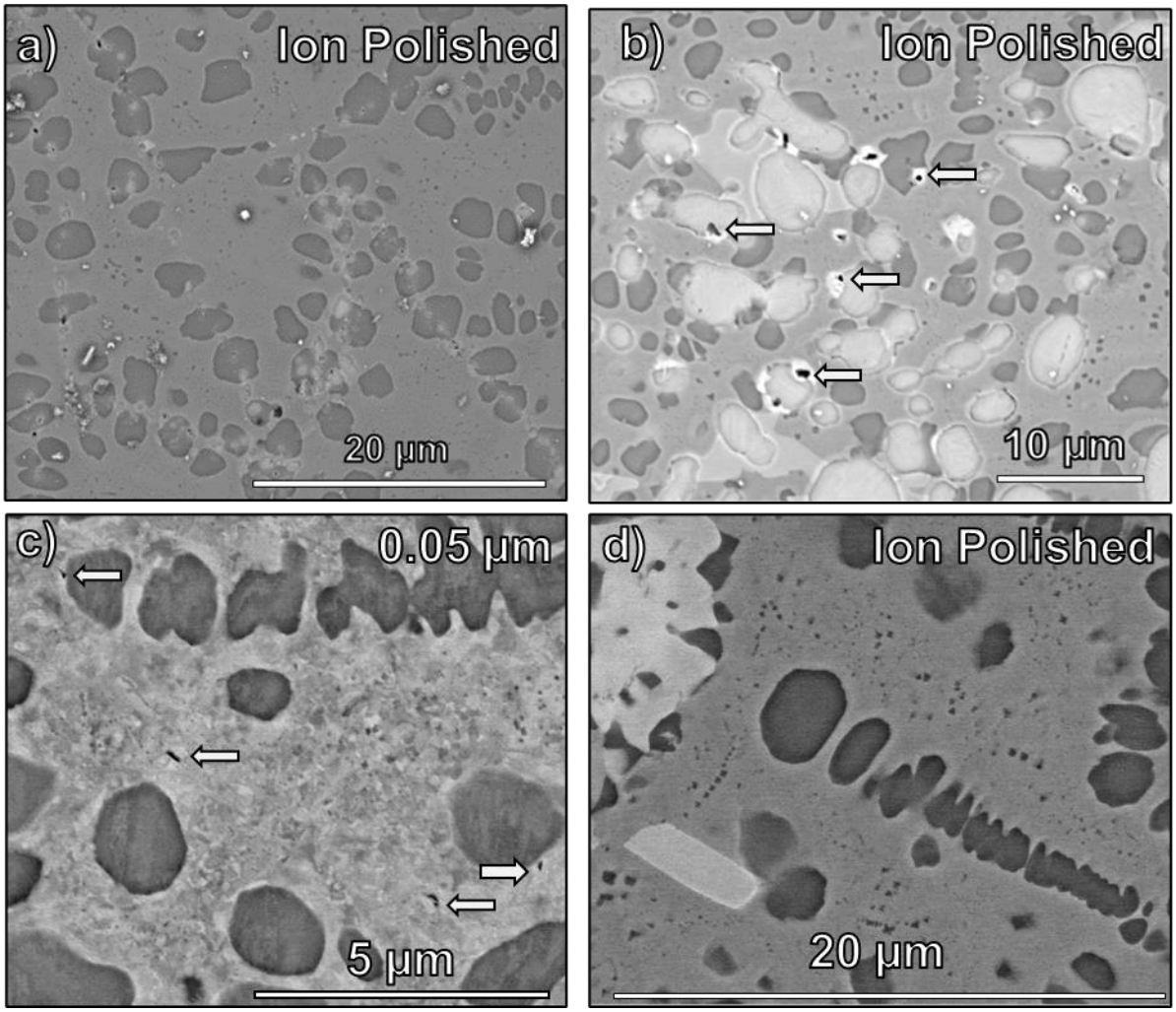

Figure 2.14: Backscattered electron micrographs of 6 wt% Ti after a potentostatic hold, (a and b) at an ion-polished finish and c) at a 0.05 µm finish. The pale, somewhat translucent phase on the surface of the ion-polished samples (a,b) is rich in Zr and is not seen in uncorroded samples. d) depicts an ion-polished sample before corrosion testing, clearly showing smaller secondary precipitates and a much less mottled matrix. The lightest phase in d) shows concentrations of Mo and Ti, but not Zr, during EDS. (As seen in Figure 2.15)

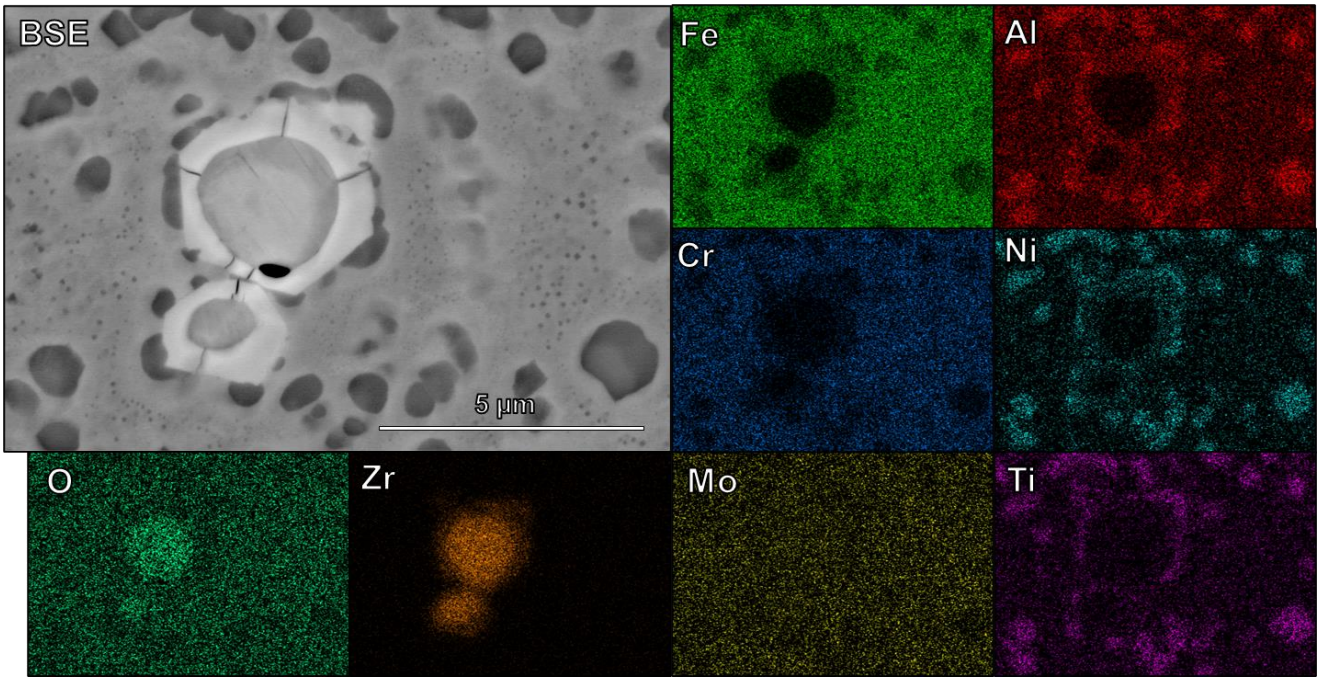

Figure 2.15: SEM-EDS map of a pit initiation site on an ion-polished sample of FBB8+3wt% Ti after a series of anodic potentiostatic holds.

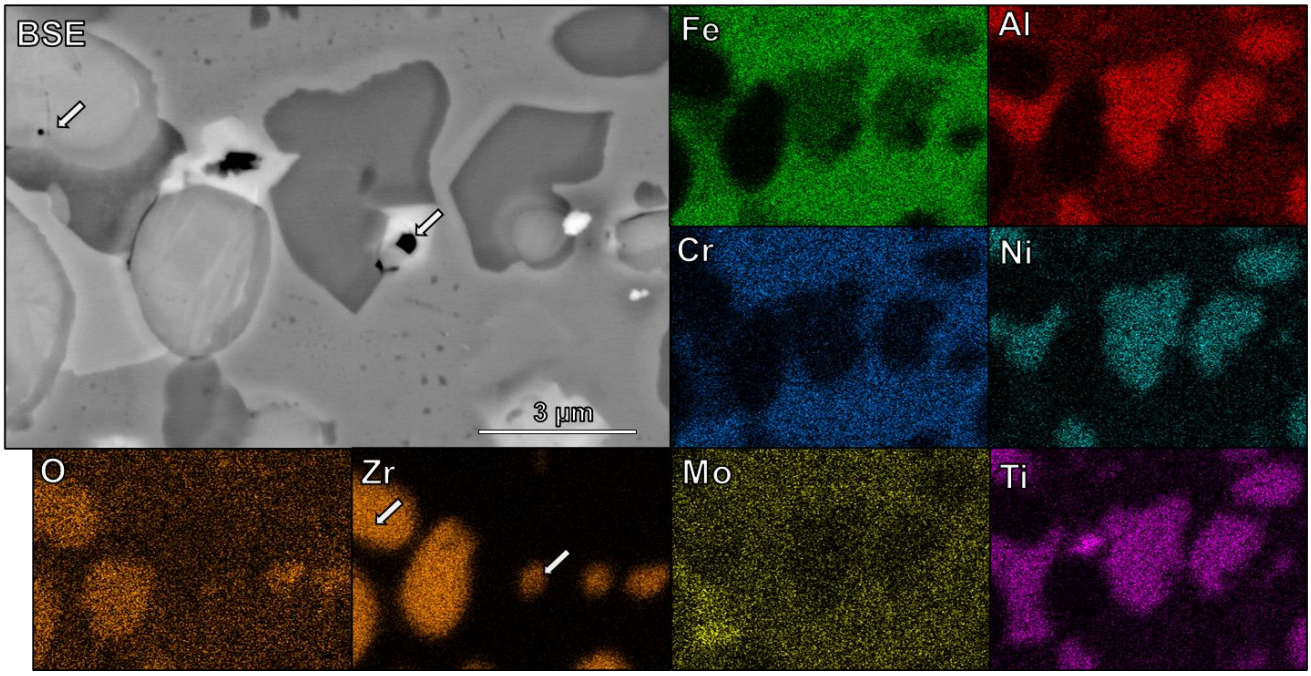

Figure 2.16: SEM-EDS map of pit initiation sites on an ion-polished sample of FBB8+6wt% Ti after a series of anodic potentiostatic holds. Note the white arrows, which denote both pitting initiation sites and corresponding concentrations of Zr. Also note that some areas which show elevated Zr do not appear in the O-specific EDS map.

2.5 Discussion

2.5.1 Uniform Corrosion

Local corrosion modes that are typically seen in passive alloys are presently examined. Such passivity depends on specific elements in the matrix or precipitate phases that form stable oxides in a pH 5.6 chloride solution. [19] Under these environmental conditions, passivating elements include Al, Ti, Cr, and to a lesser extent, Ni. [20] These elements exist in sufficient concentrations in both the Heusler phase and ferritic matrix as evident from anodic upward polarization scans (Tables 2.2 and 2.3) to provide stable or metastable passivity in each phase. Concentrations of Al, Ti, and Cr are near, at or above the threshold concentrations required for passivation or act in synergistic combination. [16][22][23] Mo is a well-known dissolution blocker in stainless steels. [24] Recently, Mo has been found to enhance the thermodynamic stability of Cr2O3 [25] and the synergistic effect with Cr via Mo-doping in Cr2O3 is well documented. [26]

The results from the 0.05 µm-finished samples demonstrate passive corrosion behavior, reflective of the passive current density of the matrix and precipitate phases determined by their composition and nanostructure, and weighted by the area fraction of each phase. The lack of any statistically significant trend in the global uniform corrosion (ipass) and micro-galvanic coupling behavior (icorr) of the FBB8+Ti system is not surprising because of the level of passivating elements which are present in each phase at each Ti concentration. For instance, the matrix contains >12% Cr for both 2.5% and 6% Ti alloys. It is found that the global passive corrosion performance is independent of precipitate size, volume fraction, and other corresponding changes with Ti additions. Moreover, all compositions of the FBB8+Ti system are shown to have low corrosion rates within the passive region, relative to SS 316L, which suggests that they will have superior long-term uniform corrosion performance. This is perhaps due to the combination of Ti, Al, Cr at sufficient levels to form passive films and Mo-doping, as discussed above. Further investigations in more concentrated chloride solutions are recommended. In contrast, when specimens were prepared with a subsequent ion polish step, the alloys exhibit increasing corrosion rates with increasing Ti content. In particular, those with the semi-coherent Heusler phase precipitate structure (i.e. 3.5% Ti and above) were more susceptible to a higher rate of uniform corrosion. One simple explanation for the observed trend with Ti may be associated with a very slight preferential corrosion of the second phase, once the biasing contribution of mechanical damage is eliminated. Samples with higher Ti content clearly had higher second phase contents and particle sizes (Figure 2.2).

2.5.2 Localized Corrosion

Concerning local corrosion which involves oxide break down and pit stabilization, the ion milled surfaces had a statistically significant higher Epit than the 0.05 um finish. (Figure 10) This is typically observed for smoother surfaces on steel, stainless steels and other alloys which possess a more positive Epit. [6][15][21] However, this does not explain the present results, as the ion-polished surfaces are actually slightly rougher than the mechanically polished (see Table 4 & Figure 7). Ion implantation of ion-etched surfaces, while unintentional in this study, is another possibility that could impact the corrosion performance of the ion polished samples. Studies have noted the presence of a lower-density surface layer on ion polished samples on the order of 10 nm thick with elevated levels of argon, up to 5 atomic percent. [27][28] Argon ion implantation has also been shown to promote greater thicknesses of air-formed oxides on iron, specifically the inner magnetite (Fe_3O_4) layer [27]. This could be one reason for the enhanced pitting potentials of the ion-polished samples (Figure 11).

It is also observed that ion polishing removed the plastic damage (dislocations) induced by mechanical polishing (see Figure 6 and compare Figures 1 and 14 c, d). The effects of plastic deformation under an overlying passive film have an unclear role; misfit dislocations at surfaces can affect oxides. [29] Combined corrosion/microstructural investigations show that pitting initiated predominantly in the ferrite matrix on alloys with the 0.05 um finish (Figure 14 (c)). In contrast, the ion milled surfaces were found to pit primarily on precipitates and on phase boundaries. Note the white arrows in Figure 14 (b), which denote both pitting initiation sites and corresponding concentrations of Zr, also seen in Figures 15 and 16. It is possible that the transition in pitting location is related to the alteration of the dislocation microstructure of the metal. Perhaps pitting is primarily associated with the matrix due to the abundance of dislocations in the matrix of the mechanically polished sample variant. In contrast it is primarily associated with the precipitate interfaces of the ion-polished samples because interfacial dislocations are still present even after ion polishing.

Diffusion length helps stabilize pits formed by metal dissolution, cation hydrolysis and Cl^- accumulation in the acid pitting mechanism common to stainless steels. These process helps a surface pit site attain a critical Cl^- concentration and pH drop to stabilize a pit. [30] These effects of diffusion length might dominate pit initiation between more or less susceptible metallurgical sites, however the current results suggest that the major phases within the mechanically polished FBB8+Ti system have compositions and structures that are amenable to a similar level of passivation. Breakdown and pitting site selection in these alloys could be controlled by subtle factors such as details related to the state of the surface altered by surface preparations.

At the risk of repetition, any distinctions in the microgalvanic coupling between the matrix and precipitate phases, or in the passivation/breakdown behavior of the oxides that form on those different phases, are not significantly altered within the range of Ti concentrations explored, except perhaps in the ion-polished samples. It could be serendipitous in the present case, since the alloy

was developed with creep resistance in mind [1], however these results suggest that the chemistry of the FBB8 steels may be optimized on the basis of the mechanical properties and high temperature oxidation performance, with an expectation of equivalent room temperature aqueous corrosion performance across the range of alloy chemistries investigated.

2.6 Summary

An analysis of the room temperature, aqueous corrosion performance of a new class of compositionally and microstructurally complex ferritic steels, FBB8, was conducted across a range of titanium additions between 2 and 6 weight percent. The size and volume fraction of Heusler- (Ni_2TiAl) and B2- (NiAl) phase strengthening precipitates was found to increase monotonically with titanium content. The average pitting potential across all compositions was found to be 0.428 ± 0.074 V vs SCE at a 0.05 μm finish, and 0.894 ± 0.130 V vs SCE at an ion-polished finish in 0.01 M NaCl. When samples are prepared to a 0.05 μm finish, uniform passive aqueous corrosion behavior was found to be independent of microstructure and composition within the range of titanium content investigated, and localized metastable pitting occurred in the matrix.

When samples are ion-polished, the predominant location of metastable pitting changes from the matrix to the precipitate phase, or phase boundary. This too is a positive result, since it reveals the delicate balance in preference for pitting locations within the matrix and associated with the second phase strengtheners. Further investigation would be required to definitively conclude what induced this change in pitting location, but one candidate is related to dislocations which were originally present throughout the matrix, due to mechanical polishing, and then are relegated to the semi-coherent phase boundaries between the matrix and the precipitate in the ion-polished state.

2.7 Acknowledgements

The authors would like to thank the Office of Naval Research for their support through ONR BAA #N00014-18-1-2621, directed by Dr. Airan Perez and Dr. David Shifler.

2.8 References

[1] G. Song, “Microstructure and Creep Deformation Behavior of a Hierarchical-Precipitate-Strengthened Ferritic Alloy with Extreme Creep Resistance,” University of Tennessee, Knoxville, 2016.

[2] Z. Sun, “Microstructures and Mechanical Behavior of NiAl-Strengthened Ferritic Alloys at Room and Elevated Temperatures,” University of Tennessee, Knoxville, 2015.

[3] M. J. S. Rawlings, C. H. Liebscher, M. Asta, and D. C. Dunand, “Effect of titanium additions upon microstructure and properties of precipitation-strengthened Fe-Ni-Al-Cr ferritic alloys,” Acta Mater., vol. 128, pp. 103–112, 2017, doi: 10.1016/j.actamat.2017.02.028.

[4] S. Il Baik, M. J. S. Rawlings, and D. C. Dunand, “Atom probe tomography study of Fe-Ni-Al-Cr-Ti ferritic steels with hierarchically-structured precipitates,” Acta Mater., vol. 144, pp. 707–715, 2018, doi: 10.1016/j.actamat.2017.11.013.

[5] G. Song et al., “Ferritic Alloys with Extreme Creep Resistance via Coherent Hierarchical Precipitates,” Sci. Rep., vol. 5, pp. 1–14, 2015, doi: 10.1038/srep16327.

[6] G. T. Burstein and P. C. Pistorius, “Surface roughness and the metastable pitting of stainless steel in chloride solutions,” Corrosion, vol. 51, no. 5, pp. 380–385, 1995, doi: 10.5006/1.3293603.

[7] C. A. Schneider, W. S. Rasband, and K. W. Eliceiri, “HISTORICAL commentary NIH Image to ImageJ : 25 years of image analysis,” Nat. Methods, vol. 9, no. 7, pp. 671–675, 2012, doi: 10.1038/nmeth.2089.

[8] A. U. Malik, P. C. Mayan Kutty, N. A. Siddiqi, I. N. Andijani, and S. Ahmed, “The influence of pH and chloride concentration on the corrosion behaviour of AISI 316L steel in aqueous solutions,” Corros. Sci., vol. 33, no. 11, pp. 1809–1827, 1992, doi: 10.1016/0010-938X(92)90011-Q.

[9] S. T. Pride, J. R. Scully, and J. L. Hudson, “Metastable Pitting of Aluminum and Criteria for the Transition to Stable Pit Growth,” J. Electrochem. Soc., vol. 141, no. 11, pp. 3028–3040, 1994, doi: 10.1149/1.2059275.

[10] R. K. Gupta, N. L. Sukiman, M. K. Cavanaugh, B. R. W. Hinton, C. R. Hutchinson, and N. Birbilis, “Metastable pitting characteristics of aluminium alloys measured using current transients during potentiostatic polarisation,” Electrochim. Acta, vol. 66, pp. 245–254, 2012, doi: 10.1016/j.electacta.2012.01.090.

[11] G. S. Frankel, L. Stockert, F. Hunkeler, and H. Boehni, “Perspective on ‘Metastable pitting of stainless steel,’” Corrosion, vol. 75, no. 16, pp. 126–136, 2019, doi: 10.5006/3032.

[12] M. Wischhusen, C. Glover, J. Scully, P. K. Liaw, and S. Agnew, “An Investigation into the Link Between Microstructure and Pitting Corrosion of Novel Alloy FBB8+Ti,” TMS 2020 149th Annu. Meet. Exhib. Suppl. Proc., pp. 1561–1571, 2020.

[13] S. Yamasaki, M. Mitsuhara, K. Ikeda, S. Hata, and H. Nakashima, “3D visualization of dislocation arrangement using scanning electron microscope serial sectioning method,” Scr. Mater., vol. 101, pp. 80–83, 2015, doi: 10.1016/j.scriptamat.2015.02.001.

[14] W. Eckstein and W. Möller, “Computer simulation of preferential sputtering,” Nucl. Inst. Methods Phys. Res. B, vol. 7–8, no. PART 2, pp. 727–734, 1985, doi: 10.1016/0168-583X(85)90460-4.

[15] K. Sasaki and G. T. Burstein, “The generation of surface roughness during slurry erosion-corrosion and its effect on the pitting potential,” Corros. Sci., vol. 38, no. 12, pp. 2111–2120, 1996, doi: 10.1016/S0010-938X(96)00066-2.

[16] P. E. Manning, D. J. Duquette, and W. F. Savage, “The Effect of Test Method and Surface Condition on Pitting Potential of Single and Duplex Phase 304L Stainless Steel,” Natl. Assoc. Corros. Eng., vol. 35, no. 4, pp. 151–157, 1979.
[17] M. Pourbaix, H. Zhang, and A. Pourbaix, “Presentation of an Atlas of chemical and electrochemical equilibria in the presence of a gaseous phase,” Mater. Sci. Forum, vol. 251–254, pp. 143–148, 1997, doi: 10.4028/www.scientific.net/msf.251-254.143.
[18] Y. Tsutsumi, A. Nishikata, and T. Tsuru, “Pitting corrosion mechanism of Type 304 stainless steel under a droplet of chloride solutions,” Corros. Sci., vol. 49, no. 3, pp. 1394–1407, 2007, doi: 10.1016/j.corsci.2006.08.016.
[19] C. D. Taylor, P. Lu, J. Saal, G. S. Frankel, and J. R. Scully, “Integrated computational materials engineering of corrosion resistant alloys,” NJP - Mater. Degrad., vol. 2, no. 1, 2018, doi: 10.1038/s41529-018-0027-4.
[20] P. Marcus, “On some fundamental factors in the effect of alloying elements on passivation of alloys,” Corros. Sci., vol. 36, no. 12, pp. 2155–2158, 1994, doi: 10.1016/0010-938X(94)90013-2.
[21] N. D. Greene and M. G. Fontana, “A critical analysis of pitting corrosion,” in National Association of Corrosion Engineers, Fourteenth Annual Conefernce, 1958.
[22] S. Qian, R. C. Newman, R. A. Cottis, and K. Sieradzki, “Computer simulation of alloy passivation and activation,” Corros. Sci., vol. 31, no. C, pp. 621–626, 1990, doi: 10.1016/0010-938X(90)90171-Z.
[23] D. Artymoicz, K. Sieradzki, and R. C. Newman, “Passivation in Non-Random Solid Solution Alloys,” ECS Trans., vol. 53, no. 21, pp. 15–22, 2013.
[24] V. Maurice and P. Marcus, “Current developments of nanoscale insight into corrosion protection by passive oxide films,” Curr. Opin. Solid State Mater. Sci., vol. 33, no. 0, pp. 1–44, 2018.
[25] K. L. Cwalina, C. R. Demarest, A. Y. Gerard, and J. R. Scully, “Revisiting the effects of molybdenum and tungsten alloying on corrosion behavior of nickel-chromium alloys in aqueous corrosion,” Curr. Opin. Solid State Mater. Sci., vol. 23, no. 3, pp. 129–141, 2019, doi: 10.1016/j.cossms.2019.03.002.
[26] E. McCafferty, Introduction to Corrosion Science. New York, NY: Springer New York, 2010.
[27] V. Ashworth, W. A. Grant, R. P. M. Procter, and T. C. Wellington, “The Effect of Ion Implantation on the Corrosion Behavior of Pure Iron - Argon Ion Implantation,” Corros. Sci., vol. 16, no. April 1975, pp. 393–403, 1976.
[28] C. Schönjahn, L. A. Donohue, D. B. Lewis, W.-D. Münz, R. D. Twesten, and I. Petrov, “Enhanced adhesion through local epitaxy of transition-metal nitride coatings on ferritic steel promoted by metal ion etching in a combined cathodic arc/unbalanced magnetron deposition system,” J. Vac. Sci. Technol. A Vacuum, Surfaces, Film., vol. 18, no. 4, pp. 1718–1723, 2000, doi: 10.1116/1.582414.
[29] J. P. Hirth, B. Pieraggi, and R. A. Rapp, “The role of interface dislocations and ledges as sources/sinks for point defects in scaling reactions,” Acta Metall. Mater., vol. 43, no. 3, pp. 1065–1073, 1995, doi: 10.1016/0956-7151(94)00296-T.
[30] J. R. Galvele, “Transport Processes and the Mechanism of Pitting of Metals,” J. Electrochem. Soc., vol. 123, no. 4, pp. 464–474, 1976, doi: 10.1149/1.2132857.

3. Al-stabilized $L2_1$-Heusler phase in FCC Compositionally Complex Alloys and Control of its Volume Fraction

This chapter is intended for submission to a peer-reviewed scientific journal with co-authors Jishnu J. Bhattacharyya, Diego Ibarra, Jie Qi, Joseph Poon, Peter Connors, John R. Scully, Sean R. Agnew[2].

3.1 Abstract

An alloy design effort focused on producing lightweight, low-cost compositionally complex alloys with high strength, ductility and aqueous corrosion resistance unexpectedly produced a dual-phase alloy with these qualities. A series of dual-phase alloy chemistries were arc-melted and cast, heat treated, then characterized via Scanning- and Transmission Electron Microscopy and X-ray Diffraction methods. Results were analyzed in the context of thermodynamic stability as determined via Thermo-Calc software and the TCHEA 3 database. Scheil-Gulliver simulations of rapid cooling suggest that the second phase becomes favorable as the chemistry of the melt becomes enriched in solute. Al was found to be the most potent single elemental addition for stabilizing this phase, which was identified as the $L2_1$ Heusler (Ni_2TiAl) phase. While results call the exact position of zero-fraction phase boundaries predicted by Thermo-Calc into question, it was also found that the volume fraction of the Heusler phase may be controlled most potently through the use of a tie line, i.e. the nominal composition of an alloy may be determined by the desired volume fraction of each phase and their predicted endpoint compositions.

[2] Author contributions: **Mark A. Wischhusen**: Investigation, Formal Analysis, Writing (Original Draft), **Jishnu J. Bhattacharyya**: Investigation and Formal Analysis (TEM), **Jie Qi:** Resources, **Diego Ibarra:** Resources, **Joseph Poon:** Conceptualization, Funding Acquisition and Writing (Review & Editing), **Peter Connors**: Investigation (Thermodynamic modeling and phase diagrams), **John R. Scully:** Conceptualization, Funding Acquisition and Writing (Review & Editing), **Sean R. Agnew:** Conceptualization, Funding Acquisition and Writing (Review & Editing)

3.2 Introduction:

As technology advances, the materials of construction for components are frequently exposed to increasingly extreme environments. Similarly, as the understanding of material behavior and the effects of alloying grow, materials can be designed which supply the required properties of an application while simultaneously reducing the amount of material necessary, or the weight of a part. To this end, there has been an effort to design alloys within the "compositionally complex" alloy space (CCAs) which simultaneously realize low density and cost with high strength, ductility and aqueous corrosion resistance. [1] In this particular instance, alloys intended for use in ocean environments must avoid a ductile-to-brittle transition temperature (DBTT) above that of frigid seawater. Naturally, this requirement has guided the current design effort towards single-phase, FCC-structured alloys to avoid both the DBTT and any solute depletion or galvanic coupling which may occur due to the presence of the second phase. Despite the use of a machine learning algorithm for phase prediction, a dual-phase alloy was produced which retained a second phase even after homogenization treatment. Serendipitously, this alloy also met the design needs of the research thrust, with the added benefit of strengthening via a second phase. Electron microscopy and X-ray diffraction confirmed the identity of this second phase – the $L2_1$ Heusler phase, Ni_2TiAl. Having positively identified the second phase, and having observed its high hardness, it was next sought to understand how its volume fraction might be tuned for the purpose of mechanical reinforcement.

3.3 Methods

3.3.1 Sample Synthesis and Preparation

Of the first few alloys which retained a second phase after homogenization, $Al_{0.3}Cr_{0.5}Fe_2Mn_{0.25}Mo_{0.15}Ni_{1.5}Ti_{0.3}$ (referred to as CCA 72,) was observed to have the best corrosion resistance and was selected as a template for further alloy chemistries. These alloys are discussed further in Table 3.2.

Alloy ingots were produced via vacuum arc melting, re-melting several times to ensure homogeneous composition, and either bar cast in a chilled Cu hearth (approximately 75 mm x 13 mm x 7mm) or suction cast into coin-shaped ingots (10 mm diameter by 5 mm thick) within a chilled Cu mold, all within an Ar environment from >99.9% pure (metals basis) elemental metal or ferrometals, with the exception of Cr which was >99.2% pure. The as-cast samples are then encapsulated in Ar-backfilled quartz tubes and homogenized for 5 hours at 1070 °C, followed by water quenching. Solutionization treatments were performed encapsulated under the same conditions for 24 hours at a somewhat higher temperature of 1150 °C (which is predicted to be

within 50 °C of the solidus temperature) and subsequent aging treatments were performed encapsulated at 1070°C for 24 hours, each followed by water quenching.

Samples were sectioned using a diamond-abrasive wafering saw. General metallographic preparation for all techniques includes grinding and polishing on SiC paper down to 1200-grit. No further preparation is used for x-ray diffraction measurements. For scanning electron microscopy, EDS and EBSD, samples were further polished using polycrystalline diamond suspensions, down to a 0.05 colloidal silica finish. After mechanical polishing was complete, SEM samples received 15 minutes of flat Ar ion milling using an accelerating voltage of 6 kV, a rotation speed of 1 per second, and a tilt angle of 10°. Samples were prepared for TEM analysis using the same procedure as above, followed by focused ion beam milling lift-outs performed on the Helios DB-FIB and subsequent Ga-ion milling to thin the sample to a thickness of 100 nm.

3.3.2 Microscopy

Scanning electron microscopy was performed using an FEI Quanta 650 SEM (Hillsboro, OR, USA) as well as a Thermo-Fischer Helios UC G4 Dual-Beam FIB-SEM (Waltham, MA, USA). Both SEMs have Oxford EDS detectors as well as the accompanying Oxford Instruments' Aztec® software. The EDS detectors have a sensitivity of > 0.1 wt% for elements with an atomic number greater than 5. Although the microscope parameters used vary between imaging modes and analytical techniques, the following common parameter set can be used for imaging and SEM-EDS: an accelerating voltage of 20 kV and a beam current 6.4 nA, which corresponds to a probe size of about 6 nm. EDS scans were performed standardless, using the vendor-supplied calibrations for each element. There was a concern that the electron interaction volume may exceed the volume of smaller microstructural features, leading to erroneous sampling of the surrounding material. The electron interaction depth (R), depicted schematically in Figure 3.1, can be approximated via a simplified form of the Kanaya-Okayama equation for electron energy loss depth [3] (Equation 3.1). Mw is the average molecular weight of the material (g/mol), Z is the average atomic number of a phase, ρ is the density (g/cm^3) of the material, and E_0 is the electron accelerating voltage in kV. These values are 55.3 g/mol, 26.1 and 7.72 g/cm^3 for the FCC phase, and 50.6 g/mol, 24.5 and 6.77 g/cm^3 for the Heusler phase. This approximation predicts that penetration depths at E_0 = 20 kV will range from 1.6 μm to 1.8 μm in the FCC and Heusler phases, respectively. The size of most microstructural features exceeded this depth, though there may be instances where a particle visible on the surface of a sample does not extend evenly below the surface.

$$R = \frac{0.0276 \cdot M_w \cdot E_0^{5/3}}{Z^{8/9} \cdot \rho} \tag{3.1}$$

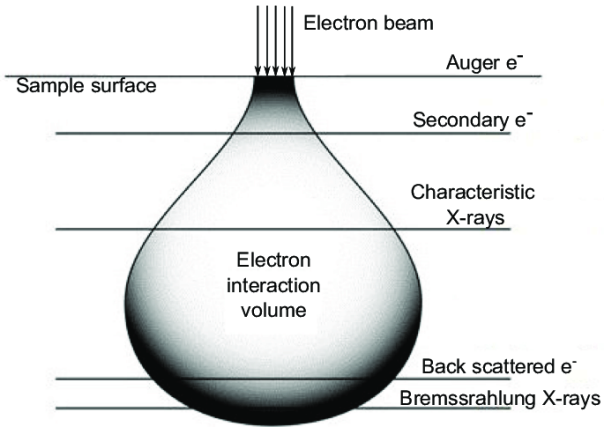

Figure 3.1: A schematic of the electron interaction volume, reproduced from [3].

X-ray diffraction experiments were performed on a Panalytical Empyrean x-ray diffractometer (Malvern, UK). Powder diffraction was performed on bulk metallic samples in a Bragg-Brentano para-focusing geometry. Incident beam optics include the Bragg-Brentano HD Cu prefix module, 0.02 mm soller slits, a 4 mm mask, a 0.25-degree divergence slit and an incident 1-degree anti-scatter slit. These optics produce an x-ray footprint of about 7.4 mm by 9.7 mm on the sample, and data were collected on a spinning sample rotating at 8 seconds per revolution.

Transmission electron microscopy was performed using an FEI Titan TEM at an accelerating voltage of 200 kV. The FEI SuperXG2 EDS detector was used to determine local chemistry. Selective-Area Electron Diffraction (SAED) was performed along various zone axes of the FCC crystals using a screen current of 39.2 pA, an extractor voltage of 3700 V to determine the crystallographic structure of the various phases.

In light of the solidification behavior described below, the cooling rate of suction-cast and bar-cast samples was estimated using Equation 3.2 [4]. The cooling rate, ε (K/s) is calculated from the dendrite spacing, λ1, where 1 denotes primary dendrite arm spacing. The dendrite spacing is modified by k and n, which are log/log fitting parameters obtained from controlled cooling rate experiments. For this study, values for k and n obtained by [5] for 316 stainless steel were used: for primary dendrites, k = 80 and n = 0.333. Electron micrographs similar to Figure 3.8 were analyzed using ImageJ software [6].

$$\varepsilon = \left(\frac{\lambda_i}{k}\right)^{-\frac{1}{n}} \tag{3.2}$$

3.3.3 Thermo-Calc Software

In order to better understand the presence of the Heusler phase, Thermo-Calc software, which is based in the Calculation of Phase Diagrams (CALPHAD) method, was used to model the chemical space in the vicinity of CCA 72. The majority of the calculations in Thermo-Calc are performed in the context of thermodynamic equilibrium. The time scales involved to reach equilibrium are frequently very large, and therefore, may not accurately reflect the state of cast samples that solidify quickly. In the case of equilibrium cooling, it is assumed that there is complete diffusion in both the liquid and solid phases, leading to uniform chemical potential across all phases, and that the solid-liquid interface exists at equilibrium. In the context of a binary system, the concentration of solute in the liquid phase is represented by Equation 3.3, where C_0 is the composition of the liquid, C_s ¬and C_L are the endpoint compositions at the boundaries of the two-phase region, and f_S and f_L are the weight fractions of the solid and liquid phases. In the case of rapid solidification, a relationship has been derived by G.H. Gulliver [7] and E. Scheil [8] which considers a case where there is no diffusion in the solid, but still infinite diffusion in the liquid. The concentration of solute in the liquid in this case is represented by Equation 3.4, in which k is the equilibrium partition coefficient of the solute. These two cases can be considered as bounding conditions, with the reality of solidification falling somewhere between the two, which are also known as the equilibrium lever rule and the non-equilibrium level rule, respectively.

$$C_s f_s + C_L f_L = C_0 \tag{3.3}$$

$$C_L = C_0 f_L^{(k-1)} \tag{3.4}$$

In the Al-Cr-Fe-Mn-Mo-Ni-Ti system, Thermo-Calc predicts over 100 possible phases. In order to reduce calculation times and improve stability, pseudo-binary isopleth diagrams were generated using a reduced list of phases. The phase list was based on a series of equilibrium cooling calculations performed across a coarse (e.g. 5 atomic percent) step size in aluminum concentration, as described in greater detail below.

3.4 Results

3.4.1 Identification of the Heusler Phase

The first analysis performed on the 2-phase alloy, $Al_{0.3}Cr_{0.5}Fe_2Mn_{0.25}Mo_{0.15}Ni_{1.5}Ti_{0.3}$ (CCA 72,) was backscattered electron imaging which is sensitive to chemical variation within the microstructure and SEM-EDS. The results of multiple EDS point scans on each phase were averaged and used to guide the fabrication of samples of each phase in isolation. Perhaps due to

the small size of Heusler phase particles in CCA 72, which could lead to erroneous sampling of the matrix phase beneath a particle, a second iteration on the Heusler phase chemistry was necessary. These experiments produced three new alloys; CCA 81 (Matrix), CCA 82 (Heusler v1) and CCA 90 (Heusler v2). The microstructures of these alloys are compared in Figure 3.2 and their chemistries can be found in Table 3.1.

In order to confirm the crystal structure of each phase, x-ray powder diffraction experiments were performed. The majority phase is easily identified as face-centered cubic (FCC), though the reflections of the minority second phase only suggest that it is body-centered cubic (BCC) like, e.g., it cannot be definitively determined whether it is BCC, B2 or Heusler phase. Further diffraction experiments on the alloys planned based on EDS results show superlattice reflections indicative of a chemically ordered phase, which become clearer and more prominent as the phase chemistry is refined. Powder spectra for three alloys are shown in Figure 3.3. It should be noted that an ordered B2 structure will produce a diffraction pattern very similar to that of an ordered $L2_1$ structure. For instance, the ordered Heusler compound $Al_{3.79}Fe_{2.46}Ni_{5.54}Ti_{4.21}$ [9] and the ordered B2 compound $Al_{0.624}Fe_{0.54}Ni_{0.836}$ [10] the $L2_1$ structure has a higher-order (200) peak at nearly the same position as the (100) super lattice reflection of B2 at 30.38 and 31.07 degrees 2θ, respectively. The same is true of the $L2_1$ (220) and the fundamental B2 (110) at 43.50 and 44.51 degrees 2θ. Two $L2_1$ reflections which do not lie closely adjacent to B2 reflections are the $L2_1$ (111) and (311), both of which are clearly visible in the diffraction pattern of CCA 90.

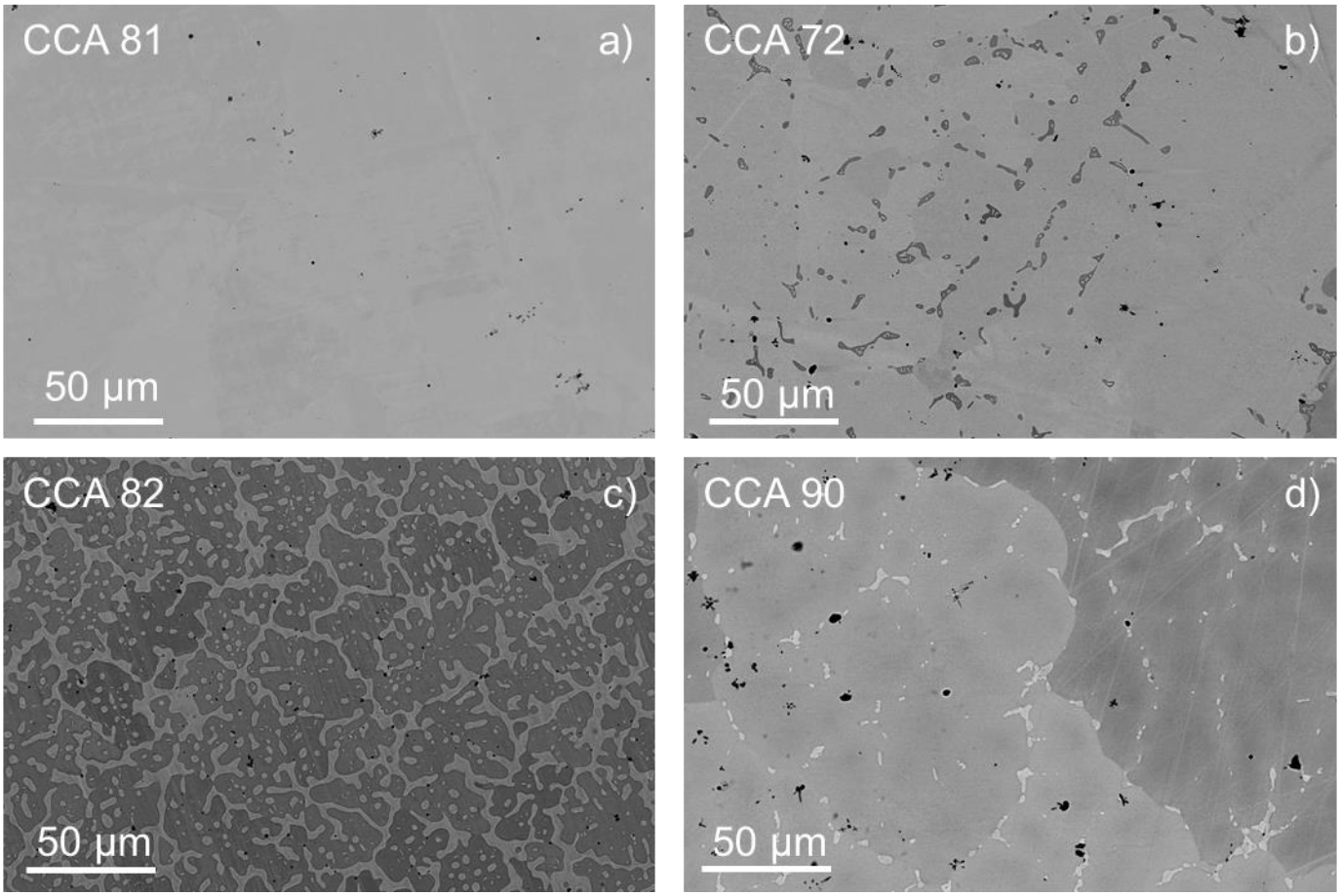

Figure 3.2: Backscattered electron micrographs of the microstructures of a) the matrix phase alloy, b) the original two-phase composite, c) the Heusler phase alloy based on SEM-EDS of CCA 72 and d) the Heusler phase alloy based on SEM-EDS of CCA 82.

Further definitive proof of the $L2_1$ Heusler phase was sought through TEM-SAED, and TEM-EDS was also performed to take advantage of the thin sample geometry to eliminate the possibility of probing more than one phase during analysis. The electron diffraction patterns for each phase are shown in Figure 3.4. The chemistries obtained from TEM-EDS are also listed in Table 3.1. TEM-EDS also identifies small-scale (~50 nm) Mo segregation at grain and interphase boundaries in CCA 72, in addition to small (~20 nm) Heusler precipitates decorating grain boundaries. The EDS results are summarized in Figure 3.5.

Table 3.1: The planned chemistry of CCA 72 and the measured phase chemistries obtained from EDS, relevant to Figure 3.2. The measured phase chemistries of CCA 72 from TEM-EDS are provided for comparison.

(in atomic %)	Al	Cr	Fe	Mn	Mo	Ni	Ti
CCA 72 – planned composition	6	10	40	5	3	30	6
Matrix:							
CCA 81 (SEM-EDS)	3.7	11.0	42.6	5.2	3.1	28.8	5.6
CCA 72 Matrix (TEM-EDS)	4.9	10.0	43.7	5.8	2.1	28.3	5.2
Reinforcement:							
CCA 82 (SEM-EDS)	14.3	3.5	17.2	4.2	0.9	44.1	15.9
CCA 90 (SEM-EDS)	19.7	1.5	10.4	4.0	0.3	44.7	19.4
CCA 72 Heusler (TEM-EDS)	18.7	2.1	13.7	4.1	0.4	45.8	15.2

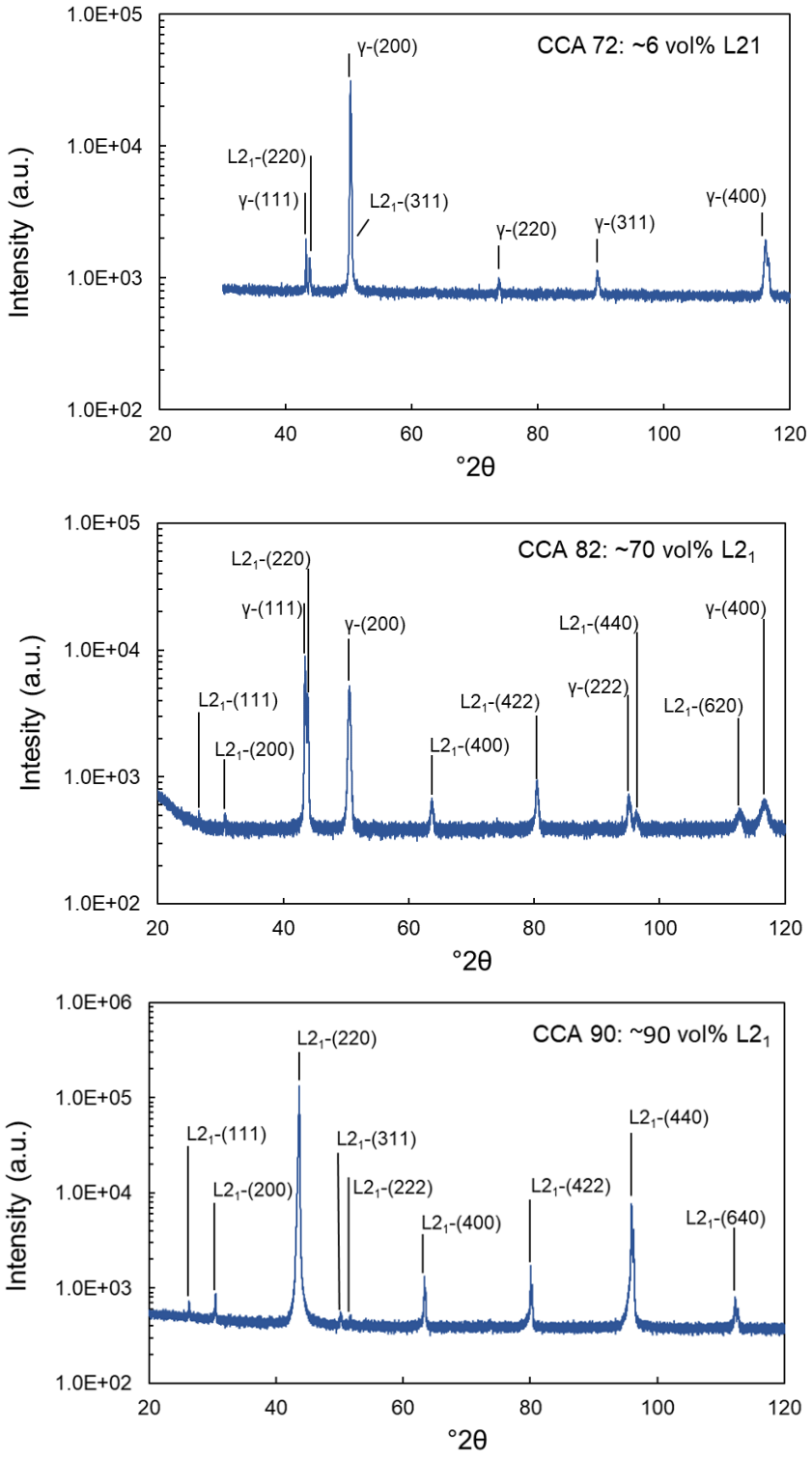

Figure 3.3: Powder x-ray diffraction patterns of CCAs 72, 82 and 90. As the volume fraction of Heusler phase increases, the characteristic peaks of the $L2_1$ structure become clearly visible.

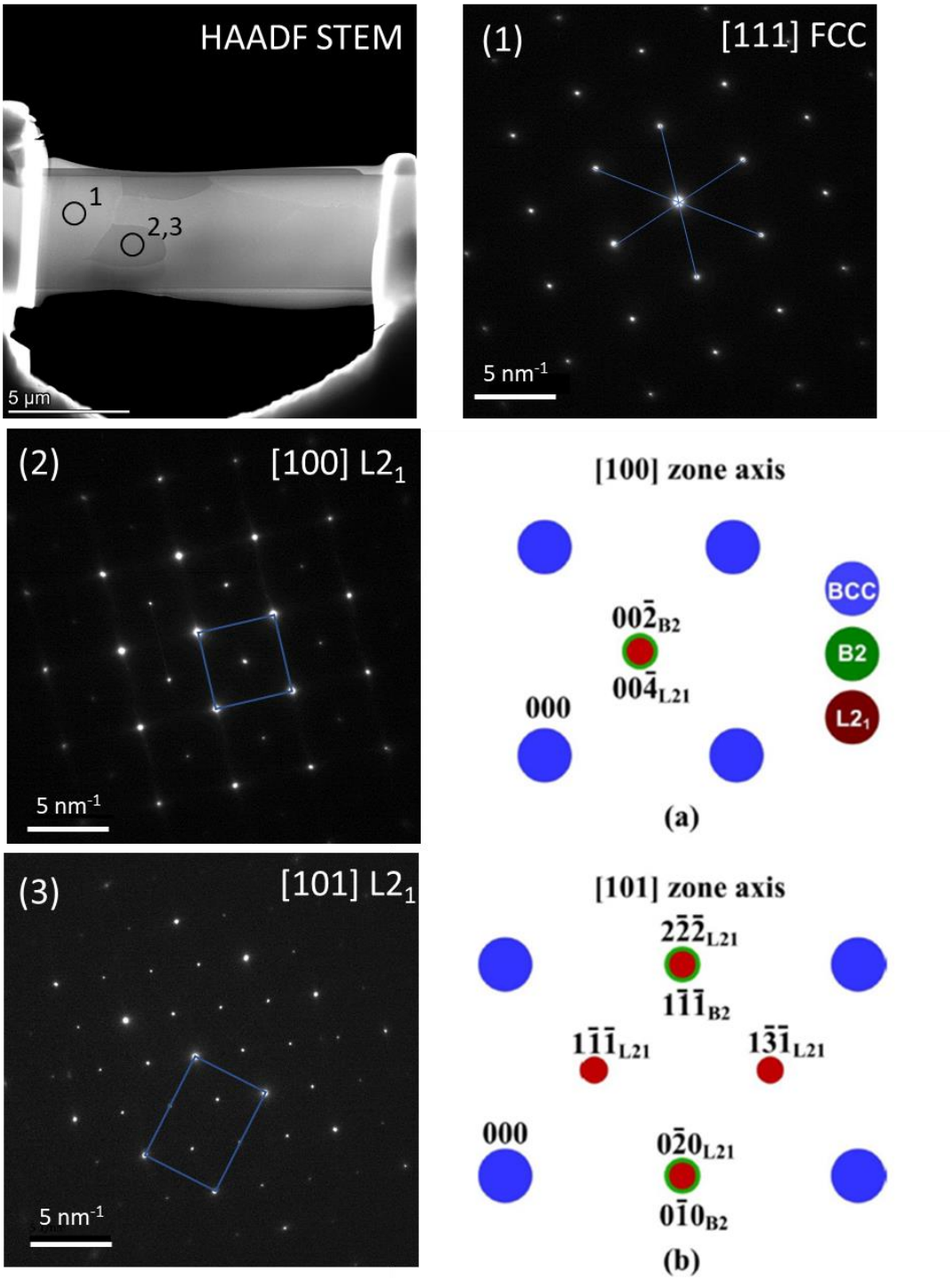

Figure 3.4: High-Angle Annular Dark Field Scanning Transmission Electron Micrograph (HAADF-STEM) and accompanying SAED patterns of the matrix (1) and Heusler (2,3) phases. A schematic diffraction pattern is reproduced from G. Song (2016) [11] to highlight the unique elements of an $L2_1$ diffraction pattern along the [101] zone axis, which are clearly visible in the experimental SAED pattern (3).

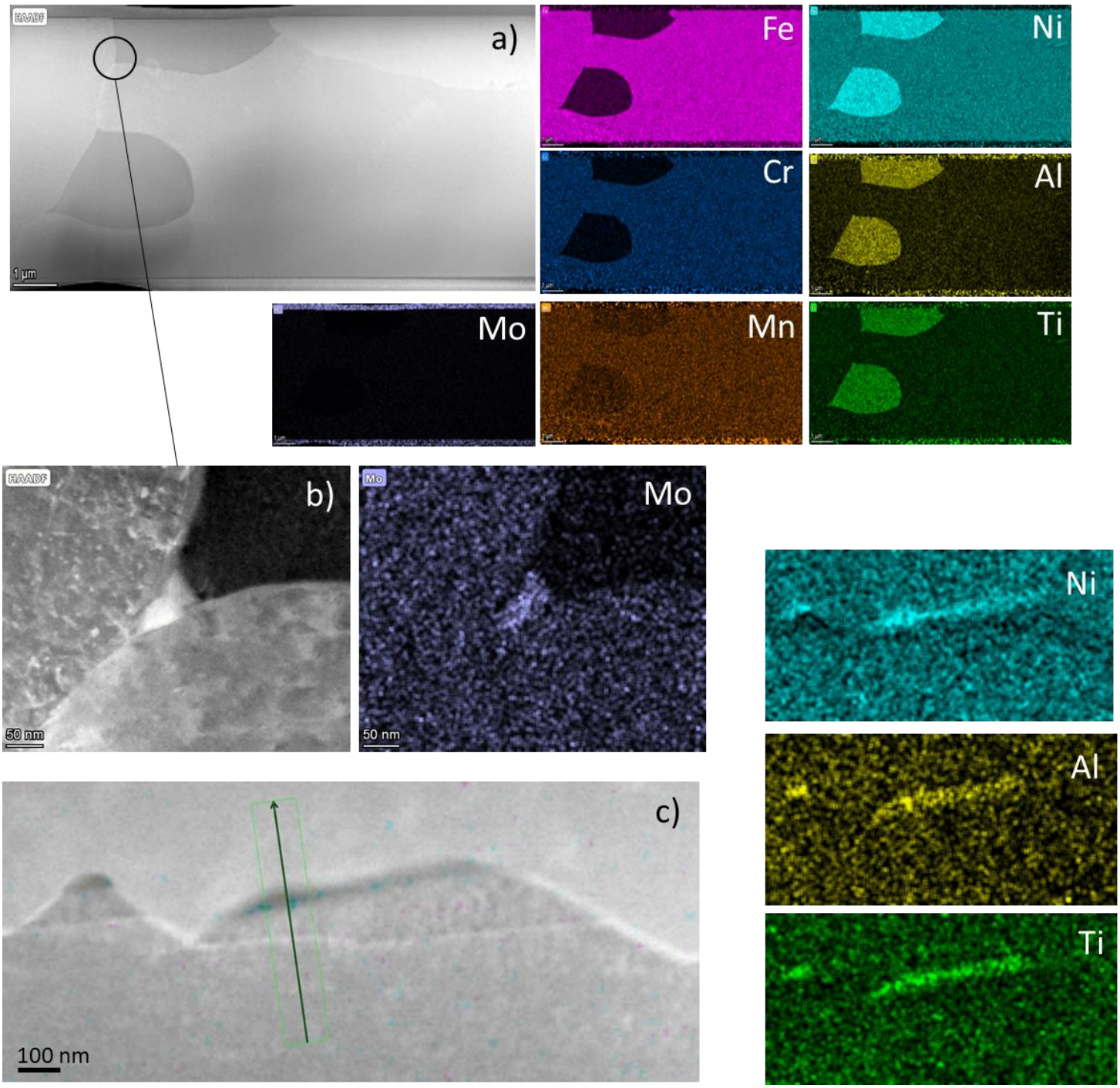

Figure 3.5: TEM-EDS data showing a) the general partitioning behavior of elements in CCA 72, showing Fe, Cr and slight Mn enrichment in the matrix, with Ni, Al and Ti enrichment in the Heusler phase. The enrichment of Mo along the top and bottom of the TEM sample is likely due to redeposition of Mo during the ion milling lift-out procedure. b) shows Mo enrichment at a grain triple point, and c) shows the formation of fine Heusler precipitates along grain boundaries.

An alloy with a higher aluminum concentration, CCA 95, was also examined via TEM. In addition to the FCC and Heusler phases, plates of an Fe- and Cr-rich phase were found within the Heusler phase grains and on Heusler grain boundaries. This hierarchical microstructure is reminiscent of the FBB8 alloys previously examined by the present researchers [12] which was shown to exhibit a excellent creep resistance by a collaboration between researchers at Northwestern University and the University of Tennessee [13][14]. Although the structure of the present plate-like precipitates has not been confirmed using SAED, the chemistry of this phase suggests that it is the $P4_2/mnm$, $(Cr,Fe)_{10}(Cr,Fe)_4(Cr,Fe)_{16}$ Sigma phase [15]. Observations and analysis of this plate-like phase are summarized in Figure 3.6.

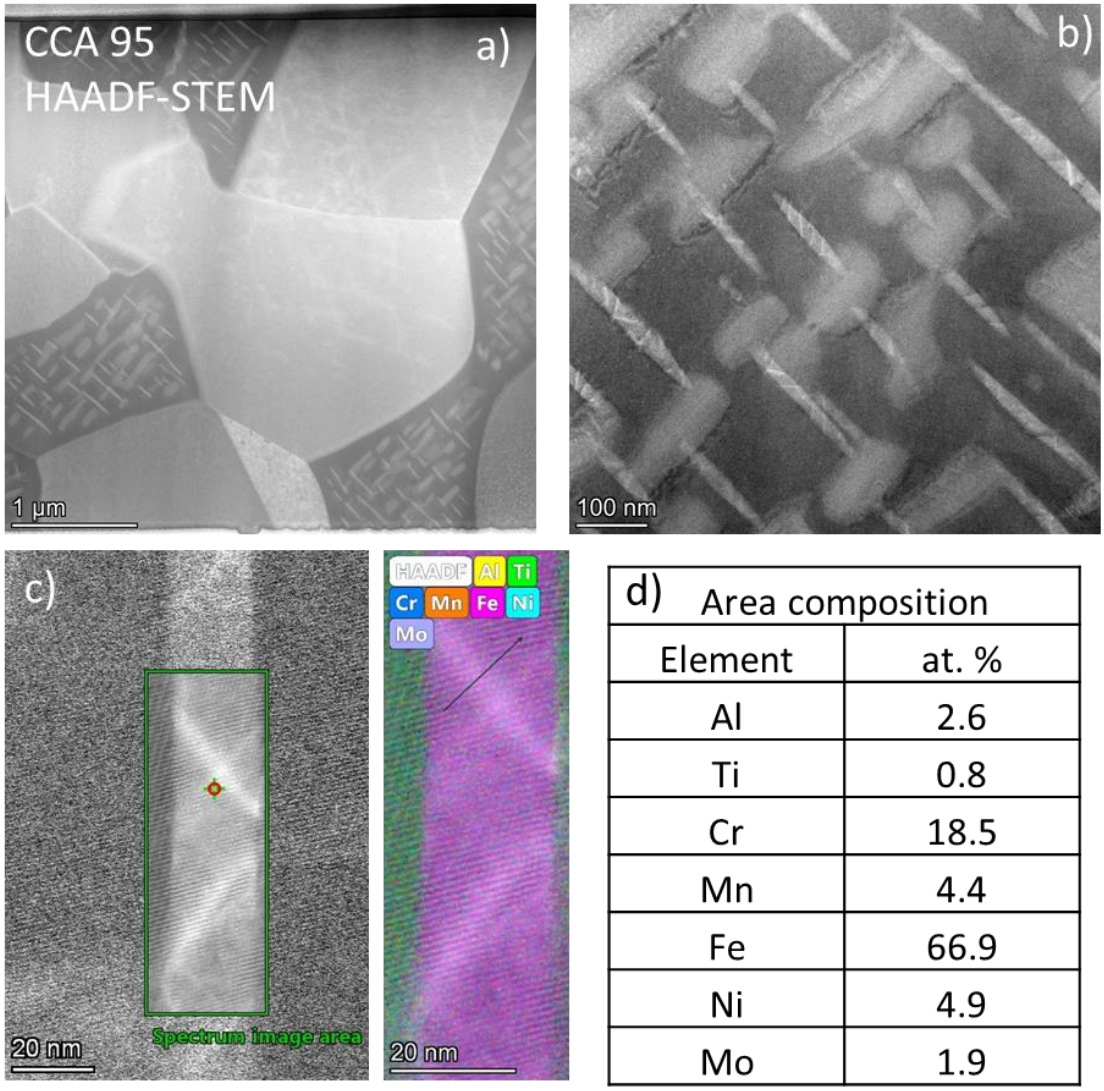

d) Area composition

Element	at. %
Al	2.6
Ti	0.8
Cr	18.5
Mn	4.4
Fe	66.9
Ni	4.9
Mo	1.9

Figure 3.6: a,b) TEM micrographs of CCA 95, a higher (~14.3 at%) Al composition which formed a hierarchical microstructure with plate-like precipitates within the Heusler phase, which most likely represent the $P4_2$ /mnm Sigma phase. A TEM-EDS scan and element-color map are shown in c), and d) lists the obtained chemistry of that area, showing primarily Fe and Cr enrichment.

3.4.2 Thermo-Calc Calculations

Equilibrium cooling calculations were performed first to identify which phases are stable in CCA 72 as a function of temperature. At the chosen homogenization temperature of 1070°C, Thermo-Calc predicts that CCA 72 will be a single-phase FCC solid solution, which is in agreement with the predictions of the machine learning tool [1] developed as part of this collaborative research effort. However, multiple castings of the CCA 72 chemistry have been observed to contain multiple phases even after homogenization annealing at 1070°C for 5 hours, as shown in Figure 3.2b. It is acknowledged that the homogenization treatment is a short one; the temperature and duration were selected in light of the limitations of the available annealing furnace. To explore the possibility of non-equilibrium phase formation, Scheil-Gulliver solidification calculations were performed in Thermo-Calc. The Scheil calculations predict that during rapid solidification of the alloy, the chemistry of the melt pool will change such that the Heusler phase will precipitate after the majority of the alloy has solidified as disordered FCC. Specifically, 2.4 vol% Heusler phase is predicted to form during rapid cooling, alongside 1.9 vol% of a P63/mmc (C14) Laves phase enriched in Ti, Ni and Fe. The Laves phase is not observed experimentally in cast or homogenized samples, though it is noted that the total amount of non-FCC phases, 4.6 vol%, closely matches the observed Heusler volume fraction of about 5% in homogenized samples. In some castings, a Mo-rich phase is observed, but this phase is completely dissolved during homogenization. The equilibrium and Scheil cooling are compared in Figure 3.7. These calculations provide a reasonable explanation for the presence of the Heusler phase after casting. Further supporting evidence for this explanation is provided by observations of dendritic microstructures in cast samples, as shown in Figure 3.8, in which the Heusler phase forms within the interdendritic spaces which become solute enriched during solidification.

Using the primary dendrite arm spacing, cooling rates were approximated via Equation 3.2. For the bar-cast samples, an average dendrite arm spacing of 19.8 ± 2.9 mm and a cooling rate of 74.8 K/s were obtained. For suction-cast samples, an average dendrite arm spacing of 6.75 ± 1.4 mm and a cooling rate of 1660 K/s were obtained. These values are within the bounds of casting and arc welding, respectively, as described in [4].

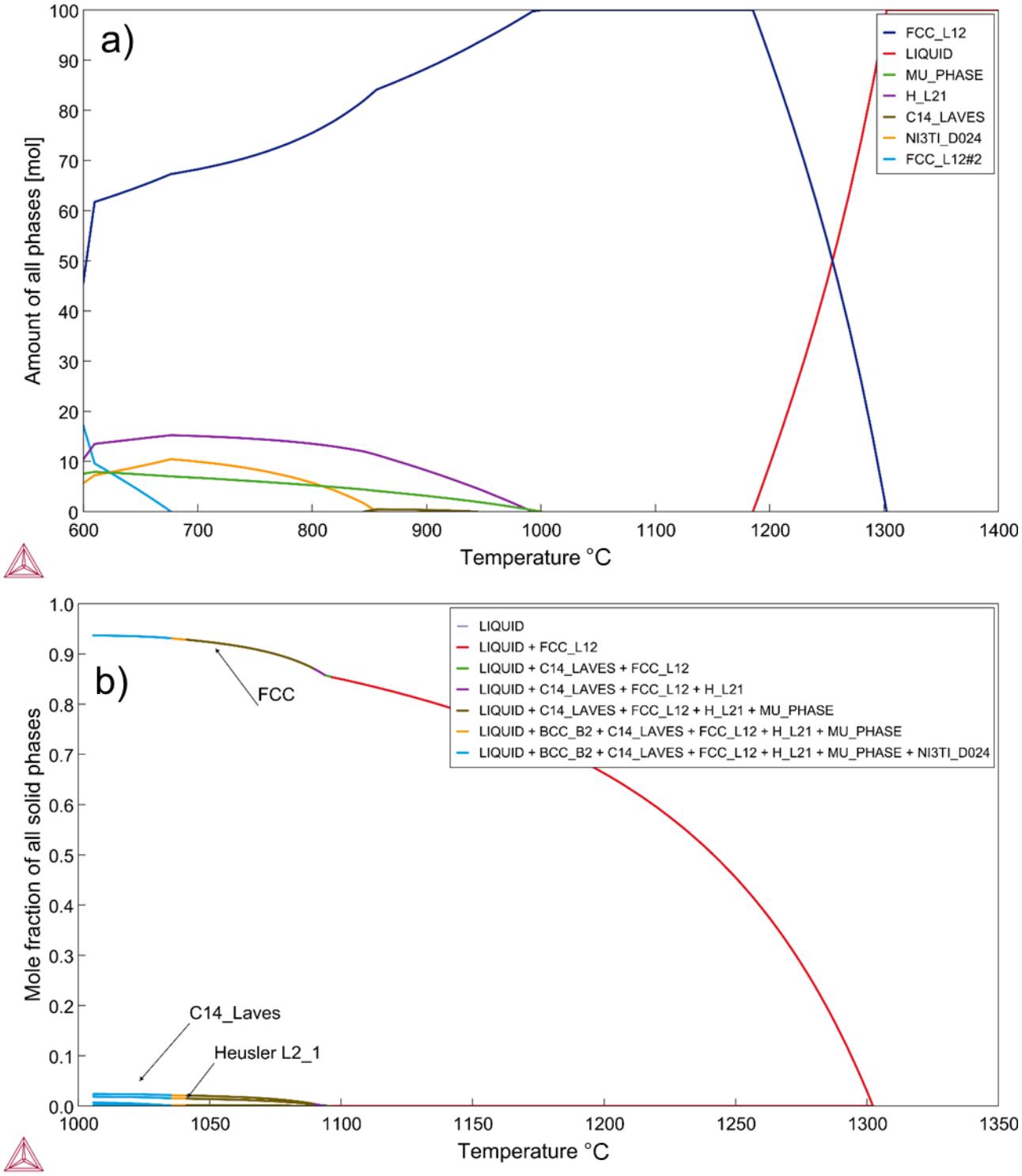

Figure 3.7: Thermo-Calc Equilibrium Cooling (a) and Scheil Cooling (b) calculations for CCA 72. While equilibrium predicted a single-phase FCC solid solution at 1070 °C, Scheil cooling predicted the formation of other phases as the remaining melt becomes enriched in solute.

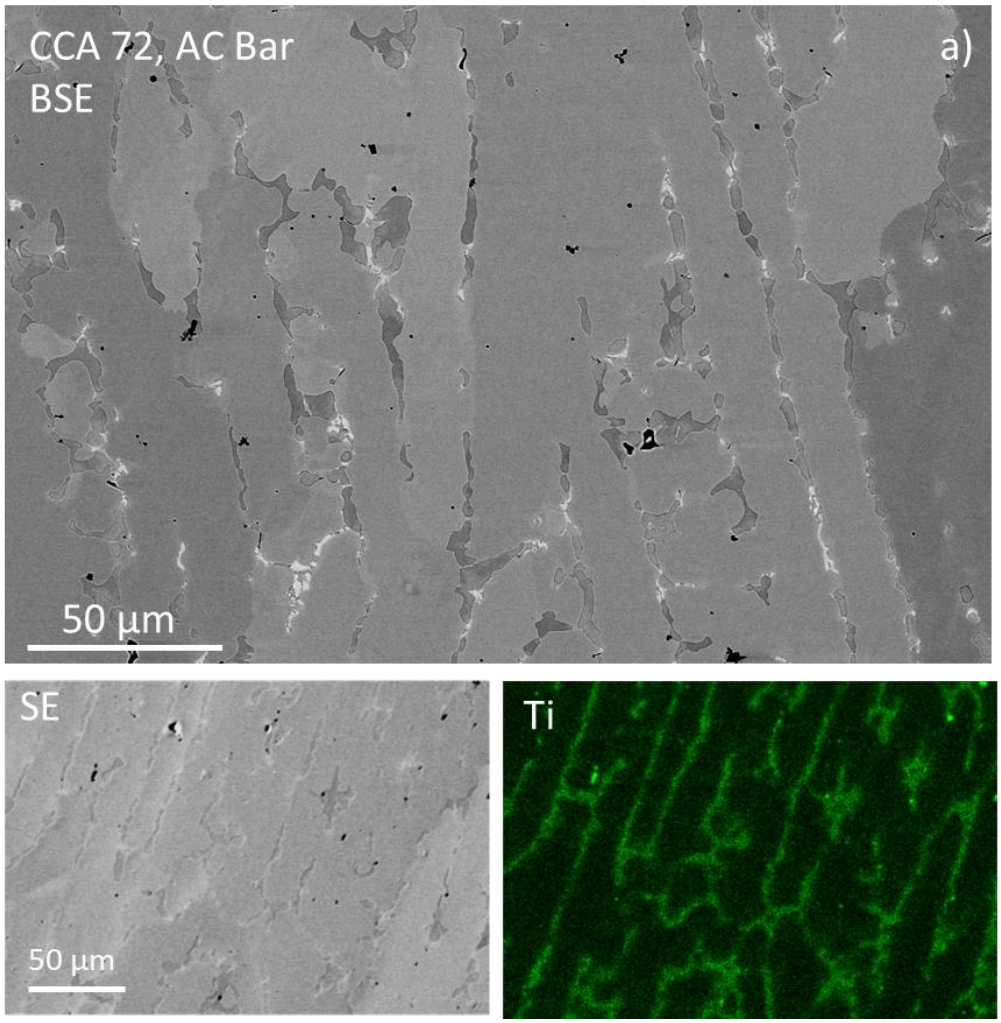

Figure 3.8: a) Backscattered electron micrograph of CCA 72 bar casting, in which interdendritic Heusler phase and bright, Mo-rich phase are clearly observed. b) Secondary electron micrograph and accompanying SEM-EDS map (c) of Ti enrichment at dendrite boundaries.

A series of single-axis equilibrium calculations was performed in Thermo-Calc, using CCA 72 as a basis, this time by varying the concentration of a single element with Fe acting as a balance. This process was used to identify which elements, among Ni, Ti and Al, and to what extent the volume fraction of the Heusler phase could be influenced by changes in alloy chemistry. The equilibrium calculations for Fe, Cr, Mn and Mo are located in Appendix A. It was found that Al had the greatest effect, in that the highest volume fraction of Heusler phase was predicted as a function of Al variation within the range of chemistries investigated at 1070°C. It should be noted that Ti variation can achieve a slightly higher volume fraction of the Heusler phase, however it was also predicted to lead to partial melting of the alloys at the selected homogenization temperature and was therefore deemed unsuitable for phase control. Ni was found to further stabilize the FCC phase. Select results from these calculations are presented in Figure 3.9.

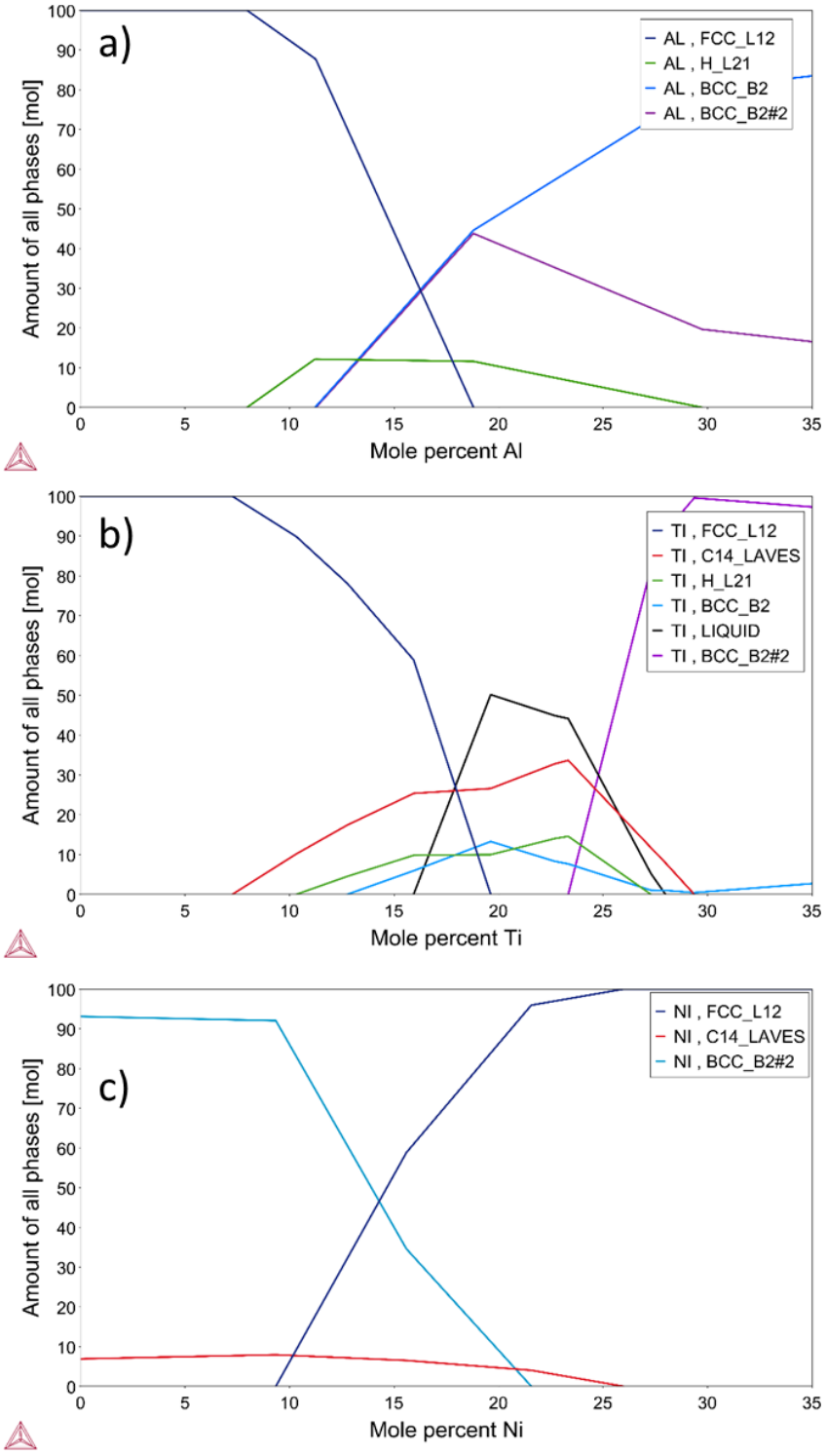

Figure 3.9: Thermo-Calc equilibrium calculations of phase content in CCA 72 as a function of a) Al, b) Ti and c) Ni. Despite the participation of all three elements in the Heusler phase, increasing Ti is predicted to lead to melting at 1070°C, whereas increasing Ni further stabilized the FCC phase. As such, Al is identified as the most potent influencer of Heusler phase content.

Continuing with a base chemistry of CCA 72, it was next sought to describe the stable phases of the alloy system as a function of both temperature and aluminum concentration. To that end an isopleth diagram was generated, in which phase space is described by a series of overlapping "zero-fraction" lines, rather than definitive phase boundaries. The chemistry of the alloy has been defined such that there are finite amounts of all alloying elements except for aluminum, which is varied by its atomic percent concentration as $(Cr_{10}Fe_{40}Mn_5Mo_3Ni_{30}Ti_6)_{1-X}Al_X$. The diagram, shown in Figure 3.10, can be thought of as a pseudo-binary in the sense that only the proportion of these two halves of the chemistry are changing. Within the range of aluminum concentration investigated, a stable FCC + $L2_1$ region is identified at roughly 1275 to 1400 K between 6.3 and 11.5 at% aluminum. It is important to note that the Heusler phase is stable beyond these boundaries, though other phases will begin to form as well.

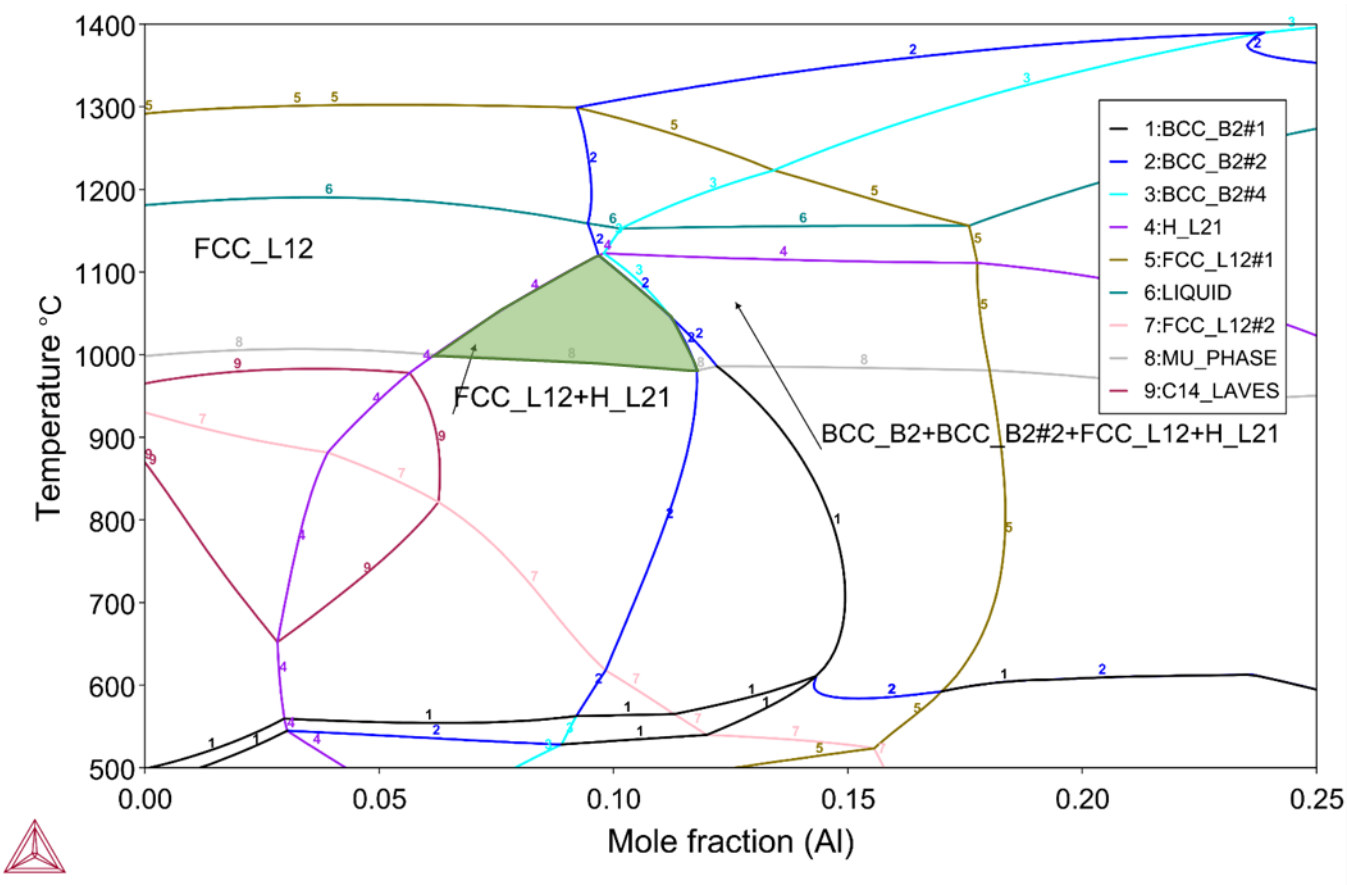

Figure 3.10: The pseudo-binary isopleth equilibrium phase diagram generated as a function of Al concentration. Contrary to a traditional phase diagram, the boundaries depicted are zero-fraction lines rather than well-defined phase boundaries. The FCC + $L2_1$ phase region of interest is highlighted in green.

To generate the isopleth, it was necessary to limit the number of phases considered by Thermo-Calc for calculation. This was achieved by generating single-axis equilibrium curves, similar to Figure 3.7 a, from 0 to 25 at% aluminum in steps of 5 atomic percent. Through these calculations, the stable phases of interest were determined to be: BCC_B2, BCC_B2#2, C14_Laves, FCC_L12, FCC_L12#2, H_L21 (the Heusler phase), Liquid, Mu_phase, Ni3Ti_D024 and Sigma phase. Note that when using TCHEA3, disordered and ordered BCC / FCC structures are not discriminated in the naming convention, but phases with the same structure and distinct chemistry are denoted by distinct, identifying numbers. The ultimate determination of ordered versus disordered is revealed decided by the predicted lattice site occupancy, which Thermo-Calc supplies as part of an equilibrium calculation. From the isopleth diagram, a series of alloy compositions was generated with the intention of controlling the Heusler phase content by varying aluminum concentration. The resulting alloys, along with those based on EDS analysis of individual phases are summarized in Table 3.2. These alloys were synthesized and examined via SEM-EDS to confirm their bulk chemistries and backscattered electron micrographs were analyzed based on a contrast threshold using ImageJ software [16] to obtain phase area fractions, which are summarized in Table 3.3. Most alloys were found to be slightly enriched in Al beyond their planned compositions.

Table 3.2: The planned chemistries of the alloys of interest, guided by the ML tool (72), SEM-EDS (81, 82, 90) and Thermo-Calc. The chemistries of 316L [17] and AL-6XN [18] are provided as comparison to commercial corrosion-resistant steels.

(at%)	Al	Cr	Fe	Mn	Mo	Ni	Ti
CCA 81	3.7	11.0	42.6	5.2	3.1	28.8	5.6
CCA 72	6.0	10.0	40.0	5.0	3.0	30.0	6.0
CCA 94	8.2	9.8	39.1	4.8	2.9	29.3	5.9
CCA 91	9.4	9.6	38.5	4.8	2.9	29.0	5.8
CCA 92	11.4	9.4	37.7	4.7	2.8	28.3	5.7
CCA 95	14.3	9.1	36.6	4.6	1.7	27.4	6.5
CCA 82	14.3	3.5	17.2	4.2	0.9	44.1	15.9
CCA 90	19.7	1.5	10.4	4.0	0.3	44.7	19.4
SS 316L	-	19.3	62.1	0.02	0.02	13.3	-
AL6XN	-	24.0	42.4	0.02	0.04	24.7	-

Table 3.3: The measured chemistries of synthesized alloys in the homogenized state, and their corresponding $L2_1$ volume fractions obtained from image analysis.

(at%)	Al	Cr	Fe	Mn	Mo	Ni	Ti	$L2_1$ vol% (Hm)
CCA 81	4.3	11.3	42.1	5.2	2.8	28.5	5.8	0
CCA 72	6.1	10.6	40.7	5.6	2.1	29.7	5.2	5
CCA 94	8.4	10.2	39.0	5.1	2.0	29.2	6.1	10
CCA 91	10.3	10.1	39.3	4.1	2.7	27.5	6.0	40
CCA 92	13.1	9.7	36.4	5.0	2.8	26.7	6.3	46
CCA 95	14.3	9.5	36.8	4.5	1.0	27.4	6.5	50
CCA 82	15.8	3.5	16.5	4.6	0.8	42.8	16.0	70
CCA 90	20.0	1.2	10.2	3.9	0.2	44.2	20.3	90

Despite the prediction of a thermodynamically stable FCC+$L2_1$ region, the question remains as to why the Heusler phase is apparently stable at 1070°C in CCA 72, which sits outside of the predicted 2-phase region. To address this question, an as-cast sample of CCA 72 was solutionized at 1150°C for 24 hours, just below the predicted solidus temperature of 1190°C. The Heusler phase was observed to dissolve completely into the FCC matrix, with a small increase in the phase fraction of titanium nitride particles, which have also been observed in cast and homogenized samples. After solutionization, the same sample of CCA 72 was aged at 1070°C to determine whether the Heusler phase would re-precipitate. After aging for 24 hours, nitride impurities increased in volume fraction and an additional phase formed which was not the Heusler phase, but was rich in aluminum. The as-cast, solutionized and aged microstructures are compared in Figure 3.11, and relevant EDS chemistries are presented in Table 3.4. Subsequently, a millimeter of material was removed from the surface of the aged sample with SiC paper to investigate whether the nitrides were limited to the near-surface region of the material. Indeed, below the nitrogen-rich surface layer, the Heusler phase was observed to have precipitated from the matrix, primarily at grain boundaries and along other imperfections such as voids. Unlike what had been previously observed for CCA 72, plates similar to those in Figure 3.6 are observed within the Heusler phase. Micrographs and EDS maps of the newly-precipitated Heusler phase are shown in Figure 3.12.

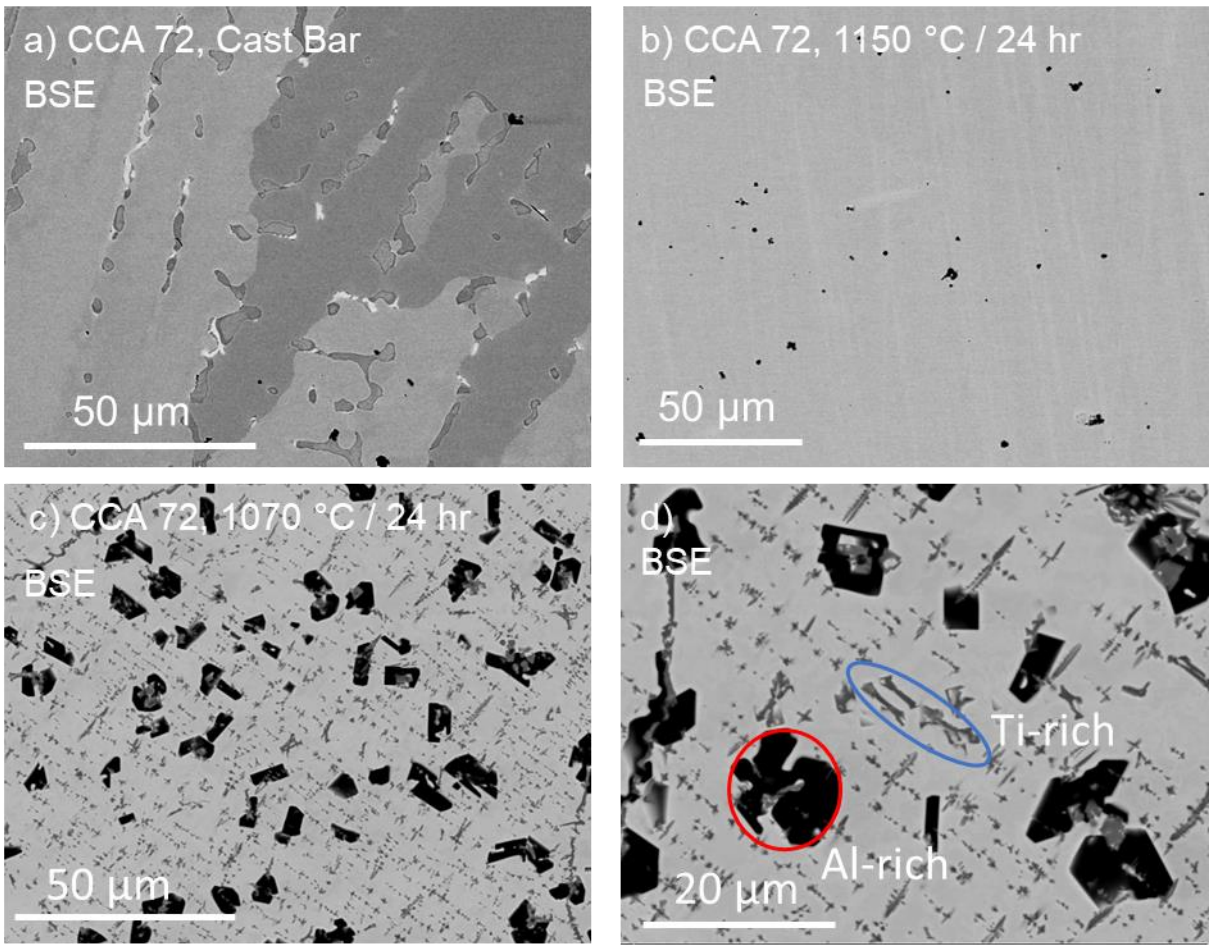

Figure 3.11: Micrographs of CCA 72 in the a) as-cast, b) solutionized (1150°C / 24hr) and c) aged (1070°C / 24hr) states. A close-up of Ti- and Al-rich precipitates which form after aging is shown in d).

It is acknowledged that the chemistry of each phase will change, when only varying aluminum concentration to control the volume fraction of the Heusler phase. This could impact the properties of the phases. Individual phase chemistries were predicted via Thermo-Calc (Table 3.5) and measured for select samples via SEM-EDS (Table 3.6). A more ideal strategy would be to vary the chemistries of the alloys by moving along a tie-line between the compositions of the end-member FCC and Heusler phases.

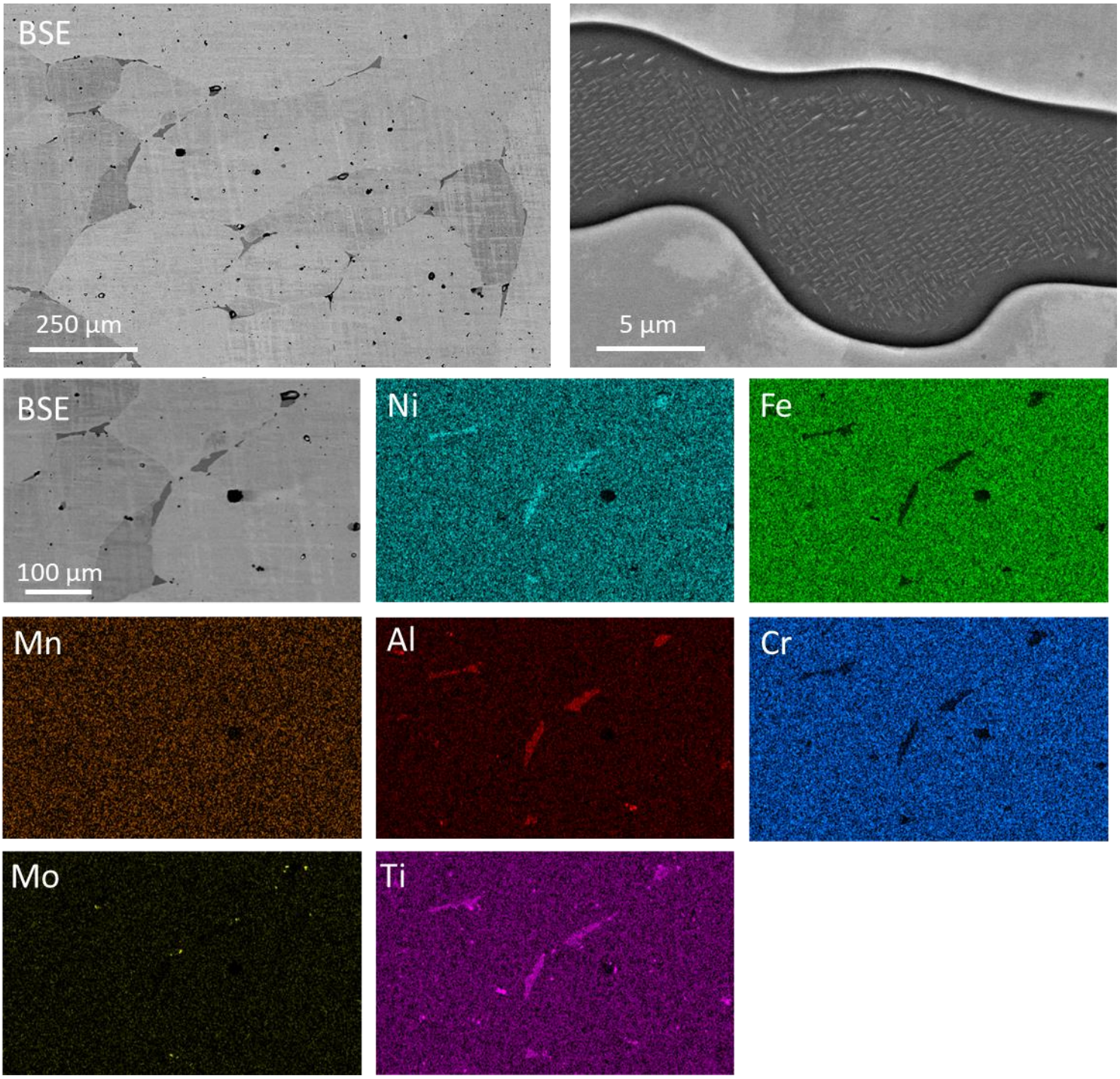

Figure 3.12: a) The microstructure of the aged CCA 72 sample 1mm below the sample surface. The Heusler phase has precipitated from solution onto austenite grain boundaries. b) Close-up of a Heusler phase grain in the aged material showing plates of an Fe-rich phase. c) EDS maps showing similar element partitioning to that observed in Figure 3.5.

Table 3.4: EDS-measured chemistries of the phases present at the sample surface in CCA 72 after aging at 1070°C for 24 hours.

(at%)	Al	Cr	Fe	Mn	Mo	Ni	Ti	N	O
Matrix:	1.0	11.7	45.6	5.8	2.4	33.1	0.4	-	-
Al-rich precipitates:	38.6	1.0	3.3	0.5	0.2	2.1	10.3	42.7	1.4
Ti-rich precipitates:	1.1	4.1	15.8	2.1	0.8	11.7	22.7	38.9	2.8

Table 3.5: Phase chemistries for select alloys as predicted by Thermo-Calc at equilibrium. The phase compositions of CCA 91, marked with an asterisk, were used as reference chemistries for the tie-line calculations.

(at%)	Al	Cr	Fe	Mn	Mo	Ni	Ti
Matrix:							
CCA 72	6.0	10.0	40.0	5.0	3.0	30.0	6.0
CCA 94	8.1	10.1	39.3	4.8	2.9	29.2	5.8
CCA 91*	8.5	10.1	40.4	5.0	3.1	27.8	5.0
CCA 92	9.1	10.2	42.1	5.2	3.1	26.0	4.2
Heusler phase:							
CCA 72 (Scheil)	23.9	0	0	0	0	54.1	22.0
CCA 94	26.4	0	0	0	0	52.4	21.2
CCA 91*	27.0	0	0	0	0	52.1	20.9
CCA 92	27.8	0	0	0	0	51.7	20.5

Table 3.6: Phase chemistries for select alloys as observed via SEM-EDS. The primary difference between these chemistries and those listed in Table 3.5 is significant Fe solubility in the Heusler phase.

(at%)	Al	Cr	Fe	Mn	Mo	Ni	Ti
Matrix:							
CCA 72	3.6	11.1	42.6	5.2	3.1	28.8	5.6
CCA 94	5.7	11.4	43.7	5.3	2.7	26.8	4.4
CCA 91	5.5	11.6	45.2	5.3	3.0	25.3	4.0
Heusler phase:							
CCA 72	13.8	3.6	17.3	4.3	0.9	44.4	15.9
CCA 94	21.1	2.7	15.2	4.4	0.4	42.7	13.4
CCA 91	21.3	2.8	15.8	4.7	0.5	42.4	12.5

As may be done in any two-phase field, it was also sought to determine whether a "tie-line" of sorts could be defined for the FCC+$L2_1$ phase region, such that the volume fraction of Heusler phase can be tuned for mechanical purposes without affecting the endpoint chemistries. Using CCA 91 as a reference point, which lies in the center of the predicted FCC+$L2_1$ phase region, equilibrium endpoint chemistries were defined for each phase. Nominal alloy chemistries were calculated via a mole-fraction rule of mixtures based on the endpoint phase chemistries of element 'X', defined in Equation 3.5. The reference endpoint chemistries, a selection of calculated alloy chemistries and their chemistry error values are summarized in Table 3.7.

$$C_X^{alloy} = N_{FCC} C_X^{FCC} + N_{L21} C_X^{L21} \tag{3.5}$$

Table 3.7: Calculated bulk chemistries generated by the "tie-line" method. Thermo-Calc does not predict any deviation from tie-line behavior at equilibrium, and so the volume fractions of each phase may be varied freely without changing the chemistry of either phase.

$L2_1$ vol%	Al (at%)	Cr	Fe	Mn	Mo	Ni	Ti
0	8.5	10.1	40.4	5.0	3.1	27.8	5.0
5.2	9.4	9.6	38.4	4.8	2.9	29.0	5.8
16.1	11.3	8.6	34.4	4.3	2.6	31.5	7.4
26.5	13.1	7.6	30.3	3.8	2.3	33.9	9.0
51.9	17.7	5.0	20.2	2.5	1.5	40.0	13.0
76.4	22.4	2.5	10.1	1.3	0.8	46.0	16.9

3.5 Discussion

The Heusler phase has been positively identified to be present in alloys with chemistries near that of CCA72, both in as-cast and annealed conditions through various diffraction techniques, with TEM-SAED providing the clearest results. The fact that it includes high concentrations of Al and Ti, which promote passive oxide scale formation, suggests that the corrosion resistance of this Heusler phase may be compatible with the FCC matrix and, hence, able to be tuned for mechanical property enhancement without fear of degrading the corrosion resistance of the alloy [19]. TEM was also able to identify an additional phase within the Heusler phase, which although it has likely been observed as part of past SEM analysis could not be characterized outside of TEM due to its small length scale. The presence of additional phases forming 'hierarchical' microstructures in the Heusler phase is not unprecedented, as a B2 phase was observed to nucleate on Heusler particles within the ferrite-plus-$L2_1$ alloy FBB8. [11] It is worth noting that the Sigma phase is not predicted by Thermo-Calc to be stable at 1070°C, though it is predicted at lower temperatures around 775°C. Similarly, while the experimentally observed chemistry of the Heusler phase deviates from the chemistry predicted by Thermo-Calc (see Tables 3.6 (EDS) and Table 3.5 (T-C),) the Fe solubility is not unheard of; Yang et al. [20] observed 6.7 at% Fe solubility in stoichiometric Ni2TiAl. In an investigation of the quaternary Ti-Fe-Ni-Al system, Yan et al. [21] found a region of pure Heusler phase stability at 900°C. In a separate study, Yan et al. [9] also studied the $Ti_{25}(Fe_{50-X}Ni_X)Al_{25}$ Heusler phase and found that both Fe and Ni can occupy the 8c sites in the $L2_1$ structure, with primarily Ti with small amounts of Al on 4a sites and the remaining Ti and Al sitting on 4b sites. In this study, Thermo-Calc predicts similar occupancy of 8c sites as Ni, with one sublattice (4a, for instance) occupied by a mixture of approximately 0.8 Ti and 0.2 Al, with the other being primarily (0.9) Al with some (~0.1) Ni occupancy. Based on the observed chemistries of the Heusler phase, which contains more than 50 atomic percent Ni and Fe, the following hypothesis is proposed: the majority of the Fe sits on 8c sites, shared with Ni,

and all the Ti atoms sit on 4a sites. Due to the higher proportion of Al to Ti, it is likely that the Ti sites host more than the predicted proportion of Al atoms, while the 4b Al sites accommodate the excess Ni displaced from 8c sites by Fe. Such Ni anti-site defects have been known to occur in Ni-rich NiAl [22]. The small amounts of Cr and Mn measured likely also occupy 8c sites.

The pseudo-binary isopleth diagram, while far from a complete description of the Al-Cr-Fe-Mn-Mo-Ni-Ti system, provides a large amount of guidance for alloy design. It reinforces the choice of a high annealing temperature; 1070°C was originally selected as 0.8 times the predicted melting temperature of the early CCAs examined in this study, including CCA 72. Below 1000°C, multiple intermetallic phases become stable, starting with the Mu phase. A similar bounding value is found for Al concentration, roughly 10.7 at% Al at 1070°C. It has been confirmed experimentally that a single-phase, FCC solid solution exists at 6 at% Al and 1150°C. If it is assumed that the Thermo-Calc equilibrium predictions are correct, the Scheil cooling calculations provide a reasonable explanation for why the Heusler phase is observed beyond its predicted zero-fraction boundaries, as the $L2_1$ would be a metastable phase. However, despite the formation of nitrogen-rich phases on the sample surface after aging at 1070°C for 24 hours, the Heusler phase is confirmed to precipitate from solution at FCC grain boundaries deeper within the material after subsequent annealing at 1070 °C, suggesting that the Heusler phase is, in fact, thermodynamically stable. It can be concluded from these results that, while there is a single-phase solid solution present at higher temperatures, the zero-fraction line for the Heusler phase is not quite accurately drawn by Thermo-Calc, which may in reality lie farther toward the Al-lean side of the isopleth diagram, shown schematically in Figure 3.13. The presence of plates within the Heusler phase in aged CCA 72 also suggest that there is either a phase which forms that is not predicted by Thermo-Calc at all, or the formation of the Sigma phase is predicted at too low of a temperature by Thermo-Calc. It is also possible that the Heusler phase has less solubility for Fe across all alloys investigated than what can be concluded from the EDS-measured chemistries, given the Fe-rich nature of the observed plate-like phase.

The ultimate goal of varying the Heusler phase fraction in these novel alloys is the realization of an optimum microstructure which would maximize alloy toughness. The interdendritic nature of the Heusler phase, combined with very little observed microstructural change between the as-cast and homogenized states suggests that the solidification microstructure is a deciding factor of the overall microstructure. As such, for a finer distribution of Heusler phase, faster cooling rates than those provided by arc melting and suction casting will be necessary. While Al was shown to promote higher Heusler phase volume fractions, it has been shown in past studies that the elastic constants of NiAl are sensitive to changes in chemistry [22]–[24], and given the similarities between the B2 and $L2_1$ structures, it is not unreasonable to assume that the Heusler phase might display a similar sensitivity to changes in chemistry. These changes in chemistry, noted in Table 3.6, will affect the elastic contrast between the matrix and reinforcing phases, and a decrease in that contrast is undesirable [25][26]. Changes in the chemistry of the matrix could also be impactful, in terms of solid solution strengthening [27]. It will be difficult to quantify the impact of the Heusler phase volume fraction on mechanical properties if the phase chemistries are in flux. Future alloy compositions will benefit from the tie-line approach to dialing phase fractions.

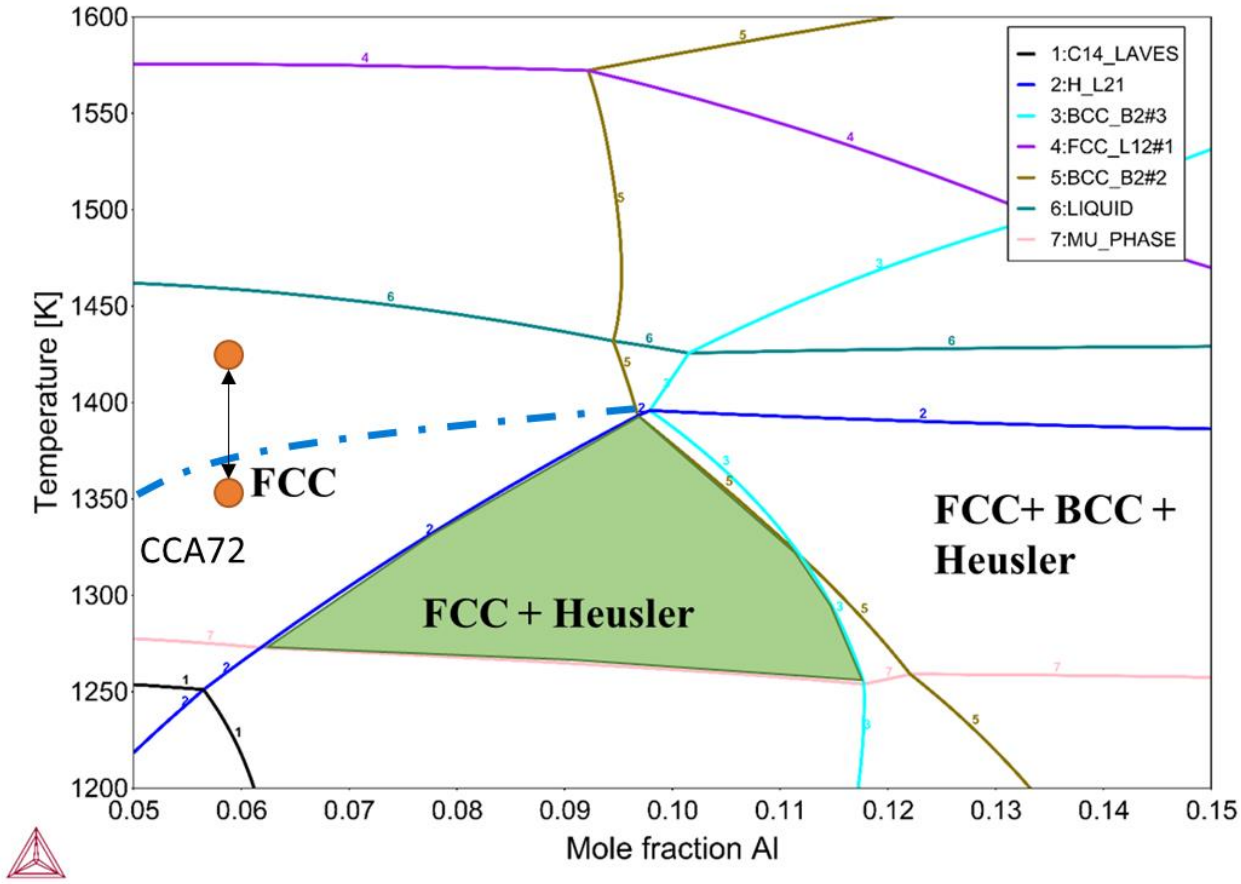

Figure 3.13: A schematic illustration of the proposed $L2_1$ zero-fraction line, to allow for the presence of the Heusler phase in the CCA 72 chemistry (denoted by orange circles) after solutionization (1150 °C / 24 hr) and aging (1070 °C / 24 hr).

3.5 Conclusions:

Using characteristic features of both x-ray and electron diffraction data, the second phase emerging in alloys was positively identified as the $L2_1$-structured, Ni_2TiAl-type Heusler phase. EDS data confirmed solubility for both Fe and Mn in the Heusler phase. While this phase was not predicted to be stable at the selected annealing temperature of 1070°C, by the machine learning tool or CALPHAD, Scheil-Gulliver simulations of rapid cooling suggest that the Heusler phase becomes favorable as the chemistry of the melt becomes enriched in solute. The phase-space predicted by Thermo-Calc has been shown to have some uncertainty, but the addition of Al to the CCA 72 alloy was shown to stabilize higher volume fractions of the Heusler phase at 1070°C. This fact has been used to control the volume fraction of the Heusler phase, up to the limit where additional Al would result in the formation of other BCC- and B2-structured phases. Further analysis also showed that the chemistry of alloys can be adjusted via the lever-rule, moving along

a tie-line across the two-phase field of a multi-component alloy phase diagram, resulting in complete control over the Heusler phase volume fraction without alteration of phase chemistries. In the context of future alloy design, utilizing the tie-line is recommended.

.

3.6 Acknowledgements

The authors would like to thank the Office of Naval Research for their support through ONR BAA #N00014-19-1-2420, directed by Dr. Airan Perez and Dr. David Shifler.

The authors would also like to thank Helge Heinrich of the UVA NMCF for his help with preparation of TEM samples and collection of the TEM data, and to thank Sam Inman for his discussions and insights of Thermo-Calc and CCA design.

3.7 References

[1] J. J. Bhattacharyya et al., "Lightweight, Low Cost Compositionally Complex Multiphase Alloys with Optimized Strength, Ductility and Corrosion Resistance: Discovery, Design and Mechanistic Understandings," Mater. Des., vol. 228, p. 111831, 2023, doi: 10.1016/j.matdes.2023.111831.

[2] K. Kanaya and S. Okayama, "Penetration and energy-loss theory of electrons in solid targets," J. Phys. D. Appl. Phys., vol. 5, no. 1, pp. 43–58, 1972, doi: 10.1088/0022-3727/5/1/308.

[3] N. Marturi, "Vision and Visual Servoing for Nanomanipulation and Nanocharacterization using Scanning Electron Microscope," Universite de Franche-Comte, 2006.

[4] J. W. Elmer, S. M. Allen, and T. W. Eagar, "Microstructural Development during Solidification of Stainless Steel Alloys," Metall. Mater. Trans. A, no. October, 1989, doi: 10.1007/BF02650298.

[5] S. Katayama and A. Matsunawa, "Solidification microstructure of laser welded stainless steels," ICALEO® '84 Proc. Laser Mater. Process. Symp., vol. 60, no. 1984, pp. 2–10, 2017, doi: 10.2351/1.5057623.

[6] C. A. Schneider, W. S. Rasband, and K. W. Eliceiri, "HISTORICAL commentary NIH Image to ImageJ : 25 years of image analysis," Nat. Methods, vol. 9, no. 7, pp. 671–675, 2012, doi: 10.1038/nmeth.2089.

[7] G. H. Gulliver, "Appendix," in Metallic Alloys, London, England: Charles Griffin & Co., Ltd., 1922.

[8] E. Scheil, "Bemerkungen zur Schichtkreistallbildung," Int. J. Mater. Res., vol. 34, no. 3, pp. 70–72, 1942.

[9] X. Yan, A. Grytsiv, P. Rogl, V. Pomjakushin, and M. Palm, "The Heusler phase Ti 25(Fe 50 - X Ni x)Al 25 (0 ≤x≤50); Structure and constitution," Journal of Phase Equilibria and Diffusion, vol. 29, no. 6. pp. 500–508, 2008, doi: 10.1007/s11669-008-9389-6.

[10] I. Chumak, K. W. Richter, and H. Ipser, "Isothermal sections in the (Fe, Ni)-rich part of the Fe-Ni-Al phase diagram," J. Phase Equilibria Diffus., vol. 29, no. 4, pp. 300–304, 2008, doi: 10.1007/s11669-008-9319-7.

[11] G. Song, “Microstructure and Creep Deformation Behavior of a Hierarchical-Precipitate-Strengthened Ferritic Alloy with Extreme Creep Resistance,” University of Tennessee, Knoxville, 2016.
[12] M. Wischhusen, C. Glover, P. K. Liaw, J. R. Scully, and S. Agnew, “Pitting Corrosion Susceptibility of Microstructural Features in a Compositionally Complex Ferritic Steel as a Function of Titanium Concentration,” Corrosion, vol. 78, no. 3, pp. 280–292, 2022, doi: 10.5006/3933.
[13] N. Q. Vo, C. H. Liebscher, M. J. S. Rawlings, M. Asta, and D. C. Dunand, “Creep properties and microstructure of a precipitation-strengthened ferritic Fe-Al-Ni-Cr alloy,” Acta Mater., vol. 71, pp. 89–99, 2014, doi: 10.1016/j.actamat.2014.02.020.
[14] G. Song et al., “Ferritic Alloys with Extreme Creep Resistance via Coherent Hierarchical Precipitates,” Sci. Rep., vol. 5, pp. 1–14, 2015, doi: 10.1038/srep16327.
[15] A. Jacob, E. Povoden-Karadeniz, and E. Kozeschnik, “Revised thermodynamic description of the Fe-Cr system based on an improved sublattice model of the σ phase,” Calphad: Computer Coupling of Phase Diagrams and Thermochemistry, vol. 60. pp. 16–28, 2018, doi: 10.1016/j.calphad.2017.10.002.
[16] C. A. Schneider, W. S. Rasband, and K. W. Eliceiri, “NIH Image to ImageJ: 25 years of image analysis,” Nat. Methods, vol. 9, no. 7, pp. 671–675, 2012, doi: 10.1038/nmeth.2089.
[17] “316/316L Data Sheet,” Product Specification. Rolled Alloys, Temperance, MI, USA, 2020.
[18] “AL-6XN Data Sheet,” Product Specification. Rolled Alloys, Temperance, MI, USA, 2020.
[19] S. B. Inman et al., “Effect of Mn Content on the Passivation and Compositionally Complex Face-Centered Cubic Alloys,” Corrosion, vol. 78, no. 1, pp. 32–48, 2022.
[20] R. Yang, J. A. Leake, R. W. Cahn, A. Couret, D. Caillard, and M. G., “An In-situ Observation of Dissociated <111> Glide of Ni2AlTi in a Three-Phase Alloy,” Scr. Metall. Mater., vol. 25, no. c, pp. 2463–2468, 1991.
[21] X. Yan, A. Grytsiv, P. Rogl, V. Pomjakushin, and H. Schmidt, “On the quaternary system Ti-Fe-Ni-Al,” J. Phase Equilibria Diffus., vol. 29, no. 5, pp. 414–428, 2008, doi: 10.1007/s11669-008-9352-6.
[22] W. Cai and W. D. Nix, “Point Defect Equilibria,” in Imperfections in Crystalline Solids, Cambridge University Press, 2016, pp. 140–174.
[23] D. B. Miracle, “Overview No. 104: The Physical and Mechanical Properties of NiAl,” Acta Met. Mater., vol. 41, no. 3, pp. 649–684, 1993.
[24] N. Rusovic and H. Warlimont, “The Elastic Behavior of β2-NiAl alloys,” Phys. Status Solidi, vol. 44, p. 609, 1977.
[25] R. J. Wasilewski, “Thermal vacancies in NiAl,” Acta Met., vol. 15, p. 1757, 1967.
[26] J. J. Bhattacharyya and S. R. Agnew, “Microstructure Design of Multiphase Alloys I - Effects of Strength Contrast and Strain Hardening,” J. Mech. Phys. Solids, no. Manuscript submitted for publication.
[27] J. J. Bhattacharyya, M. A. Wischhusen, and S. R. Agnew, “Microstructure Design of Multiphase Alloys II - Use of a Genetic Algorithm and a Vanishing Cracked Particle Model,” J. Mech. Phys. Solids, no. Manuscript submitted for publication.
[28] C. Varvenne, A. Luque, and W. A. Curtin, “Theory of strengthening in fcc high entropy alloys,” Acta Mater., vol. 118, pp. 164–176, 2016, doi: 10.1016/j.actamat.2016.07.040.

3.8 Appendix A: Thermo-Calc Single Axis Equilibrium Calculations

Presented below are the additional single-axis equilibrium calculations for Fe, Cr, Mn and Mo as referenced in Section 3.4.2.

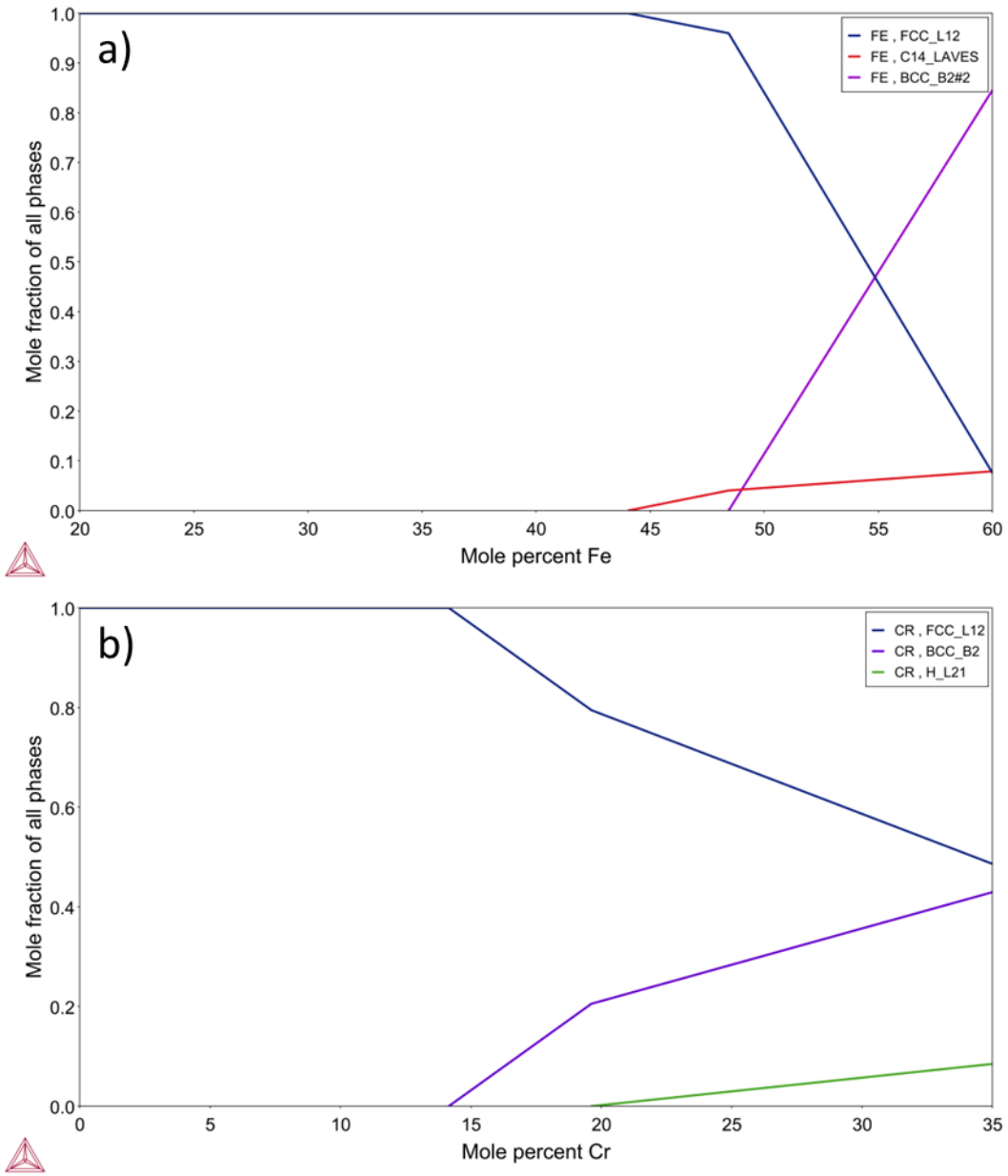

Figure 3.A1: Thermo-Calc equilibrium calculations of phase content in CCA 72 as a function of a) Fe and b) Cr. Fe is predicted to stabilize the formation of Laves and BCC phases in addition to the FCC solid solution. Cr addition above 15 at% is predicted to promote the formation of an $L2_1$ phase, but with the undesirable effect of also stabilizing a BCC phase.

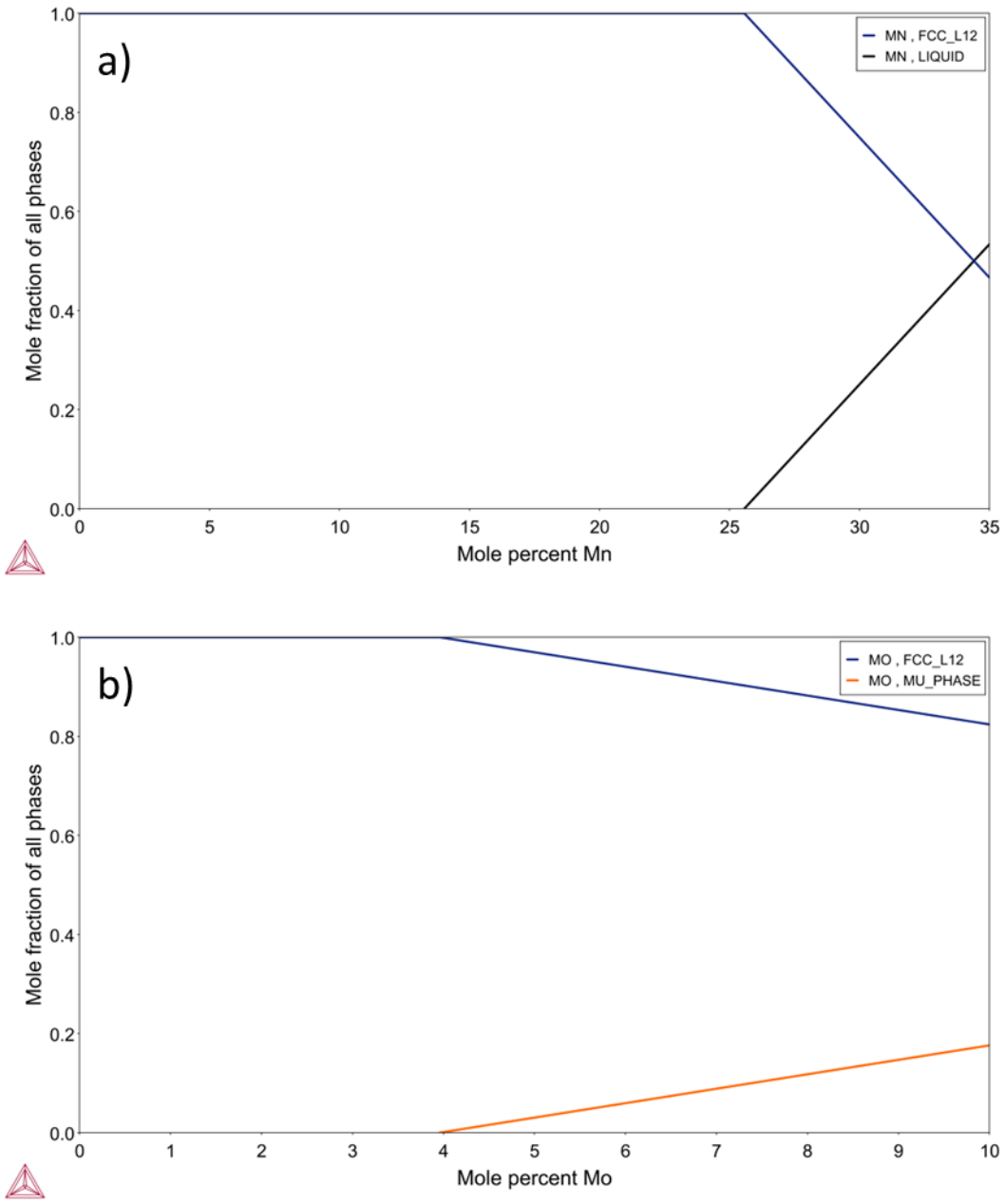

Figure 3.A2: Thermo-Calc equilibrium calculations of phase content in CCA 72 as a function of a) Mn and b) Mo. Like Ti, the addition of Mn is predicted to lower the overall melting point such that partial melting can occur at 1070°C. The addition of Mo is predicted to stabilize the Mu phase.

4. The Thermomechanical Processing Response of FCC+$L2_1$ Composites

This chapter is intended for submission to a peer-reviewed scientific journal, with co-authors, Jishnu J. Bhattacharyya, Diego Ibarra, Jie Qi, Joseph Poon, John R. Scully and Sean R. Agnew.[3]

4.1 Abstract

The thermomechanical processing response of novel, dual-phase FCC+$L2_1$ compositionally complex alloys (CCAs) was investigated. Cold rolling and static annealing were selected due to their simplicity and low cost, and such a processing schedule is compared to the typical processing of various steels. The evolution of the microstructure and texture of the alloys were investigated, and a strong relationship was found between increasing volume fractions of the Heusler phase and austenitic grain refinement. On the other hand, the crystallographic texture of the materials investigated was found to be mild and essentially independent of the Heusler phase fraction. The FCC matrix shared similarities to stainless steels and the texture of the Heusler phase resembled a BCC alloy which has deformed via {hkl}<111> "pencil glide". The recrystallization behavior was investigated, and it was found that the novel alloys recrystallize rapidly, most likely via a continuous static recrystallization mechanism.

4.2 Introduction

As part of an effort to develop low-cost, lightweight and corrosion resistant alloys for naval applications, a series of dual-phase, compositionally complex alloys have been created which utilizes a disordered FCC matrix strengthened by the intermetallic $L2_1$ Heusler phase (Cu2MnAl archetype). This work is focused on the thermomechanical processing response of those alloys.

Thermomechanical processing is an important part of the production of engineering materials, and can have a pronounced effect on the properties of the finished product. Austenitic stainless steels, being intrinsically ductile, are typically processed through a mixture of hot and cold rolling. [1]–[5] The subsequent heat treatments vary, depending on the use of precipitation strengthening, but typically take place between 700 and 1050°C due to the high temperature nature of austenite. Water quenching is a common practice, in order to avoid unwanted phase transformations [1]–[5]. Dual phase and duplex steels are processed in a similar manner over a larger temperature range, with a greater emphasis on control of cooling rates and aging treatments to facilitate the desired phase transformations in what are typically

[3] Author contributions: **Mark A. Wischhusen**: Investigation, Formal Analysis, Writing (Original Draft), **Jishnu J. Bhattacharyya:** Formal Analysis, **Jie Qi:** Resources, **Diego Ibarra:** Resources, **Joseph Poon:** Conceptualization, Funding Acquisition and Writing (Review & Editing), **John R. Scully:** Conceptualization, Funding Acquisition and Writing (Review & Editing), **Sean R. Agnew:** Conceptualization, Funding Acquisition and Writing (Review & Editing)

ferrite(α)-austenite(γ) or ferrite(α)-martensite(α') microstructures [6]–[10]. Pre-rolling anneals occur around 1200 to 1350°C, and austenitization and intercritical (α+γ) annealing between 700 and 900°C.

The umbrella of 'intermetallic compounds' is very broad, and therefore encompasses a very wide range of processing routes. For the purposes of this study, intermetallics containing Fe, Al and Ni are of the most interest. Due to their lack of room temperature ductility, bulk processing of intermetallic compounds like B2-structured FeAl and NiAl is typically limited to processing at high temperatures; hot rolling and extrusion are two common techniques. While the initial homogenization and final annealing temperatures used will vary with each compound, hot rolling and extrusion are conducted around 900 to 1200°C [11]–[14]. Multi-principal element alloys (MPEAs,) high entropy alloys (HEAs), and otherwise compositionally complex alloys (CCAs) have a similarly wide range of possible processing parameters. Single-phase CCAs are typically amenable to cold rolling, potentially even at cryogenic temperatures [15]–[17], and some multi-phase alloys such as those with lamellar or eutectic microstructures are also ductile enough to process at room temperature [18][19]. Other multiphase CCAs with larger second phase grains benefit from initial hot rolling at temperatures similar to the aforementioned steels, followed by cold finish rolling to the desired sheet thickness [20][21]. Very little attention has been paid to $L2_1$-structured intermetallics for reinforcement purposes, primarily due to their "catastrophically brittle" nature at room temperature [22], and only in the three years or so have authors begun publishing studies of FCC+$L2_1$ composites [23]–[25].

The materials systems and thermomechanical processing schedules outlined above encompass the processing considerations for the alloys studied. Cold rolling and static annealing have been selected both due to the simple, low-cost nature of the techniques and to the similarities of the majority matrix phase of the alloys to stainless steels. However, unlike the materials discussed previously, cold rolling takes place at a greater initial thickness and/or to a greater extent than is typically seen in alloys strengthened by an intermetallic phase. The Heusler phase is well known for its lack of room temperature ductility [22][26], however the presence of hydrostatic stress imposed by the deforming FCC matrix is expected to suppress the brittle nature of the Heusler phase, elevating its fracture strain, allowing it to yield [27]–[29]. In addition to how the novel FCC+$L2_1$ alloys might be processed, the microstructural and textural evolution of the alloys are of interest, as well as the predominant mechanisms of recrystallization. Mechanisms operative in multiphase and/or highly alloyed metals will also be discussed, such as Zener pinning, solute drag, and particle stimulated nucleation of recrystallization (PSN).

4.3 Methods

4.3.1 Sample Synthesis and Preparation

Alloy ingots were produced via vacuum arc melting, re-melting several times to ensure homogeneous composition, and either bar cast in a chilled Cu hearth (approximately 75 mm x 13 mm x 7mm) or suction cast into coin-shaped ingots (10 mm diameter by 5 mm thick) in an Ar environment from >99% pure (metal basis) elemental metal or ferrometals. The as-cast samples are then encapsulated in Ar-backfilled quartz tubes and homogenized for 5 hours at 1070 °C in a box furnace, followed by water quenching. Bar ingots are further prepared for processing by removing 1.5 mm from the top of each ingot on a milling machine. This top layer is expected to contain a large amount of porosity and other casting defects, and its removal also ensured parallel ingot surfaces during rolling. A series of alloys with varied Al concentration was synthesized as discussed in [30], and three of those alloys were the primary focus of this work: CCAs 81, 72 and 91. An alloy intermediate to CCAs 72 and 91 was also studied – CCA 94. These compositions are listed in Table 4.1.

Table 4.1: The nominal composition of CCAs 81, 72, 94 and 91, listed in order of increasing Al concentration. The $L2_1$ volume fraction observed in the homogenized state is included.

(at%)	Al	Cr	Fe	Mn	Mo	Ni	Ti	$L2_1$ (vol.%) Hm.
CCA 81	3.7	11.0	42.6	5.2	3.1	28.8	5.6	0
CCA 72	6.0	10.0	40.0	5.0	3.0	30.0	6.0	5
CCA 94	8.2	9.8	39.1	4.8	2.9	29.3	5.9	10
CCA 91	9.4	9.6	38.5	4.8	2.9	29.0	5.8	40

Cold rolling was performed on a Fenn Two-High rolling mill (East Berlin, CT, USA). The roller wheels were initially cleaned and lubricated with three-in-one oil, which was re-applied (infrequently) as needed between samples. Samples were wrapped in Teflon tape for the initial stages of rolling, and the Teflon was not re-applied during later passes. Both types of castings were cold rolled to the maximum extent possible, defined as either reducing thickness to the minimum roll gap of 0.5 mm or the point of apparent cracking in the material. Each rolling pass reduces the instantaneous thickness of the sample by 5-10%, achieving total reductions of 60-89%, with a constant rolling direction. Rolled samples were given recrystallization anneals of varying times at 1070°C in air, whereas anneals lasting longer than 1 hour were performed only after samples were encapsulated in Ar. Samples annealed for less than 1 hour did not show significant oxidation in air at 1070°C, and the oxide that did form was easily ground away with SiC paper.

Hardness testing was performed using a Tinius-Olsen FH 14-1 hardness tester (Horsham, PA, USA) operated in Automatic mode, using a load of 500 grams and a dwell time of 15s for a total of 10 indents per sample. A magnification of 10X or 50X was used as appropriate, determined by the size of the indent on the material. Samples were prepared to a 1200-grit (P4000) finish on SiC paper for hardness testing.

Sample preparation for the various characterization techniques employed include standard metallographic grinding and polishing on SiC paper. X-ray diffraction samples were prepared unmounted and ground to a 1200-grit (P4000) finish. Samples for Scanning Electron Microscopy (SEM) were first mounted, then ground and further prepared on cloth polishing pads to a 0.05-micron colloidal silica finish, followed by 15 minutes of flat ion milling on a Hitachi-HighTech IM4000 ion mill (Schaumburg, IL, USA). Ion milling was performed using an Ar plasma at an angle of 10°, distance of 5 mm, accelerating voltage of 6V and discharge voltage of 1.5V.

4.3.2 X-ray Diffraction and Electron Microscopy

Powder x-ray diffraction experiments were performed on a Panalytical Empyrean x-ray diffractometer (Malvern, UK) on bulk metallic samples in a Bragg-Brentano para-focusing geometry. Incident beam optics include the Bragg-Brentano HD Cu prefix module, 0.02 mm soller slits, a 4 mm mask, a 0.25-degree divergence slit and an incident 1-degree anti-scatter slit. These optics produce an x-ray footprint of about 7.4 mm by 9.7 mm on the sample, and data were collected on a spinning sample rotating at 8 seconds per revolution. X-ray diffraction for texture collection was performed on a Panalytical X'Pert diffractometer. Texture measurements were performed in point-focus mode using a detector-side parallel plate collimator and a proportional Xe detector. Samples were mounted a chi-phi-Z stage and scanned from 0 to 70 degrees chi tilt in 5° increments with continuous phi rotation. Background measurements were collected at appropriate 2θ positions which did not coincide with a diffraction peak and were used to correct measured data. X-ray measurements were primarily used to characterize only the texture of the FCC matrix, due to the lack of strong, sufficiently isolated 2nd-phase reflections in the x-ray data.

Scanning electron microscopy was performed using a Thermo-Fischer Helios UC G4 Dual-Beam FIB-SEM (Waltham, MA, USA), equipped with an Oxford Instruments Symmetry Electron-Backscatter Diffraction (EBSD) detector and accompanying Oxford AZtec® software. EBSD was used to characterize the microstructures of the worked and annealed samples, as well as to perform phase content and grain size quantification. Kikuchi patterns were obtained at 1x1 binning for maximum resolution and an exposure time of 5 milliseconds. As a general rule of thumb, EBSD scans are performed with a step size such that each microstructural feature of interest contains at least 5 scanning points. Calculated lattice spacings were combined with site occupancy values from Thermo-Calc to generate crystal files for EBSD phase indexing using Oxford Instruments software Channel5 HKL Twist. The lattice constants of the component phases, 3.62 Å for the FCC

and 5.88 Å for the $L2_1$, were calculated from powder x-ray diffraction peak positions via Bragg's Law and the relationship between lattice parameter (a) and interplanar spacing (d) in FCC crystals. [30] Grain size quantification was performed with Oxford Instruments software Channel5 HKL Tango, using a critical misorientation angle of 15° to define grain boundaries. Grain diameters are calculated from constructed circles of equivalent area to the identified grains.

Both x-ray and EBSD-based texture data were analyzed with MathWorks MATLAB 2022a software and the MATLAB toolbox MTEX (version 5.7.0) [31]. Averaged textures are calculated from a minimum of three EBSD data sets, collected at a sufficient magnification to capture 100-200 grains in-frame. All texture analysis used cubic ($m\bar{3}m$) crystal symmetry and triclinic sample symmetry. EBSD data is presented untreated and as-indexed by AZtec, though the MTEX analysis script does interpolate grain boundaries in zero-solution areas. Common FCC texture components were calculated using the definitions listed in Table 4.2.

Table 4.2: The five common FCC texture components tracked in this study, in Bunge notation. For the purposes of quantification, a radius of 15° about each orientation is employed.

Component	Indices	φ_1	Φ	φ_2
Cube	$\{001\} < 100 >$	45	0	45
Copper	$\{112\} < 11\bar{1} >$	90	35	45
S	$\{123\} < 63\bar{4} >$	59	34	65
Brass	$\{110\} < \bar{1}12 >$	35	45	0
Goss	$\{110\} < 001 >$	0	45	0

The Williamson-Hall method [32] was used to qualitatively relate x-ray peak broadening of the FCC matrix phase to the recrystallization state of deformed and annealed material. The broadening of the FCC (111), (200), (220) and (311) peaks, represented by the integral breadth of each peak. Diffraction techniques like these can also be used to estimate the dislocation content of a material, though such quantitative analysis is beyond the scope of the present work. As dislocations exit the material or annihilate during annealing, broadening will decrease and the slope of a linear fit of β^* vs d^* (Equation 4.1) will decrease as a function of the extent of recrystallization. In these equations, β is the peak broadening which comes from multiple sources, e.g. coherently scattering crystallite domains, variations in lattice parameter due to deformation, and instrumental broadening. Experimental measurements were corrected for instrumental broadening using a lanthanum hexaboride (LaB6) powder standard. d is the interplanar spacing, β^* and d^* are the reciprocal space equivalents of β and d, K is a shape constant typically equal to 0.9, t is the crystallite size, θ is the Bragg angle and λ is the relevant x-ray wavelength, equal to 1.54056 Å for Cu-Kα x-rays. The method is used under the assumption of uniform deformation stress, σ, (Equation 4.2) rather than the typical assumption of uniform deformation, to account for

elastic anisotropy in the FCC matrix phase [33]. The necessary diffraction elastic moduli (Ehkl) were obtained from neutron diffraction experiments, discussed in detail in [34].

$$\beta^* = \frac{\beta cos(\theta)}{\lambda} \qquad d^* = \frac{2\sin(\theta)}{\lambda} \tag{4.1}$$

$$\beta^* = \frac{K}{t} + 2\sigma \frac{d^*}{E_{hkl}} \tag{4.2}$$

The Avrami Equation [35]–[37] can used to describe the kinetics of recrystallization. Equation 4.3 generally describes any process which is defined by nucleation and growth. In the context of recrystallization, the fraction of recrystallized material, Xv, is a function of a rate constant B, time t and the Avrami exponent, n, which varies from 3 to 4 depending on how the rate of nucleation is treated. In the absence of significant recovery before recrystallization [38], processes which follow the Avrami equation will produce characteristic S-shaped curves characterized by an upper and lower plateau separated by a linear transition when plotted on a logarithmic time scale. For the purposes of a qualitative analysis, the times at which each of these three stages occur is of interest.

$$X_v = 1 - \exp(-Bt^n) \tag{4.3}$$

4.4 Results

In general, the FCC-$L2_1$ composites examined in this study were receptive to cold working. When prepared with parallel faces, 6mm-thick ingots with 6 and 16 volume percent Heusler phase were able to be cold deformed by as much as 89% reduction in thickness without significant cracking. Samples with 25 volume percent Heusler phase were less receptive, but could still be rolled up to 70% reduction in thickness if initially reduced to 4mm in thickness before rolling. This is due to the plane strain conditions induced by cold rolling – ideally, there is no transverse expansion of the sample during thickness reduction and expansion parallel to the rolling direction. Despite some departure from ideal behavior, the friction force between the roller wheels and the sample provides additional pressure which reduces stress triaxiality and ultimately delays the brittle fracture of the Heusler phase.

Samples of CCAs 81, 72 and 91 were examined after cold rolling and static annealing at 1070°C for times ranging from 5 to 90 minutes, summarized in Table 4.3. For the purposes of comparison, all samples used for EBSD and other analyses were deformed to between 70-75% reduction in thickness. Two samples each of CCAs 81 and 91 were examined, and in both cases one sample showed retained cold work after a 30 minute anneal at 1070°C. Processing was repeated on a second sample of each alloy, which was observed to recrystallize rapidly in line with the annealing response of CCA 72. The obtained EBSD maps suggest a strong relationship

between Heusler phase content and grain refinement, as well as resistance to coarsening. Worked and annealed microstructures tended to be fairly equiaxed with abundant 60° <111> annealing twins in the FCC matrix. At large rolling reductions, cracking of the Heusler phase was observed, the extent of which varied with the amount of Heusler phase present. In CCA 72, cracking was only observed in the Heusler phase after a cold reduction of 89%, but in CCA 91 cracking was observed after 43% cold reduction. Images of Heusler phase particles cracked by rolling are shown in Figures 4.1 and 4.2 for CCAs 72 and 91, respectively. In this instance, CCA 91 also contained a third, high-Z phase which is typical of higher Al concentrations. This phase is closely associated with the majority of observed cracks. When ingot thickness was reduced to 4mm prior to cold rolling, CCA 91 was able to withstand 70% cold reduction without any observed cracking in the Heusler phase, shown in Figure 4.3. To reiterate, the thinner ingot is able to benefit from conditions closer to plane strain, which better constrain the Heusler phase and delay its fracture.

Table 4.3: The compositions, second phase volume fractions and levels of cold reduction for the EBSD and recrystallization studies. "s1" and "s2" denote Sample 1 and Sample 2, respectively.

Alloy	Composition (at%)	$L2_1$ vol%	Cold Reduction
CCA 81	$Al_{3.7}Cr_{11}Fe_{42.6}Mn_{5.2}Mo_{3.1}Ni_{28.8}Ti_{5.6}$	0	70% (s1)
			71% (s2)
CCA 72	$Al_6Cr_{10}Fe_{40}Mn_5Mo_3Ni_{30}Ti_6$	6	70%
CCA 94	$Al_{8.2}Cr_{9.8}Fe_{39.1}Mn_{4.8}Mo_{2.9}Ni_{29.3}Ti_{5.9}$	16	85%
CCA 91	$Al_{9.4}Cr_{9.6}Fe_{38.5}Mn_{4.8}Mo_{2.9}Ni_{29}Ti_{5.8}$	25	75% (s1)
			73% (s2)

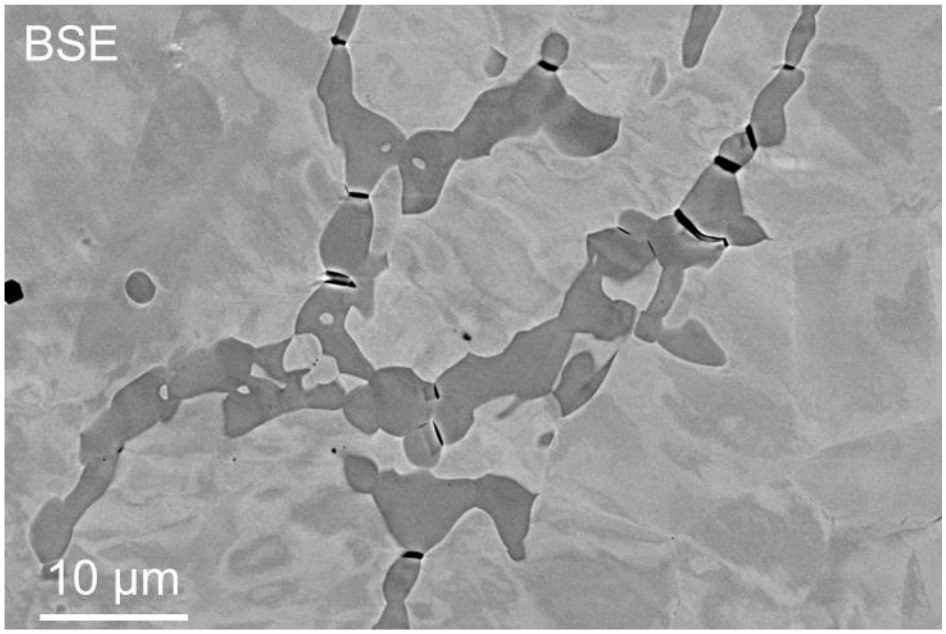

Figure 4.1: CCA 72 after 89% cold reduction and annealing at 1070°C / 90 min. Intergranular cracking was observed in large clusters of Heusler grains.

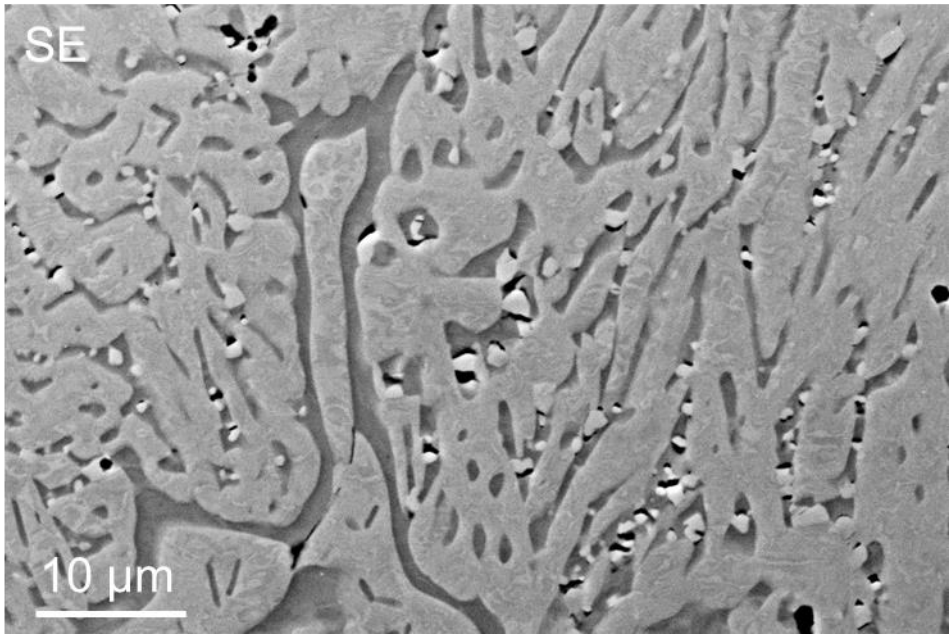

Figure 4.2: CCA 91 after 43% cold reduction from an initial thickness of 6mm. The cracking observed is largely associated with the presence of a third phase, which is stable at higher Al concentrations.

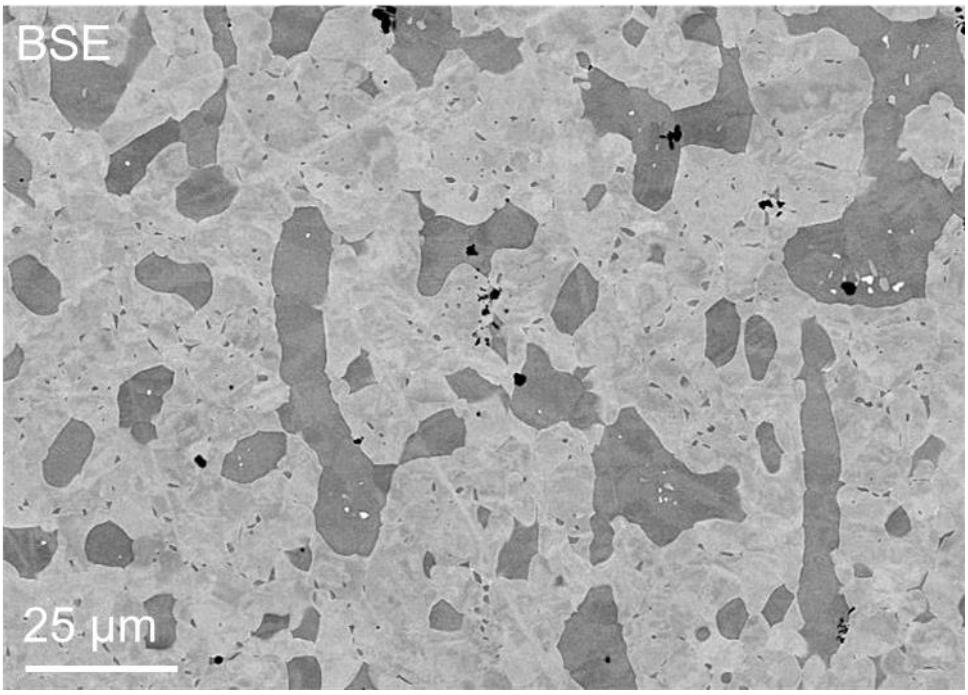

Figure 4.3: CCA 91, cold deformed 70% and annealed 1070°C / 60 min from an initial thickness of 4mm. In this case, the Heusler phase did not show cracking.

Microstructural evolution in these alloys was investigated as a function of processing, beginning with the as-cast microstructures of the three alloys depicted in Figure 4.4. The cast microstructures consist of large matrix grains with dendritic features and interdendritic regions of solute enrichment and second phase particles. A closer view of the microstructure of both phases in cast and homogenized CCA 72 is shown in Figure 4.5. The Heusler phase particles which solidified between FCC dendrite arms formed irregular shapes [30]. It was also noted that, since clusters of the Heusler grains tended to have identical orientations, the possibility exists that Heusler grains with very similar orientations are all part of a contiguous, dendritic grain on a three-dimensional scale. The Heusler phase grains appear to exert a pinning effect on matrix grain boundaries in the cast material (see Figure 4.5). Such behavior suggests that the FCC-$L2_1$ interface is fairly low-energy.

Phase quantification was performed via EBSD on CCA 72 in the as-cast state, and was found to contain 5.7 vol% Heusler phase. This volume fraction was not observed to change significantly after cold working and annealing. While CCA 91 was not examined in the as-cast state in sufficient detail for phase quantification, it is assumed that the amount of Heusler phase in the higher-Al composition is similarly stable throughout processing.

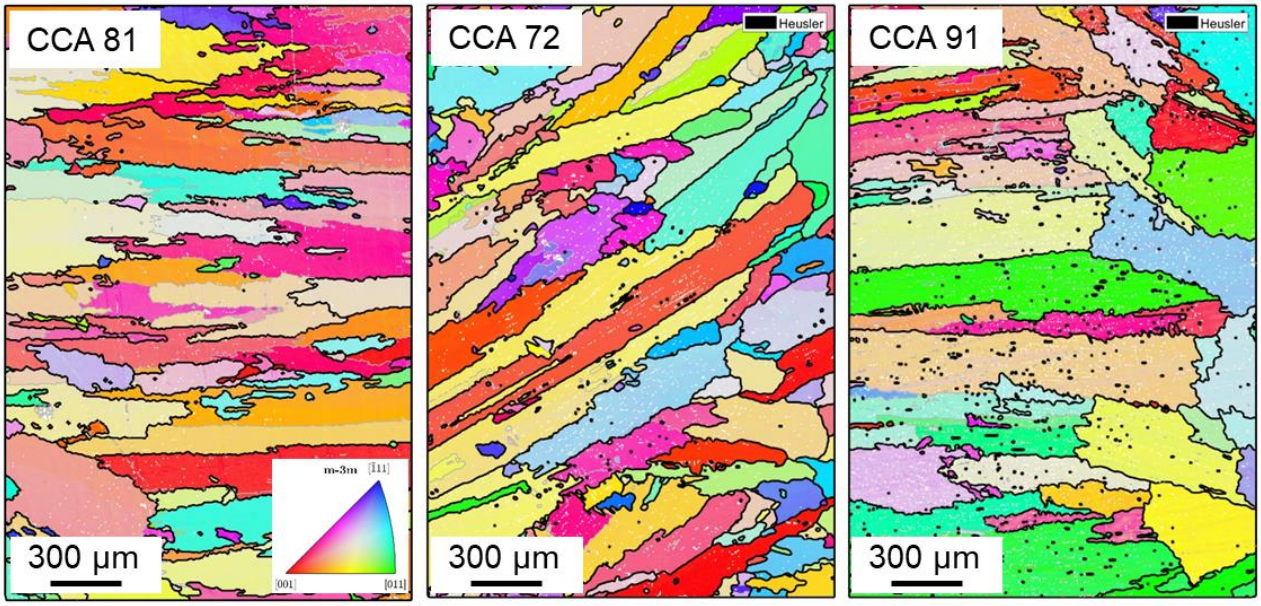

Figure 4.4: EBSD IPF-Z orientation maps of the as-cast microstructures of CCAs 81, 72 and 91. All three possess similar as-cast microstructures composed of large, elongated grains.

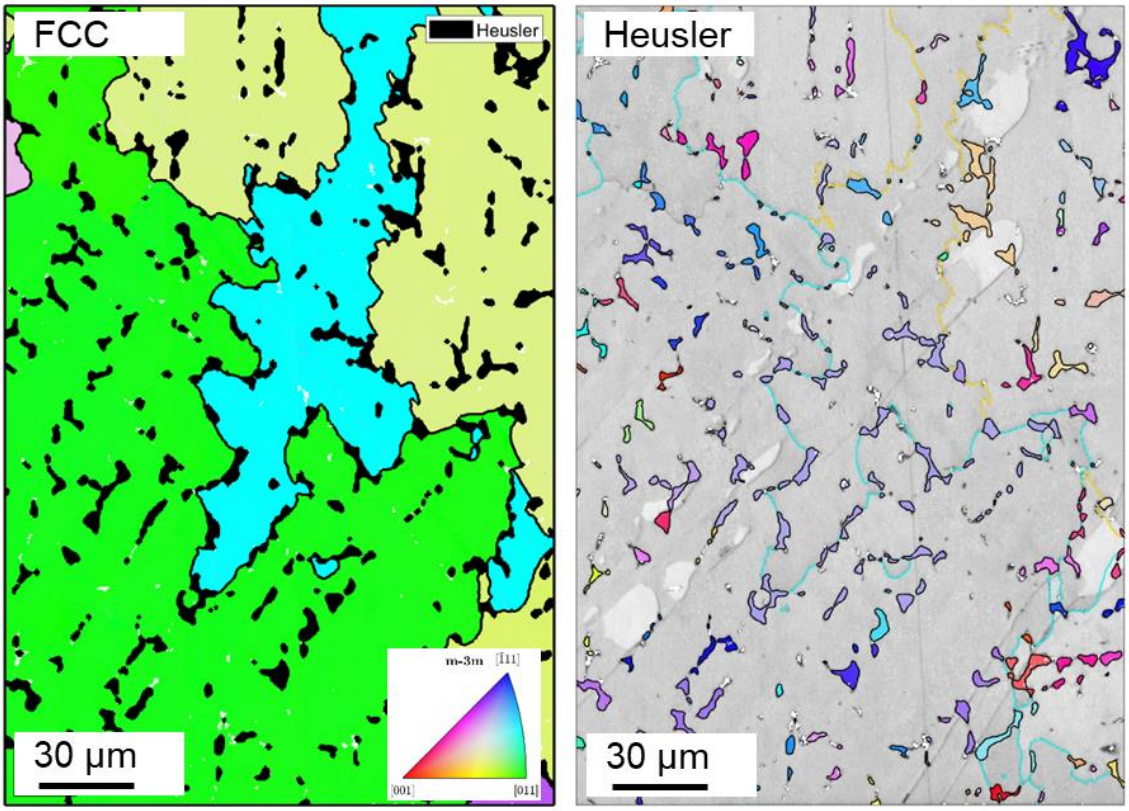

Figure 4.5: EBSD IPF-Z orientation maps of the FCC and Heusler phases in CCA 72 in the as-cast state. Note the large cluster of Heusler grains near the center of the map which all have a lavender coloring – it is hypothesized that all of these grains are part of the same grain which solidified between FCC dendrite arms.

Figure 4.6 shows the evolution of grain size as a function of annealing time after cold deformation. For the most part, no significant coarsening is observed outside of the standard deviation of the grain sizes observed up to 90 minutes at 1070°C. One outlier exists in the CCA 91 data where a much coarser microstructure is observed from the material which was rolled to 70 percent reduction without significant cracking. This sample showed evidence of retained cold work after 30 minutes of annealing at 1070°C. In the deformed microstructure, the grains are large but also highly substructured which leads the analysis software to report a larger grain size. Upon further annealing, those grains would recrystallize into smaller grains separated by high-angle boundaries, thus decreasing the observed grain size, likely to the level of the other CCA 91 samples. In the case of samples which were fully recrystallized, the Heusler phase grain size stayed constant across the range of annealing times investigated for CCA 72 and 91 at 3.5 ± 0.95 µm and 1.2 ± 0.70 µm, respectively. In the sample of CCA 91 which showed retained cold work, Heusler grains tended to be much larger, on the order of 5.5 ± 3.0 µm.

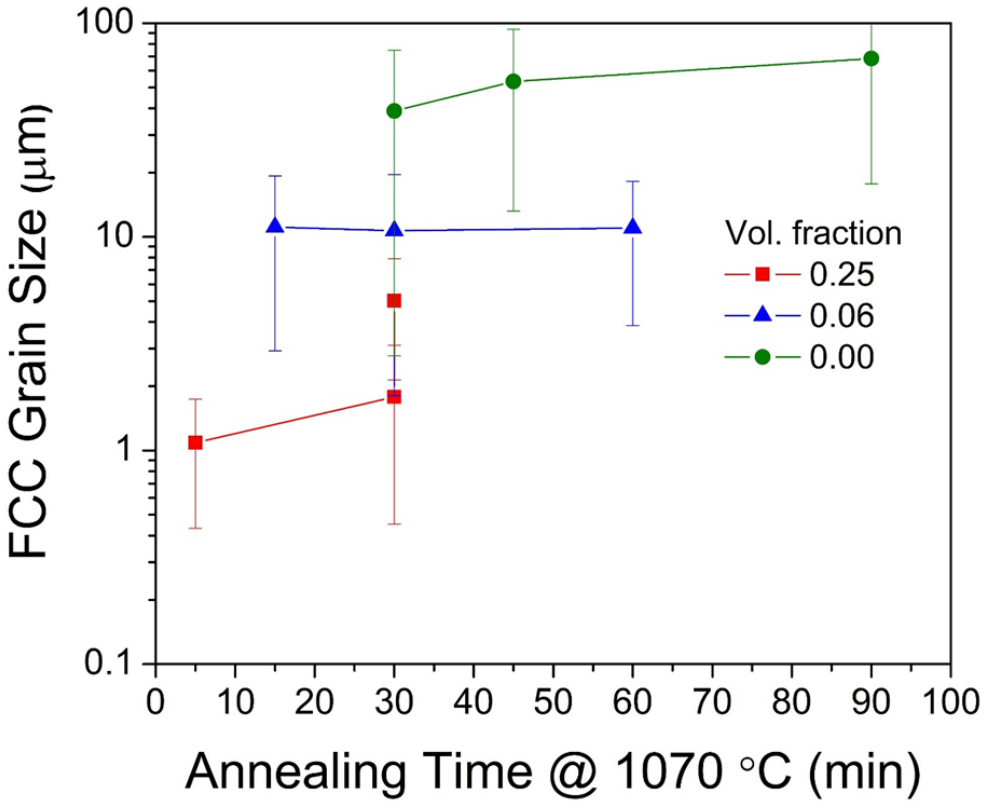

Figure 4.6: The evolution of the FCC grain sizes as a function of annealing time at 1070°C, after deformation. The larger-grained of the two 0.25 volume fraction samples was observed to be only partially recrystallized.

Figures 4.7, 4.8 and 4.10 show an assortment of inverse pole figure (IPF) grain maps, with crystal orientation shown relative to the direction normal to the sample surface for the FCC phase (i.e. IPF-Z). Figures 4.9 and 4.11 show the corresponding Heusler grain orientations for CCAs 72 and 91. The effect that the Heusler phase has on reducing the recrystallized grain size is readily apparent, with the sizes of FCC and Heusler grains approaching parity in the 25 vol% $L2_1$ material. It is also evident, especially in the higher volume fraction material, that the Heusler phase particles have become polycrystalline as a result of processing. In light of the observation that monocrystalline Heuser phase particles form during casting, the formation of polycrystalline recrystallized particles would not be possible without deformation of the Heusler phase prior to annealing. Furthermore, in the sample of CCA 91 which showed evidence of retained cold work (Figure 4.11), the Heusler phase appears to be substructured, further supporting the assertion that the Heusler phase is deforming as part of the composite material despite its brittle nature at room temperature in isolation.

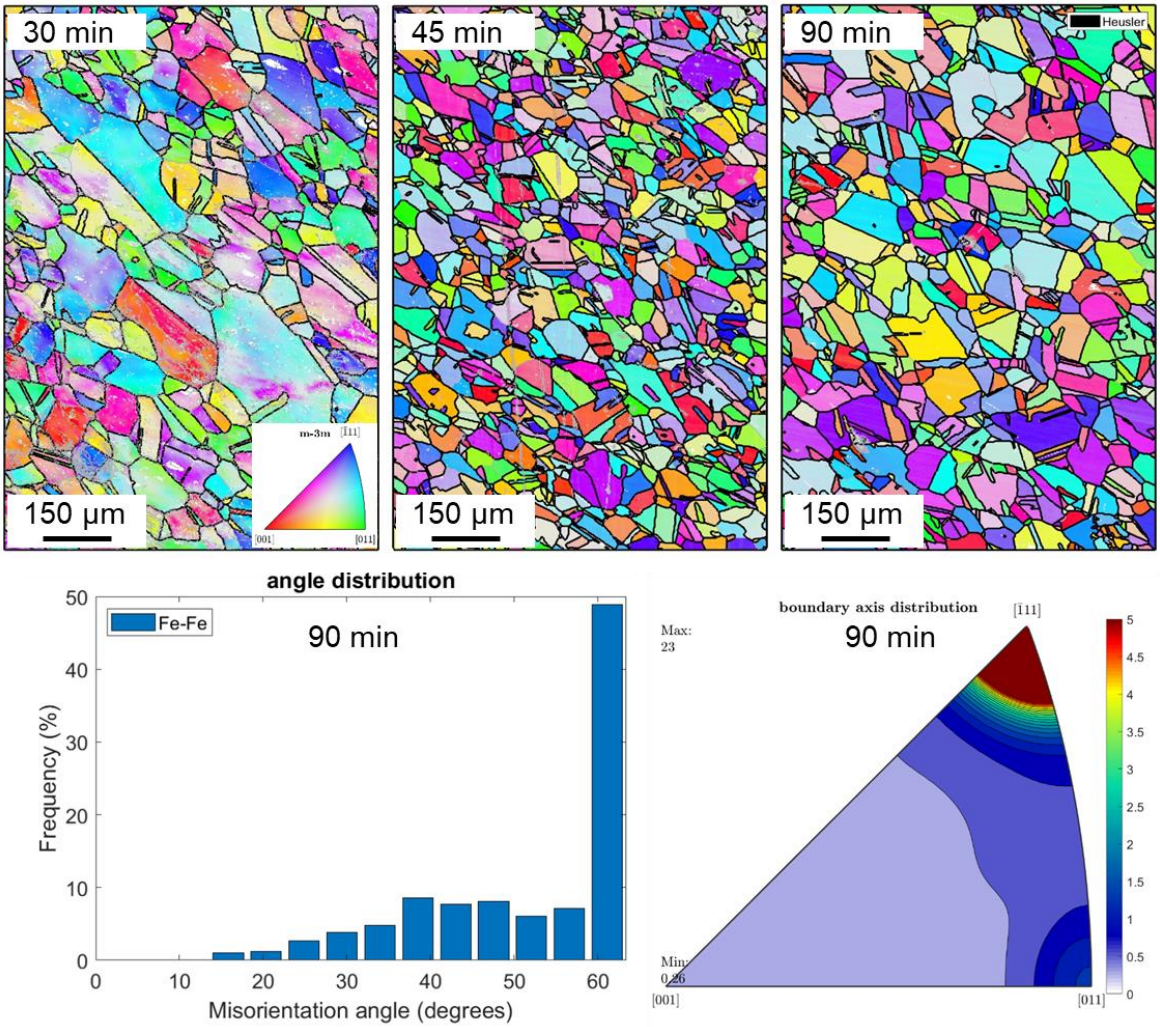

Figure 4.7: EBSD IPF-Z orientation maps of rolled-and-annealed CCA 81 after various annealing times at 1070°C, with plots of the intergranular FCC boundary misorientation and axis.

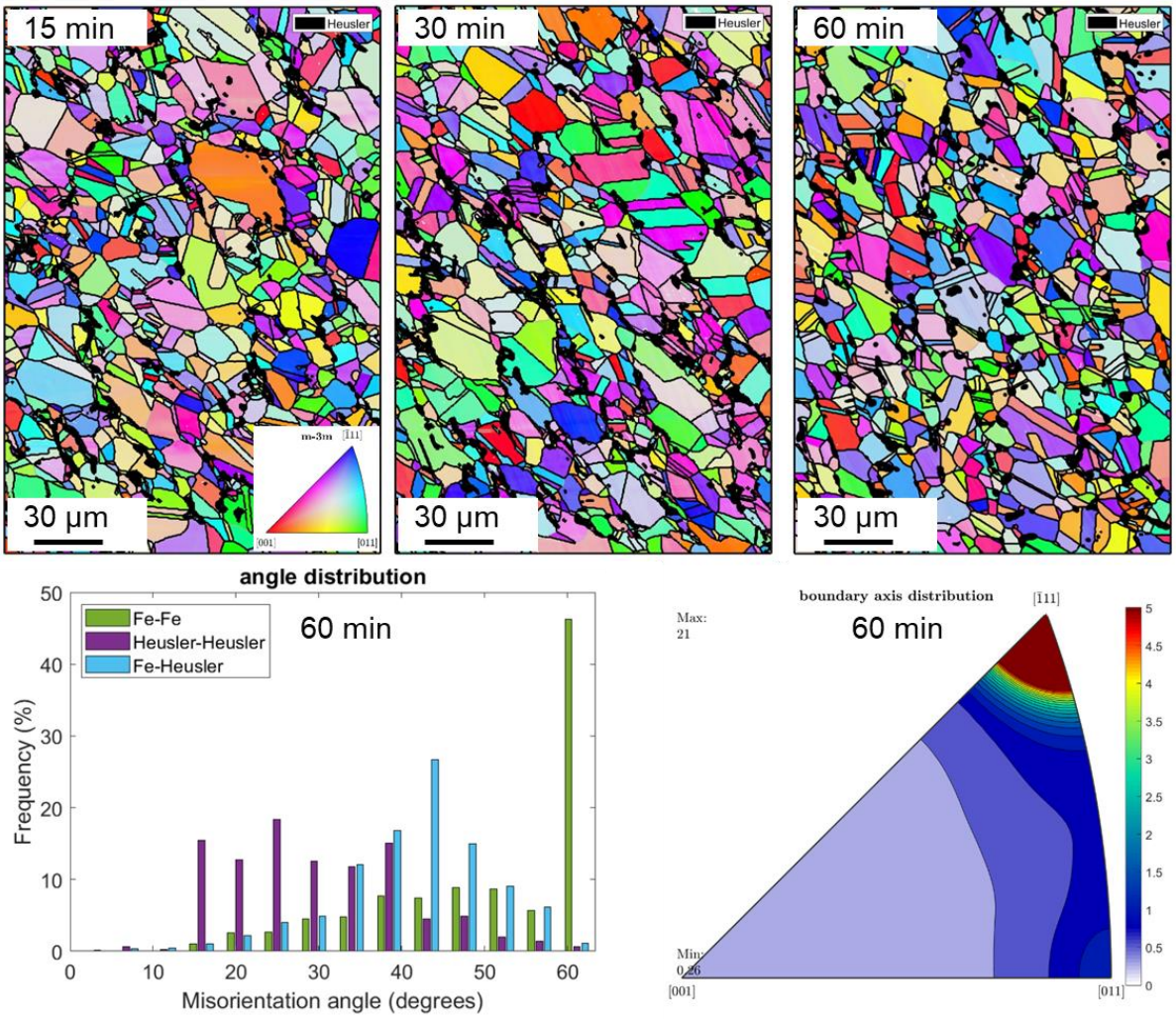

Figure 4.8: EBSD IPF-Z orientation maps of rolled-and-annealed CCA 72 after various annealing times at 1070°C, with plots of the intergranular FCC, Heusler, and interphase boundary misorientations, as well as the FCC boundary misorientation axis.

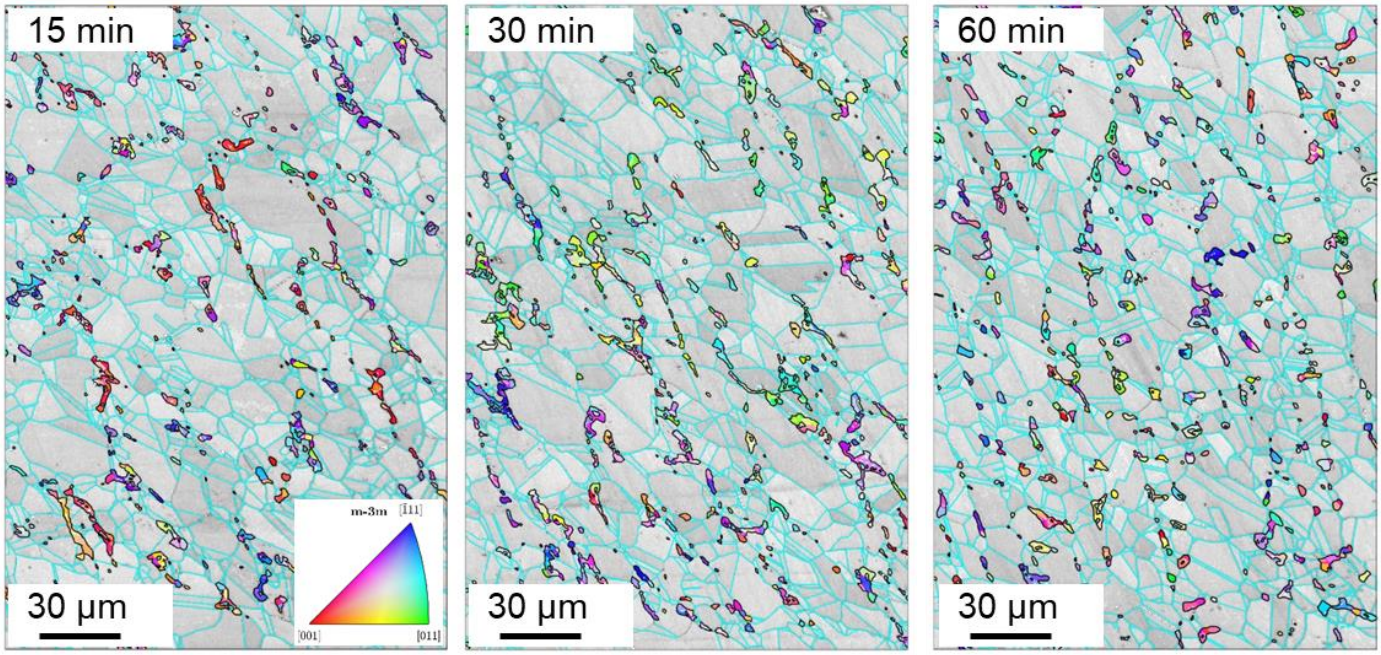

Figure 4.9: The corresponding EBSD IPF-Z orientation maps of the Heusler phase grains shown in Figure 4.8.

The microhardness of the alloys of interest was measured after various annealing times at 1070°C in order to investigate the recrystallization kinetics of the composite material (Figure 4.12). In addition to the aforementioned CCA 91 sample, one sample of CCA 81 also shows retained cold work, however upon further annealing beyond 30 minutes the hardness of both samples reached the level of the fully recrystallized samples. Due to their respective hardness falling below the as-rolled measurements, it is assumed that there has been some level of reordering and/or recrystallization in these samples, though it is otherwise unknown why they show retained cold work compared to the samples which recrystallized rapidly. In the rapidly recrystallized samples, nearly complete recrystallization is observed in as little as 5 minutes at 1070°C. Due to the limitations of the box furnace used, anneals shorter than 5 minutes could not be performed reliably, and as such no state of intermediate recrystallization could be observed. Using these same samples, a Williamson-Hall analysis was performed to qualitatively examine the evolution of the dislocation density of the three alloys. Those results are shown in Figure 4.13, in which a drastic decrease in slope can be observed between the as-rolled and short duration anneals (either 5 or 30 minutes,) but very little difference is observed between the shorter-duration anneals and the 24 hour anneals. That is to say, as the slope in a Williamson-Hall plot relates to the dislocation density of a material, the large decrease in slope during early anneals compared to the mild decrease in later anneals can be interpreted to mean that the majority of dislocation movement and annihilation happen during the initial 5- or 30-minute heat treatments. The intercept of the Williamson-Hall curves, which relate to crystallite size broadening, also provide further insight. Despite less than perfect correlation factors, in general the intercept experiences a drastic decrease between the as-rolled

and short-duration annealed states, with very little change after the 24 hour anneals, which further suggests that there is very little dislocation activity after the initial anneals.

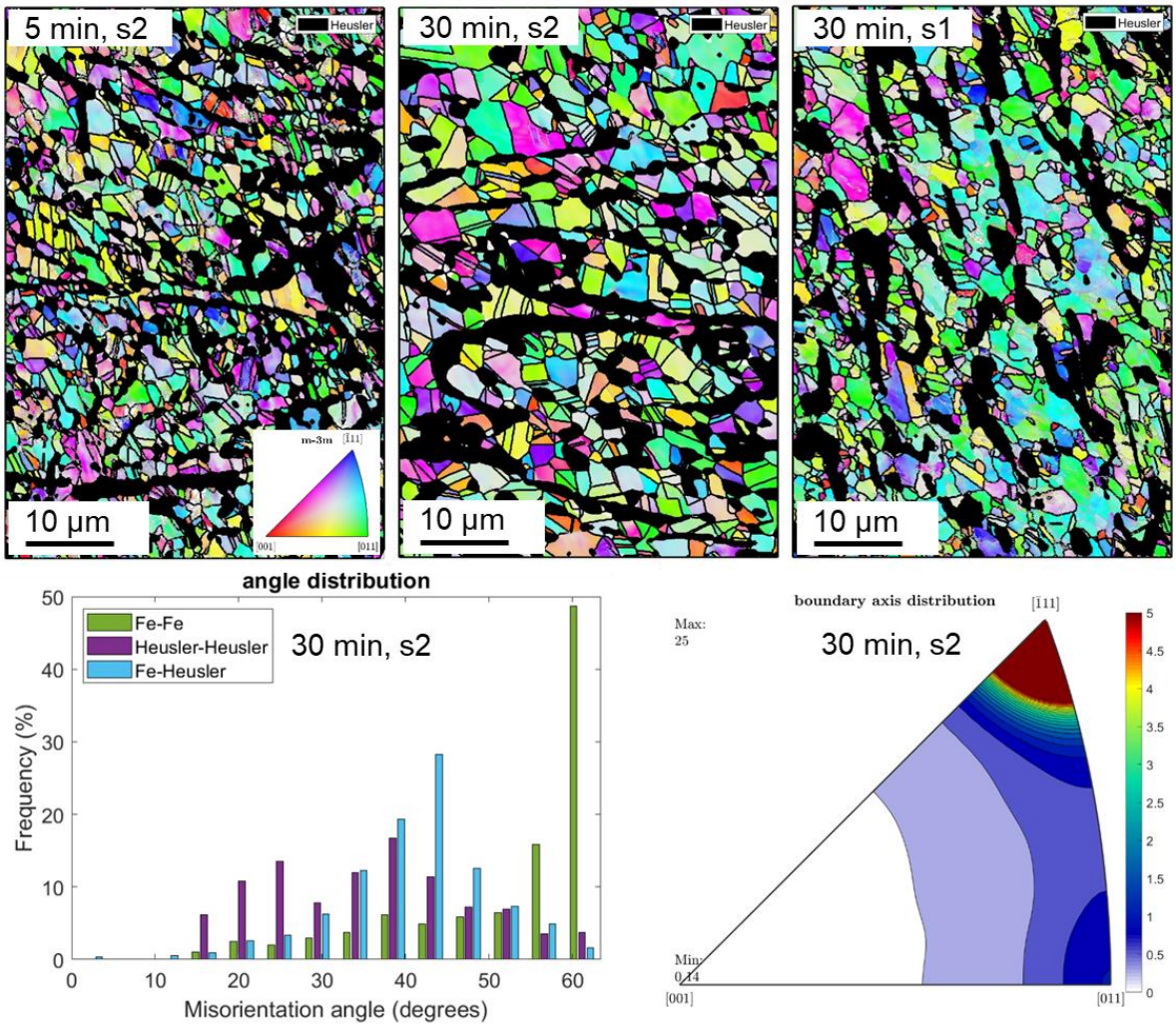

Figure 4.10: EBSD IPF-Z orientation maps of rolled-and-annealed CCA 91 after various annealing times at 1070°C, with plots of the intergranular FCC, Heusler, and interphase boundary misorientations, as well as the FCC boundary misorientation axis. “s1” and “s2” denote Sample 1 and Sample 2, respectively. Sample 1 was observed to be only partially recrystallized.

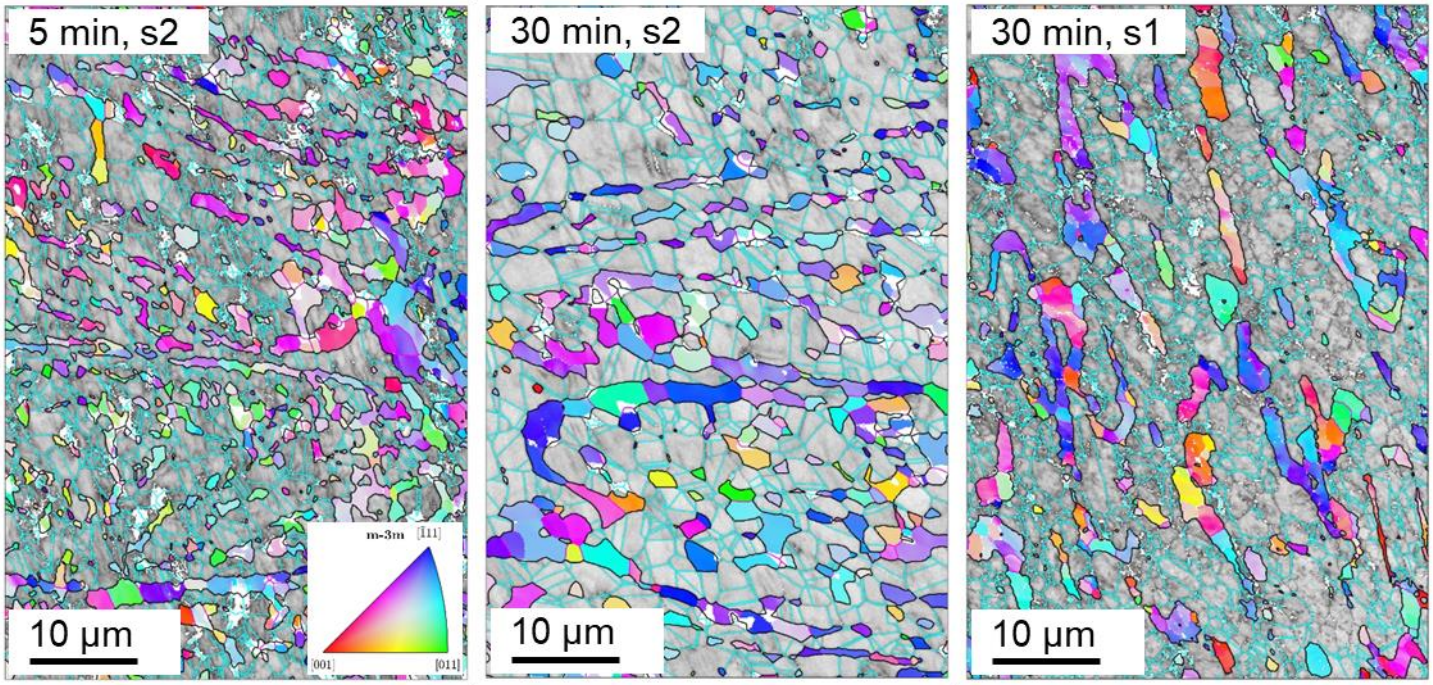

Figure 4.11: Corresponding EBSD IPF-Z orientation maps of the Heusler phase grains shown in Figure 4.10. Heusler grains which still possess some deformed substructure were observed in the partially recrystallized Sample 1.

The texture evolution of the composite alloys was examined via both x-ray diffraction and EBSD. While more grains are interrogated via x-ray diffraction, EBSD is able to characterize the texture of the Heusler phase even when the volume fraction of Heusler phase is not sufficient for x-ray measurement. The measured textures are weak across all samples, rarely rising above 4 multiples of a random distribution (MRD) in a pole figure. The x-ray pole figures and corresponding ODF sections of the FCC phase of CCA 81 in the as-rolled state are presented in Figure 4.14, and for the rolled-and-annealed state in Figure 4.15. The basic form of the as-rolled texture was retained after annealing, though it was weakened slightly. The pole figures and ODF sections of the matrix phase of CCA 72 are shown in Figure 4.16; the presence of 6 vol% Heusler phase did not have significant effect on the deformation texture of the matrix. For samples containing 25 vol% Heusler phase, very little difference from CCAs 81 and 72 was observed.

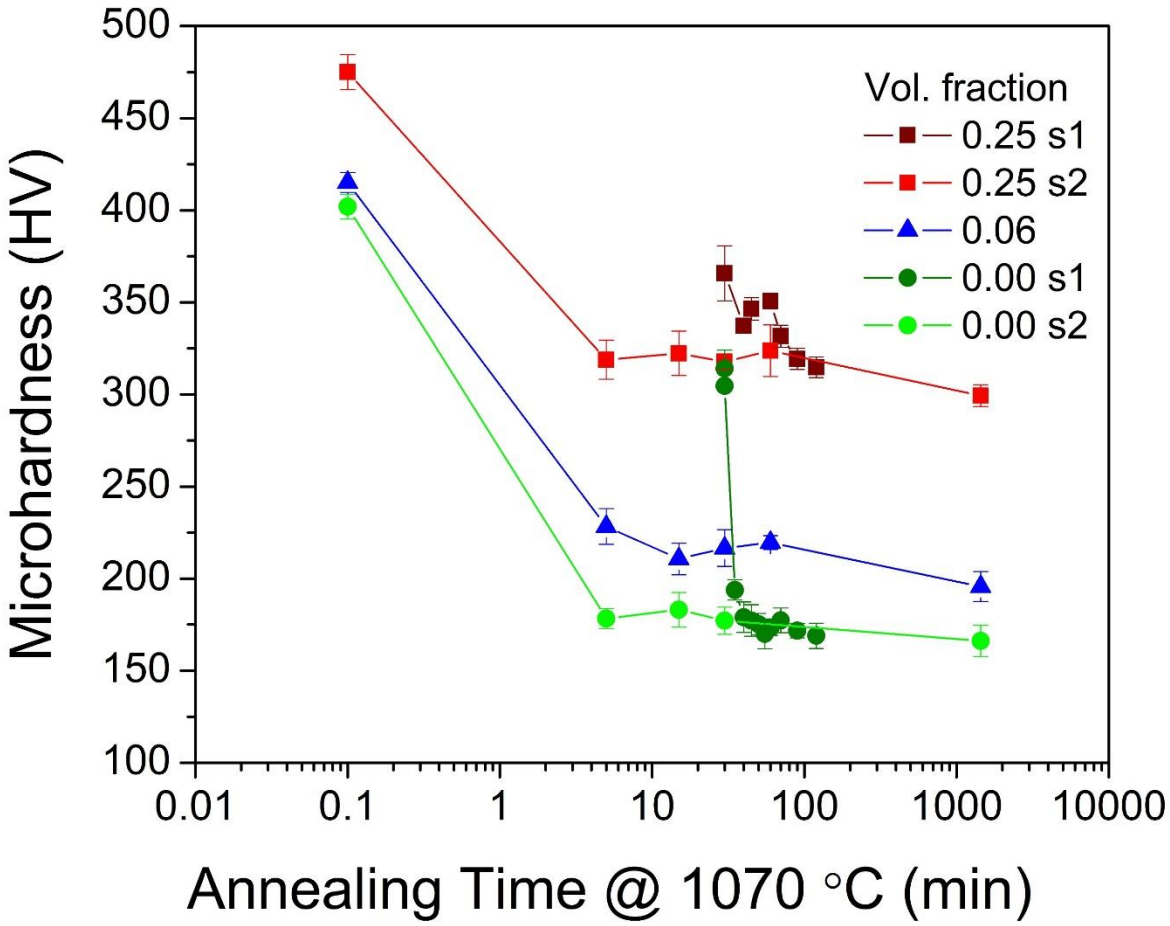

Figure 4.12: Avrami curves for the samples investigated. Due to the rapid nature of recrystallization in these alloys, the transition from nucleation to grain growth was not observed. The hardness of the partially recrystallized samples approaches that of the fully recrystallized samples upon further annealing at 1070° beyond the initial 30 minutes.

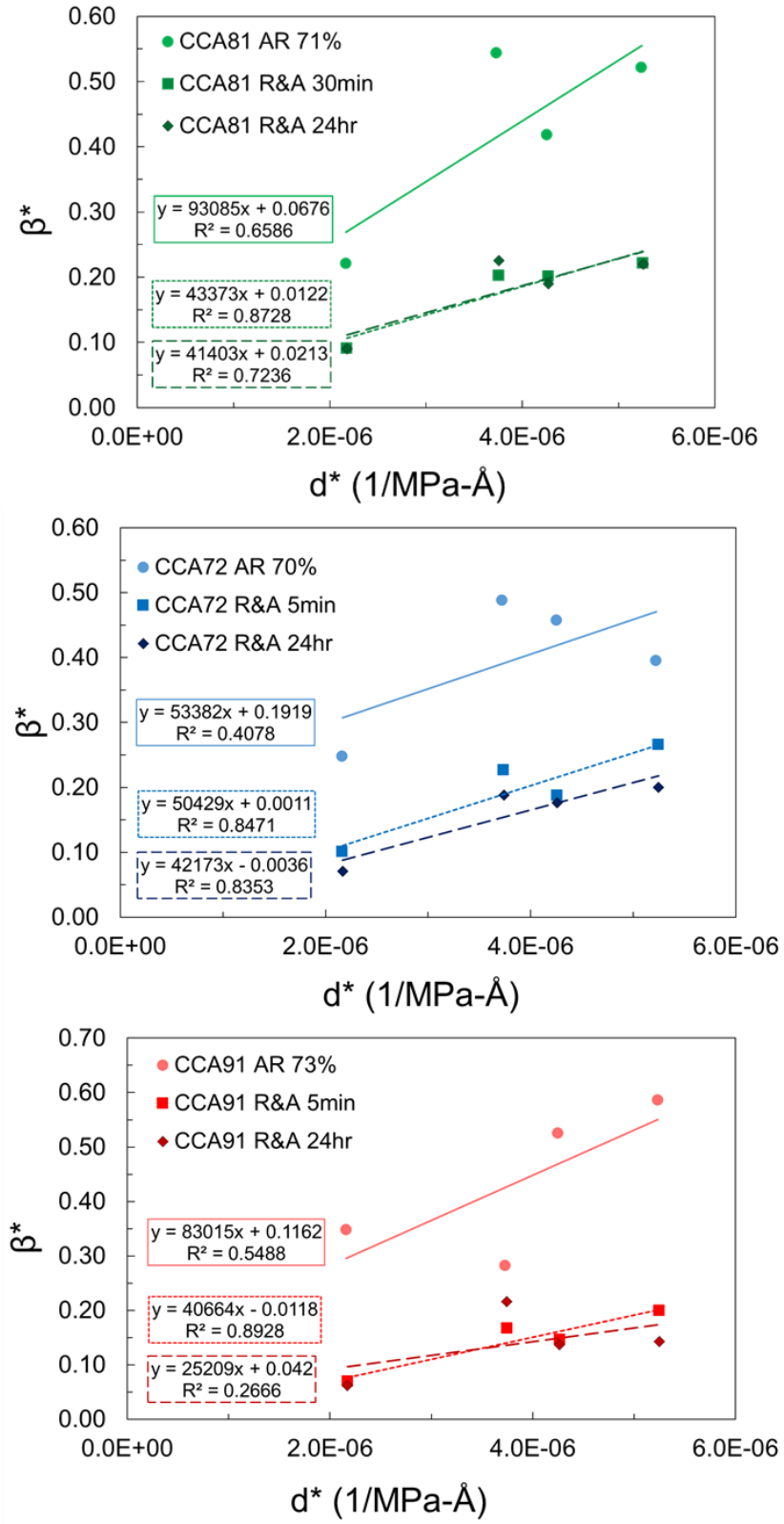

Figure 4.13: Williamson Hall plots for CCAs 81, 72 and 91 calculated under the assumption of uniform deformation stress. The majority of slope evolution occurs during the short-duration anneals, with very little change after the 24 hour anneals.

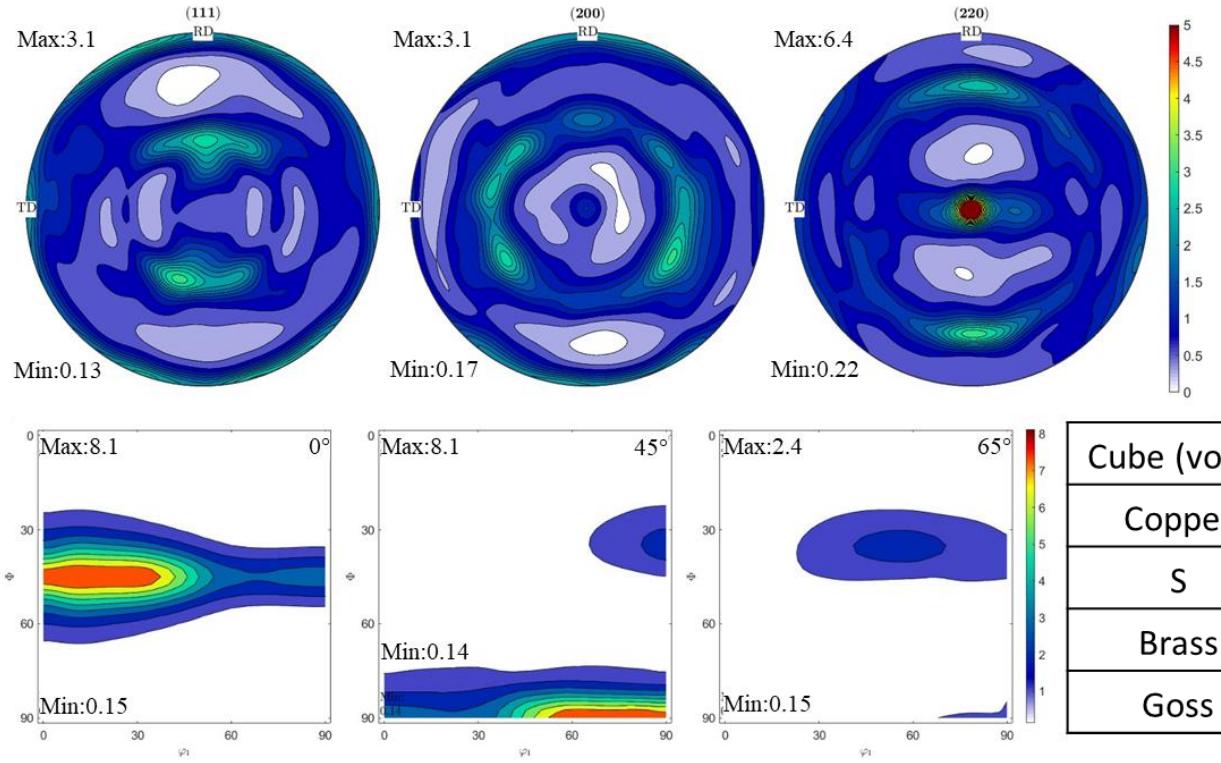

Cube (vol%)	2.18
Copper	3.62
S	3.82
Brass	7.52
Goss	8.14

Figure 4.14: As-rolled x-ray texture pole figures and φ2 (0, 45 and 65°) ODF sections for CCA 81, with texture component volume fractions.

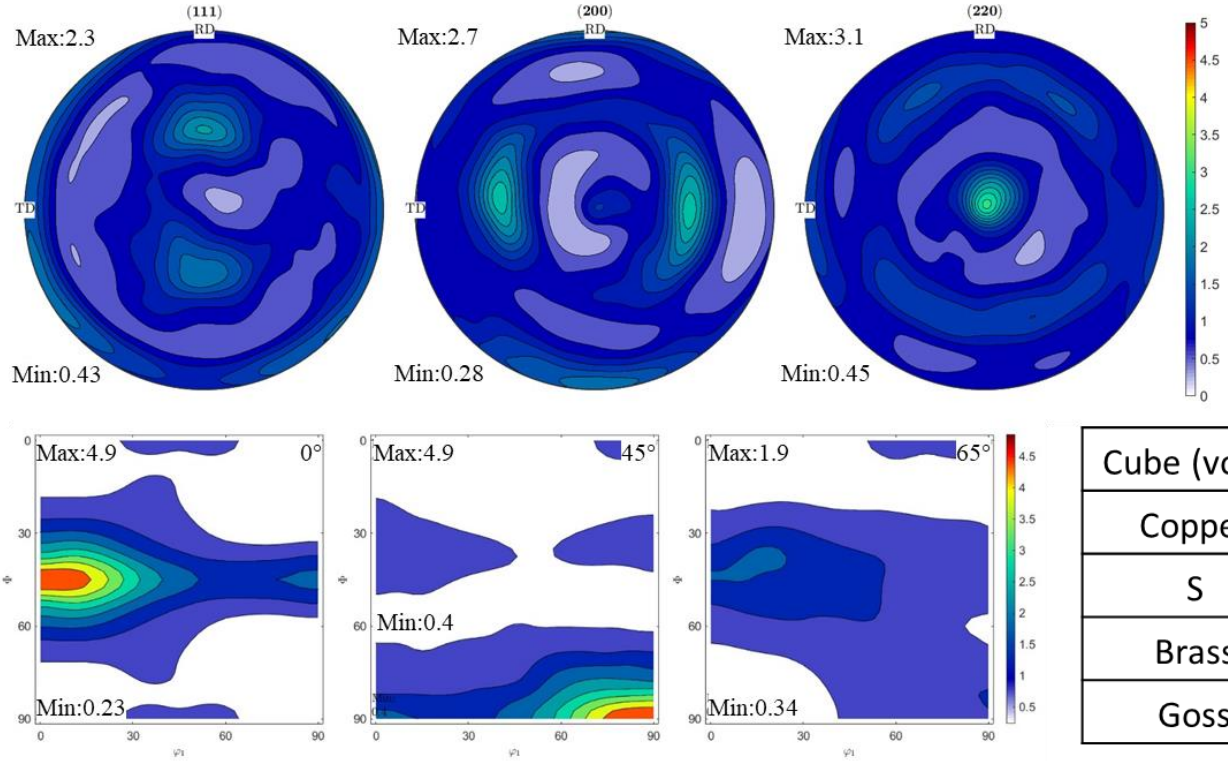

Cube (vol%)	1.47
Copper	1.74
S	2.22
Brass	4.23
Goss	7.68

Figure 4.15: Rolled-and-annealed x-ray texture pole figures and φ2 (0, 45 and 65°) ODF sections for CCA 81, with texture component volume fractions.

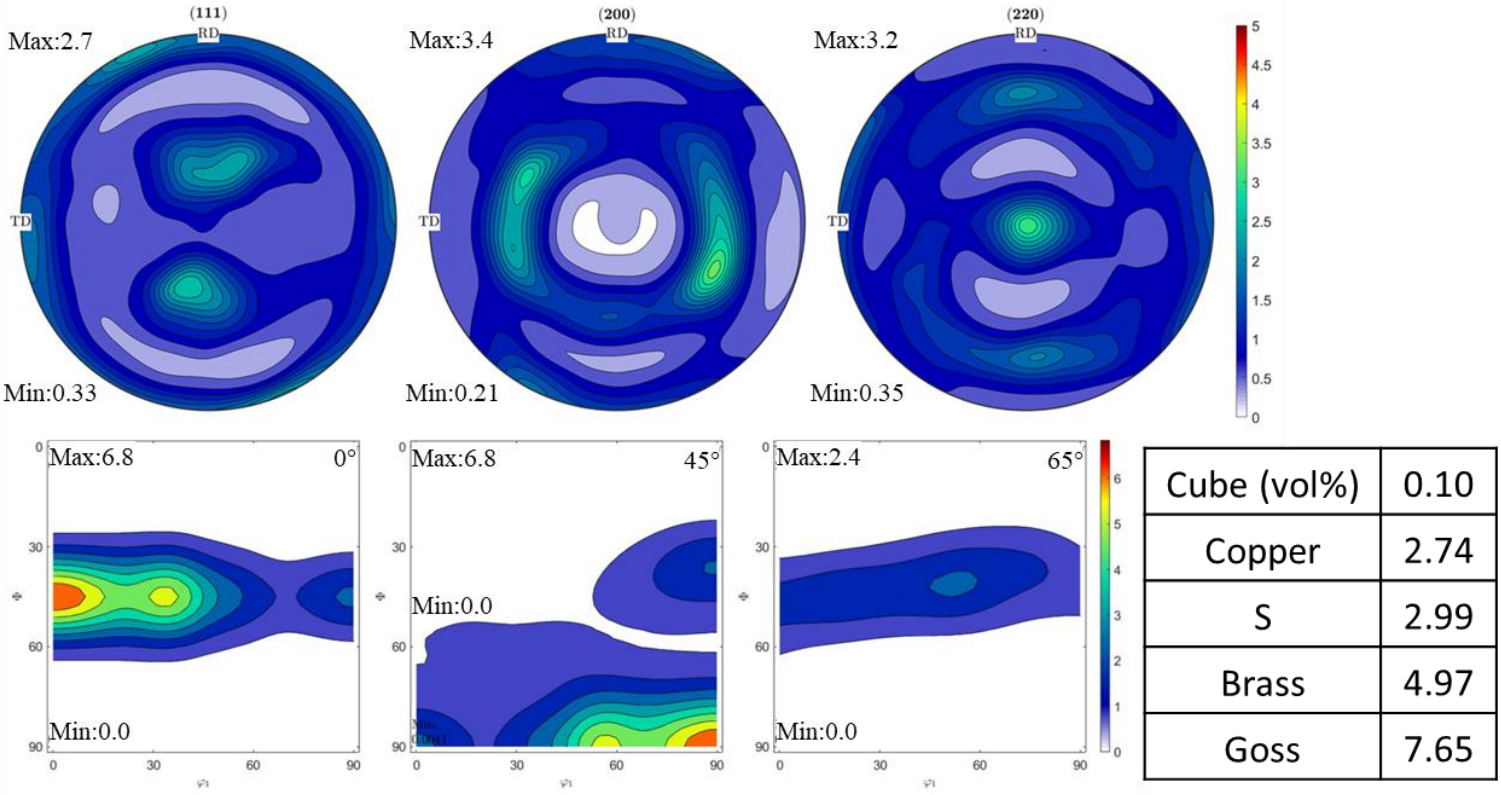

Cube (vol%)	0.10
Copper	2.74
S	2.99
Brass	4.97
Goss	7.65

Figure 4.16: As-rolled x-ray texture pole figures and φ2 (0, 45 and 65°) ODF sections for CCA 72, with texture component volume fractions.

The most obvious Heusler phase texture was observed in rolled-and-annealed CCA 94, which was measured as having 16 vol% Heusler phase. This texture is presented in Figure 4.17a. The Heusler phase shows a similar, albeit slightly more diffuse texture in rolled-and-annealed CCA 91. Multiple data sets from CCA 91 were averaged to improve grain statistics shown in Figure 4.17b. Despite the face-centered cubic lattice of the Heusler phase, the resulting annealing texture shows great similarity to the deformation texture of a BCC metal which has deformed via <111>{hkl} pencil glide, an example of which was generated using a Visco-Plastic Self-Consistent (VPSC) crystal plasticity model and is shown in Figure 4.17c. As discussed below, this similarity implies that the Heusler phase has a low anti-phase boundary (APB) energy.

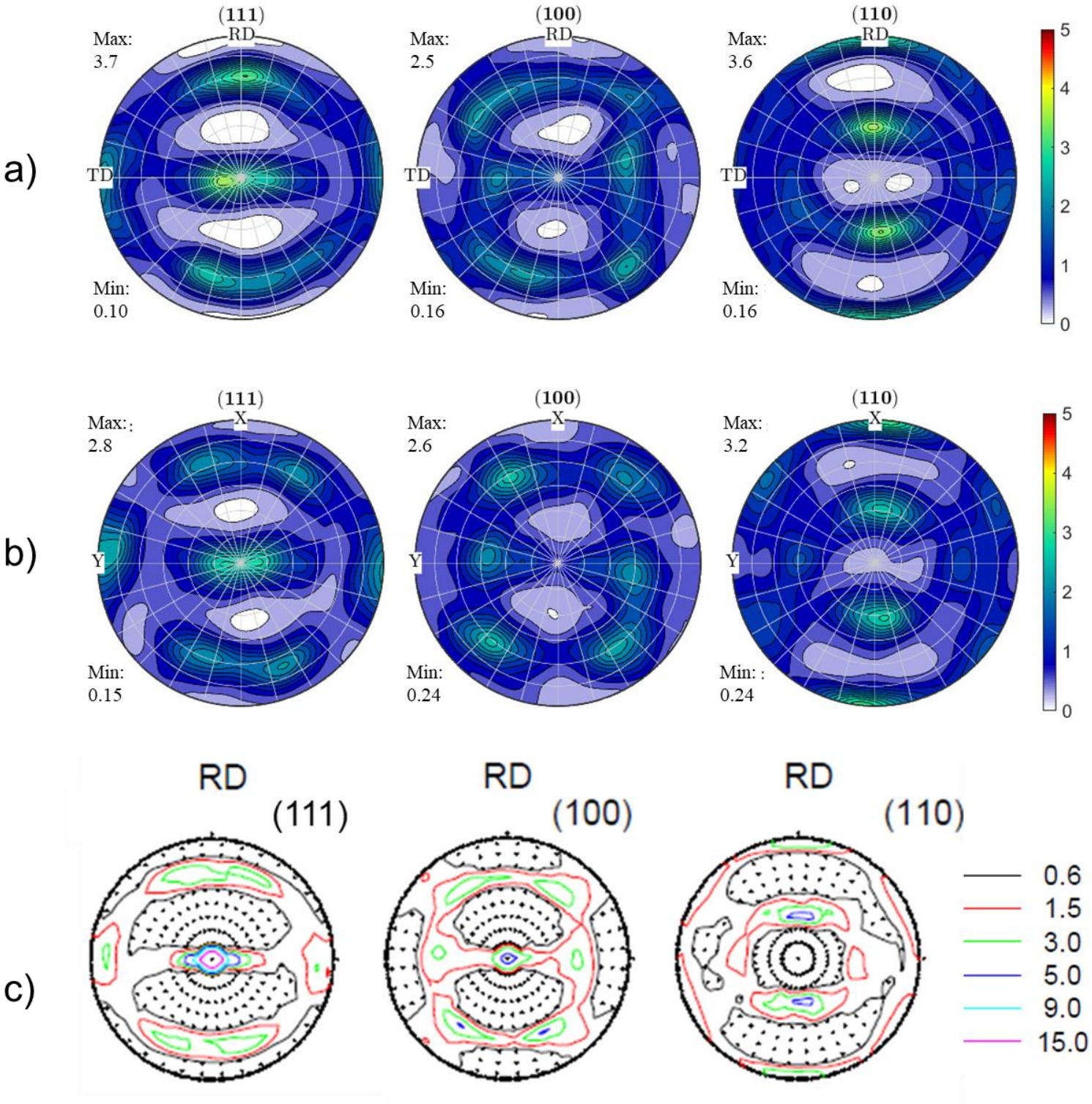

Figure 4.17: a) EBSD texture pole figures of the Heusler phase in CCA 94. b) EBSD texture pole figures of the Heusler phase in CCA 91; an average of data obtained from Sample 2 after 5 and 30 minute anneals. c) VPSC simulation of a BCC pencil glide texture after 63% rolling reduction, corresponding to a true strain of 1.0.

4.5 Discussion

The novel dual-phase CCAs were, in general, found to be amenable to cold rolling and static recrystallization. The Ni2TiAl-type Heusler phase has only rarely been found to be deformable, when part of a composite [39]. In the present case, plastic deformation of the Heusler phase was also confirmed through observations of substructured Heusler grains and polycrystalline Heusler particles, despite the lack of intragranular misorientation within Heusler grains in the cast and homogenized state. The deformation of the Heusler phase is attributed to the hydrostatic pressure present during rolling deformation. Alloys with higher volume fractions of Heusler phase tended to crack at lower cold reductions compared to those with lower volume fractions. Which is consistent with the notion that more strain partitions to the Heusler phase in the earlier stages of deformation in such cases. This causes the Heusler phase to reach its fracture stress at lower macroscopic strains.

The texture evolution of the FCC+$L2_1$ alloys is largely characterized by a relatively weak overall deformation texture, predominantly formed from the $\{110\}\langle \bar{1}12 \rangle$ Brass and {110}<011> Goss components, which is retained after annealing. In the context of rolling textures, both of these components are representative of the FCC α-fiber texture. (Not to be confused with the BCC fiber of the same name, which extends through Bunge space in the plane of φ1=0°, the FCC a-fiber extends from the Goss orientation through Brass along the Φ=90° plane [40].) A similar deformation texture is typically observed in austenitic stainless steels, especially those with lower stacking fault energy (SFE) [40]–[42], though the Brass component is typically stronger than Goss. So-called "pure metal" textures, typically associated with high-SFE materials and elevated deformation temperatures [43] are composed instead of the copper, S, and Brass components, which are collectively known as the β-fiber. The FCC+$L2_1$ alloys of the present study are considered to be intermediate-SFE materials. The Goss texture is associated with the material it derives its name from – grain-oriented silicon steel. Such steels usually develop the $\{110\}\langle 1\bar{1}0 \rangle$ texture component following shear deformation during rolling, and these shear bands serve as preferential nucleation sites for Goss-oriented nuclei which can undergo abnormal grain growth at higher annealing temperatures. Dorner et al. also note an association between $\{111\}\langle\langle 11\bar{2} \rangle$grains and the Goss texture [44], though this orientation is unobserved in both the deformed and annealed states of the novel FCC+$L2_1$ CCAs. Donadille et al. attribute the retention of {110} rolling texture components to the strong solute effect of molybdenum, as it relates to a reduction in dislocation mobility [41], likely due to the dependence of solute-dislocation interactions on atomic size misfit [45]. Given that the FCC matrix phase is primarily Fe and Ni, and Mo partitions preferentially to the matrix phase, it is likely similar solute effects on texture are being observed in this case.

A very clear connection between the presence of the Heusler phase and the size of recrystallized austenite grains was observed, with final matrix grain size showing an inverse relationship to the volume fraction of Heusler phase. There are many potential contributors to grain

refinement, and outside of a rigorous study of the recrystallization behavior, it is still worth contemplating from the perspective of a processing-properties relationship. Zener pinning, for instance, it is unlikely to be a controlling factor in the present alloys. For a given volume fraction of second phase, the pinning pressure a distribution of large (e.g. ≥1 μm) particles will be inversely proportional to the radius of the particle, because larger particles will naturally have lower number densities. While the pinning force exerted by smaller particles is lower, their greater number density makes for a greater obstacle [46]. The fact remains that grains of a second phase will still serve as obstacles to the motion of both subgrain and grain boundaries during recovery and grain growth, which has likely contributed to the observed refinement of the austenite. Solute drag – mentioned already in the context of the effect of Mo on the retention of a rolling texture - is a complicated question, with many inter-dependencies between activation energies, diffusivities, material structure and boundary velocities [47]. It is not within the scope of this work to quantify the effects of solute drag, however given the previous similarities to Mo-bearing stainless steels and the highly-alloy nature of the materials of interest, solute drag cannot be ruled out as a contributor to the recrystallization behavior observed.

The presence of large particles, (≥ 1μm in diameter,) can serve as additional nucleation sites for defect-free grains during annealing. Recrystallization characterized by distinct nucleation and growth events is often referred to as discontinuous recrystallization, as the regions which have and have not recrystallized are easily distinguished. [48] Particle stimulated nucleation of recrystallization (PSN) is often used in multi-phase engineering materials to produce finer grain sizes, weakened texture, and is typically active when the second phase particles have a diameter of 1μm or larger. [49] Humphreys and Hatherly offer a first-order approximation of how the ratio of volume fraction (F_v) and radius (r) of particles can accelerate of hinder recrystallization. When $F_v/r < 0.2 \mu m^{-1}$, recrystallization is generally found to be accelerated compared to the particle-free matrix, and when $F_v/r > 0.2\ \mu m^{-1}$, it is expected that recrystallization will be hindered, even if the second phase particles are sufficiently large enough for PSN [50]. CCA 72 (6 vol% $L2_1$) was found to have an F_v/r ratio of 0.027 to 0.048 μm^{-1}, when considering the full range of grain sizes observed, and CCA 91 (25 vol% $L2_1$) was found to have a ratio of 0.26 to 0.95 μm^{-1}. CCA 91 shares similarities with some metal-matrix composites (MMCs) in that it contains a larger volume fraction of second phase stable at high temperatures. Previous studies [51][52] have observed that, in such MMCs with $F_v/r > 0.2\mu m^{-1}$, discontinuous recrystallization was hindered and the materials instead recrystallized through a more homogeneous mechanism. These mechanisms are known as extended recovery and/or continuous recrystallization. Extended recovery is an annealing phenomenon whereby the migration of low-angle subgrain boundaries is limited by the interparticle spacing of a finely dispersed second phase. The subgrains can only grow larger as the second phase particles coarsen over time. [53] Continuous recrystallization operates in a similar fashion, in that a relatively equiaxed microstructure may form upon annealing via localized boundary migration. Due to the lack of distinct nucleation of undeformed grains, the recrystallized and non-recrystallized regions of the material are not as readily distinguished as with discontinuous recrystallization [48]. While continuous recrystallization need not necessarily be influenced by the

presence of a second phase, it is likely that a second phase would hinder the migration of high-angle grain boundaries due to pinning effects similar but not equivalent to the Zener pinning on dislocations [54]. Such particle mediated grain growth is a good match for the microstructures observed in both CCAs 72 and 91, in which neither phase shows significant coarsening during the annealing times investigated. While it is possible that multiple recrystallization mechanisms are active in these alloys, the short recrystallization times of the dual-phase CCAs precluded direct observation of PSN, so the majority of recrystallization is therefore attributed to continuous recrystallization.

The recrystallization kinetics observed tended to be rather rapid on average, and all alloys of interest achieved complete recrystallization within 5 minutes at 1070°C. Intercritical annealing temperatures for typical ferrite(α)-martensite(α') dual-phase (DP) steels tend to be on the order of 700-850 °C, followed by either controlled cooling or a lower-temperature hold to achieve the desired martensite transformation. [55] In studies of the recrystallization kinetics of DP steels in the intercritial temperature regime, complete recrystallization of samples after cold-rolling was achieved on the order of 3 to 5 minutes. [56][46] For cold-rolled, austenitic stainless steels, annealing temperatures tend to be slightly higher, ranging from 750 to 1000°C [41].

Donadille et al. observed complete recrystallization within 3 minutes only after 90% cold reduction at 900°C, though complete recrystallization was achieved for most samples of AISI 316L stainless steel at any level of cold deformation when annealed at 1000°C for 10 to 120 minutes. The FCC+$L2_1$ composite alloys of interest to this study show similar behavior to these more common steels, though the situation is somewhat different, due to the intentional lack of any phase transformations or precipitation events which may compete with recrystallization, as well as the use of the "homogenization" or stabilization temperature for recrystallization annealing [57][50].

In a more general sense, it is not unusual that the composite alloys studied recrystallize rapidly. As was noted earlier, these alloys share some similarities to metal-matrix composites, which are known to recrystallize rapidly compared to the relevant matrix phase in isolation [58]. Dual-phase alloys often have a larger number of possible nucleation sites at the particle-matrix interface, and the incompatibility between phases leads to the generation of geometrically necessary dislocations which increase the driving force for recrystallization. Despite CCA 91 having a particle dispersion parameter greater than 0. $2\mu m^{-1}$, it was not observed to have slower recrystallization kinetics compared to the other CCAs. As can be seen in Figure 4.11, the Heusler phase tends to form large polycrystalline bands, which could act as particles with a much larger effective radius and would therefore not hinder discontinuous recrystallization as much. Past studies [59]–[61] have also noted that PSN preferentially occurs at pairs or clusters of particles, such that the Heusler particles not present in bands could still collectively serve as nucleation sites.

Though as-rolled texture of the Heusler phase could not be observed, the deformed and annealed texture does provide some insight as to how the Heusler phase is deforming. The observed annealing texture bears close similarity to that of a BCC metal which has undergone

{hkl}<111> “pencil glide”. Such texture usually develops during the cold deformation of BCC metals [62], and in this case the $L2_1$ phase has retained that deformation texture after annealing. <111> glide is within the range of possible slip directions in $L2_1$ compounds outlined by Yamaguchi et al [63], though for Ni2TiAl and other more highly-ordered Heusler compounds, studies have noted a preference for <110> slip on high-index $\{h\bar{h}k\}$ planes in single crystals deformed at ≥650°C [26][64]. Conversely, in a study of a multiphase β (B2)-β’ ($L2_1$)-γ’ (DO3) alloy, Yang et al. [39] do report evidence of <111> slip in the $L2_1$ phase, deformed at room temperature during in-situ TEM straining. Unit 2[111] dislocations (with reference to the underlying BCC-type structure of the $L2_1$) were observed to dissociate into pairs of [111] superpartial dislocations which travel together primarily on the $(\bar{1}\bar{1}2)$ plane. Further BCC-like behavior is observed in the morphological evolution of the Heusler phase, namely a phenomenon known as grain curling. In the context of wire drawing of BCC polycrystals at low homologous ($T/T_m < 0.3$) temperature, meso-scale (e.g. 10-20μm) clusters of grains which must maintain strain compatibility during deformation naturally develop strain heterogeneities [65]. Over the course of deformation these strain heterogeneities will convert an initially equiaxed microstructure to a so-called “Van Gogh Sky” structure, with long, curly grains when viewed along the drawing axis. It has been shown that the minimum plastic work necessary for deformation via modes within the <110> BCC fiber texture occurs for strains close plane strain conditions [65], such as those imposed by cold rolling. This phenomenon could explain the apparent shape change observed in the Heusler phase grains in CCA 72, whereby the relatively evenly spaced, interdendritic and potentially monolithic Heuser grains before deformation have adopted a more elongated, stringer-like morphology. Due to strain incompatibilities between the FCC matrix and $L2_1$ grains, the interdendritic Heusler grains have deformed in such a way as to consolidate them laterally into curved structures generally aligned with the rolling direction, which recrystallize upon annealing. These grain curling effects might be more evident when viewed along RD, rather than ND.

4.6 Conclusions

The dual-phase, FCC+$L2_1$ compositionally complex alloys studied were able to be cold rolled to reductions of 70% or more, with those having smaller $L2_1$ volume fractions being more workable. In general, the Heusler phase deformed plastically without cracking. However cracked Heusler phase particles were observed at the upper limits of deformation for a given volume fraction even when macroscopic cracking of the sheet was not.

After working, all alloys recrystallized rapidly at 1070 °C, reaching complete recrystallization within 5 minutes, which is on par with more common dual-phase alloys. The final matrix grain size of alloys was greatly refined by up to two orders of magnitude in alloys containing the Heusler phase, ranging from hundred- to single-micron grain sizes with larger volume fractions yielding finer microstructures. Based on the available evidence these alloys likely recrystallized through a mechanism of continuous recrystallization.

The texture of the alloys studied was generally very mild, and each phase retained their respective deformation textures after annealing. The FCC matrix behaved similar to austenitic stainless steel, with prominent Goss and Brass texture components. The Heusler phase deformed in a similar manner to a BCC metal alloy, and developed an {hkl}<111> pencil glide texture.

4.7 Acknowledgements

The authors would like to thank the Office of Naval Research for their support through ONR BAA #N00014-18-1-2621, directed by Dr. Airan Perez and Dr. David Shifler.

4.8 References

[1] M. Nezakat, H. Akhiani, M. Hoseini, and J. Szpunar, “Materials Characterization Effect of thermo-mechanical processing on texture evolution in austenitic stainless steel 316L,” Mater. Charact., vol. 98, pp. 10–17, 2014, doi: 10.1016/j.matchar.2014.10.006.
[2] M. Nezakat, H. Akhiani, S. Penttilä, S. Morteza, and J. Szpunar, “Effect of thermo-mechanical processing on oxidation of austenitic stainless steel 316L in supercritical water,” Corros. Sci., vol. 94, pp. 197–206, 2015, doi: 10.1016/j.corsci.2015.02.008.
[3] J. H. Shin et al., “Materials Science & Engineering A Development of thermo-mechanical processing to form high density of uniformly distributed nanosized carbides in austenitic stainless steels,” Mater. Sci. Eng. A, vol. 775, no. November 2019, p. 138986, 2020, doi: 10.1016/j.msea.2020.138986.
[4] D. L. Engelberg, R. C. Newman, and T. J. Marrow, “Effect of thermomechanical process history on grain boundary control in an austenitic stainless steel,” vol. 59, pp. 554–557, 2008, doi: 10.1016/j.scriptamat.2008.05.012.

[5] J. Huang, X. Ye, J. Gu, X. Chen, and Z. Xu, “Enhanced mechanical properties of type AISI301LN austenitic stainless steel through advanced thermo mechanical process,” Mater. Sci. Eng. A, vol. 532, pp. 190–195, 2012, doi: 10.1016/j.msea.2011.10.080.
[6] Y. Mazaheri, A. Kermanpur, and A. Najafizadeh, “Strengthening Mechanisms of Ultrafine Grained Dual Phase Steels Developed by New Thermomechanical Processing,” vol. 55, no. 1, pp. 218–226, 2015.
[7] R. Rana, C. Liu, and R. K. Ray, “Evolution of microstructure and mechanical properties during thermomechanical processing of a low-density multiphase steel for automotive application,” Acta Mater., vol. 75, pp. 227–245, 2014, doi: 10.1016/j.actamat.2014.04.031.
[8] Q. Lai et al., “Influence of martensite volume fraction and hardness on the plastic behavior of dual-phase steels : Experiments and micromechanical modeling,” vol. 80, pp. 187–203, 2016, doi: 10.1016/j.ijplas.2015.09.006.
[9] T. Maki, T. Furuhara, and K. Tsuzaki, “Microstructure Development by Thermomechanical Processing in Duplex Stainless Steel,” vol. 41, no. 6, pp. 571–579, 2001.
[10] M. Calcagnotto, D. Ponge, and D. Raabe, “Effect of grain refinement to 1um on strength and toughness of dual-phase steels,” Mater. Sci. Eng. A, vol. 527, no. 29–30, pp. 7832–7840, 2010, doi: 10.1016/j.msea.2010.08.062.
[11] Y. Kaneno, T. Yamaguchi, and T. Takasugi, “Hot rolling workability , texture and grain boundary character distribution of B2-type FeAl , NiAl and CoTi intermetallic compounds,” J. Mater. Sci., vol. 40, pp. 733–740, 2005.
[12] E. P. George et al., “Characterization , Processing , and Alloy Design of NiAI-Based Shape Memory Alloys,” Mater. Charact., vol. 32, pp. 139–160, 1994.
[13] S. C. Deevi and V. K. Sikka, “Nickel and iron aluminides : an overview on properties , processing , and applications,” Intermetallics, vol. 4, pp. 357–375, 1996.
[14] P. V Durga, K. S. Prasad, S. B. Chandrasekhar, A. V Reddy, S. R. Bakshi, and R. Vijay, “Microstructural and mechanical properties of oxide dispersion strengthened iron aluminides produced by mechanical milling and hot extrusion,” J. Alloys Compd., vol. 834, p. 155218, 2020, doi: 10.1016/j.jallcom.2020.155218.
[15] R. Sabban, K. Dash, S. Suwas, and B. S. Murty, “Strength – Ductility Synergy in High Entropy Alloys by Tuning the Thermo - Mechanical Process,” J. Indian Inst. Sci., vol. 102, no. 1, pp. 91–116, 2022, doi: 10.1007/s41745-022-00299-9.
[16] A. Semenyuk, M. Klimova, D. Shaysultanov, G. Salishchev, S. Zherebtsov, and N. Stepanov, “Effect of nitrogen on microstructure and mechanical properties of the CoCrFeMnNi high-entropy alloy after cold rolling and subsequent annealing,” J. Alloys Compd., vol. 888, p. 161452, 2021, doi: 10.1016/j.jallcom.2021.161452.
[17] J. Moon, O. Bouaziz, H. Seop, and Y. Estrin, “Scripta Materialia Twinning Engineering of a CoCrFeMnNi High-Entropy Alloy,” Scr. Mater., vol. 197, p. 113808, 2021, doi: 10.1016/j.scriptamat.2021.113808.
[18] I. S. Wani, T. Bhattacharjee, S. Sheikh, P. P. Bhattacharjee, S. Guo, and N. Tsuji, “Materials Science & Engineering A eutectic high entropy alloy using thermo-mechanical processing,” Mater. Sci. Eng. A, vol. 675, pp. 99–109, 2016, doi: 10.1016/j.msea.2016.08.048.
[19] B. Tripathy, S. R. K. Malladi, and P. P. Bhattacharjee, “Materials Science & Engineering A Development of ultrafine grained cobalt-free AlCrFe 2 Ni 2 high entropy alloy with superior mechanical properties by thermo-mechanical processing,” Mater. Sci. Eng. A, vol. 831, no. July 2021, p. 142190, 2022, doi: 10.1016/j.msea.2021.142190.

[20] S. Kim, H. Kim, and N. J. Kim, “Brittle intermetallic compound makes ultrastrong low-density steel with large ductility,” Nature, vol. 518, pp. 77–79, 2014, doi: 10.1038/nature14144.
[21] Z. Teng, “Processing , Microstructures , and Properties of Aluminide- Strengthened Ferritic Steels,” University of Tennessee, Knoxville, 2011.
[22] R. W. Cahn, “Multiphase intermetallics,” Philos. Trans. R. Soc. London A, vol. 351, pp. 497–509, 1995.
[23] Y. Qi, Y. Wu, T. Cao, L. He, and F. Jiang, “L21-strengthened face-centered cubic high-entropy alloy with high strength and ductility,” Mater. Sci. Eng. A, vol. 797, no. March, p. 140056, 2020, doi: 10.1016/j.msea.2020.140056.
[24] R. K. Nutor et al., “Quasi-superplasticity in the AlCoNiV medium-entropy alloy with Heusler L21 Precipitataes,” APL Mater., vol. 10, 2022, doi: 10.1063/5.0113926.
[25] J. Tian, B. Chen, Y. Wu, J. Pang, T. Cao, and F. Jiang, “Microstructural evolution and duplex structure-enhanced high-temperature mechanical properties of Al-doped VCoNi medium entropy alloy,” J. Alloys Compd., vol. 965, no. April, p. 171322, 2023, doi: 10.1016/j.jallcom.2023.171322.
[26] M. Yamaguchi, Y. Umakoshi, and T. Yamane, “Plastic deformation of Ni2AlTi,” Philos. Mag. A, vol. 50, no. 2, pp. 205–220, 1984, doi: 10.1080/01418618408244223.
[27] L. Zhonghua and G. Haicheng, “Hydrostatic Stresses and Their Effect on the Macroflow Behavior and Microfracture Mechanism of Two-Phase Alloys,” Metall. Trans. A, vol. 22A, pp. 2695–2702, 1991, doi: 10.1007/BF02851363.
[28] R. W. Margevicius and J. J. Lewandowski, “The Influene of Hydrostatic Pressure on Fracture of Single-Crystal and Polycrystalline NiAl,” Metall. Mater. Trans. A, vol. 25A, pp. 1457–1470, 1994.
[29] J. J. Lewandowski and P. Lowhaphandu, “Effects of hydrostatic pressure on mechanical behaviour and deformation processing of materials Effects of hydrostatic pressure on mechanical behaviour and deformation processing of materials,” Int. Mater. Rev., vol. 43, no. 4, pp. 145–187, 1998, doi: 10.1179/imr.1998.43.4.145.
[30] M. A. Wischhusen et al., “Al-stabilized L21-Heusler phase in FCC Compositionally Complex Alloys and Control of its Volume Fraction,” Manuscr. Prep., 2024.
[31] F. Bachmann, R. Hielscher, and H. Schaeben, “Texture Analysis with MTEX – Free and Open Source Software Toolbox,” Solid State Phenom., vol. 160, pp. 63–68, 2010, doi: 10.4028/www.scientific.net/SSP.160.63.
[32] G. K. Williamson and W. H. Hall, “X-Ray Line Broadening from Filed Aluminium and Wolfram,” Acta Metall., vol. 1, pp. 22–31, 1953.
[33] G. Madhu, V. C. Bose, K. Maniammal, A. S. A. Raj, and V. Biju, “Microstrain in nanostructured nickel oxide studied using isotropic and anisotropic models,” Phys. B Phys. Condens. Matter, vol. 421, pp. 87–91, 2013, doi: 10.1016/j.physb.2013.04.028.
[34] M. A. Wischhusen et al., “Strengthening Mechanisms and Mechanical Properties of FCC+ Ordered BCC-type Intermetallic Compound Composites,” Manuscr. Prep.
[35] M. Avrami, “Kinetics of Phase Change. I General Theory,” J. Chem. Phys., vol. 7, pp. 1103–1112, 1939.
[36] M. Avrami, “Kinetics of Phase Change. II Transformation-Time Relations for Random Distribution of Nuclei.pdf,” J. Chem. Phys., vol. 8, pp. 212–224, 1940.
[37] C. W. Price, “Use of Kolmogorov-Johnson-Mehl-Avrami Kinetics in Recrystallization of Metals and Crystallization of Metallic Glasses,” Acta Metall. Mater., vol. 38, no. 5, pp. 727–738, 1990.

[38] F. J. Humphreys and M. Hatherly, “Recrystallization of Single-Phase Alloys,” in Recrystallization and Related Annealing Phenomena, First edit., Elsevier Science Ltd, 1995, pp. 173–219.
[39] R. Yang, J. A. Leake, R. W. Cahn, A. Couret, D. Caillard, and M. G., “An In-situ Observation of Dissociated <111> Glide of Ni2AlTi in a Three-Phase Alloy,” Scr. Metall. Mater., vol. 25, no. c, pp. 2463–2468, 1991.
[40] L. A. I. Kestens and H. Pirgazi, “Texture formation in metal alloys with cubic crystal structures,” Mater. Sci. Technol., vol. 32, no. 13, pp. 1303–1315, 2016, doi: 10.1080/02670836.2016.1231746.
[41] C. Donadille, R. Valle, P. Dervin, and R. Penelle, “Overview - Development of Texture and Microstructure During Cold-Rolling and Annealing of Stainless Steel,” Acta Metall., vol. 37, no. 6, pp. 1547–1571, 1989.
[42] D. N. Wasnik, I. K. Gopalakrishnan, J. V Yakhmi, V. Kain, and I. Samajdar, “Cold Rolled Texture and Microstructure in Types 304 and 316L Austenitic Stainless Steels,” ISIJ Int., vol. 43, no. 10, pp. 1581–1589, 2003.
[43] A. D. Rollett and S. I. Wright, “Typical Textures in Metals,” in Texture and Anisotropy, First edit., U. F. Kocks, C. N. Tome, and H.-R. Wenk, Eds. Cambridge University Press, 1998, pp. 179–239.
[44] D. Dorner, S. Zaefferer, L. Lahn, and D. Raabe, “Overview of Microstructure and Microtexture Development in Grain-oriented Silicon Steel,” J. Magn. Magn. Mater., vol. 304, pp. 183–186, 2006, doi: 10.1016/j.jmmm.2006.02.116.
[45] Y. Tian, F. Chen, Z. Cui, and X. Tian, “Effects of atomic size misfit on dislocation mobility in FCC dense solid solution : Atomic simulations and phenomenological modeling,” Int. J. Plast., vol. 160, no. November 2022, p. 103504, 2023, doi: 10.1016/j.ijplas.2022.103504.
[46] M. Bellavoine, M. Dumont, J. Drillet, V. Hebert, and P. Maugis, “Combined Effect of Heating Rate and Microalloying Elements on Recrystallization During Annealing of Dual-Phase Steels,” Metall. Mater. Trans. A, vol. 49A, no. July, pp. 2865–2875, 2018, doi: 10.1007/s11661-018-4642-z.
[47] J. W. Cahn, “The impurity-drag effect in grain boundary motion,” Acta <etallurgica, vol. 10, no. 5, pp. 789–798, 1962.
[48] H. Jazaeri and F. J. Humphreys, “The transition from discontinuous to continuous recrystallization in some aluminium alloys II – annealing behaviour,” Acta Mater., vol. 52, pp. 3251–3262, 2004, doi: 10.1016/j.actamat.2004.03.031.
[49] F. J. Humphreys and M. Hatherly, “Recrystallization of Two-Phase Alloys,” in Recrystallization and Related Annealing Phenomena, First edit., Elsevier Science Ltd, 1995, pp. 235–280.
[50] F. J. Humphreys, “Recrystallization mechanisms in two-phase alloys,” Met. Sci., vol. 13, no. 3–4, pp. 136–145, 1979, doi: 10.1179/msc.1979.13.3-4.136.
[51] F. J. Humphreys, “Mechanical and Physical Behaviour of Metallic and Ceramic Composites - Proc. 9th Int. Risø Symp.,” in Proc. 9th Int. Risø Symp., 1988.
[52] Y. L. Liu, N. Hansen, and D. Juul Jensen, “Proc. 12th Int. Risø Symp.,” in Proc. 12th Int. Risø Symp., 1991.
[53] F. J. Humphreys and M. Hatherly, “Recovery after Deformation,” in Recrystallization and Related Annealing Phenomena, First edit., Elsevier Science Ltd, 1995, pp. 127–172.
[54] M. Hillert, “Inhibition of grain growth by second-phase particles,” Acta. Met., vol. 36, no. 12, pp. 3177–3181, 1988.

[55] C. C. Tasan et al., “An Overview of Dual-Phase Steels : Advances in Processing and Micromechanically Guided Design,” Annu. Rev. Mater. Res., vol. 45, pp. 391–431, 2015, doi: 10.1146/annurev-matsci-070214-021103.
[56] D. Barbier, L. Germain, A. Hazotte, M. Goune, and A. Chbihi, “Microstructures resulting from the interaction between ferrite recrystallization and austenite formation in dual-phase steels,” J. Mater. Sci., vol. 50, pp. 374–381, 2015, doi: 10.1007/s10853-014-8596-2.
[57] N. Peranio, Y. J. Li, F. Roters, and D. Raabe, “Microstructure and texture evolution in dual-phase steels : Competition between recovery , recrystallization , and phase transformation,” Mater. Sci. Eng. A, vol. 527, no. 16–17, pp. 4161–4168, 2010, doi: 10.1016/j.msea.2010.03.028.
[58] M. Ferry and P. R. Munroe, “Recrystallization kinetics and final grain size in a cold rolled particulate reinforced Al-based MMC q,” Compos. Part A, vol. 35, no. 2004, pp. 1017–1025, 2014, doi: 10.1016/j.compositesa.2004.03.014.
[59] D. T. Gawne and G. T. Higgins, “Associations between spherical particles of two dissimilar phases,” J. Mater. Sci., vol. 6, pp. 403–412, 1971.
[60] P. Herbst and J. Huber, “Textures of Materials,” Proc. ICOTOM5, p. 452, 1978.
[61] B. Bay and N. Hansen, “Initial stages of recrystallization in aluminum of commercial purity,” Met. Trans A, vol. 10, pp. 279–288, 1979.
[62] S. M’Guil, W. Wen, S. Ahzi, and J. J. Gracio, “Modeling of large plastic deformation behavior and anisotropy evolution in cold rolled bcc steels using the viscoplastic -model-based grain-interaction,” Mater. Sci. Eng. A, vol. 528, no. 18, pp. 5840–5853, 2011, doi: 10.1016/j.msea.2011.03.110.
[63] M. Yamaguchi and Y. Umakoshit, “The Deformation Behaviour of Intermetallic Superlattice Compounds,” Prog. Mater. Sci., vol. 34, pp. 1–148, 1991.
[64] P. R. Strutt, R. S. Polvani, and J. C. Ingram, “Creep behavior of the heusler type structure alloy Ni2AlTi,” Metall. Trans. A, vol. 7, pp. 23–31, 1979.
[65] J. G. Sevillano, C. Garcia-Rosales, and J. Flaquer Fuster, “Texture and large-strain deformation microstructure,” Philos. Trans. Math. Phys. Eng. Sci., vol. 357, no. 1756, pp. 1603–1619, 1999.

5. Strengthening Mechanisms and Mechanical Properties of FCC + Ordered, BCC-type Intermetallic Compound Composites

5.1 Abstract

The present study is part of a larger design effort which seeks to produce lightweight, low-cost, compositionally complex alloys (CCAs) with high strength, ductility, and aqueous corrosion resistance. Novel alloys with an FCC matrix reinforced by the $L2_1$ intermetallic reinforcing phase were studied and compared with similar FCC austenitic steels reinforced by the B2 intermetallic phase. The $L2_1$ reinforcement phase was observed to be quite hard (600 VHN, suggesting a possible 2 GPa-level tensile strength), but previous rolling experiments revealed that it is capable of plastic deformation as part of the composite. Neutron diffraction experiments performed at the Oak Ridge National Laboratory – Spallation Neutron Source (ORNL-SNS) Beamline 7, VULCAN provided diffraction elastic moduli for each phase in the two classes of alloy, and single crystal elastic constants were calculated from these data. Simple tension and load-unload-reload experiments were performed and revealed a strain hysteresis in both classes of alloy. The strain hysteresis is more prominent in the FCC+$L2_1$ alloys, and the level of back stresses revealed the hardening in these alloys to be predominately kinematic. Sources of back-stress are interphase, intergranular, and intragranular (dislocation-based). Without a comprehensive model it is not possible to quantitatively parse these contributions, however, there is evidence within the lattice strain data that Heusler phase grains accumulate residual stress (are a source of back-stress) over the course of repeated straining.

5.2 Introduction

The design methodology behind dual-phase steels has long been to combine the mechanical strength of a hard phase with the ductility of a softer phase. Combinations of phases such as ferrite and martensite have been very well explored, but the new design paradigm of high-entropy and otherwise compositionally complex alloys presents an opportunity to explore a greater number of phase combinations to achieve alloys which are strong, lightweight, and may have other desirable properties such as good resistance to aqueous corrosion. Hard intermetallic phases, specifically, present ample opportunity for strengthening and density reduction, if their intrinsically brittle behavior at room temperature can be overcome. The present study is inspired by such steels, in particular an Fe-Mn-Al-Ni-C advanced high-strength steel (AHSS) from POSTECH which has displayed not only a good strength-to-weight ratio, but also yield strengths up to 1 GPa with total elongations in excess of 30% [1][2]. A series of FCC+$L2_1$, Ni_2TiAl Heusler phase-reinforced alloys has been designed with the aim of achieving a similar balance of properties of the FCC+B2 FeAl steels, with the added benefit of aqueous corrosion resistance. Both classes of alloy have shown a sensitivity of second phase volume fraction to the nominal concentration of Al. Notably, the FCC+$L2_1$ alloys do not use an interstitial strengthener, like C. Both classes of alloy

are expected to benefit from the generation of back stresses due to inhomogeneous deformation of the soft and hard phases. The FCC+B2 alloys also served to benchmark the capabilities of neutron diffraction experiments for analyzing dual phase composites.

There are many micro-scale contributors to the strength of a crystalline material, which deforms by dislocation glide and may be summarized in the form of Equation 1. From left to right, these terms relate the contributions of the lattice resistance, solid solution strengthening, grain boundary hardening, precipitation strengthening and the contribution of other (forest) dislocations. These effects are present in each phase, the FCC matrix as well as the intermetallic phase. A polycrystal (composite) homogenization scheme based upon the self-consistent approach is employed to account for meso-scale, composite effects.

$$\tau = \tau_0 + \Delta\tau_{ss} + \Delta\tau_{gb} + \sqrt{\Delta\tau_{ppt}^2 + \Delta\tau_f^2} \quad (1)$$

The lattice resistance τ_0, also known was the Peierl's stress, must be overcome to move an otherwise unimpeded dislocation through a crystal lattice. It depends on characteristics of both the dislocation and the lattice in which it exists. In the case of close-packed, face-centered cubic materials the lattice resistance at ambient temperatures and above is typically low. [3] Therefore, lattice resistance is not expected to be a significant contributor to strength of the matrix phase. However, it is highly likely that the intermetallic phase(s) will exhibit a substantial lattice resistance. Experiments performed in the course of this research provide a means of assessing the strength of these phases.

Solid solution strengthening arises due to interactions between dislocations and solute atoms. Historically, researchers have thought of this in terms of atomic size mismatch and modulus mismatch between the solute and solvent. Theoretical treatments of these interactions, in particular the statistical sampling of the solute in or near the glide plane, can be generally divided into two limiting cases; the discrete point-interactions of the Friedel-Fleischer model versus the collective interactions of the Labusch model. The model of Friedel-Fleischer is typically held to be appropriate for dilute solid solutions [4][5], in fact, recent assessments place the limiting concentration below 10^{-4} [5]. In contrast, the model of Labusch describes the distortion of the dislocation line as a result of interaction with the multiple nearby solute atoms, which is relevant to more concentrated alloys, such as those considered here [6][7]. All of the above considerations require knowledge of the interaction force (or energy) between solute and dislocations. Recently, researchers such as Leyson and Curtin have attempted to accurately calculate such dislocation-solute interaction energies using ab-initio calculations. Using these interaction energies and an extended Labusch treatment, they have developed a parameter-free model which describes solid solution strengthening in FCC metals [6][8]. Varvenne and Curtin have expanded the applicability of the aforementioned model to multi-principle element alloys (MPEAs) through the use of an average effective medium approximation [9][10]. This effective medium model was applied to make first-order approximations of the solid solution strengthening of the FCC matrix phase.

Effects of chemical short-range order (CSRO) are a topic of recent interest in the study of HEAs and CCAs, which would also affect dislocation motion in a chemically complex alloy. Recent studies [11][12] have successfully characterized SRO and found experimentally that there is an effect on the mechanical properties of alloys, but it is not significant [12].

The presence of grain boundaries serves as an additional barrier to the motion of dislocations in a polycrystalline material. This strengthening effect is understood through the Hall-Petch relation, Equation 2, in which k_y is a "locking parameter" that varies by material [13] and d is the grain size of the material.

$$\Delta\tau_{gb} = k_y d^{-1/2} \tag{2}$$

Precipitation strengthening is a major engineering control in what are known as age-hardenable alloys, which includes many Al- and Ni-based engineering materials. These materials are alloyed such that, after being solutionized, quenched and upon being held at sufficient temperature for a prescribed time, a second phase will precipitate from the supersaturated solid solution within the matrix grains and serve as an additional barrier to dislocations. As outlined in preceding chapters, it is possible to solutionize and reprecipitate the Heusler phase. However, the location, size, volume fraction and morphology prevent the Heusler phase from being an effective obstacle to dislocation motion in the FCC + $L2_1$ CCAs. Therefore, age hardening was not considered to be a contributor to strength. Instead, the CCAs of interest are considered as dual-phase composites, and the interactions of the phases are considered at a grain-to-grain level. Experiments performed in this course of this research will show that this is the case. For instance, in Figure 11 of a previous study of the thermomechanical processing response of FCC+$L2_1$ composites [14], the Heusler phase exists predominantly, if not exclusively, between austenite grains. Crystal plasticity simulations have confirmed that it is the elastic mismatch between phases which produces a strengthening effect for the composite [15][16]. Within the scope of the current work, it is not sought to completely understand the strengthening mechanisms which contribute to the properties of the Heusler phase itself, (for instance, see the presence of a phase within the $L2_1$ in Figure 6 of [17],) only to consider the strengthening it provides to the alloy as if it were a homogeneous second phase.

The presence of "forest dislocations," which accumulate in a metal during cold deformation increases the number of dislocation-dislocation interactions, and provides a strengthening effect commonly known as Taylor hardening or isotropic strain hardening. This strengthening effect is described by Equation 3, in which α is a correlation factor which varies by material and is roughly 0.2 for FCC metals, μ is the shear modulus, b is the Burgers vector length and ρ is the dislocation density.

$$\Delta\tau_f = \alpha\mu b\sqrt{\rho} \tag{3}$$

Isotropic hardening in the matrix phase was not explored in detail, in favor of examining the contributions of kinematic hardening. Kinematic hardening has a variety of potential intergranular and intragranular sources. Intragranular sources include dislocation pile-ups and other geometrically necessary dislocation structures, and while these sources are likely still active in the polycrystalline materials of interest [18][19], kinematic hardening is primarily considered here as an intergranular phenomenon. Hardening in this case arising from the inhomogeneous deformation of differently oriented or otherwise mechanically dissimilar grains, such as a strong reinforcing phase along with the softer matrix phase. "Back-stresses" accumulate which assist reverse deformation, such that a material that undergoes kinematic hardening yields at a lower stress in compression after first being deformed in tension. In fact, reverse plastic deformation (yielding) can even occur upon the release of a tensile load, i.e., unloading. This is also known as the Bauschinger effect, which produces a characteristic hysteresis in the stress-strain curve of a material upon unloading and reloading. The observed back stress is quantified very simply from visual inspection of where the load and unload curves deviate from elastic linearity (i.e., the so-called proportional limit yield stress,) following Equation 4 in which σ_b is the back stress, σ_{fw} is the yield stress upon reloading and σ_{rev} is the yield stress upon unloading and/or reverse loading.

$$\sigma_b = \frac{\sigma_{fw} - \sigma_{rev}}{2} \tag{4}$$

The overall mechanical behavior, including kinematic hardening behavior, of the dual-phase CCAs in general were examined through a combination of uniaxial tension tests and in-situ neutron diffraction.

5.3 Methods

The alloys examined in this study are the same as were studied in [14], with the addition of the two POSTECH Fe-Mn-Ni steels with different volume fractions of B2-FeAl reinforcement. Alloys "A" and "B" refer to the non-banded and banded states, respectively, which reflect the morphology and distribution of the B2 phase as described in the literature [2]. The POSTECH material was received as 1 mm sheet in the as-rolled state, and was annealed for 15 minutes at 900°C followed by water quenching prior to testing. Alloy chemistries and their respective volume fractions of reinforcement are summarized in Table 5.1. FCC+$L2_1$ samples were processed differently, depending on the necessary sample dimensions of the experiment. Generally, simple tension samples followed the processing described in [14]. Load-unload-reload samples were treated similarly, but were rolled to 85-89% cold reduction and annealed at 1070°C for 90 minutes.

Table 5.1: The chemistries and second phase volume fractions of alloys selected for this study.

Alloy	Composition (at%)	2^{nd} phase vol%
CCA 81	$Al_{3.7}Cr_{11}Fe_{42.6}Mn_{5.2}Mo_{3.1}Ni_{28.8}Ti_{5.6}$	($L2_1$) 0%

CCA 72	$Al_6Cr_{10}Fe_{40}Mn_5Mo_3Ni_{30}Ti_6$	($L2_1$) 6%
CCA 94	$Al_{8.2}Cr_{9.8}Fe_{39.1}Mn_{4.8}Mo_{2.9}Ni_{29.3}Ti_{5.9}$	($L2_1$) 16%
CCA 91	$Al_{9.4}Cr_{9.6}Fe_{38.5}Mn_{4.8}Mo_{2.9}Ni_{29}Ti_{5.8}$	($L2_1$) 25%
POSTECH-A (non-banded) [15]	$Fe_{62.4}Mn_{14.5}Al_{14.8}C_{4.1}Ni_{4.2}$	(B2) 9%
POSTECH-B (banded) [15]	$Fe_{60.9}Mn_{13.4}Al_{18.2}C_{3.3}Ni_{4.2}$	(B2) 28%

A previous study [17] outlined the strategy by which the CCAs in Table 5.1 were designed. Figure 5.1 shows these compositions schematically, overlaid on top of an isopleth phase diagram. Note that this diagram is delineated by zero-fraction lines, rather than definitive phase boundaries. The microhardness of this series of alloys was also investigated, and revealed a linear relationship between the microhardness of alloys and their volume fraction of Heusler phase. The single-phase has a hardness of 157 HV, while the pure $L2_1$ phase has a hardness of 597 HV. Hardness data for alloys in the cast and homogenized state (1070°C / 5 hrs) are shown in Figure 5.2. Such a relationship between hardness and second phase content is consistent with an upper-bound rule of mixtures approximation.

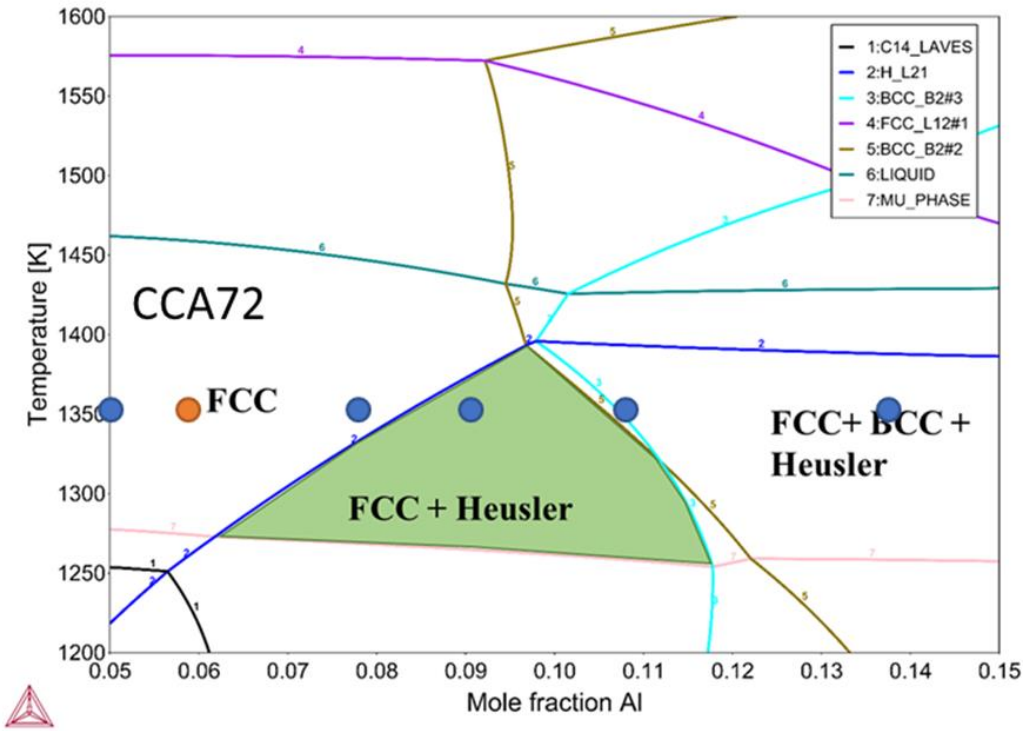

Figure 5.1: Isopleth phase diagram of the CCA system of interest. The phase fraction of the Heusler phase was controlled through the addition of Al. The CCA 72 composition is highlighted in orange.

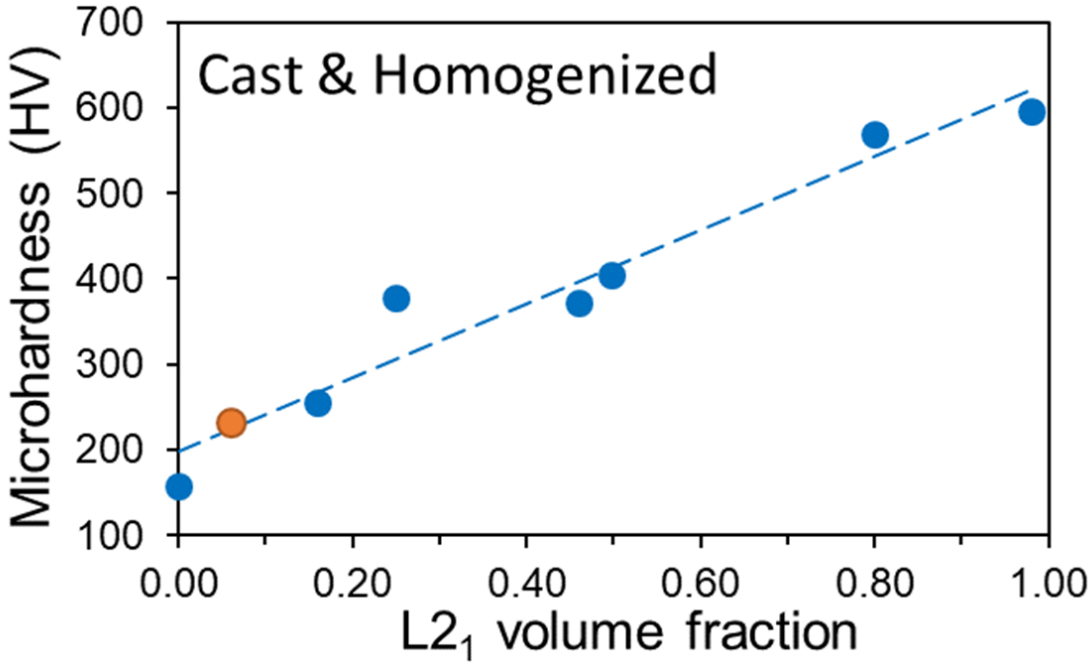

Figure 5.2: Vickers microhardness data for FCC+$L2_1$ CCAs in the cast and homogenized (1070°C / 5 hrs) state. The CCA 72 composition is highlighted in orange.

In order to calculate solid solution strengthening effects, it was first necessary to determine the volumes of atoms in solution. This was accomplished through Vegard's Law, which states that the average atomic volume of an atom in an ideal binary solid solution is the compositionally-weighted average of the pure atomic radii [20]. The volumes in question are the Seitz volume of each atom, which is the total volume of a unit cell divided by the number of atoms present. When determining the volume of individual atoms in solution, the size factors observed by King [21] are employed. The atomic radius of Mn determined by Varvenne et al. in equitatomic FCC HEAs [9] was used in all cases. The average atomic volume for the alloy environment was taken as a compositionally-weighted average of the adjusted individual atomic volumes. This approach has been shown to be quite accurate for many CCAs/HEAs [22]. The atomic volumes and thermoelastic properties of elements utilized for the calculations are listed in Table 5.2.

Table 5.2: The volume, lattice parameter and room temperature shear modulus, Poisson's ratio and Young's Modulus of pure elements used to calculate solid solution strengthening. The lattice parameter assumes an FCC structure, and is calculated as $4V_i^{1/3}$.

	V (Å^3)	a (Å)	μ (GPa)	ν	E (GPa)
Al	12.55	3.689	26.2	0.345	70.4
Cr	12.07	3.641	113.9	0.201	273.5
Fe	12.10	3.644	78.7	0.298	204.4
Mn	12.60	3.694	78.0	0.240	198.0
Mo	13.38	3.768	125.0	0.293	323.2
Ni	10.94	3.524	84.7	0.302	220.6
Ti	14.16	3.840	43.4	0.322	114.7

A model proposed by Varvenne, Luque and Curtin [9][10] was used to calculate the solid solution strengthening contribution to yield strength in the FCC matrix phase of the novel dual-phase alloys. This model provides a first-order approximation of dislocation interactions with random fluctuations in local concentration in an effective medium, with sensitivity to temperature and strain rate. The model can be briefly summarized by Equations 5-7, which describe the zero-temperature flow stress (τ_{y0}), energy barrier for thermally activated glide (ΔE_b) and the final flow stress as a function of temperature and strain rate, respectively.

$$\tau_{y0} = 0.01785\alpha^{-\frac{1}{3}}\bar{\mu}\left(\frac{1+\bar{\upsilon}}{1-\bar{\upsilon}}\right)^{\frac{4}{3}}\left[\frac{\sum_n c_n \Delta V_n^2}{\bar{b}^6}\right]^{\frac{2}{3}} \quad (5)$$

$$\Delta E_b = 1.5618\alpha^{\frac{1}{3}}\bar{\mu}b^3\left(\frac{1+\bar{\upsilon}}{1-\bar{\upsilon}}\right)^{\frac{2}{3}}\left[\frac{\sum_n c_n \Delta V_n^2}{\bar{b}^6}\right]^{\frac{1}{3}} \quad (6)$$

$$\tau_y(T,\dot{\varepsilon}) = \tau_{y0}(T)\left(-\frac{kT}{0.55\Delta E_b(T)}ln\left(\frac{\dot{\varepsilon}_0}{\dot{\varepsilon}}\right)\right) \quad (7)$$

For these equations, any average properties such as the shear modulus ($\bar{\mu}$) and Poisson's ration ($\bar{\upsilon}$) are calculated as compositionally weighted averages of the room temperature properties of the constituent elements, utilizing values available in [23]. α is a constant related to dislocation line tension and is equal to 0.123, obtained from an atomistically measured edge dislocation in an embedded-atom method (EAM), FeNiCr effective matrix [24]. $c_n\Delta V_n$ is a compositionally-weighted misfit parameter which compares the atomic volume of constituent elements to the effective medium. The Burger's vector length ($\bar{b}$) is calculated from the average lattice parameter of the effective medium as $b = \frac{a\sqrt{2}}{2}$. In Equation 7, k is Boltzmann's constant and $\dot{\varepsilon}_0$ and $\dot{\varepsilon}$ are the reference and experimental strain rates, which are equal to 10^4 and 10^{-4}, respectively. $\tau_{y0}(T)$ and $\Delta E_b(T)$ in Equation 7 denote the use of finite-temperature elastic constants for calculations at a given temperature, T.

Austenite grains were identified via EBSD and the grain size was approximated as the diameter of a circle of equivalent area, as described in [14]. While the Hall-Petch locking coefficient is unknown for the novel CCAs, austenitic stainless steels are well-studied and Stainless Steel 316L in particular was used as a proxy for properties. A brief search of the literature [25]–[29] reveals a wide range of Hall-Petch coefficients for SS 316L ranging from 0.77 to 320.4 MPa$\sqrt{\mu m}$, so an average value of 150 MPa$\sqrt{\mu m}$ was used. Notably, this is close to the parameter observed by a number of researchers [26][28][29]. As an example of the selected approach, the Hall-Petch parameters for other highly-alloyed austenitic steels such as AL6XN are less plentiful, though some studies [30] have found the parameter for SS316L to be a suitable stand-in.

Tensile testing was conducted using an MTS Sintech 10/GL load frame with a 50 kN load cell. Sub-sized tensile specimens were excised from the sheet material via electrical discharge machining (EDM). A sample schematic is shown in Figure 5.3; the tensile specimens had a gage length of 15.75 mm long by 1.10 mm wide. The thickness of tensile sample varied based on the thermomechanical processing employed, but was close to 0.5 mm. Given the observed grain size of 10 μm, this sample thickness was deemed sufficient to have a statistically large enough sample of grains through the cross section and, thereby, yield an accurate assessment of the bulk polycrystalline response.

More information on thermomechanical processing can be found in [14]. For both simple tension and tensile load-unload-reload tests, samples were pre-loaded to 80 N to eliminate slack in the load train. The unload cycles of the LUR testing involved a relaxation of load at predetermined strain intervals to the initial pre-loading value of 80 N. All testing was conducted at a strain rate of 10-3 1/s, and straining was measured via a 10mm gage extensometer. Initial tests revealed that the sub-sized tensile specimens were flaw sensitive, so all further samples were ground using SiC paper to produce a 600-grit surface finish.

The Young's modulus of each sample was determined from a linear fit of the elastic portion of the straining curve as recorded by the extensometer, and yield strength was determined via the 0.2% strain offset method. Extensometer strain data (EXT) was then corrected for elasticity,

following Equation 8, to produce a plastic flow (ε^P) curve. Data for samples which exceeded the 10 percent strain limit of the extensometer were reported as strain calculated from crosshead displacement (ΔL_{CH}) and corrected for machine compliance, following Equation 9. Compliance correction involves the use of a fitting parameter for the effective gage length of the sample, L_{eff}, which is adjusted such that the plastic flow curves of extensometer and crosshead data (CH) achieve close agreement. In some cases, the data were offset by a constant strain value such that the initial loading curve intercepted the origin (zero stress at zero applied strain).

$$\varepsilon_{EXT}^{P} = \varepsilon_{EXT} - \frac{\sigma}{E_{EXT}} \tag{8}$$

$$\varepsilon_{CH}^{P} = \frac{\Delta L_{CH}}{L_{eff}} - \frac{\sigma}{E_{CH}} \tag{9}$$

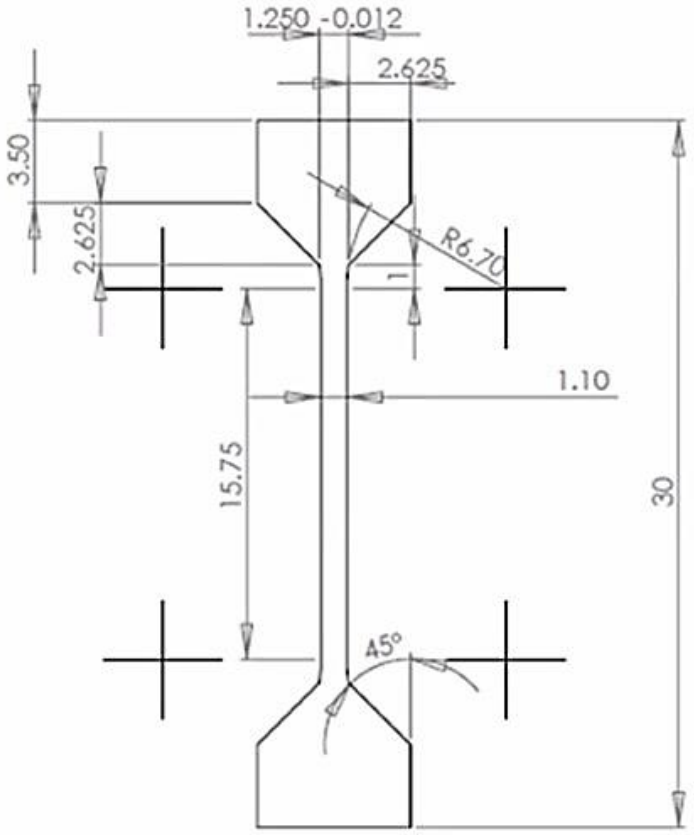

Figure 5.3: Sub-sized tensile sample schematic for in-lab CCA tensile testing. All measurements are in mm.

Samples for in-situ neutron diffraction were also prepared via EDM and tested in the as-rolled thickness. Samples of the FCC+B2 POSTECH alloys were machined by Superior Cutting Service, LLC (Holland, MI), while samples of the FCC+$L2_1$ CCAs were machined at UVA. Samples were produced to match the recommended tension sample dimensions thin plate, shown schematically in Figure 5.4 [31]. The FCC+B2 POSTECH samples were produced at 1mm thickness, as it was received in the rolled state. The FCC+$L2_1$ CCAs were produced at an average thickness of 0.5mm, due to the initially small size of the as-cast ingots and desire to impart a large rolling reduction in thickness (~80-90%) necessary to impart the desired microstructural transformations detailed in chapter 4. The negative consequence of such a thin sample thickness is an increased counting time to obtain diffraction data of sufficient quality during neutron measurements.

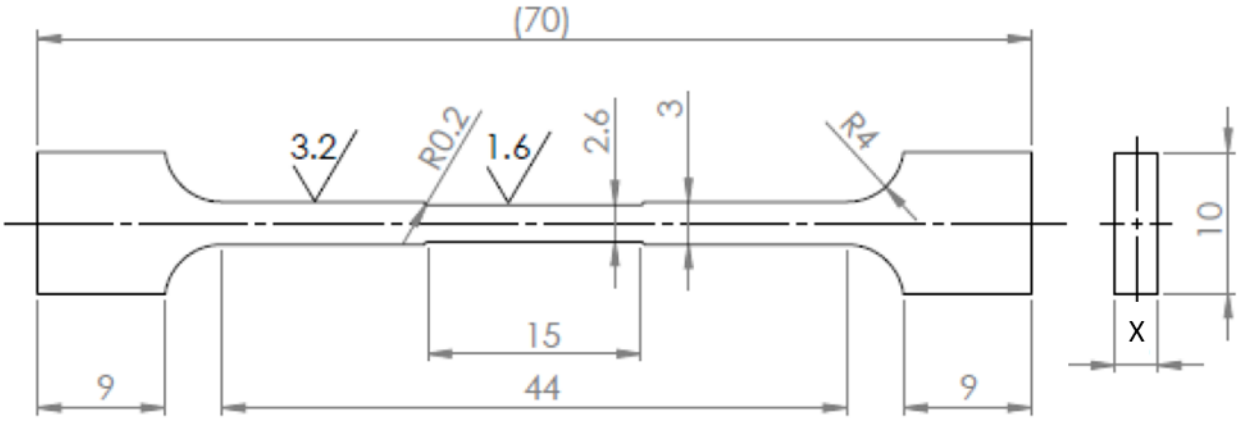

Figure 5.4: Tensile sample schematic for in-situ neutron diffraction samples. Thickness X was equal to 1mm for the POSTECH samples, and 0.5 mm for the FCC+$L2_1$ CCAs.

In-situ neutron diffraction experiments were conducted at the Oak Ridge National Lab Spallation Neutron Source (ORNL-SNS) Beamline 7 (VULCAN). The first round of experiments focused on the POSTECH alloys and involved both simple tension and tensile load-unload-reload experiments. The load-unload tests were interrupted at regular intervals to allow for diffraction data collection, while the simple tension experiment was performed continuously and the data were binned. The second set of experiments focused the novel FCC+$L2_1$ CCAs and involved only load-unload-reload tests, with continuous data collection and subsequent binning. Neutron time-of-flight data were recorded on a series of 2D detector banks, situated at different positions around the sample, and the optics were adjusted such that the entire 15mm by 2.6mm gage section was illuminated. Data from detector bank 1, corresponding to the loading direction, were the primary focus of analysis.

The ORNL-SNS data analysis cluster was used for post-processing and analysis of neutron diffraction data. BL-7 VULCAN has a suite of premade programs known as VDRIVE [32] for data reduction, i.e. the conversion of data acquired on a 2-D detector into a one-dimensional spectrum, and binning, or the summation of individual spectra over a defined time interval. An example of the output of the single-peak fitting algorithm is shown in Figure 5.5; the positions of

peaks are specified and located by the software for each 'bin' of diffraction data, and the determined peak position is used to compare the instantaneous lattice spacing to its strain-free value. The analysis cluster features an installation of the General Structure Analysis System (GSAS-I), a Rietveld program [33], combined with the graphical user interface for GSAS, EXPGUI [34]. GSAS was used to convert time-of-flight data to lattice spacing and to perform serial peak fitting to track the evolution of lattice strains, which are calculated via Equation 10. ε_{hkl} is the strain associated with grains that are oriented such that they contribute to the diffraction peak of a reflection (hkl), d^0_{hkl} is the strain-free lattice spacing of that reflection, determined by the first measured point in a data set, and d_{hkl} is the instantaneous measurement of interplanar spacing for any subsequent measurement.

$$\varepsilon_{hkl} = \frac{d_{hkl} - d^0_{hkl}}{d^0_{hkl}} \tag{10}$$

After the neutron data was postprocessed, it was exported from the analysis cluster and analyzed further with standard plotting and spreadsheet programs. Analyses included linear fitting of bulk and lattice strain data, to obtain the macroscopic and diffraction elastic moduli, as well as visual inspection of the strain data for yielding, stress partitioning and back stress.

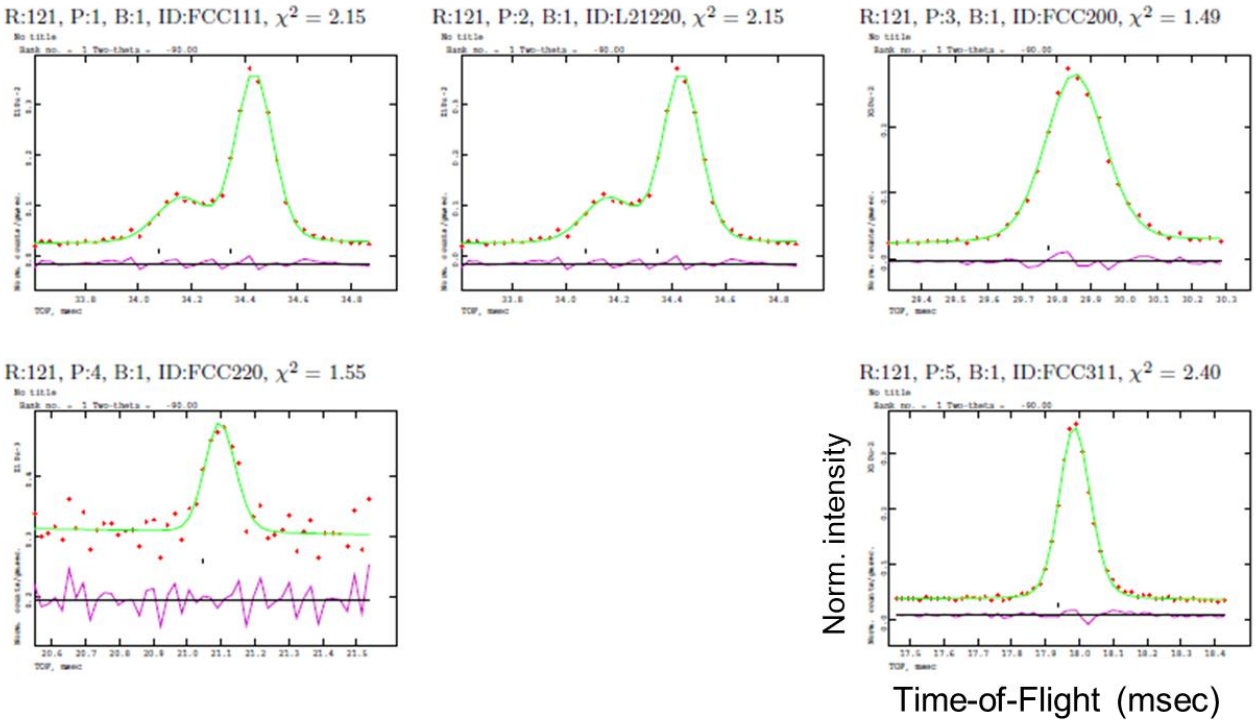

Figure 5.5: Example single peak fit output for the neutron diffraction experiments for the FCC+$L2_1$ alloys.

5.4 Results

The primary goal of this research was to investigate the strengthening provided by the Heuser phase. To that end, the contributions to the strength of a Heusler-free alloy were quantified, so the single- and dual-phase alloys may be compared, hopefully isolating the contribution of the second phase to the strength of the composite alloys. The results of the application of the Varvenne and Curtin model for solid solution strengthening in FCC metals are presented in Table 5.3, in which the flow stresses obtained from Equation 7 have been multiplied by the Taylor factor for FCC metals, M = 3.06. The treatment of the Seitz radius of Al has a notable effect on the obtained yield stress, due to the large difference between the pure metal and King solute radii.

Table 5.3: The results of the Varvenne-Curtin model for solid solution strengthening in FCC alloys. The SEM-EDS measured austenite matrix chemistries are presented with the calculated average shear modulus and Poisson's ratio for each chemistry, in addition to solid solution strengthening expected. The shear stresses calculated by the model have been converted to yield stresses through multiplication with the Taylor factor for FCC structures, M = 3.06.

Alloy	Measured FCC Matrix Composition (at%)	$\bar{\mu}$ (GPa)	$\bar{\upsilon}$ (GPa)	$\sigma_{y,SS}$ (MPa)
CCA 81	$Al_{3.6}Cr_{11.1}Fe_{42.6}Mn_{5.3}Mo_{3.2}Ni_{28.7}Ti_{5.5}$	81.9	0.284	173.6
CCA 72	$Al_{4.9}Cr_{10}Fe_{43.7}Mn_{5.8}Mo_{2.1}Ni_{28.3}Ti_{5.2}$	80.4	0.285	170.7
CCA 94	$Al_{5.7}Cr_{11.4}Fe_{43.7}Mn_{5.3}Mo_{2.7}Ni_{26.8}Ti_{4.4}$	80.9	0.283	153.1
CCA 91	$Al_{5.5}Cr_{11.6}Fe_{45.3}Mn_{5.3}Mo_{3.0}Ni_{25.3}Ti_{4}$	81.1	0.283	146.9

Using the grain size data discussed in [14] a range of Hall-Petch strengthening contributions were calculated, as shown in Table 5.4. As with solid solution strengthening, the calculated shear stresses have been converted to yield strength by multiplication with the Taylor factor. The contribution of Taylor hardening, in the absence of a quantification of dislocation density, will be estimated below from the observed yield strength minus the contributions of solute strengthening and grain size.

Table 5.4: Average austenite grain sizes for each chemistry after thermomechanical processing, and the corresponding Hall-Petch strengthening effect. Using the mean and standard deviation listed, each alloy shows relatively good agreement with a log-normal distribution of grain size. Calculated shear stresses have been converted to yield stresses through multiplication with the Taylor factor for FCC structures, M = 3.06.

Alloy	$L2_1$ phase vol%	Grain size (μm)	$\sigma_{y,HP}$ (MPa)
CCA 81	0%	53.5 ± 42.3	62.8
CCA 72	6%	10.9 ± 8.1	138.8
CCA 91	25%	1.4 ± 1.0	383.2

In preparation for the in-situ neutron experiments, the tensile properties of the POSTECH steels were briefly examined in both simple tension (Figure 5.6) and tensile load-unload-reload (LUR) testing (Figure 5.7). There is reasonable agreement with the properties reported by G. Park et al. [2]. In the case of the non-banded material, slightly lower yield strengths were observed during the in-situ testing; 1100 MPa and 1160 MPa for the RD and TD straining orientations, respectively. The observed yield strength of the non-banded material is significantly higher than that reported in the literature, however it is consistent with the yield strength observed in the LUR tests. The observed yield strengths and total elongations are summarized and compared to the literature values [2] in Table 5.5. Both the banded and non-banded alloys show yield point peak behavior consistent with Lüders banding, which is attributed to the presence of carbon.

After straining, the tensile samples were examined and the non-banded alloy was found to have a much finer microstructure than the banded alloy, which could explain the difference in strength. The observed microstructures are shown in Figure 5.8. During SEM characterization of the POSTECH alloys, strong backscattered contrast between phases was not observed, which complicated phase identification. Instead, in-lab x-ray diffraction experiments were used to confirm the presence of the B2 phase, as shown in Figure 5.9.

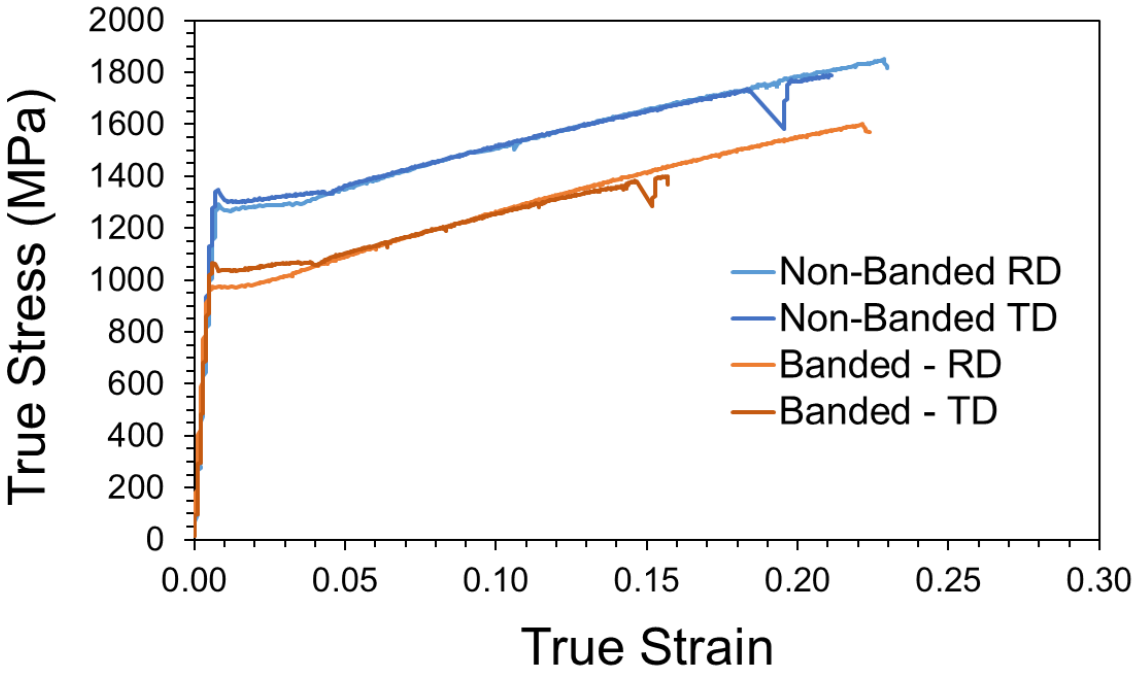

Figure 5.6: Simple tension curves for the banded and non-banded POSTECH alloys. The deflections in two curves are believed to correspond to the sample slipping in the grips.

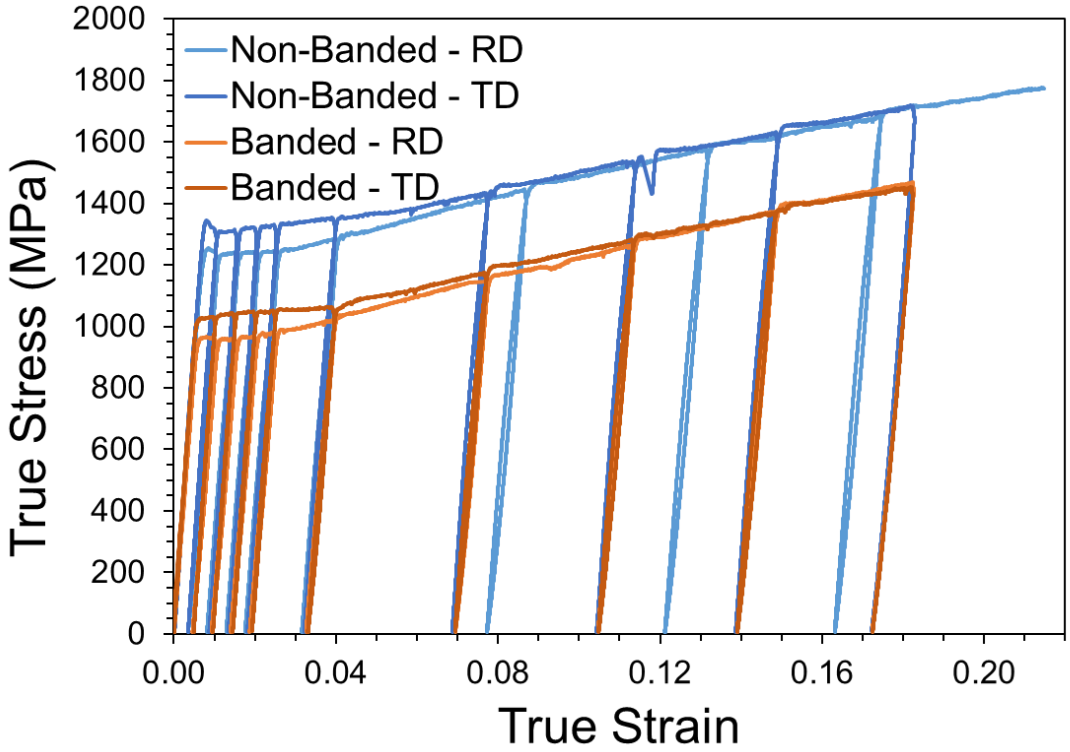

Figure 5.7: Load-Unload-Reload tension curves for the banded and non-banded POSTECH alloys. Small strain hysteresis is observed. The deflection in one curve is believed to correspond to the sample slipping in the grips.

Table 5.5: The observed yield strengths and total elongations for the POSTECH alloys, compared to values available in the literature. Engineering stress (0.2% offset) and strain are presented for consistency with the values reported in the literature.

Alloy	Observed σ_y (MPa)	Literature σ_y (MPa) [2]	Observed ε	Literature ε [2]
A-RD (non-banded)	1253	965	0.257	0.317
A-TD (non-banded)	1284	1001	0.235	0.252
B-RD (banded)	977	971	0.247	0.359
B-TD (banded)	1030	947	0.169	0.355

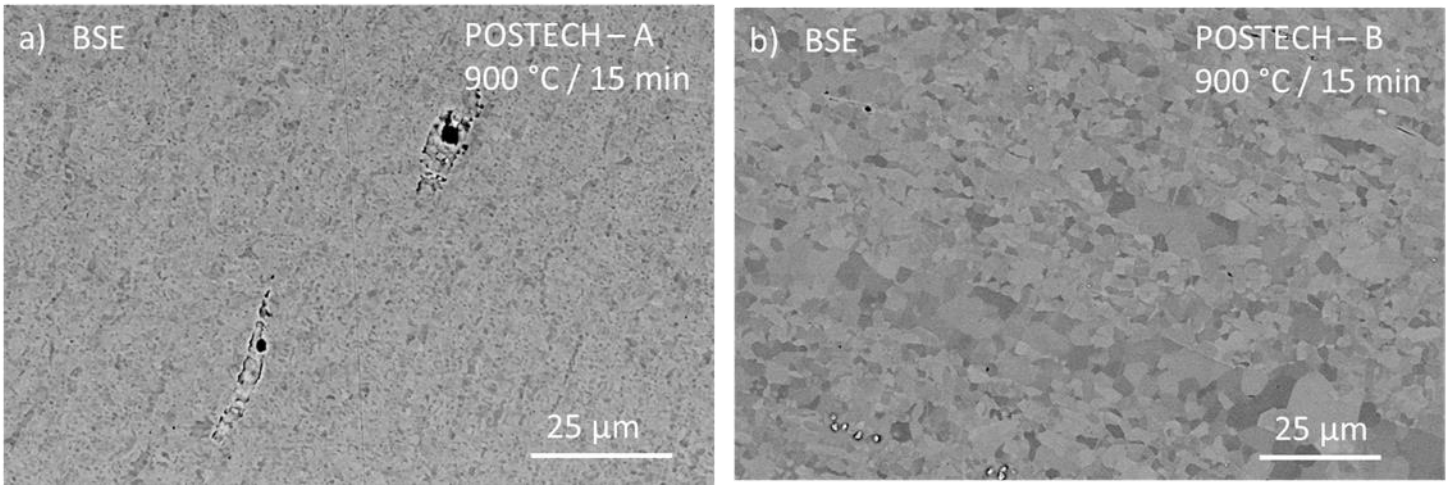

Figure 5.8: Representative microstructures of the a) non-banded and b) banded POSTECH alloys. Both alloys received the same annealing procedure, but the non-banded alloy was observed to have a much finer microstructure, which could explain the higher-than-normal observed strengths for the non-banded composition.

During the simple tension experiment of non-banded POSTECH alloy strained in the rolling direction (RD), data was collected continuously and subsequently binned. The macroscopic strain and lattice strain data, up to the point before unload, are presented in Figure 5.10. By inspecting the slopes of each lattice strain curve, it can be seen that the slopes in the B2 phase are nearly identical. In contrast, the slopes for each reflection in the FCC phase are all different. This behavior is highly suggestive of elastic anisotropy in the B2 phase, however calculated C_{ij} values for the B2 phase (Table 5.7) reveal a very mild anisotropy. Note that the FCC (220) and B2 (210) strain curves are identical – it is suspected that these two peaks overlapped during measurement. For example, the strain-free lattice spacing values of the FCC (220) and B2 (210) are 1.282 and 1.259 Å, respectively. These lattice spacings translate to an expected time-of-flight of 21.096 ms and 20.718 ms; this is the smallest time-of-flight difference between two reflections within either

phase, and between both phases. Accounting for peak breadth, as well as peak broadening due to straining, it is quite likely that the two peaks became convoluted during the in-situ experiments. Considering the relative volume fractions of phases, this peak should largely reflect the strain of FCC (220), however the elastic behavior of the lattice strain very closely matches that of the other B2 reflections. As such, the data have been included with each phase for the purposes of comparison. Note also the correspondence between the FCC (200) and B2 (211) lattice strain curves, which deflect to the right at the same time. It is presently unknown whether an orientation relationship exists between the phases such that yielding in one phase might influence the other.

From these data, diffraction elastic moduli (Ehkl) have been obtained and are summarized in Table 5.6. Following the work of Zhang et al. [35], Dr. Jishnu Bhattacharyya derived the elastic constants (Cij) of each phase from the diffraction elastic constants. These results are also presented in Table 5.7, to highlight the utility of in-situ experiments such as these in providing the properties of individual phases for the crystal plasticity modeling of composite materials. The observed elastic constants of the B2 phase are somewhat similar to the martensite of a traditional dual-phase steel, with less anisotropy than ferrite.

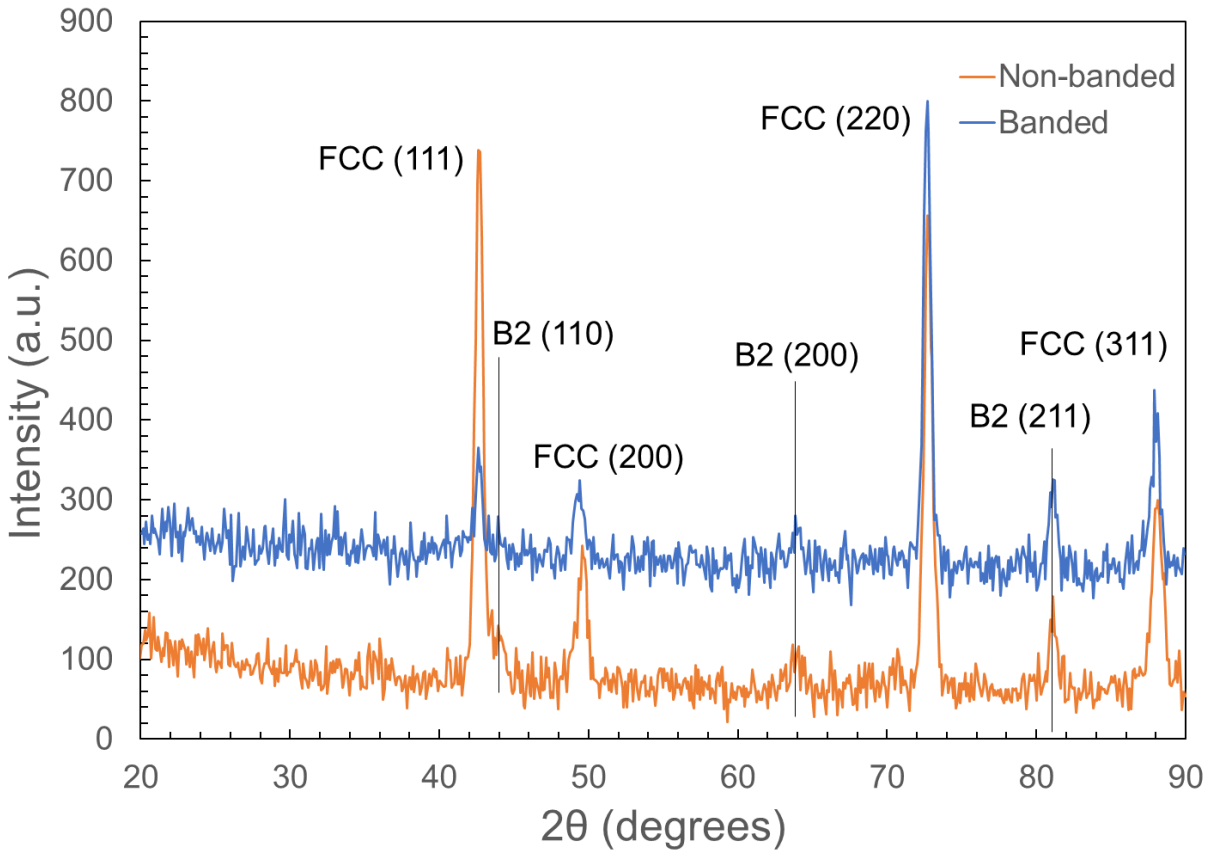

Figure 5.9: In-lab XRD of the POSTECH banded and non-banded material. The B2 phase is confirmed within each alloy. The spectra have been offset for clarity.

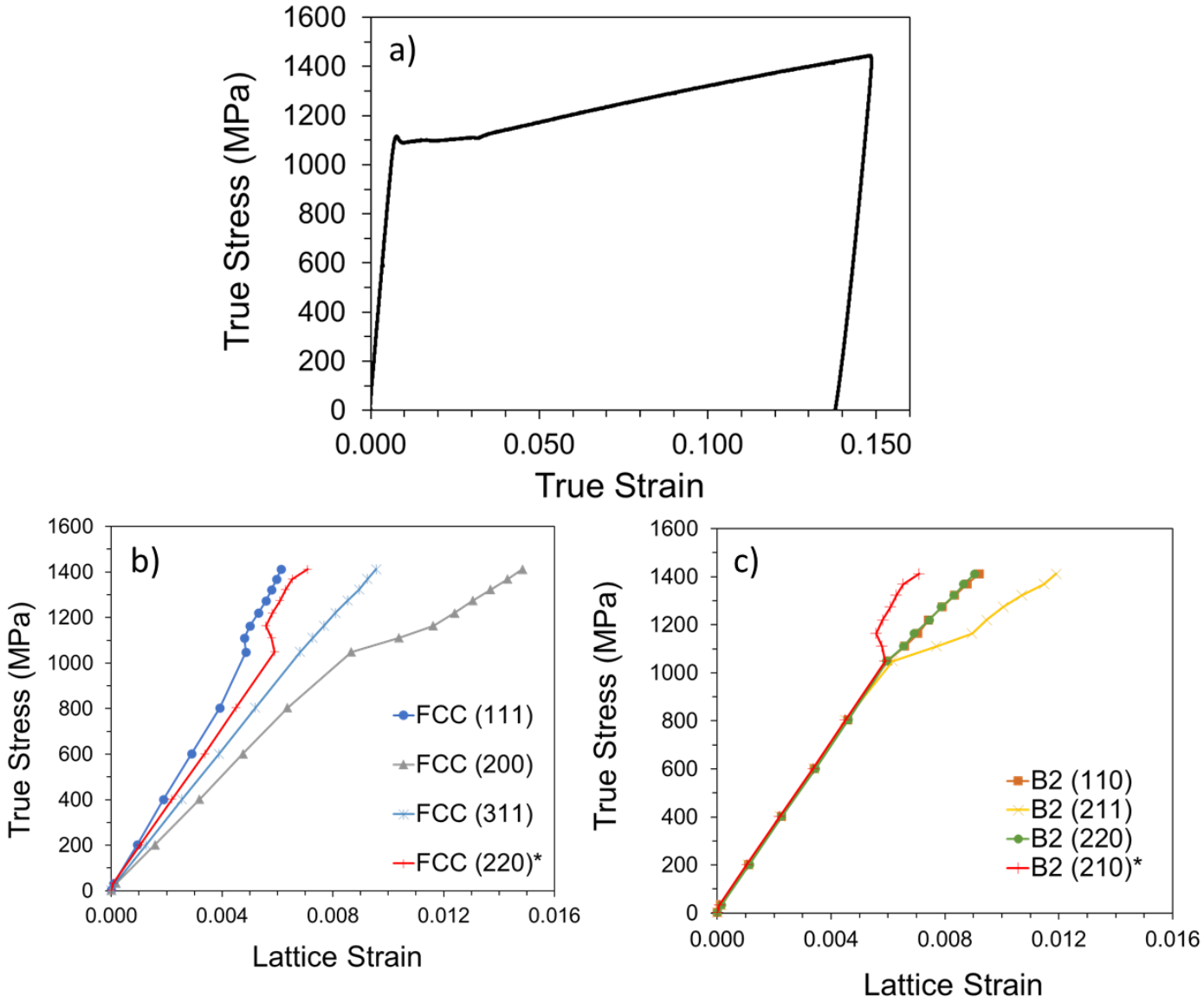

Figure 5.10: a) Tensile strain curve from the in-situ neutron diffraction test of the non-banded POSTECH alloy in the RD orientation. The lattice strains, up to the point before unloading, are presented for the b) FCC phase and c) B2 phase. The FCC (220) and B2 (210) peaks are suspected to have overlapped during measurement. While measurement of these convoluted peaks likely reflects mostly FCC behavior, it has been included with the B2 phase due to the similarity of the observed elastic moduli.

Table 5.6: The obtained diffraction elastic moduli for each (hkl) reflection observed during simple tension of the non-banded (RD) POSTECH alloy. The consistency of moduli in the B2 phase suggest a very small degree of elastic anisotropy.

FCC	E_{hkl} (GPa)		B2	E_{hkl} (GPa)
(111)	203.8		(110)	173.7
(200)	125.1		(211)	176.8
(311)	153.0		(220)	173.3
(220) + B2(210)	175.3			

Table 5.7: The derived elastic constants of the FCC and B2 phases in the non-banded POSTECH alloy, compared to an advanced high-strength Ferrite/Martensite steel (AHSS) from the literature. The calculated polycrystalline shear and Young's moduli as well as the calculated Zener anisotropy ratio are also reported. Note that the Zener ratio only applies to cubic structures, and not the tetragonal martensite.

(GPa)	C_{11}	C_{12}	C_{44}	μ	E	Zener ratio
FCC	174	112	99	56	159	3.17
B2	260	162	77	61	174	1.57
Ferrite [36]	218	113	108	-	-	2.01
Martensite [36]	282	116	79	-	-	*

The results of the in-situ load-unload-reload tests of the non-banded POSTECH alloy strained in the transverse direction (TD) (Figure 5.11) provided insight into the interaction of the FCC matrix and the B2 reinforcement during straining. These experiments were conducted by loading the sample to a predetermined stress or strain, pausing for neutron diffraction, then resuming straining. The strain hysteresis is also clearly visible in the lattice strain data (Figure 5.12), and deviations in the lattice strain curves upon unloading and reloading suggest yielding in reverse due to the accumulation of back stress. The observed yield strength upon reloading was much lower than the yield-point peak value, likely due to the freeing of dislocations from the solute atmosphere created by interstitial C atoms [37]. These data also clearly illustrate the concept of strain equilibrium – as tensile strain accumulates in (200)-oriented grains in the FCC matrix, (220)-oriented grains must, in turn, develop compressive strains. In total, the collective response of all orientations within a material must equal its composite response. A gradual decrease of the composite Young's modulus was observed through examination of the hysteresis loops of the macroscopic strain curve, and is shown in Figure 5.13. This could either be due to the accumulation of damage via microcracking in the B2 phase, or due to dependence of the instantaneous Young's modulus on pre-strain, as noted by Yoshida et al. [38]. Following the work of Yoshida et. al, Yang et al. [37] propose that the accumulation of mobile dislocations at boundaries, produces both this "permanent softening" (i.e., reduction of solute drag from C) and the decrease in apparent Young's modulus. Through this mechanism, there is actually a distribution of effective Young's moduli throughout each grain. The effective Young's modulus tends to be lower near the grain boundaries, so as more dislocations accumulate within the material, the overall modulus is lowered towards a saturated lower-bound value.

A similar experiment was conducted on a banded sample (TD) of the POSTECH alloy, however an experimental error caused the test to end prematurely. Of the data available, no new behavior was observed and the results have been omitted for brevity.

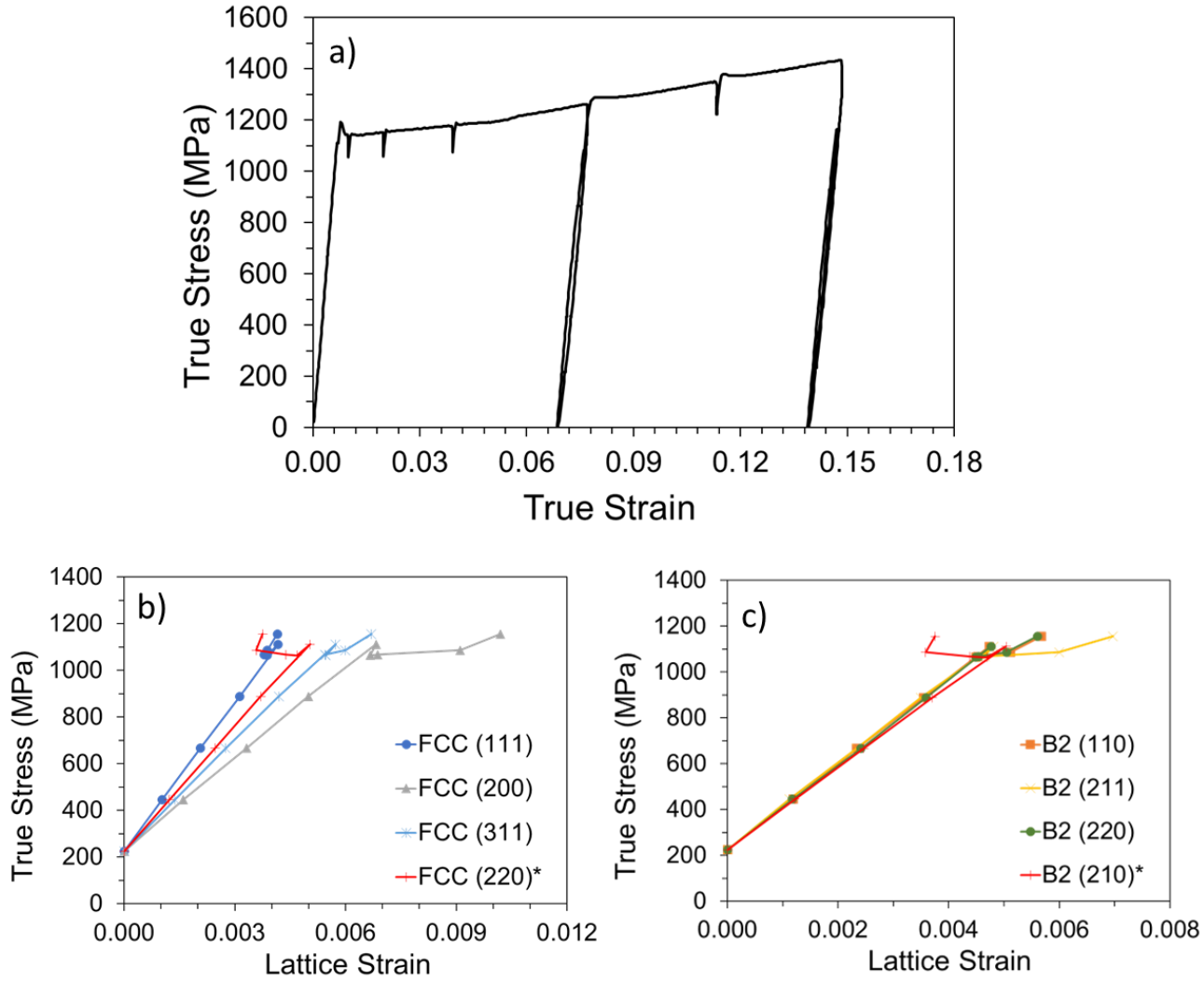

Figure 5.11: a) Tensile strain curve for the non-banded (TD) POSTECH alloy during in-situ neutron diffraction. The deflections in the strain curve correspond to relaxation in the sample during data acquisition. The lattice strains, up to the point before unloading, are presented for the b) FCC phase and c) B2 phase. The FCC (220) and B2 (210) peaks are suspected to have overlapped during measurement, and therefore the data collected has been presented with each phase.

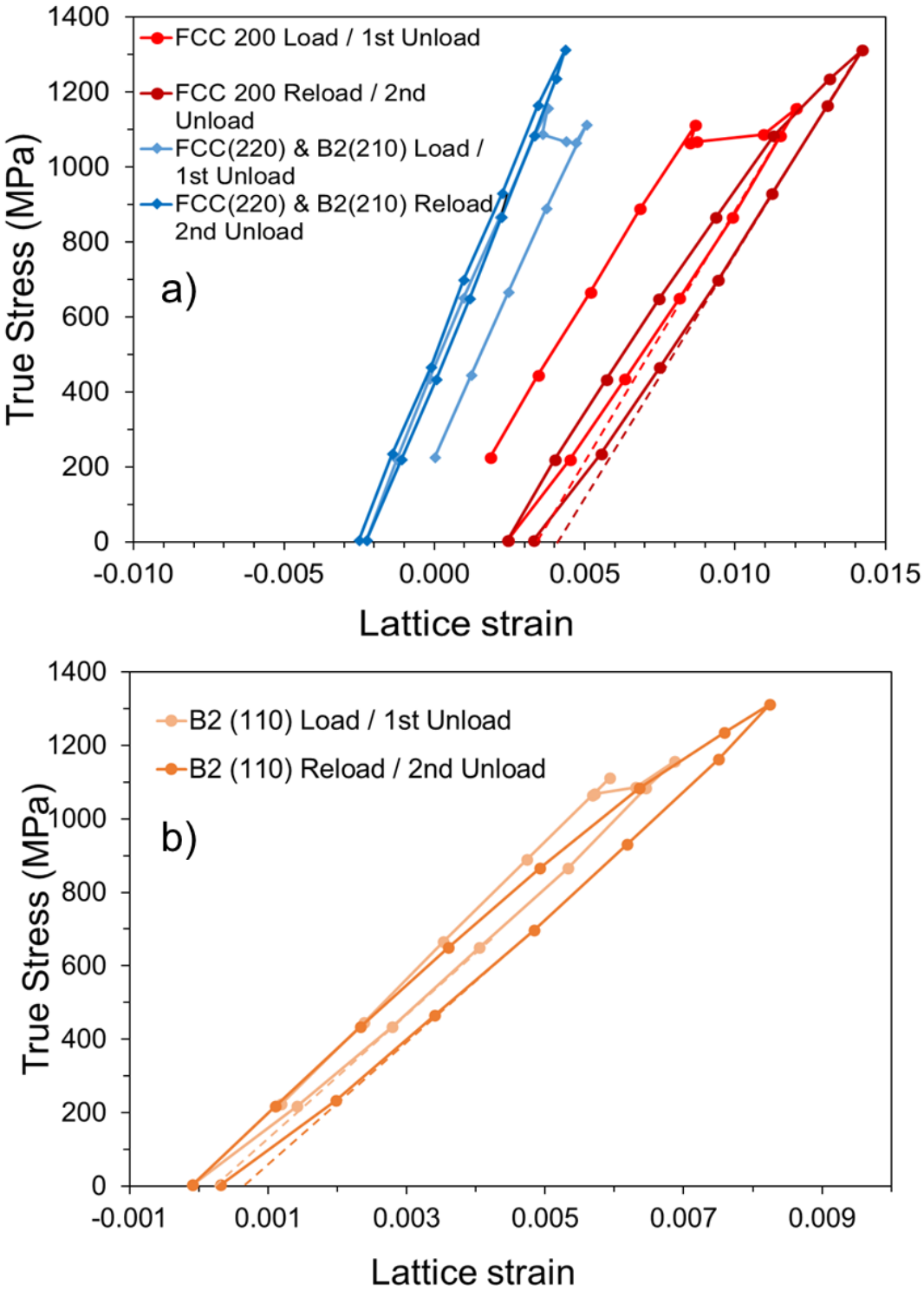

Figure 5.12: Lattice strains in the non-banded (TD) POSTECH alloy during loading and unloading for select reflections in the a) FCC matrix and b) B2 reinforcement. The dashed lines depict linear unloading behavior. This behavior was also observed in the lattice strains of the convoluted FCC (220) peak, though it was much less pronounced than in the FCC (200) or B2 (110).

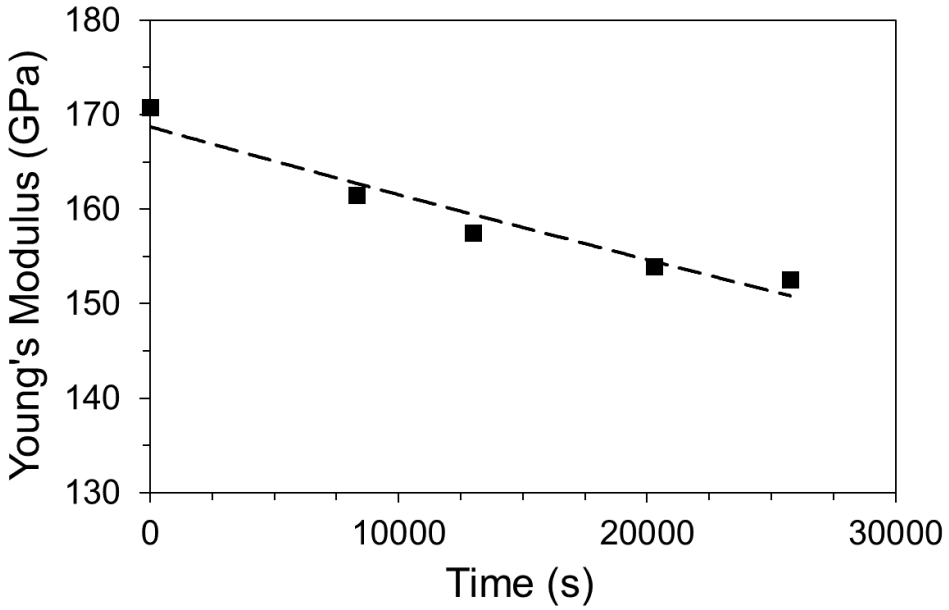

Figure 5.13: The evolution of the composite Young's modulus of the non-banded (TD) POSTECH alloy, obtained from the unload-reload loops during in-situ testing. The data suggest an exponential decay, but a linear fit describes the data equally well. Note that time is not the independent variable in this case – it is intended to show that, in the order in which load and unload steps were applied, there is a gradual decrease in the observed Young's modulus.

The plastic flow curves obtained from simple tension experiments of the FCC+$L2_1$ CCAs are presented in Figure 5.14. There is a stark difference in the observed hardening behavior of CCA 72 compared to CCAs 81 and 91, which is attributed to the use of intermediate anneals during cold rolling. The obtained composite Young's moduli, 0.2% offset yield strengths and total elongations before failure are summarized in Table 5.8. While the differences in thermomechanical processing make it difficult to draw an immediate conclusion as to the effect of the Heuser phase alone, the typical strength-ductility tradeoff is observed between CCAs 81 (0 vol%) and CCA 91 (25 vol%), as well as the observed grain refinement the presence of the second phase provides. The possibility exists that CCA 72 is near an ideal volume fraction of the Heusler phase, such that intergranular back stress is able to contribute to material hardening without cracking in the Heusler phase severely decreasing the ductility of the alloy. Furthermore, the samples of CCAs 81 and 91 are the same samples which were observed to be only partially recrystallized (see Figure 12 of [14]). In the absence of retained cold work, CCA 81 would likely have yielded at a lower stress and achieved similar ductility, but less hardening, than CCA 72.

After tensile testing, the microstructures of deformed samples were examined to determine whether Heusler phase grains tended to debond from the matrix or fracture. Micrographs (Figure 5.15) of the alloys after tensile testing reveal an apparent shift from primarily debonding with some transgranular $L2_1$ fracture in the lower volume fraction material, CCA 72 (6v% $L2_1$), to predominantly intergranular fracture within the $L2_1$ grains and along $L2_1$-$L2_1$ grain boundaries in

the higher volume fraction alloy, CCA 91 (25 vol% $L2_1$). Figure 5.15c shows the presence of a plate-like phase within the Heusler phase as was noted previously in [14], which also decorates $L2_1$-$L2_1$ grain boundaries. This transition is likely due to the relative volume fractions of the Heusler phase – in the lower volume fraction alloy, the matrix experiences the critical stress for debonding before the fracture stress of the Heusler phase is reached. In the higher volume fraction alloy, the Heusler phase is forced to bear more of the macroscopic strain, leading to a concentration of stress in the $L2_1$ which exceeds the fracture stress of the second phase. It also stands to reason that, at lower macroscopic strains, the hydrostatic stress imposed by the matrix on the second phase would be lower, which allows for fracture of the Heusler phase at lower applied stress.

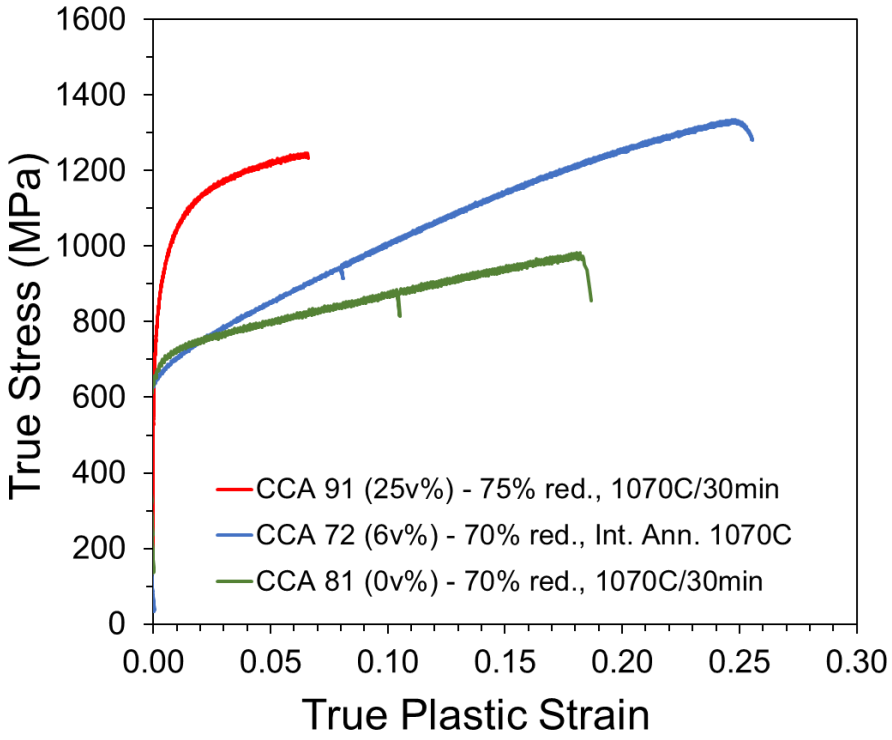

Figure 5.14: Plastic strain curves for three FCC+$L2_1$ CCAs. CCA 72 received two, 1-hour intermediate anneals at 1070°C during the cold rolling process, followed by a final 30 minute anneal at 1070°C. CCAs 81 and 91 received only one final anneal at 1070°C for 30 minutes, but were observed to be only partially recrystallized [14]. The deflections in two curves correspond to the removal of the extensometer at its strain limit.

Table 5.8: The obtained Young's modulus, 0.2% offset yield strength, ultimate tensile strength and total elongation for the three FCC+$L2_1$ CCAs depicted in Figure 5.12.

Alloy	E (GPa)	σ_y (MPa)	UTS (MPa)	ε
CCA 81 - TD	159.6	670	984	0.178
CCA 72 - TD	150.5	600	1335	0.250
CCA 91 - TD	160.1	860	1246	0.066

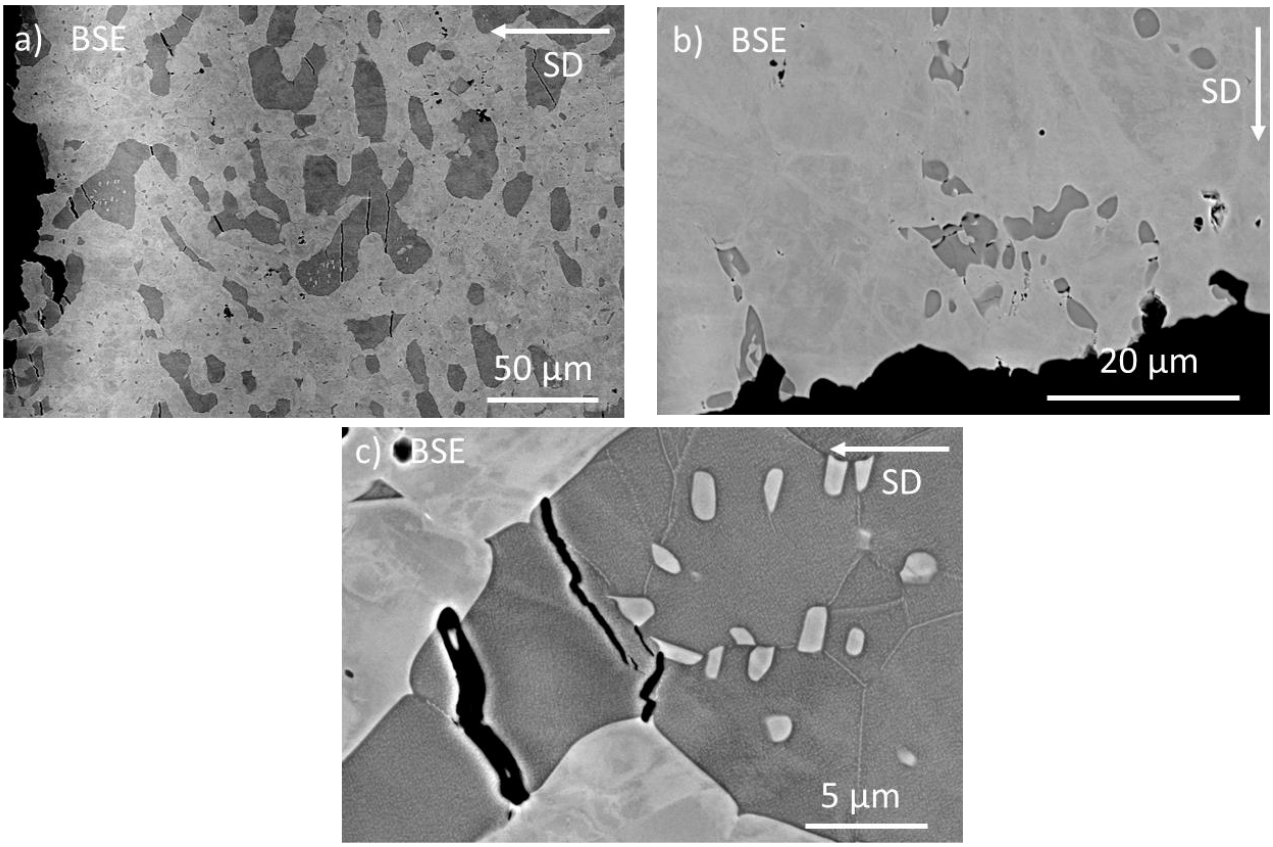

Figure 5.15: Micrographs of cracked Heusler phase grains in a) CCA 91 and b) CCA 72 after tensile testing. Heusler grains were observed to fracture in tension primarily perpendicular to the straining direction. c) depicts a cluster of Heusler phase grains shown in a), in which both inter- and intragranular crack propagation in the Heusler phase can be seen.

Having observed a yield strength of 670 MPa in the Heusler-free CCA 81, the contribution of Taylor Hardening can be approximated. Based on the calculated contributions of solid solution strengthening and grain boundary (i.e. Hall-Petch) strengthening, 173 and 63 MPa respectively, Taylor hardening would account for about 434 MPa of the observed yield strength, which corresponds to a dislocation density on the order of 10^{15} m^{-2}. While this is physically feasible, such a dislocation density would correspond to a heavily cold-worked material, in contrast to the observation of CCA 81 being only partially recrystallized. These estimations should therefore be treated with a measure of skepticism, as there is an unexplained factor at play, which could relate to the sample of CCA 81 not receiving the full extent of the thermomechanical processing applied to it.

The load-unload-reload (LUR) curves for CCAs 72 and 94, as well as the evolution of the Young's modulus of CCA 72 during testing, are shown in Figure 5.16. It should be noted that these samples received different thermomechanical processing from those discussed above. The LUR samples received more cold deformation, were annealed for longer, and upon further inspection a fraction of Heusler phase grains was observed to be cracked before mechanical testing, as shown in Figure 5.17. The obtained Young's modulus, 0.2% strain offset yield strength and average

obtained back stress values are presented in Table 5.9. CCA 72 appears to have superior properties to CCA 94, however in light of the presence of cracked Heusler phase grains after processing, it is difficult to draw a direct comparison between the two. While the extent of cracking was not quantified, the presence of any cracking reduces the load bearing capacity of the Heusler phase and provides damage initiation sites for void nucleation and coalescence. Calculation of the back stresses in CCA 72 revealed a trend of a steady increase in back stress with further straining. The level of strain hardening in CCA 72 was observed to be about 195 MPa, from the 0.2% strain offset yield strength to its UTS, and of that hardening 171 MPa on average can be contributed to back stress. In other words, the contribution of kinematic hardening to the strength of the material is significant compared to isotropic hardening. Given the magnitude of the increase in back-stress as a function of straining, it is likely that the majority of kinematic hardening arises early in deformation, during the elasto-plastic transition, due to interactions between differently-oriented matrix grains.

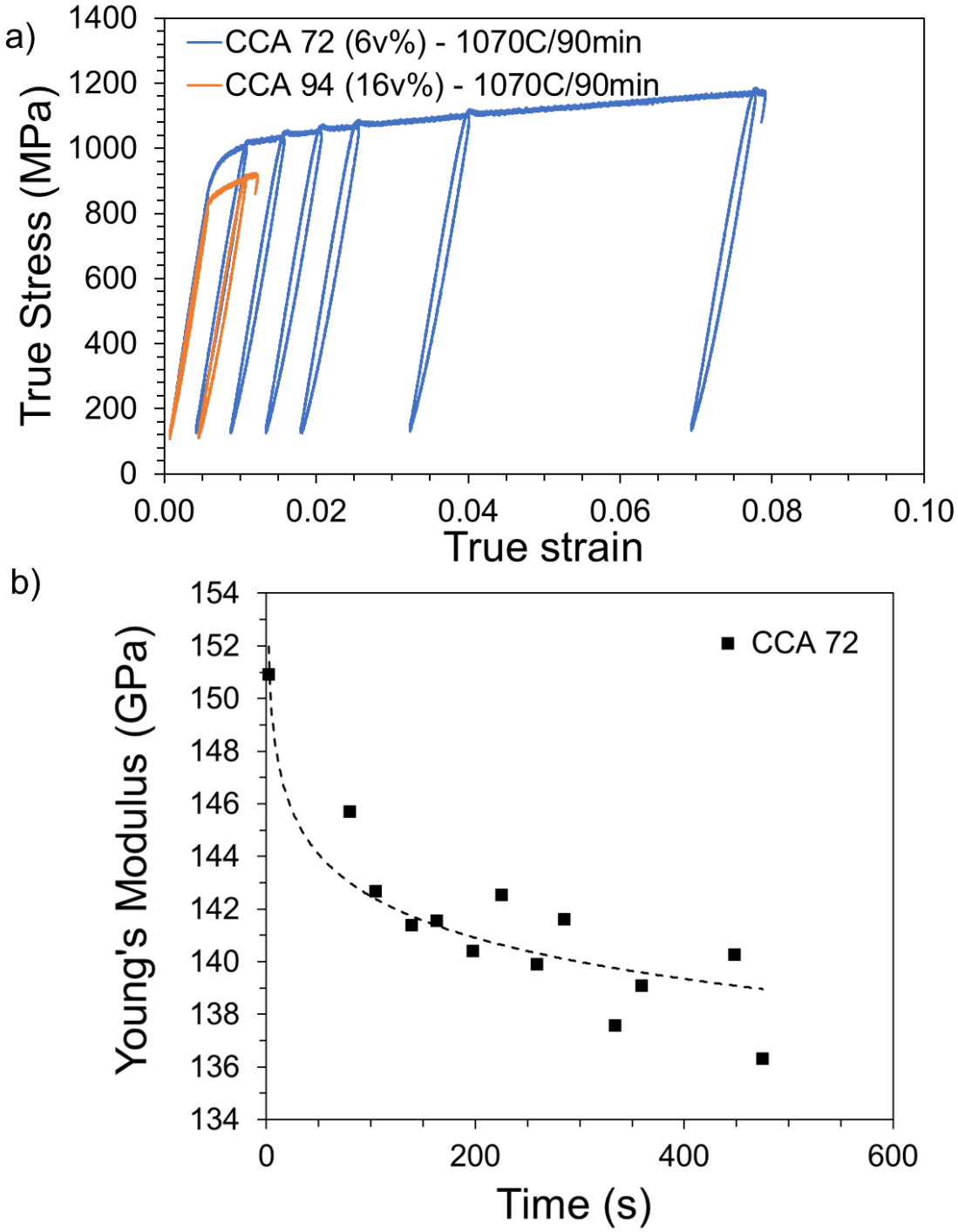

Figure 5.16: a) Load-Unload-Reload tension curves for CCAs 72 and 94, prepared under the same conditions as the in-situ neutron diffraction samples. Strain hysteresis was observed in both samples. Compared to the data in Figure 5.14, HEA 72 is stronger, less ductile, and does not harden as rapidly. b) The evolution of the composite Young's modulus of CCA 72, obtained from the unload-reload loops. The dashed line is intended as a guide to the eye, depicting a trend of decline towards a lower-bound value.

Table 5.9: The initial Young's modulus, 0.2% offset yield strength and calculated average back stress across all load-unload cycles from the LUR testing of CCAs 72 and 94. The first unload cycle for both tests took place within the elastic region before yielding, and were omitted from calculations.

Alloy	Vol% $L2_1$	E (GPa)	σ_y (MPa)	σ_b (MPa)
CCA 72 - RD	6	150.9	980	172
CCA 94 - TD	16	143.1	880	185

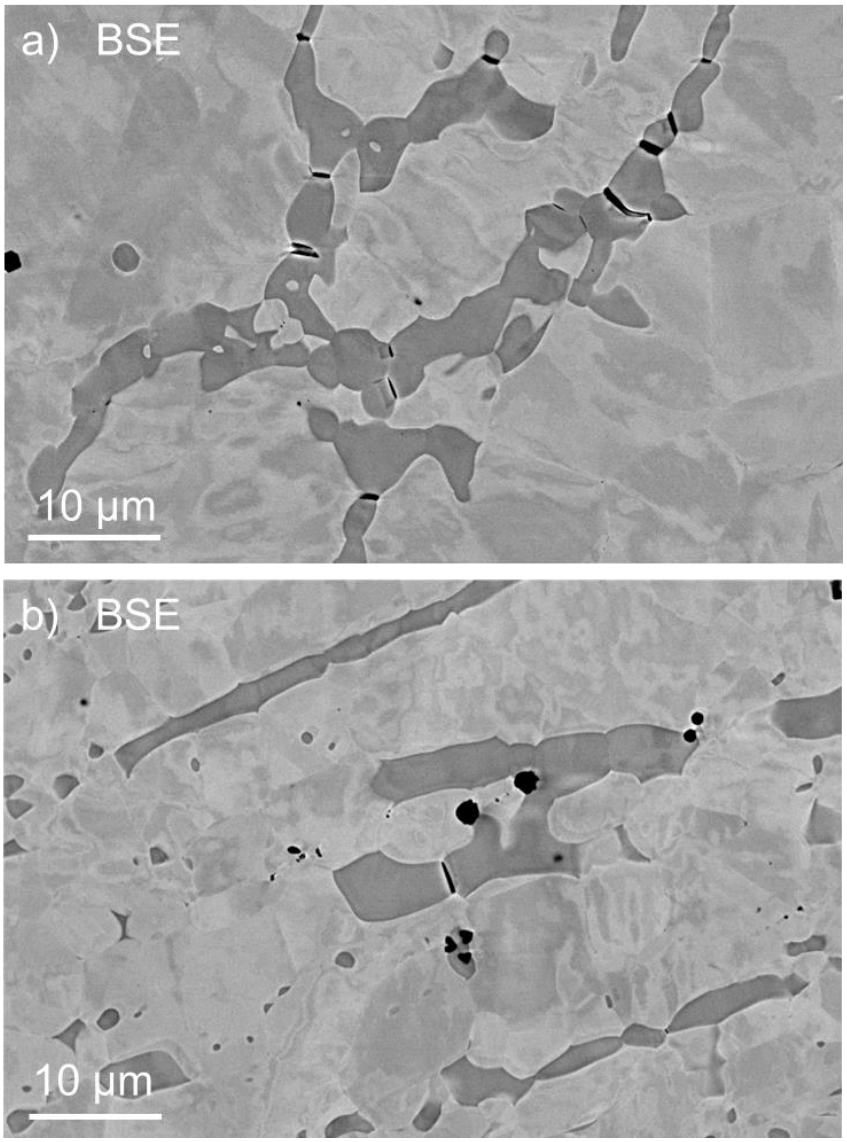

Figure 5.17: Micrographs of cracked Heusler phase grains in a) CCA 72 and b) CCA 94 after thermomechanical processing, but before straining. The presence of pre-cracked Heusler phase is expected to decrease the strength and ductility of the alloys.

Similar in-situ neutron diffraction experiments were conducted on the novel FCC + $L2_1$ CCAs. Neutron diffraction data were collected continuously then binned into 120-second intervals with a 60-second overlap between intervals, leading to some averaging between data points. Complications with sample production and processing lead to sample conditions which were not ideal for neutron diffraction. The samples of CCAs 72 (6 vol% $L2_1$ phase) and 94 (16 vol%) were 0.5 mm thick, which necessitated a longer neutron counting time for each measurement. The presence of flaws in the material, especially the presence of cracked Heusler phase particles, produced a response that may not be representative of the un-flawed material. For instance, assuming the same behavior described by the "vanishing cracked particle model" [39], a cracked second-phase particle could be represented by an equivalent volume of matrix phase. As such, if considerable pre-cracking is present in a two-phase alloy, its response will be more akin to a single-phase material and there will be little opportunity to observe the stress and strain partitioning behavior of interest. The low Heusler volume fraction in CCA 72 did not yield any Heusler peaks which could be observed above background in the diffraction measurements, and only the (220) reflection of the Heusler phase as visible in CCA 94. Despite these challenges, some materials property information was obtained and is presented below.

The macroscopic and lattice strains for CCA 94 (RD) are presented in Figure 5.18, and the corresponding diffraction elastic constant are reported in Table 5.10. As with the FCC+B2 alloys, an attempt was made to calculate the elastic stiffnesses of the FCC matrix phase in CCA 94, presented in Tabe 5.11. In the case of CCA 94, the FCC (220) peak was not tracked accurately, due to a small peak-to-background ratio during measurement arising from sample texture. It has been found previously [14] that these alloys retain a mild FCC rolling texture after annealing, which does not have many (220)-oriented grains aligned with the rolling direction. Due to this lack of signal to the axial detector bank and the difficulties of accurately tracking a small peak, the deflection of the FCC (220) strain curve to the left of the FCC (311) is likely not real. The lack of ductility in CCA 94 (see Figure 5.16) limited these tests to very small strains, as well. The unload-reload behavior of FCC and $L2_1$ lattice strains are shown in Figure 5.19. Unlike as was observed with the POSTECH alloy, there is a milder deviation from linear elastic behavior in lattice strains during unloading or reloading. However, there is still notable macroscopic strain hysteresis. It is also noted that, upon unloading, both the FCC and $L2_1$ phases are accumulating residual stresses on the order of 95-100 MPa. Despite the lack of distinguishable $L2_1$ peaks, the superior ductility of CCA 72 (RD) allowed for larger stains to be examined. The macroscopic and lattice strains are shown in Figure 5.20, in which the FCC (220) peak was tracked slightly better by the peak fitting algorithm, despite similar complicating texture effects. The diffraction elastic constants were also calculated for the FCC phase in CCA 72, reported in Table 5.12. The unload-reload behavior of the FCC (111), (200) and (220) peaks, corresponding to a stiff, a compliant and an intermediate crystallographic FCC orientation, respectively, are shown in Figure 5.21. These lattice strain data show the same deviations from linearity as were noted in Figure 5.12, albeit slightly less pronounced, meaning that there is also yielding upon unloading in CCA 72. The lattice strain data for the FCC (220) reflection are chaotic, and are considered to be subject to a large degree of experimental uncertainty. However, considering the behavior observed in the FCC (220) strains of

the POSTECH alloy, (see Figure 5.12,) and given the seeming shift towards the left in Figure 5.21b, it can be concluded that in the FCC+$L2_1$ alloys the FCC (220)-oriented grains serve a similar function of accumulating compressive strains to ensure equilibrium in the composite. Using the calculated elastic constants for CCA 94, E_{220} in CCA 72 is estimated to be 173.9 GPa. The small difference in chemistry between the two matrix phases should have no effect on the estimated modulus, which is insensitive to chemistry. Compared to an observed value of 189 GPa based on the lattice strain data, there is confidence that the behavior observed is approximately representative of the FCC (220)-oriented grains, despite the experimental uncertainty.

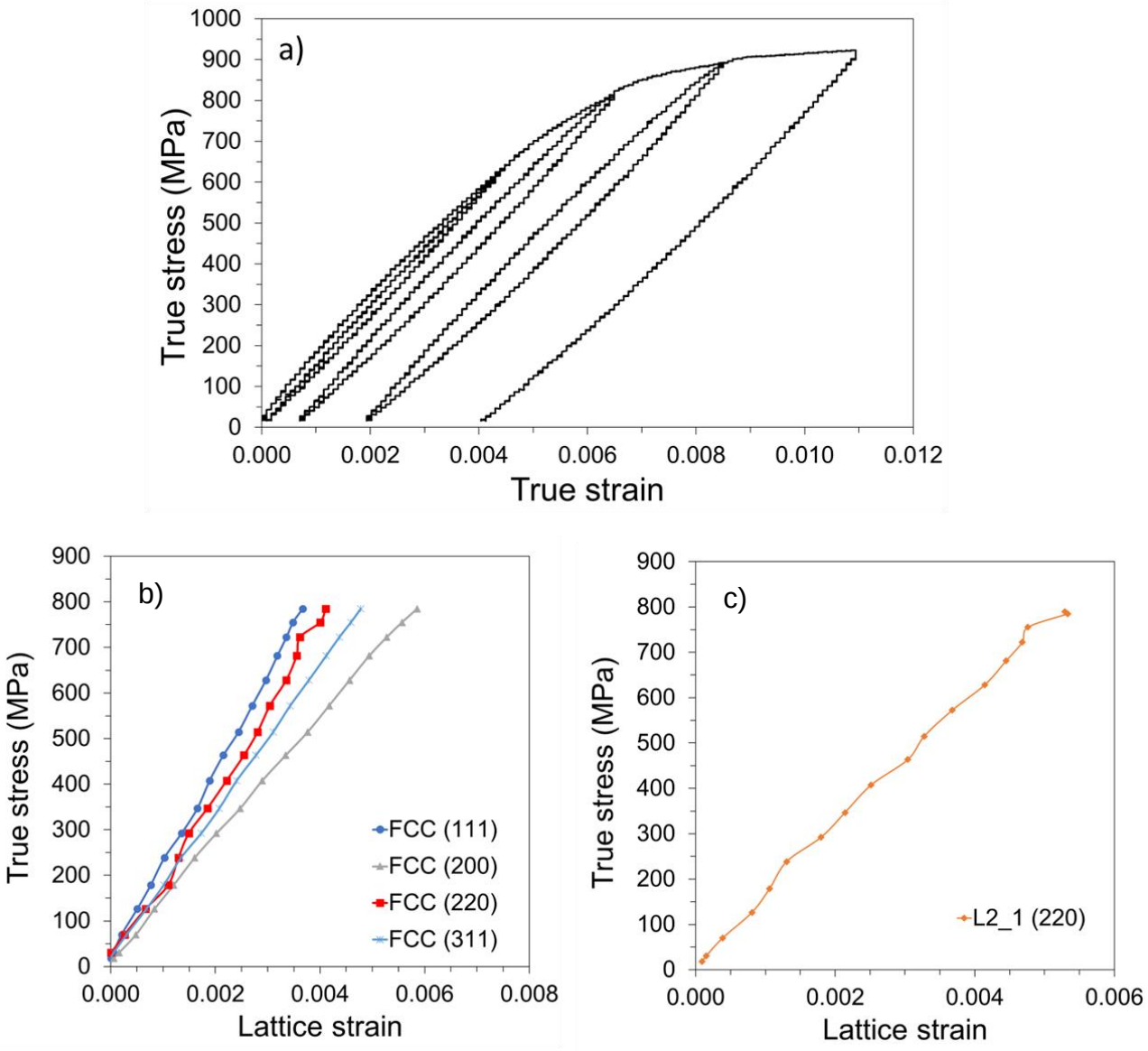

Figure 5.18: a) Load-Unload-Reload tensile strain data from the in-situ diffraction of CCA 94. Lattice strains for the b) FCC and c) $L2_1$ phases. The first reload cycle is shown due to better tracking of the FCC (220) peak. The initial deflection of strain in the FCC (220) below the FCC (311) is believed to be due to experimental noise. Only one $L2_1$ reflection, the (220), was able to be observed.

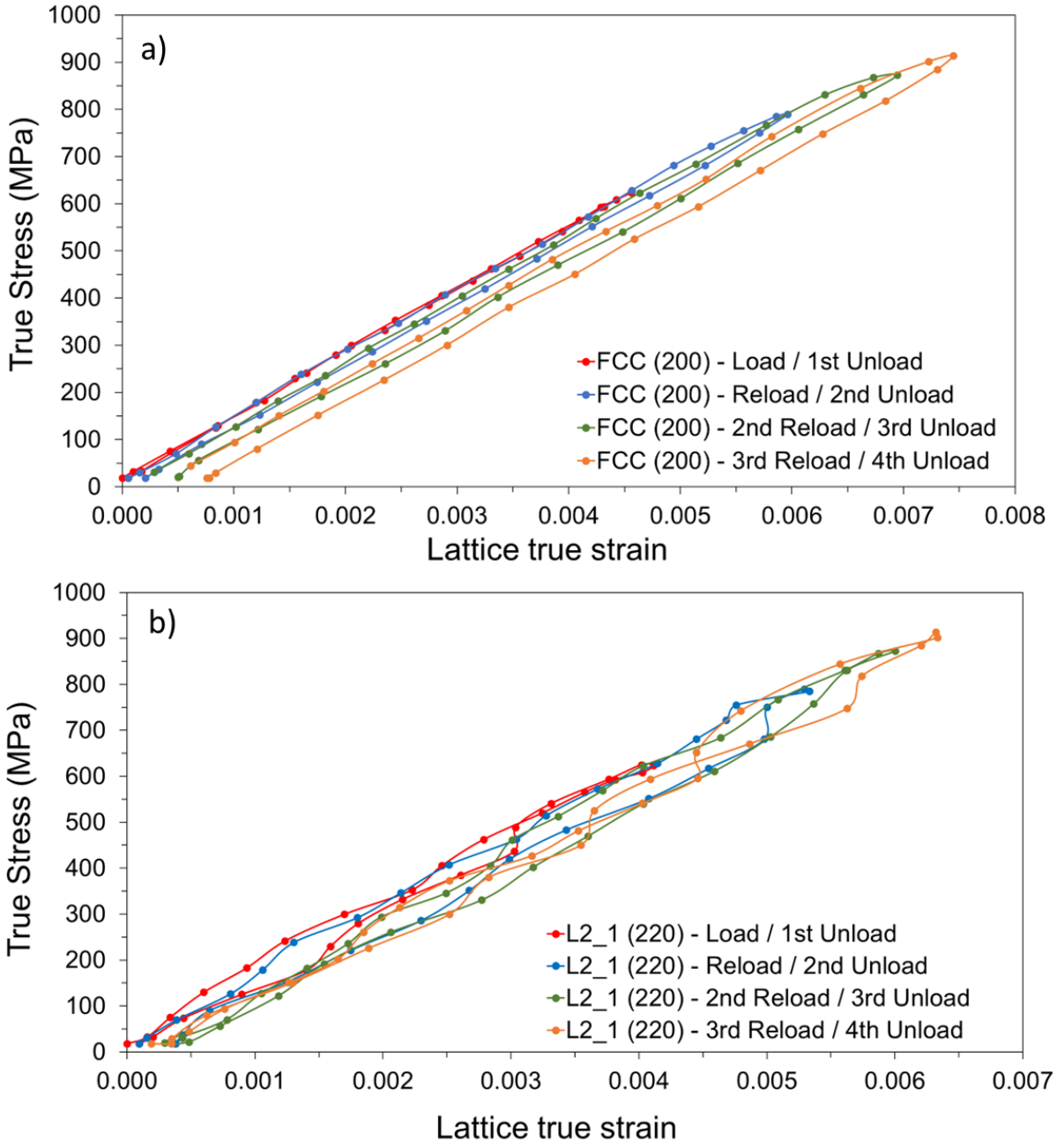

Figure 5.19: The evolution of lattice strains for the a) FCC (200) and b) $L2_1$ (220) reflections during LUR testing of CCA 94. There was no observed deviation from linearity upon unloading observed. Data in the 3rd and 4th unload cycle have been corrected by hand using a pixel-to-scale method on spectra produced by the automatic peak fit routine, which failed to fit those few points accurately.

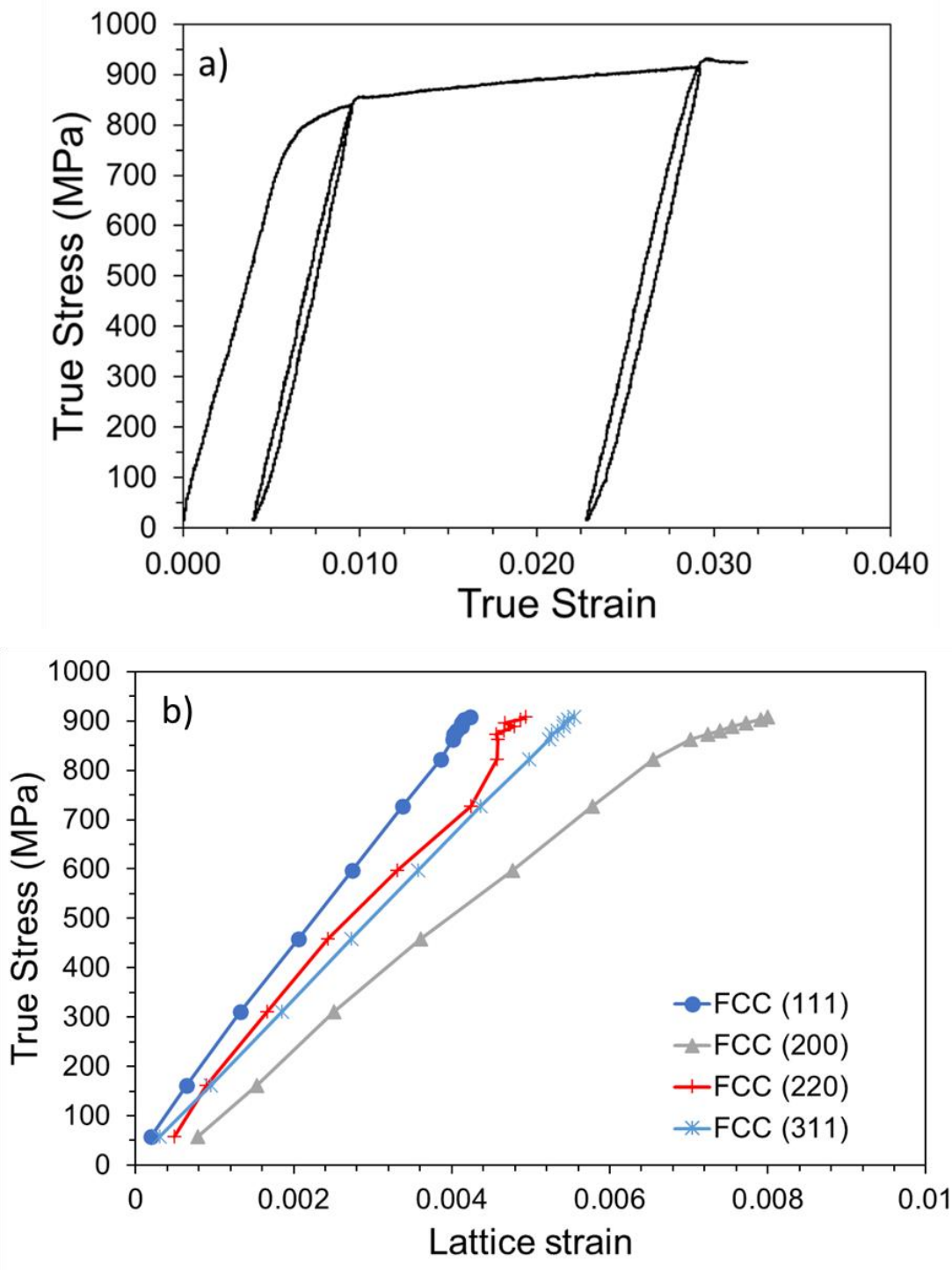

Figure 5.20: Load-Unload-Reload tensile strain data from the in-situ diffraction of CCA 72. b) Calculated lattice strains for the FCC phase. No $L2_1$ could be observed during measurement. The lattice strain data shown are from the first reload cycle. Texture effects weakened the (220) reflection, leading to uncertainty in the calculated strains.

Table 5.10: The obtained diffraction elastic moduli for each (hkl) reflection observed during LUR tension of CCA 94.

FCC	E_{hkl} (GPa)		$L2_1$	E_{hkl} (GPa)
(111)	205.8		(220)	154.5
(200)	135.3			
(220)	179.5			
(311)	160.4			

Table 5.11: The derived elastic constants of the FCC matrix phase in CCA 94. The calculated polycrystalline shear and Young's moduli as well as the calculated Zener anisotropy ratio are also reported.

(GPa)	C_{11}	C_{12}	C_{44}	μ	E	Zener ratio
FCC	178	93	88	61	167	2.08

Table 5.12: The obtained diffraction elastic moduli for each (hkl) reflection observed during LUR tension of CCA 72. The observed zero-strain interplanar spacings are also compared to predictions of the lattice spacing based on the Seitz volume of the atoms occupying the FCC unit cell.

FCC	E_{hkl} (GPa)	Predicted d (Å)	Experimental d (Å)
(111)	209.8	2.0929	2.0910
(200)	132.1	1.8125	1.8128
(220)	189.0	1.2816	1.2813
(311)	163.2	1.0930	1.0920

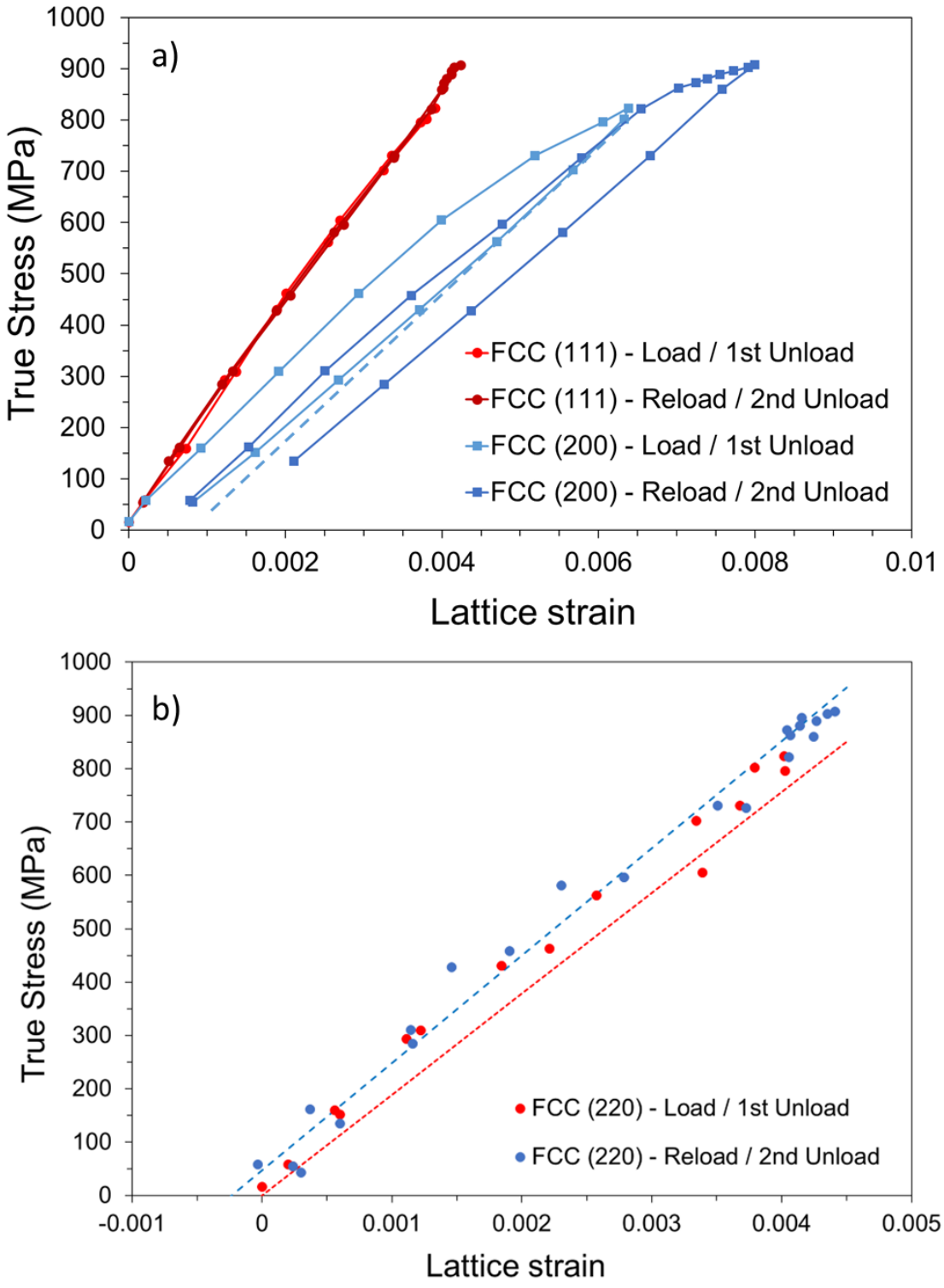

Figure 5.21: The evolution of lattice strains for the a) FCC (111) and b) FCC (200) reflections during L-U-R testing of CCA 72. Despite experimental uncertainty, compressive strains can be seen to build within FCC (220)-oriented grains.

5.5 Discussion

In the context of the alloying strategy described in [17], a trend of decreasing solid solution strengthening is observed with increasing nominal Al concentration in the alloy. As Al is added, additional Ni and Ti are depleted from the matrix in order to form additional Ni_2TiAl. While Ti has a more potent size effect, Ni is depleted in greater quantities to form more of the Ni_2TiAl Heusler phase, which together decrease the expected strengthening. The Hall-Petch strengthening effect increases as the volume fraction of Heusler phase increases, which is to be expected given the effect the Heusler phase has on refining the austenite grain size [14]. The trend between microhardness and Heusler phase volume fraction is undeniable, and it is easily seen that the $L2_1$ phase is very hard compared to the matrix. While one should always be careful when applying upper- or lower-bound estimations using the rule of mixtures, it is useful here to consider these trends, given the uncertainty of the experimentally measured properties. Applying Tabor's method for relating microhardness to yield strength for purely qualitative purposes, one can estimate the yield strength of the FCC matrix to be about 513 MPa, and the strength of the $L2_1$ to be about 1952 MPa. At a yield strength of 513 MPa, (compared to 670 MPa observed experimentally,) solid solution and grain boundary contributions of 173 and 63 MPa, respectively, leave 277 MPa to be attributed to Taylor hardening in the single-phase alloy. This corresponds to a dislocation density on the order of $5x10^{14}m^{-2}$, which is somewhat more consistent with the supposed level of cold work. Using the hardness-derived strength approximations, the upper-bound strengths of CCAs 72 (6 vol%) and 91 (25 vol%) would be 599 and 873 MPa, respectively, compared to observed values of 600 MPa and 860 MPa. The corresponding lower-bound approximations would be 537 and 629 MPa, respectively. These estimations cast the experimentally observed values in a positive light; despite the experimental complications, the values obtained are reasonable. However, the truth of these materials is found between the upper and lower bound, which is an area best explored by things such as self-consistent crystal plasticity modeling.

The simple tension and load-unload-reload tests conducted on the POSTECH alloy at UVA served the purpose of setting expectations for the in-situ neutron diffraction experiments. No new tensile behavior outside of what is reported in the literature was observed, aside from the increased strength of the non-banded material which can be attributed to the fine microstructure of both the matrix and B2 precipitates. The strengthening provided by interstitial C is clearly apparent in all of the tensile data, and while the hysteresis loops are compact, there does appear to be some level of a Bauschinger effect which arises through similar intergranular and interphase sources as were observed in the FCC+$L2_1$ alloys.

Simple tension and load-unload-reload experiments on the dual-phase FCC+$L2_1$ CCAs were complicated by differences in processing, ultimately due to the small-batch nature of sample production. Despite these difficulties, mechanical data were acquired that might serve as evidence of these alloys' potential as engineering materials. Between CCAs 81 and 91, both of which showed signs of being only partially recrystallized, the presence of 25% Heusler phase in CCA 91 increased the yield strength by 190 MPa and the ultimate tensile strength by 262 MPa. It is worth noting that the increase in yield strength falls below the predicted difference in Hall-Petch

strengthening between the two alloys of 320 MPa. This could be due to the partially recrystallized state of both samples, which would suggest that the single-phase material has achieved a higher dislocation density than the 25 vol%-$L2_1$ alloy. A Williamson-Hall analysis [14] did find that CCA 81 exhibited a steeper slope in the as-worked state, which supports that observation, though without a quantification of dislocation density in the two materials it is difficult to say if this could explain the remaining 130 MPa. The use of an average Hall-Petch coefficient for stainless steel may not have been appropriate, as stainless steel tends to have low stacking fault energy (SFE), whereas the FCC+$L2_1$ alloys possess intermediate SFE. At higher levels of cold work, higher-SFE materials have been found to exhibit stronger Hall-Petch effects [46], and the present alloys of interest have been shown previously to maintain aspects of a cold-worked microstricture even after annealing [14]. Use of the maximum value of the Hall-Petch coefficient for stainless steel found in the literature ($320.4\ \mathrm{MPa}\sqrt{\mu\mathrm{m}}$) yields a tensile strength contribution of 134 – 566 MPa.

An examination of the strain hysteresis of CCA 72 revealed an average strengthening effect upon reload of 171 MPa, though sufficient evidence has not been found to definitively attribute that strengthening to back stresses caused by the Heusler phase, as opposed to interactions between FCC grains. The finer details of composite effects, stress and strain partitioning, etc. cannot be determined by simple mechanical testing alone, and are better explored with techniques that can distinguish between phases, such as neutron diffraction. Observation of cracked Heusler grains in the deformed microstructures yielded valuable information for crystal plasticity modeling efforts, justifying the use of the so-called "Vanishing Cracked Particle" model [39] over other methods of tracking damage accumulation during straining. The proper implementation of such models will still require phase-specific mechanical and elastic properties, however. It is recommended that additional experimentation be performed to determine these properties, and nanoindentation may be useful in this regard.

The capabilities of in-situ neutron diffraction for providing phase-specific elastic properties and elucidating composite behavior was well demonstrated with the POSTECH alloys. Lattice strain data have revealed that while the FCC matrix is elastically anisotropic, the B2-FeAl phase is close to elastically isotropic (i.e. a Zener ratio of 1.5, where 1.0 would be anisotropic). Diffraction elastic moduli were obtained for each phase, which allowed for the calculation of the elastic constants of each phase. In addition to clear evidence of yielding upon the release of stress, which can be attributed to the accumulation of back stresses due to the presence of a second phase, examination of the hysteresis loops also revealed a gradual decrease in the composite Young's modulus. Such a decrease has been noted previously in the literature, and there are two probable explanations. Following Celentano and Chaboche [40], this evolution can be viewed as the accumulation of plastic damage in a ductile material. This damage generally takes the form of microcracks and cavities, and the accumulation of damage leads to a decrease in material strength, stiffness and toughness, etc. In the case of a composite material, the fracture or debonding of a reinforcing phase particle could also be considered two such forms of damage which accumulates and deleteriously affects material properties [39]. Other authors, such as Yoshida et al. [38][41] and Chen and Wagoner [42][43] view this degradation in Young's modulus as a function of the accumulation of plastic strain within the material, with no necessary relation to the formation of flaws or damage. Yoshida et al. propose a "Chord modulus" [38] which depends upon the initial

modulus, an asymptotic lower-bound modulus and the total plastic strain. Between the two classes of alloy examined, the POSTECH alloys appeared to reach a lower bound, likely due to those alloys achieving large strains. The FCC+$L2_1$ alloys, which received much more closely-spaced load and unload cycles better resembled an exponential decrease. Taken together, both classes of alloy show behavior in agreement with Yoshida et al.'s model. It should be noted that the accumulation of plastic strain within a material and the accumulation of damage, especially that of fractured particles in a dual-phase material, are not mutually exclusive. However, considering the presence of some level of strain hysteresis in both the POSTECH and FCC+$L2_1$ alloys, both that hysteresis and a decrease in the Young's modulus as a function of strain can be explained by the accumulation of dislocations due to intergranular and possibly interphase back-stresses.

Within the lattice strain data of the non-banded POSTECH material, a yield event can be clearly seen as a deflection in each reflection from their elastic behavior. However, perhaps due to the incremental nature of the neutron measurements a distinct yield event in each phase is not visible, and as such the B2 phase is assumed to yield shortly after the austenite. Using Hooke's Law, the diffraction elastic modulus of each phase in the non-banded POSTECH alloy and the lattice strain at the lower yield point, the stress borne by each group of grains oriented along a particular direction can be approximated. Using the strain and diffraction elastic modulus of the middle-most FCC reflection (111), (which yielded first,) and the B2 (211) reflection, produces the yield strengths of the FCC and B2 phases as 990 MPa and 1575 MPa, respectively. The FCC (200) and B2 (211) both show a point of inflection at 1163 MPa applied stress, which was taken as the yield point of the B2 phase (Figure 5.10). However, the possibility exists that an orientation relationship (i.e. Kurdjumov-Sachs or Nishiyama-Wasserman, etc.) exists between the two phases such that they would flow together. Definitive evidence of an orientation relationship could not be located in the literature. The estimated strength of the austenite agrees will with estimations based on Hall-Petch and precipitation strengthening reported in the literature of 937 MPa [2], but the estimated strength of the B2 phase disagrees specifically with the Hall-Petch-based estimation of the strength of polygonal B2-FeAl precipitates in the same study, reported as 2373 MPa in the non-banded material. However, in the banded material, the strength of polygonal B2 is reported as 1404 MPa, and the strength of retained B2-bands is reported as 1525 MPa, which agree very well with the observed strength of the B2 phase. This departure from previously recorded behavior could be explained through either the consideration of composite effects, such as the superposition of a hydrostatic stress caused by the deforming austenite matrix on the B2, causing it to yield at a lower applied stress than would be expected, or simply through differences in B2 morphology despite similar thermomechanical processing. The (211) reflection of the B2 phase does show a significant increase in lattice strain corresponding to stress partitioning to the B2 phase, which may provide the aforementioned pressure.

The capabilities of in-situ neutron diffraction for the examination of dual-phase alloys were well demonstrated, allowing at minimum a determination of single crystal elastic constants for the FCC matrix phase. These data essential for any sort of micromechanical modeling of the mechanical properties of these materials. The lackluster results obtained for the Heusler phase suggest that repeat testing with thicker samples containing a higher fraction ($\geq$16 vol%) would yield the necessary information to obtain the elastic constants of the constituent phases. It is further

suggested that nanoindentation may be a useful tool for determining the phase-specific elastic properties of this material. Such testing necessitates the ability to produce larger quantities of the dual-phase CCAs that may be rolled to a suitable thickness without fracturing the Heusler phase. The diffraction elastic moduli obtained for the FCC matrix phase are on par with those observed in the POSTECH alloy, as well as the yield strengths of the LUR samples. The observed yield in reverse of the lattice strain data suggests an accumulation of dislocations which is likely due to intergranular back stresses. It is possible that the previously mentioned intragranular sources of reduced resistance to dislocation motion in reverse [19] are also at work, however the majority of the hardening in the FCC+$L2_1$ alloys was shown to be kinematic in nature. There is also insufficient evidence to determine what portion of this hardening is due to interphase interactions, though the geometrically necessary dislocation structures introduced by a second phase could contribute to the observed increase in back stress as a function of straining. The yielding observed upon unloading, combined with the decrease in composite Young's modulus with increasing strain strongly suggests that the mechanism described by Yoshida et al. is active in these materials. As such, it is believed that the majority of the back stress observed in the present study is intragranular in nature, having more to do with heterogeneous dislocation distributions (i.e. "softer" orientations yielding before "harder" ones,) and the long-range stresses which arise as a result of the need for compatibility during plastic deformation [44].

5.6 Conclusions

The observed yield strength for the novel FCC+$L2_1$ composite alloys fell between 600 and 900 MPa, which fall within upper- and lower-bound approximations based on the respective microhardness of the component phases. Experimental complications prevented a precise correlation between the Heusler phase content and alloy yield strength. There is, however, a strong linear relationship between alloy microhardness and Heusler phase content, suggestive of an upper-bound rule of mixtures relationship. Estimations based on hardness suggest the strength of the FCC matrix phase is about 500 MPa, and the strength of the Heusler phase could be near 2 GPa.

A mole fraction-weighted average of atomic radii agreed with those measured experimentally using X-ray diffraction. This is a prerequisite of the Varvenne et al. model employed to estimate solid solution strengthening. This model relies on deviations from the mean atomic radius, and as such, Ti and Ni were found to be the most consequential additions in terms of size difference and abundance. The critical resolved shear stresses for the FCC+$L2_1$ studied alloys which can be attributed to solid solution strengthening were estimated using this model and found to be 54.6 to 56.7 MPa. After adjustment by the Taylor factor (M = 3.06), this translates to a tensile yield strength contribution of 147 - 174 MPa.

The previously determined grain size (see Table 5.4) of the FCC+$L2_1$ alloys was used to estimate the Hall-Petch strengthening contribution. This estimation produced shear stresses of 20.5 to 86.6 MPa, translating to yield strength contributions of 63 – 383 MPa. Use of the maximum

value of the Hall-Petch coefficient yields a tensile strength contribution of 134 – 566 MPa. Regardless of the exact magnitude of the Hall-Petch effect in these alloys, the effect that the Heusler phase has in refining the austenite grain size is revealed to be significant.

The contribution of Taylor (dislocation density-based) hardening of the single-phase alloy, CCA 81 was estimated by subtracting the predicted contributions of solid solution strengthening and the Hall-Petch effect from the observed strength, and this left over 400 MPa to be explained. This was deemed infeasible as an amount of dislocation hardening for an annealed material suggesting that the solid solution or grain size strengthening effect has been underestimated.

Both the FCC+B2 POSTECH alloys and FCC+$L2_1$ CCAs showed a Bauschinger effect, including yielding in reverse upon unloading, and that strain hysteresis was more pronounced in the FCC+$L2_1$ alloys. The majority of hardening in these systems can be attributed to back stresses, but without further study it is not possible to quantitatively parse these back stresses between interphase, intergranular, and intragranular / dislocation-based sources. Significant peak broadening in the neutron strain data was not observed, so intragranular back stresses are likely the lesser of the three.

Diffraction elastic moduli were obtained for both classes of alloy. Elastic constants for the FCC+B2 steels were derived from the measured moduli: For the FCC matrix, C_{11} = 174 GPa, C_{12} = 112 GPa, C_{44} = 99 GPa, μ = 56 GPa, E = 159 GPa and Zener anisotropy ratio Z = 3.17, and for the B2 phase, C_{11} = 260 GPa, C_{12} = 162 GPa, C_{44} = 77 GPa, μ = 61 GPa, E = 174 GPa and a nearly-isotropic Z = 1.57.

Using yield events in the lattice strain data, the yield strength of the FCC matrix and B2 reinforcement were found to be 990 MPa and 1575 MPa, respectively. The tests also reveal that the high carbon added to the Fe-Mn-Al-Ni-C alloy is the major source of strength.

Elastic constants were also derived for the FCC matrix of the FCC+$L2_1$ CCAs: C_{11} = 178 GPa, C_{12} = 93 GPa, C_{44} = 88 GPa, μ = 61 GPa, E = 167 GPa and Z = 2.08. There was no distinctive yield event observed in the $L2_1$ (220) lattice strain data. Examining the macroscopic strain data also revealed a strain-dependent decline in the composite Young's modulus consistent with the effects of dislocation accumulation described by F. Yoshida and colleagues which is also consistent with the effects of back stresses observed.

5.7 Acknowledgements

The author would like to thank the Office of Naval Research for their support through ONR BAA #N00014-18-1-2621, directed by Dr. Airan Perez and Dr. David Shifler.

5.8 References

[1] S. Kim, H. Kim, and N. J. Kim, “Brittle intermetallic compound makes ultrastrong low-density steel with large ductility,” Nature, vol. 518, pp. 77–79, 2014, doi: 10.1038/nature14144.

[2] G. Park, C. H. Nam, A. Zargaran, and N. J. Kim, “Effect of B2 morphology on the mechanical properties of B2-strengthened lightweight steels,” Scr. Mater., vol. 165, pp. 68–72, 2019, doi: 10.1016/j.scriptamat.2019.02.013.

[3] R. W. Hertzberg, R. P. Vinci, and J. L. Hertzberg, “Yielding and Plastic Flow,” in Deformation and Fracture Mechanics of Engineering Materials, 5th ed., John Wiley & Sons, Inc., 2013, pp. 63–142.

[4] G. P. M. Leyson and W. A. Curtin, “Friedel vs. Labusch: the strong/weak pinning transition in solute strengthened metals,” Philos. Mag., vol. 93, no. 19, pp. 2428–2444, 2013.

[5] R. L. Fleischer, “Substitutional solution hardening,” Acta Metall., vol. 11, no. 3, pp. 203–209, 1963, doi: 10.1016/0001-6160(63)90213-X.

[6] G. P. M. Leyson, W. A. Curtin, L. G. Hector, and C. F. Woodward, “Quantitative prediction of solute strengthening in aluminium alloys,” Nat. Mater., vol. 9, no. 9, pp. 750–755, 2010, doi: 10.1038/nmat2813.

[7] Z. Wu, Y. Gao, and H. Bei, “Thermal activation mechanisms and Labusch-type strengthening analysis for a family of high-entropy and equiatomic solid-solution alloys,” Acta Mater., vol. 120, pp. 108–119, 2016, doi: 10.1016/j.actamat.2016.08.047.

[8] G. P. M. Leyson, L. G. Hector, and W. A. Curtin, “Solute strengthening from first principles and application to aluminum alloys,” Acta Mater., vol. 60, no. 9, pp. 3873–3884, 2012, doi: 10.1016/j.actamat.2012.03.037.

[9] A. Luque and W. A. Curtin, “Theory of strengthening in fcc high entropy alloys,” Acta Mater., vol. 118, pp. 164–176, 2016, doi: 10.1016/j.actamat.2016.07.040.

[10] C. Varvenne and W. A. Curtin, “Predicting yield strengths of noble metal high entropy alloys,” Scr. Mater., vol. 142, pp. 92–95, 2018, doi: 10.1016/j.scriptamat.2017.08.030.

[11] R. Zhang et al., “Short-range order and its impact on the CrCoNi medium-entropy alloy,” Nature, vol. 581, no. 7808, pp. 283–287, 2020, doi: 10.1038/s41586-020-2275-z.

[12] L. Li et al., “Evolution of short-range order and its effects on the plastic deformation behavior of single crystals of the equiatomic Cr-Co-Ni medium-entropy alloy,” Acta Mater., vol. 243, no. November 2022, 2023, doi: 10.1016/j.actamat.2022.118537.

[13] R. W. Hertzberg, R. P. Vinci, and J. L. Hertzberg, “Controlling Strength,” in Deformation and Fracture Mechanics of Engineering Materials, 5th ed., John Wiley & Sons, Inc., 2013, pp. 143–188.

[14] M. A. Wischhusen et al., “The Thermomechanical Processing Response of FCC+L21 Composites,” Manuscr. Prep.

[15] J. J. Bhattacharyya and S. R. Agnew, “Microstructure Design of Multiphase Alloys I - Effects of Strength Contrast and Strain Hardening,” J. Mech. Phys. Solids, no. Manuscript submitted for publication.

[16] J. J. Bhattacharyya, M. A. Wischhusen, and S. R. Agnew, “Microstructure Design of Multiphase Alloys II - Use of a Genetic Algorithm and a Vanishing Cracked Particle Model,” J. Mech. Phys. Solids, no. Manuscript submitted for publication.

[17] M. A. Wischhusen et al., “Al-stabilized L21-Heusler phase in FCC Compositionally Complex Alloys and Control of its Volume Fraction,” Manuscr. Prep., 2024.

[18] T. H. Courtney, “Strengthening of Crystalline Materials,” in Mechanical Behavior of Materials, McGraw-Hill Publishing Company, 1990, pp. 162–219.
[19] J. A. Wollmershauser, “Mechanical Behavior of Polycrystals,” University of Virginia, 2011.
[20] M. Sauzay, “Analytical modelling of intragranular backstresses due to deformation induced dislocation microstructures,” Int. J. Plast., vol. 24, no. 5, pp. 727–745, 2008, doi: 10.1016/j.ijplas.2007.07.004.
[21] W. Cai and W. D. Nix, “Point Defect Mechanics,” in Imperfections in Crystalline Solids, Cambridge University Press, 2016, pp. 71–100.
[22] H. W. King, “Quantitative size-factors for metallic solid solutions,” J. Mater. Sci., vol. 1, pp. 79–90, 1966.
[23] C. Varvenne, A. Luque, and W. A. Curtin, “Theory of strengthening in fcc high entropy alloys,” Acta Mater., vol. 118, pp. 164–176, 2016, doi: 10.1016/j.actamat.2016.07.040.
[24] W. Cai and W. D. Nix, “Appendix A: King Table for Solid Solutions,” in Imperfections in Crystalline Solids, Cambridge University Press, 2016, pp. 488–496.
[25] B. A. Szajewski, F. Pavia, and W. A. Curtin, “Robust atomistic calculation of dislocation line tension,” Model. Simul. Mater. Sci. Eng., vol. 23, 2015, doi: 10.1088/0965-0393/23/8/085008.
[26] B. P. Kashyap and K. Tangri, “On the Hall-Petch relationship and substructural evolution in type 316L stainless steel,” Acta Metall. Mater., vol. 43, no. 11, pp. 3971–3981, 1995, [Online]. Available: https://doi.org/10.1016/0956-7151(95)00110-H.
[27] P. Follansbee, “Contributions to Strength,” in Fundamentals of Strength, The Minera., Springer, 2014.
[28] X. Feaugas and H. Haddou, “Grain-size effects on tensile behavior of nickel and AlSl 316L stainless steel,” Metall. Mater. Trans. A Phys. Metall. Mater. Sci., vol. 34 A, no. 10, pp. 2329–2340, 2003, doi: 10.1007/s11661-003-0296-5.
[29] K. K. Singh, S. Sangal, and G. S. Murty, “Hall-Petch behaviour of 316L austenitic stainless steel at room temperature,” Mater. Sci. Technol., vol. 18, no. 2, pp. 165–172, 2002, doi: 10.1179/026708301125000384.
[30] C. A. Bronkhorst, J. R. Mayeur, V. Livescu, R. Pokharel, D. W. Brown, and G. T. Gray, “Structural representation of additively manufactured 316L austenitic stainless steel,” Int. J. Plast., vol. 118, no. November 2018, pp. 70–86, 2019, doi: 10.1016/j.ijplas.2019.01.012.
[31] C. S. Kusko, J. N. Dupont, and A. R. Marder, “Influence of stress ratio on fatigue crack propagation behavior of stainless steel welds,” Weld. J. (Miami, Fla), vol. 83, no. 2, 2004.
[32] ORNL, “Neutron Sciences Directorate,” Sample Geometry - Mechanical Test. 2022, Accessed: Jan. 06, 2022. [Online]. Available: https://neutrons.ornl.gov/vulcan/users.
[33] K. An, “VDRIVE- Data Reduction and Interactive Visualization Software for Event Mode Neutron Diffraction,” Oak Ridge, TN, 2012.
[34] A. C. Larson and R. B. Von Dreele, “General structure analysis system (GSAS),” Los Alamos, New Mexico, 2004.
[35] B. H. Toby, “EXPGUI, a graphical user interface for GSAS,” J. Appl. Crystallogr., vol. 34, no. 2, pp. 210–213, 2001, doi: 10.1107/S0021889801002242.
[36] Y. Zhang, W. Chen, D. L. McDowell, Y. M. Wang, and T. Zhu, “Lattice strains and diffraction elastic constants of cubic polycrystals,” J. Mech. Phys. Solids, vol. 138, 2020, doi: 10.1016/j.jmps.2020.103899.
[37] A. M. Cantara, M. Zecevic, A. Eghtesad, C. M. Poulin, and M. Knezevic, “Predicting elastic

anisotropy of dual-phase steels based on crystal mechanics and microstructure," Int. J. Mech. Sci., vol. 151, no. December 2018, pp. 639–649, 2019, doi: 10.1016/j.ijmecsci.2018.12.021.
[38] M. Yang, Y. Akiyama, and T. Sasaki, "Evaluation of change in material properties due to plastic deformation," J. Mater. Process. Tech., vol. 151, pp. 232–236, 2004, doi: 10.1016/j.jmatprotec.2004.04.114.
[39] F. Yoshida, T. Uemori, and K. Fujiwara, "Elastic – plastic behavior of steel sheets under in-plane cyclic tension – compression at large strain," Int. J. Plast., vol. 18, pp. 633–659, 2002.
[40] R. Mueller, A. Rossoll, L. Weber, M. A. M. Bourke, D. C. Dunand, and A. Mortensen, "Tensile flow stress of ceramic particle-reinforced metal in the presence of particle cracking," Acta Mater., vol. 56, no. 16, pp. 4402–4416, 2008, doi: 10.1016/j.actamat.2008.05.004.
[41] D. J. Celentano and J. Chaboche, "Experimental and numerical characterization of damage evolution in steels," vol. 23, pp. 1739–1762, 2007, doi: 10.1016/j.ijplas.2007.03.008.
[42] F. Yoshida and T. Amaishi, "Model for description of nonlinear unloading-reloading stress-strain response with special reference to plastic-strain dependent chord modulus," Int. J. Plast., vol. 130, no. February, p. 102708, 2020, doi: 10.1016/j.ijplas.2020.102708.
[43] Z. Chen, U. Gandhi, J. Lee, and R. H. Wagoner, "Variation and consistency of Young ' s modulus in steel," J. Mater. Process. Tech., vol. 227, pp. 227–243, 2016, doi: 10.1016/j.jmatprotec.2015.08.024.
[44] Z. Chen, H. Jong, D. Li, and R. H. Wagoner, "The elastic-plastic transition of metals," Int. J. Plast., vol. 83, pp. 178–201, 2016, doi: 10.1016/j.ijplas.2016.04.009.
[45] H. Mughrabi, "Long-Range Wall and Cell Structures and Internal Stresses in Deformend Metal Crystal," Acta Met., vol. 31, no. 9, pp. 1367–1379, 1983.
[46] S.-L. Wang and L. E. Murr, "Effect of prestrain and stacking-fault energy on the application of the Hall-Petch relation in fcc metals and alloys," *Metallography*, vol. 13, no. 3, pp. 203–224, 1980, doi: https://doi.org/10.1016/0026-0800(80)90001-4.

6.1 Conclusions

The second phase observed in the synthesized CCAs was positively identified as the $L2_1$, Ni_2TiAl Heusler phase. Using Thermo-Calc software, Al concentration was determined to be the most potent single element for the control of the volume fraction of the Heusler phase. Ti was predicted to promote the Heusler phase to a greater extent, but also to lower the melting point below the chosen homogenization temperature of 1070 °C. Despite its large presence in the Heusler phase, Ni was predicted to stabilize the FCC phase, rather than promote additional Heusler formation. The extent of the FCC-$L2_1$ two-phase region was determined as a function of Al concentration, and while the predicted boundaries were later shown to not be perfectly accurate, they were still accurate enough to assist design efforts to control the $L2_1$ volume faction through alloy chemistry. In the case of CCA 72, which was predicted to be single-phase but contained Heusler phase, Scheil cooling simulations revealed that solute enrichment during solidification of the FCC matrix led to the formation of interdendritic Heusler phase.

The dual-phase, FCC+$L2_1$ compositionally complex alloys studied were able to be cold rolled to reductions of 70% or more, with those having smaller $L2_1$ volume fractions being more workable. In general, the Heusler phase deformed plastically without cracking. Recrystallization occurred rapidly at 1070°C, which is on par with more common dual-phase alloys, and likely occurs through a mechanism of continuous recrystallization. Austenite grain boundaries are generally associated with Heusler phase grains, which likely serve as barriers against coarsening of the FCC phase. A clear trend was observed between Heusler phase vol% and austenite grain size refinement, up to two orders of magnitude smaller in grain size compared to the Heusler-free matrix. A large number of 60° <111> annealing twins were observed in recrystallized austenite grains. The deformed and annealed textures suggest that the austenite matrix behaved similarly to austenitic stainless steel, and the Heusler phase behaved similarly to a BCC metal alloy, developing an {*hkl*}<111> pencil glide texture.

The observed yield strength for the novel FCC+$L2_1$ composite alloys fell between 600 and 900 MPa. Experimental complications prevented a precise correlation between the Heusler phase content and alloy yield strength, however estimations based on hardness suggest the strength of the FCC matrix phase is about 500 MPa, and the strength of the Heusler phase could be near 2 GPa.

The contribution of Taylor (dislocation density-based) hardening of the single-phase alloy, CCA 81, could not be accurately quantified, however a Bauschinger effect was observed and analysis revealed that the majority of hardening in this class of dual-phase, FCC+$L2_1$ alloys can be attributed to back stresses, but without further study it is not possible to quantitatively parse these back stresses between interphase, intergranular, and intragranular / dislocation-based sources.

Diffraction elastic moduli were obtained for both classes of alloy. Elastic constants for the FCC+B2 steels were derived from the measured moduli; for the FCC matrix, C_{11} = 174 GPa, C_{12} = 112 GPa, C_{44} = 99 GPa, μ = 56 GPa, E = 159 GPa and Zener anisotropy ratio Z = 3.17, and

for the B2 phase, C_{11} = 260 GPa, C_{12} = 162 GPa, C_{44} = 77 GPa, μ = 61 GPa, E = 174 GPa and a nearly-isotropic Z = 1.57. Using yield events in the lattice strain data, the yield strength of the FCC matrix and B2 reinforcement were found to be 990 MPa and 1575 MPa, respectively. The tests also reveal that the high carbon added to the Fe-Mn-Al-Ni-C alloy is the major source of strength.

Elastic constants were also derived for the FCC matrix of the FCC+$L2_1$ CCAs: C_{11} = 178 GPa, C_{12} = 93 GPa, C_{44} = 88 GPa, μ = 61 GPa, E = 167 GPa and Z = 2.08. There was no distinctive yield event observed in the $L2_1$ (220) lattice strain data. Examining the macroscopic strain data also revealed a strain-dependent decline in the composite Young's modulus consistent with the effects of dislocation accumulation described by F. Yoshida and colleagues which is also consistent with the effects of back stresses observed.

6.2 Future Work

First and foremost, it is recommended that alloys are synthesized from compositions along the tie-line identified in Chapter 3. It will be easier to judge the effects of Heusler phase reinforcement if phase chemistries are kept constant. Furthermore, it would be advantageous to locate a collaborating university or vendor that is able to produce and process (via hot and/or cold rolling) larger quantities of CCA. Irregularities in sample chemistry and processing history have had a deleterious effect on the clarity of the obtained data, which could be eliminated if all samples originated from the same large batch. This will allow for a robust repeat of mechanical testing which can properly probe the effects of Heusler phase vol% and straining direction.

Questions remain as to the properties of the individual phases in the FCC+$L2_1$ CCAs. There are many possible experimental techniques that could be used, including neutron diffraction on thicker samples, nanoindentation, and possible resonant ultrasound spectroscopy (RUS). A more successful neutron diffraction experiment on FCC+$L2_1$ composites would allow for measurement of diffraction elastic moduli for each phase and calculation of their respective elastic constants, as was done for the FCC+B2 steel. Neutron diffraction will also enable an examination of interphase and intragranular sources of back-stress. A combination of nanoindentation and RUS capabilities are currently present at UVA which would circumvent the need to propose experiments to a national user facility. Nanoindentation could provide the hardness, Young's moduli and strain rate sensitivity of each component phase, and RUS could be performed on alloys (synthesized from the tie-line) of pure FCC or Heusler phase to determine the elastic constants of each.